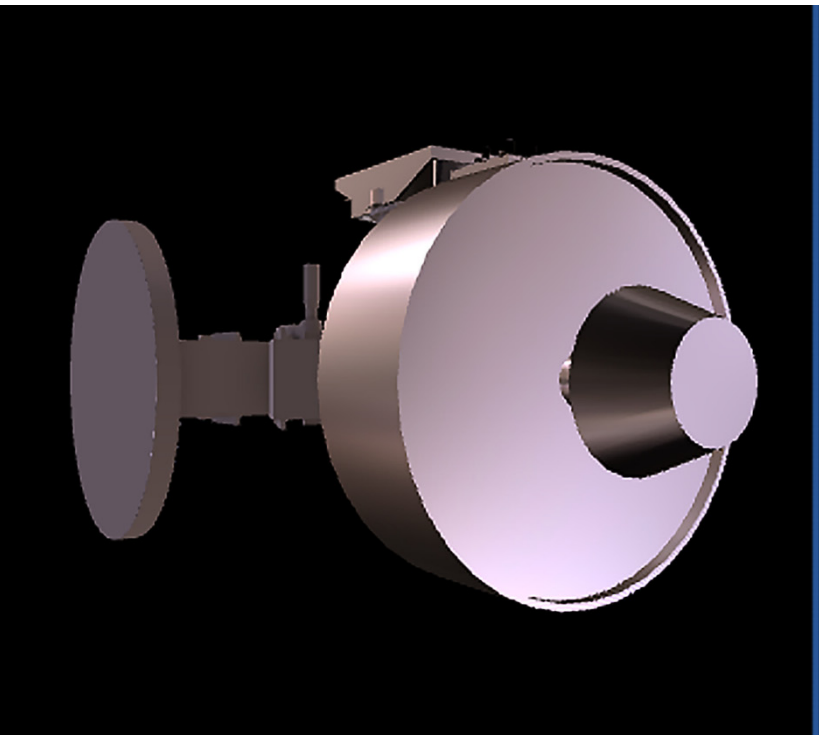

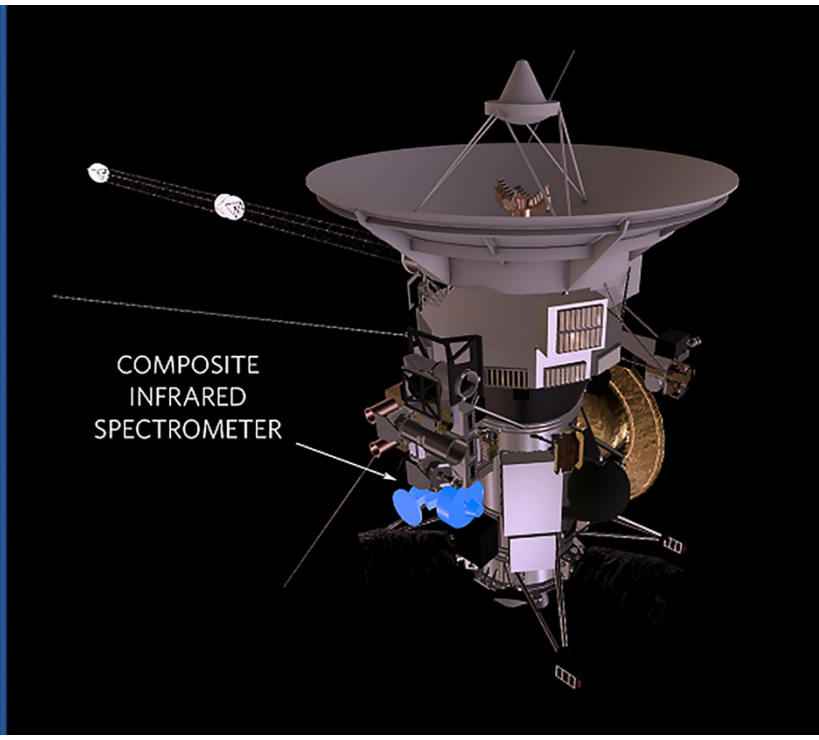

Composite Infrared Spectrometer

The Composite Infrared Spectrometer (CIRS) was an infrared Fourier Transform Spectrometer that measured infrared radiation from 7-1,000 μm that was emitted by Saturn, its rings and its moons. The **science objectives** of CIRS were to measure infrared emissions from atmospheres, rings and surfaces in the Saturn system to determine their composition, temperatures and thermal properties; to map the atmospheres of Saturn and Titan in three dimensions to determine temperature and pressure profiles with altitude, gas composition, and the distribution of aerosols and clouds. Molecular composition is determined in the infrared by the emitted or absorbed energy at specific wavelengths. The infrared spectrum identifies the gases or solids present and their relative amounts.

CIRS consisted of two interferometers that operated in the far-infrared and mid-infrared. They shared a common telescope and scan mechanism. CIRS included three sets of infrared detectors (Focal planes 1, 3, and 4) and a passive radiative cooler plate.

CONTENTS

Figures

Tables

EXECUTIVE SUMMARY

Key Science Results

Saturn

- Characterization of the great northern storm in the troposphere and stratosphere, which erupted unexpectedly in northern spring. For the first time, a detailed picture was obtained of the major disturbance in the stratosphere (warm, anticyclonic vortices, enhancement of trace hydrocarbons) that persisted for nearly three years.
- Determination for the first time of the vertical structure of Saturn's equatorial oscillation; measurement of the descending pattern of temperatures and zonal winds with time and its disruption by the great northern storm.
- Improvement in the abundance determination of methane, and as a result, of carbon.
- Characterization of the temperature and zonal wind structure of polar vortices at high spatial resolution.
- Determination of the vertical and latitude distribution and seasonal variation of stratospheric hydrocarbons.

Rings

- Slowly rotating ring particles discovered in Saturn’s main rings. These slowly rotating particles provided the first direct evidence for anisotropic thermal emission of rings versus a broad range of phase and emission angles at geometries not visible from Earth.
- First complete far-infrared (IR) roll-off measured in main ring temperature. Cassini CIRS obtained the first continuous submillimeter spectrum of Saturn’s main rings over a broad range of wavenumbers, from 25 microns to 0.5 millimeters. Until these observations, the location and shape of the spectral roll-off was not well determined. The roll-off in emissivity occurs around 200 microns and contains key information on material properties of the particles.
- A-ring particles with dense cores inferred from incomplete cooling down at solar equinox. At the solar equinox in August 2009, the CIRS onboard Cassini showed the lowest Saturn's ring temperatures ever observed. The observed equinox temperatures of Saturn's A-ring are much higher than model predictions as long as only the flux from Saturn is taken into account. This means that A-ring particles did not completely cool down at the equinox. The detailed seasonal model showed that A-ring particles have dense cores beneath the fluffy regolith mantles.

- Vertical thermal gradient detected in B-ring. A vertical thermal gradient was detected in the B-ring, which yields constraints on the diffusivity of this porous medium, and by extension on its thickness (which is unique for the thick B-ring).
- First cooling profile of main rings from near solstice through equinox CIRS observed the main rings of Saturn cool down from the orbit insertion of the spacecraft in 2004 until Saturn's equinox in 2009, and through northern summer solstice in 2017. The solar elevation varied from 26 degrees to 0 degrees with respect to the rings. The data showed that the A-ring, B-ring, and C-ring temperatures varied as much as 29–38, 22–34 and 18–23 K, respectively. Interestingly the unlit sides of the rings showed important temperature variations as well.
- First far-IR radial profile in optical depth CIRS obtained the first radial profile in optical depth in far-IR, filling in gap between near-IR and radio observations. CIRS observed a ring occultation of the far-IR source, Eta Carinae, to derive the ring optical depth.

Titan

- Discovery of a tilted stratospheric rotation [Achterberg et al. 2008].
- Observation of seasonal change in the 220 cm^{-1} absorber [Jennings et al. 2012a, 2012b, 2015].
- Observation of a late onset to the reversal of the seasonal gas distribution [Teanby et al. 2012b].
- Measurement of the vertical profile of water [Cottini et al. 2012a].
- Detection of the important $^{13}CH_3D$ [Bézard et al. 2007] and C_2HD isotopes [Coustenis et al. 2008].
- Detection of propene in the stratosphere [Nixon et al. 2013a].
- Characterization of hydrogen cyanide (HCN) ice above the south pole [de Kok et al. 2014].
- Hypothesis of grain surface chemistry to explain far-infrared absorption [Anderson et al.2016].
- Measurement of aerosol spectral opacity [Vinatier et al. 2012].
- Discovery of benzene ice [Vinatier et al. 2018].

Icy satellites

- Endogenic thermal emission from the Enceladus tiger stripes at temperatures up to 190 K, with large spatial variations on scales from 10 s of kilometers to 10 s of meters.

- Endogenic heat flow from Enceladus' south pole is larger than can be explained by simple steady-state tidal heating.
- Large spatial variations in thermal inertia on Mimas, Tethys, and Dione due to electron bombardment.
- High daytime temperature of Iapetus dark terrain, implying that thermal segregation is a major contributor to the extreme albedo dichotomy on Iapetus.
- Determining low thermal inertia throughout the Saturnian system.
- Ruling out significant activity on Dione and Tethys.
- Detecting surface temperatures of Ring Satellites.

Jupiter

- First characterization of the detailed vertical structure of Jupiter's equatorial oscillation and the discovery of an intense jet in the stratosphere centered at 4 mbar.
- Detection of the puzzling distribution of HCN and CO_2 in Jupiter's stratosphere, originally thought to be products of the SL9 impact in 1994.
- Mapping of the northern infrared auroral hot spot, and the determination of the lower limit to its penetration (4 mbar) and the composition of acetylene and ethane within the spot.
- First detection of diacetylene and the methyl radical in the northern and southern auroral hotspots.
- Discovery of anticorrelated abundance trends with latitude for acetylene and ethane.

CIRS Summary

The CIRS is an infrared Fourier Transform Spectrometer (FTS) on the Cassini orbiter that measures thermal radiation over more than two decades in wavenumber (ν) from 10 to 1400 cm^{-1} (1 mm to 7 μm). CIRS is described in detail in Kunde et al. [1996]; Flasar et al. [2004]; and Jennings et al. [2017]. Further information on CIRS and its operation throughout the mission is given in the Cassini Final Mission Report Volume 3 Instrument Performance Assessment, and the Cassini Final Mission Report Volume 5 Mission Operations System Performance Assessment.

The CIRS instrument consists of two interferometers, sharing a common telescope and scan mechanism. They operate in the far-infrared (10–600 cm^{-1}) and mid-infrared (600–1400 cm^{-1}) with a commandable, apodized spectral resolution as high as 0.5 cm^{-1}. The far-IR interferometer is a polarization interferometer, with a single focal plane consisting of two thermopile detectors with a 3.9 microradians (mrad) circular field of view (FOV), labeled FP1. The mid-IR interferometer is a

conventional Michelson interferometer with two linear focal plane arrays (FP3, FP4), each containing 10 HgCdTe detectors, with 0.273 mrad FOV per pixel. The center of the FP3 and FP4 arrays is aligned with the boresights of the other optical remote sensing instruments—Imaging Science Subsystem (ISS), wide-angle camera (WAC) and narrow-angle camera (NAC), Visual and Infrared Mapping Spectrometer (VIMS), and Ultraviolet Imaging Spectrograph (UVIS). The FP1 boresight is offset by 4 mrad [Flasar et al. 2004a; Jennings et al. 2017].

CIRS instrument operation allows data to be acquired at spectral resolutions between 0.5 cm^{-1} and 15 cm^{-1} by varying the scan length of the moving mirror. The low-resolution data have the highest signal to noise ratio (SNR) and the shortest scan length. The calibration for FP1 utilizes deep space spectra while FP3 and FP4 have, in addition, a shuttered target source at 170 K.

KEY OBJECTIVES FOR CIRS

Key Science Objectives for Saturn

1. **Formation, evolution, and internal structure:** Helium, carbon, nitrogen, and sulfur abundances in Saturn's atmosphere.

2. **Atmospheric gas composition:** Disequilibrium tropospheric compounds (PH_3, CO…), ortho-para H_2 conversion, disequilibrium stratospheric compounds (hydrocarbons), external sources—oxygen compounds.

3. **Clouds and aerosols.**

4. **Atmospheric structure and circulation:** Temperatures, zonal winds, meridional circulations, waves, eddies, compact vortices.

5. **Temporal behavior:** Seasonal, internal dynamical (northern Saturn storm, equatorial oscillation, neither fully anticipated).

Key Science Objectives for the Rings

CIRS has provided major advances over previous spacecraft infrared observations of Saturn's rings in three respects: 1) extension of the spectral range to submillimeter wavelengths; 2) higher spatial resolution on the rings as result of closer proximity during the Cassini tour, as well as of a linear detector array with much finer spatial resolution in the mid-infrared; and 3) temporal extent of the mission, which provided greatly improved sampling in illumination and viewing geometries. With its enhanced capabilities, CIRS addressed many of the rings science objectives of the Cassini mission, particularly those pertaining to radial thermal structure, ring optical depth in the mid-IR, ring particle thermal properties and rotation states, ring-scale

CIRS has provided major advances over previous spacecraft infrared observations of Saturn's rings.

properties including vertical structure, and thermal roll-off in the submillimeter. The key CIRS ring science objectives are listed below and each one is discussed in the section entitled Science Results.

1. **Ring Thermal Structure:** Determine Saturn's ring thermal structure and how the ring temperatures vary with ring optical depth, solar elevation, phase angle, azimuth angle and distance to the planet. What is the source of the temperature variations? Determine the azimuthal asymmetries in the rings, apart from the diurnal cooling/heating cycle. What is their origin?

2. **Ring optical depth at mid-IR wavelengths:** Determine the variation of ring optical depths at mid-IR wavelengths and compare to ultraviolet (UV) and near-IR optical depths.

3. **Particle-scale Properties:** Determine key particle properties such as Bond albedo, thermal inertia and particle spin. On what factors do they depend? Determine the distribution of particle spins of the ring particles. What does this distribution tell us about local dynamics? Compare the diurnal and seasonal thermal inertia and any differences between them.

4. **Ring-scale Properties:** Determine the volume filling factors for the rings. Search for an opposition surge in the thermal infrared. Is it driven by mutual shadowing alone? Determine vertical temperature gradient between lit and unlit sides of the rings. What does this tell us about the ring vertical structure and dynamics? Determine the ring thermal inertia and compare it to the particle thermal inertia. Does it change with seasons?

5. **Regolith Properties deduced from CIRS Emissivity Roll-off:** Determine the wavelength of the roll-off in ring emissivity. What do we learn from this roll-off about particle structure and composition?

Key Science Objectives for Titan

1. **Formation and evolution:** Volatiles—methane.

2. **Atmospheric composition:** Organics (hydrocarbons and nitriles), oxygen compounds, new species.

3. **Aerosols and condensates.**

4. **Atmospheric structure and circulation:** Temperatures, zonal winds, meridional transports, eddies and waves.

5. **Seasonal behavior:** Evolution of polar vortices—gas composition, condensates, temperatures and winds.

Key Science Objectives for the Icy Satellites

1. **Enceladus' Activity:** Determine Enceladus' heat flow, to help constrain its activity mechanism. Determine whether Enceladus' activity varies with seasonal change.

2. **Activity on other Satellites:** Search for activity on Dione and Tethys, and search for a ring and debris disk around Rhea.

3. **Comparative study of Saturn's icy satellites:** Compare the surface properties of Saturn's mid-sized icy satellites. Determine the uniqueness of Mimas' thermally anomalous region. Observe Saturn's small satellites as opportunities arise (including but not limited to Epimethus, Janus, Methone and Promethus).

4. **Better understand unusual surfaces:** Constrain Hyperion's unusual surface's thermophysical properties, constrain Iapetus' albedo dichotomy.

CIRS Science Assessment

Saturn

Table CIRS-1 contains an assessment of CIRS Saturn science based on the objectives in the original Announcement of Opportunity (AO) and the Cassini Traceability Matrix (TM) developed for the Equinox and Solstice missions. Each CIRS Saturn science objective is paired with an AO and TM science objective. The key AO and TM objectives addressed by CIRS are:

- **Saturn Temperature, Clouds, Composition (S_AO1):** Determine temperature field, cloud properties, and composition of the atmosphere of Saturn.
- **Saturn Winds and Weather (S_AO2):** Measure the global wind field, including wave and eddy components; observe synoptic cloud features and processes.
- **Saturn Interior Structure and Rotation (S_AO3):** Infer the internal structure and rotation of the deep atmosphere.
- **Saturn Formation and Evolution (S_AO5):** Provide observational constraints (gas composition, isotope ratios, heat flux...) on scenarios for the formation and the evolution of Saturn.
- **Seasonal Variations (SC1a):** Observe seasonal variations in temperature, clouds, and composition in three spatial dimensions.
- **Saturn's Winds (SC1b):** Observe seasonal changes in the winds at all accessible altitudes coupled with simultaneous observations of clouds, temperatures, composition, and lightning.

- **Saturn's Rotation Rate (SN1a):** Determine Saturn's rotation rate and internal structure despite the planet's unexpected high degree of axisymmetry.
- **2010–2011 Great Storm (SN1b):** Observe the aftermath of the 2010–2011 storm. Study the life cycles of Saturn's newly discovered atmospheric waves, south polar hurricane, and rediscovered north polar hexagon.
- **Saturn Trace Gases (SN1c):** Measure the spatial and temporal variability of trace gases and isotopes.

Table CIRS-1. CIRS Saturn Science Assessment: AO and TM Objectives are paired with CIRS Science objectives.

Fully/Mostly Accomplished: Partially Accomplished: Not Accomplished:

CIRS Saturn Science Objectives	AO and TM Science Objectives	CIRS Saturn Science Assessment	Comments if yellow (partially fulfilled)
Formation, evolution, internal structure			
Helium	S_AO1, S_AO5		Analysis in progress.
Carbon	S_AO1, S_AO5		
Nitrogen	S_AO1, S_AO5		
Carbon monoxide	S_AO1, S_AO5		
Internal rotation	S_AO3, SN1a		
Atmospheric gas composition			
Disequilibrium tropospheric compounds: PH_3, CO, halides	S_AO1,SN1c		
Ortho-para H_2	S_AO1,SC1b,SN1c		
Stratospheric hydrocarbons	S_AO1,SN1c		
External sources—oxygen compounds	S_AO1		Analysis in progress.
Atmospheric structure and circulation			
Temperatures & zonal winds	S_AO1, S_AO2, SC1b		
Meridional circulations	S_AO1,SC1b,SN1c		
Waves & eddies	S_AO2,SN1c		Larger scale waves done: N. hexagon, equatorial waves.
Compact vortices	S_AO2		Polar vortices.
Temporal behavior			
Seasonal	SC1a		
Northern storm	SN1b		Persisted to 2013 in stratosphere.
Equatorial oscillation	SC1a,SN1b		

Rings

Table CIRS-2 contains an assessment of CIRS ring science based on the objectives in the original AO and the Cassini TM developed for the Equinox and Solstice missions. Each CIRS ring science objective is paired with an AO and TM science objective. The key AO and TM objectives addressed by CIRS are:

- **Ring Structure and Dynamics (R_AO1):** Study configuration of the rings and dynamical processes (gravitational, viscous, erosional, and electromagnetic) responsible for ring structure.

Table CIRS-2. CIRS Ring Science Assessment: AO and TM Objectives are paired with CIRS Science objectives.

Fully/Mostly Accomplished: **Partially Accomplished:** **Not Accomplished:**

CIRS Ring Science Objectives	AO and TM Science Objectives	CIRS Ring Science Assessment	Comments if yellow (partially fulfilled)
Ring Thermal Structure			
Radius and Ring Optical Depth	R_AO1, RC1a		
Solar elevation	R_AO1, RC1a		
Phase angle	R_AO1, RC1a		
Ring Equinox temperatures	R_AO1, RC1a		
Azimuthal dependence	R_AO1, RC1a		
Ring Optical Depth at mid-IR Wavelengths	R_AO1, RC1a		
Particle-scale Properties			
Bolometric Bond Albedo	R_AO1, RC1a		
Particle Spin	R_AO1, RC1a		
Diurnal Thermal Inertia	R_AO1, RC1a		
Seasonal Thermal Inertia and Particle Size	R_AO1, RC1a		
Average Thermal Emissivity	R_AO1, RC1a		
Ring-scale Properties			
Volume Filling Factors of A-ring and B-ring	R_AO1, RC1a		
Opposition Surge	R_AO1, RC1a		
Energy budget and heat transfer in B-ring	R_AO1, RC1a		
Thermal Properties, Thickness and Surface Mass Density of B-ring	R_AO1, RC1a		
Self-gravity wakes in the A-ring	R_AO1, RC1a		
Regolith Properties Deduced from CIRS Emissivity Roll-off			
Thermal Emissivity Roll-off at Submillimeter wavelengths	R_AO1, RC1a		
F-ring Clumps	RC2a		

- **Changing Rings (RC1a):** Determine the production mechanisms of spokes, and the microscale properties of ring structure, by observing at the seasonally maximum opening angle of the rings near Solstice.
- **Ring Temporal Variability (RC1b):** Understand the time-variability of ring phenomena on decadal timescales (Encke gap, D-ring, ring edges, etc.) by substantially increasing the time baseline of observations.

Titan

Table CIRS-3 contains an assessment of CIRS Titan science based on the objectives in the original AO and the Cassini TM developed for the Equinox and Solstice missions. Each CIRS Titan science objective is paired with an AO and TM science objective. The key AO and TM objectives addressed by CIRS are:

Titan AO objectives

- **Titan Atmospheric Formation and Evolution (T_AO1):** Determine abundances of atmospheric constituents (including any noble gases), establish isotope ratios for abundant elements, constrain scenarios of formation and evolution of Titan and its atmosphere.
- **Titan Atmospheric Composition and Distribution (T_AO2):** Observe vertical and horizontal distributions of trace gases, search for more complex organic molecules, investigate energy sources for atmospheric chemistry, model the photochemistry of the stratosphere, study formation and composition of aerosols.
- **Titan Meteorology (T_AO3):** Measure winds and global temperatures; investigate cloud physics, general circulation, and seasonal effects in Titan's atmosphere; search for lightning discharges.
- **Titan Surface Characteristics and Internal Structure (T_AO4):** Determine the physical state, topography, and composition of the surface; infer the internal structure of the satellite.

Titan Cassini Solstice Mission (CSM) traceability matrix objectives

- **Titan’s Great Seas (TC1a):** Determine seasonal changes in the methane-hydrocarbon hydrological cycle: of lakes, clouds, aerosols, and their seasonal transport.
- **Titan’s Global Seasons (TC1b):** Determine seasonal changes in the high-latitude atmosphere, specifically the temperature structure and formation and breakup of the winter polar vortex.

- **Titan's Surface (TN1a):** Determine the types, composition, distribution, and ages, of surface units and materials, most notably lakes (i.e., filled versus dry and depth; liquid versus solid and composition; polar versus other latitudes and lake basin origin).
- **Titan Atmospheric Composition (TN1c):** Measure aerosol and heavy molecule layers and properties.
- **Titan Atmospheric Structure (TN2a):** Resolve current inconsistencies in atmospheric density measurements (critical to a future Flagship mission).
- **Titan Meteorology (TN2c):** Determine the surface temperature distribution, cloud distribution, and tropospheric winds.

Table CIRS-3. CIRS Titan Science Assessment: AO and TM Objectives are paired with CIRS Science objectives.

Fully/Mostly Accomplished: **Partially Accomplished:** **Not Accomplished:**

CIRS Titan Science Objectives	AO and TM Science Objectives	CIRS Titan Science Assessment	Comments if yellow (partially fulfilled)
Surface Temperature	T_AO4, TN2c		
Latitudinal variation	T_AO4, TN2c		
Temporal changes	T_AO4, TN2c		
Variation with topography and terrain	T_AO4, TN1a		Insufficient data and S/N, footprint too large.
Atmospheric Thermal and Dynamical State	T_AO3, TC1b		
Global temperature mapping	T_AO3, TC1b		
Winds and jets	T_AO3, TC1b		
Rotation axis	T_AO3, TC1b		
Global Energy Balance	T_AO3, TC1b		
Seasonal changes	T_AO3, TC1b		
Gas Composition and Chemistry	T_AO2, TN1c		
Global gas distribution near equinox	T_AO2, TN1c		
Seasonal changes	T_AO2, TN1c		
Search for new gas species	T_AO2, TC1a		
Isotopic ratios	T_AO1, N/A		Still under study to reduce errors, improve agreement between measurements.
Hazes and Condensates	T_AO2/3, TN1c		Hazes and condensates mapped, but ongoing work to elucidate composition.
Haze characteristics	T_AO2, TN1c		
Condensates: location and identification	T_AO3, TN1c		

The majority of the science goals for Titan laid down at the start of the mission (Key Objectives for CIRS) have been achieved successfully, and much progress has also been made on the revised goals from the Cassini Solstice Mission. Table CIRS-3 shows a final assessment for the surface temperatures, only the issue of correlation with topography remains uncertain, and is unlikely to be gleaned from the CIRS dataset given the large FP1 detector footprint. All atmospheric temperature science goals have been achieved, although a discrepancy between CIRS and Huygens stratopause levels may require further investigation, as described later. Gas abundance measurements have also been largely met, although isotopic ratios, which require the highest accuracy, have proved susceptible to systematic errors. More analysis is needed of the dataset in this area to resolve remaining differences between published values. Finally, much new information has been returned about hazes and condensates, although work is still ongoing to determine composition, for example with regard to the notorious 220 cm^{-1} emission feature.

Icy Satellites

The key TM questions of Icy Satellite science that CIRS has helped address are:

Level 1

- **Changes on Enceladus (IC1a):** Determine whether Enceladus exhibits any seasonal changes. Other temporal changes (e.g., mean anomaly) are also considered.
- **Enceladus' interior (IN1a):** Determine the surface temperature in active regions and constrain Enceladus' heat flow, to better constrain models of its activity.
- **Compare Saturn's mid-sized satellites (IN1b):** Compare the surface characteristics of Saturn's mid-sized satellites, including the thermally anomalous Pac-Man regions.
- **Activity on Dione (IN1c):** Determine whether Dione is currently active, or has been so on recent geological timescales.

Level 2

- **Rhea's Ring (IN2a):** Determine if there is a ring (or debris disk) around Rhea, and if so, characterize the spatial and particle size distribution.
- **Tethys and the E-ring (IN2b):** Determine whether Tethys is geologically active, and thus could be contributing to the E-ring.
- **Characterize the surfaces of Saturn's small satellites (IN2d):** Derive the surface thermophysical properties of Saturn's small satellites, including (but not limited to) Epimethys, Janus, Methone, and Promethus.

Table CIRS-4. CIRS Ice Satellite Science Assessment: AO and TM Objectives are paired with CIRS Science objectives.

Fully/Mostly Accomplished: **Partially Accomplished:** **Not Accomplished:**

CIRS Icy Satellite Science Objectives	AO and TM Science Objectives	CIRS Ring Science Assessment	Comments only if yellow or red
Enceladus			
Enceladus' Surface Temperatures	IC1a, IN1a		
Constrain Enceladus' heat flow	IC1a, IN1a		
Activity On Other Satellites			
Dione	IN1c		
Tethys	IN2b		No evidence for activity was found when looking at temperature maps of Tethys using CIRS data for in Howett et al. [2012].
Ring around Rhea	IN2a		No thermal inertia signature connected with ring infall were observed on Rhea in Howett et al. [2014], but any signature (including the 'blue dots') are likely to be too small to be resolved in this work.
Comparative Study of Saturn's Icy Satellites			
Search for thermally anomalous regions on Tethys	IN1b		
Search for thermally anomalous regions on Dione	IN1b		
Search for thermally anomalous regions on Rhea	IN1b		
Characterizing the properties of small satellites	IN2d		Work is in progress.
Unusual Surfaces			
Constrain Hyperion's thermophysical surface properties	IN2d		CIRS work included in paper by Howard et al. [2012].
Constrain Iapetus' albedo	IN1b		

CIRS Saturn System Science Results

Saturn

Formation, evolution, and internal structure

Helium, carbon, nitrogen, halides

In principle, the helium abundance can be retrieved from thermal infrared spectra, but placing tight bounds on helium has proved elusive. Three approaches have received the most attention so far.

1. Using far-infrared spectra alone. Here the helium abundance is derived from its effect on the collisionally induced absorption S(0) and S(1) lines of H_2 at 320 cm^{-1} and 600 cm^{-1}, respectively, and the translational continuum at 50–200 cm^{-1}. The difficulty arises in that the para-fraction of H_2 (f_p) deviates from its equilibrium value, and it must be retrieved along temperature and helium mole fraction [Achterberg et al. 2014b]. These variables are not independent, and as a result the problem becomes poorly constrained. One can only place a rough upper limit to [He]/[H_2] of 0.15. The smallest deviations from equilibrium f_p occur when the ratio is ~0.05.

2. Using far-infrared spectra with temperatures retrieved from radio-occultation soundings. With helium uniformly distributed the retrieved refractivity profiles translate into profiles of temperature divided by the molecular mass and of pressure times the refractivity per molecule divided by the molecular mass. In this case one greatly increases the precision of the helium abundance determination. One proceeds as before, except now the temperature-pressure profile is constrained, and determines f_p and the helium abundance. One iterates until the synthetic spectrum, computed for a particular T(P), f_p, and [He]/[H_2], matches the observed spectrum. With this technique Achterberg et al. [2016] obtained ratios [He]/[H_2] ~0.065–0.085. However, there is some evidence that systematic errors are present, particularly at mid and high latitudes, where the shape of the best-fit synthetic spectrum can exhibit large deviations from the observed one. The source of this discrepancy is under study.

3. Koskinen and Guerlet [2018] have combined Cassini stellar occultation soundings with the UVIS with CIRS mid-infrared limb spectra. The UVIS soundings provide vertical profiles the H_2 density versus radius down to the base of the thermosphere near 0.03 μbar. The CIRS observations retrieve temperature versus pressure up to the 1–3 μbar level. Hence, there is a gap of 30 or more in barometric pressure over the region that presumably contains the homopause. The pressure scale height decreases with molecular mass, and the trick here is to find a solution that matches the CIRS T-P condition at the bottom of the gap with the correct density-altitude condition from the UVIS sounding in the thermosphere. Koskinen and Guerlet [2018] argue that an isothermal profile across the gap provides the most viable solution, which yields an estimate of [He]/[H_2] = 0.124.

Saturn is enriched in carbon, relative to the Sun. Flasar et al. [2005b] reported the mole fraction of CH_4 as 4.5 ±0.9 × 10^{-3}. This was later refined by Fletcher et al. [2009b], who averaged over a larger number of CIRS observations, as 4.7 ±0.2 × 10^{-3}, about 10 times the solar value of C/H—see also the review by Fouchet et al. [2009].

Teanby et al. [2006] analyzed CIRS far-infrared spectra (10–600 cm^{-1}) to improve upper limits on hydrogen halides. Their derived 3 σ upper limits indicated that HF, HCl, and HBr were sub-solar at 500 mbar, similar to what was found for Jupiter (see the section entitled Halides). Because the

line strengths of HI are so weak and its solar abundance so small, they were not able to constrain its abundance to sub-solar values.

ISOTOPES

Fletcher et al. [2009] derived isotopic ratios in methane by modeling the emissions of $^{12}CH_4$, $^{13}CH_4$ and $^{12}CH_3D$. The derived D/H ratio in methane of (1.6 ±0.2) × 10^{-5} appears to be smaller than on Jupiter, in contrast with expectations that D-enriched ices would form a progressively larger proportional of the giant planets, moving outward from Jupiter to Neptune. The reason for this is still unclear. In contrast, the carbon isotopic ratio $^{12}C/^{13}C$ = 91.8 (+8.4/−7.8, is consistent with both the terrestrial ratio and Jovian ratio, suggesting that carbon was accreted from a shared reservoir for all of the planets.

D/H from HD/H_2. Pierel et al. [2017] made a careful modeling of the far-IR HD rotational lines on CIRS FP1. The modeling effort uncovered substantial uncertainties in current knowledge of the HD line parameters, especially the line widths at low temperatures, which contributed to substantial error bars dominated by systematic uncertainties rather than spectral noise. The bulk D/H was found to be (2.95 ±0.55) × 10^{-5} on Jupiter and somewhat lower (2.10 ±0.13) × 10^{-5} on Saturn, indicating potential interior differences. The results were compared to previous estimates from ISO and Herschel data, as well as to inferences about bulk D/H extrapolated from methane measurements. Overall, Saturn shows a trend toward slightly lower D/H than Jupiter, in contrast to expectations of a higher value, due to a larger ice/gas ratio at formation. However, the errors and spread in values is large and the difference remains statistically marginal. Further work is needed, first on better laboratory estimates of the HD and H_2 quadrapole line strengths and widths at low temperatures, followed by re-retrievals of the spectral data.

INTERNAL ROTATION

Saturn's internal rotation rate remains a subject of interest and controversy.

Saturn's internal rotation rate remains a subject of interest and controversy. Read et al. [2009] proposed a novel way to estimate the internal rotation period based on the potential vorticity, observed at the cloud tops. The authors assumed that the zonal flow was marginally stable with respect to the nonlinear stability as prescribed in Arnol'd's 2nd stability theorem. The theorem is couched in terms of the zonal phase velocity of the longest, fastest, and mostly deeply rooted Rossby waves, which presumably are closest to the internal rotation. Using the tracked cloud-top winds from Cassini imaging and temperatures retrieved from CIRS spectra, the authors computed the potential vorticity and used the stability criterion to infer an internal rotation period of 10 h 34 min 13 ±20 s for the interior.

Atmospheric gas composition

DISEQUILIBRIUM TROPOSPHERIC COMPOUNDS

Phosphine (PH_3) is a disequilibrium compound in the upper troposphere. It is generally believed to be a product of rapid vertical mixing from deep atmospheric levels. PH_3 is transported upwards in a time much shorter than the chemical depletion time in the upper troposphere, so the observed abundances represent the quenched equilibrium conditions deeper down. Hence, meridional variations in the observed abundance are diagnostic of the vertical motion. CIRS observations indicate an enhancement of PH_3 in the equatorial region [Fletcher et al. 2007a, 2009a, 2018], which is consistent with rapid vertical upwelling and the cold temperatures observed there. At 23° N (planetographic), PH_3 is depleted, suggesting subsidence, perhaps indicative of a Hadley-type cell. Lower values of PH_3 have also been inferred in the upper troposphere in the cores of the polar vortices, where there is subsidence [Fletcher et al. 2008, 2010] found a hemispheric asymmetry in the phosphine distribution over 2004–2009, with the southern hemisphere (in summer) on average having higher abundances.

Hurley et al. [2012b] investigated whether thermal disassociation associated with lightning and shock waves generated by thunder in Saturn's water clouds could generate an enhancement of tropospheric acetylene (C_2H_2) that would be transported upward to the tropopause region, and thereby serve as a chemical fingerprint of thunderstorm activity. Analyzing CIRS mid-infrared spectra, they found no systematic enhancement around regions in which there are known occurrences of normally sized (2000 km) thunderstorms, beyond what would be expected from photolysis under ambient conditions.

ORTHO-PARA H_2

CIRS far-infrared spectra can probe the para-fraction of H_2 (f_p) in the upper troposphere (100–400 mbar). Because the equilibration time between the ortho and para states are thought to be long compared to seasonal time scales, the distribution of f_p should provide an indication of vertical motion from deeper levels of the atmosphere. In the equilibrated state, f_p increases with decreasing temperature. CIRS observations show that f_p remains depressed near the equator, relative to the average over latitude in the upper troposphere, indicating upwelling, throughout the Cassini tour [Fletcher et al. 2007a, 2010, 2016, 2018]. The meridional structure at mid and high latitudes is more difficult to interpret. An exception is the depression of f_p at 20°–50° N, resulting from upward transport after the outbreak of the Saturn storm (see the section entitled Temporal behavior).

DISEQUILIBRIUM STRATOSPHERIC COMPOUNDS (HYDROCARBONS)

The review chapter by Fletcher et al. [2018] provides a good summary of CIRS observations of stratospheric hydrocarbons. Observations in nadir-viewing [Howett et al. 2007; Hesman et al. 2009; Sinclair et al. 2013; Fletcher et al. 2015] and limb-viewing [Guerlet et al. 2009; Sylvestre et al. 2015]

geometries have provided information on meridional and vertical structure of C_2H_2 and C_2H_6. Quantitative differences exist among the spatial distributions and temporal behaviors identified by different authors, but some general common trends can be identified: (i) C_2H_2 decreases from equator to pole while C_2H_6 is largely uniform with latitude; (ii) There are regional enhancements of both species at the highest latitudes within polar vortices, possibly associated with auroral chemistry and entrainment; (iii) There are general spring hemisphere enhancements and autumn hemisphere depletions in the millibar region, suggestive of stratospheric transport from the southern to the northern hemisphere that may be related to the local meridional cells associated with the equatorial oscillation (see section the entitled Equatorial Oscillation).

CIRS limb observations [Guerlet et al. 2009, 2010, 2015; Sylvestre et al. 2015] have also provided information on the spatial distributions of C_3H_8, CH_3C_2H, C_4H_2, and C_6H_6. Like those of C_2H_2 and C_2H_6, these bear little resemblance to photochemical model predictions in the absence of dynamical transport.

External sources—oxygen compounds

Prior analysis of the rotational lines of H_2O and CO has been based on disk average measurements. While CIRS observations spatially resolve Saturn, the rotational lines are weak at its spectral resolution, the relatively cold temperatures require large spectral averages for analysis. Little on this has been published as yet. Using spectral averages of nadir and limb observations, Abbas et al. [2013] analyzed the Q-branch of the ν_2 band of CO_2 in the 667 cm^{-1} region, and they did not find any discernable meridional trends, obtaining a mixing ratio ~5 × 10^{10} near ~1 mbar.

Clouds and aerosols

CIRS thermal-infrared spectra have placed fewer constraints on clouds and aerosols on Saturn that on Jupiter (see the section entitled Jupiter - Clouds and Aerosols). In part this can be attributed to the lower temperatures and signal-to-noise ratios of spectral features. Constraints from observations near-infrared, visible, and ultraviolet wavelengths have been more definitive. And unlike Titan, limb sounding in the far-infrared was not feasible at Saturn, because of the greater distance between the spacecraft and atmosphere.

There have, however been more indirect indications of the haze distribution from retrieved CIRS temperatures. One of the interesting features of Saturn's vertical temperature profile is the knee, which is an undulation that occurs over the range ~150–300 mbar and effectively broadens the tropopause region. This was originally seen in temperatures retrieved from Voyager IRIS spectra, obtained in early northern spring, mainly in the southern hemisphere. Retrieving temperatures from Cassini CIRS spectra obtained in early northern winter, Fletcher et al. [2007b] detected the temperature knee and mapped its variation with latitude. They found it to be larger in the summer hemisphere than in the winter, smaller and higher at the equator, deeper and larger in the equatorial belts, and small at the poles. They proposed solar heating of tropospheric haze as a possible mechanism for the temperature knee, with larger aerosols in the summer hemisphere.

Atmospheric structure and circulation

GLOBAL STRUCTURE

Flasar et al. [2005a] reported the first observations of Saturn by CIRS. From nadir-viewing observations, they found little variation with altitude of the zonal winds in the upper troposphere and stratosphere, except near the equator, where they found a general decay with altitude between 500 mbar and 2 mbar. Later limb and more detailed nadir observations would reveal the oscillatory undulation of the zonal winds in the stratosphere associated with the equatorial oscillation (see the section entitled Equatorial Oscillation). The earlier CIRS observation also found that the south pole was warmer than the equator in the stratosphere near 1 mbar by 15 K—about 3 times that expected just from the radiative response to solar heating in southern summer—suggesting that descending motion and adiabatic compression and heating played an important role over the south pole. Fletcher et al. [2007b] found that the south pole in the same season was 25–30 K warmer than the north pole at 1 mbar. They also quantified the knee in the vertical temperature profiles, a flattening of the temperature lapse rates between 150 and 300 mbar in the tropopause region, which was first seen in temperatures retrieved from Voyager IRIS spectra obtained in 1980–1981. This was most noticeable in the southern hemisphere, becoming more compact in the equatorial region. They suggested that this could result from solar heating of heterogeneously distributed aerosol hazes.

Li et al. [2010] undertook a careful study of Saturn's thermal emission during 2004–2009. They found an effective temperature of 96.7 K, but found that the emission from the southern hemisphere (in summer) was 17% higher than in the north. They also found evidence of seasonal and variations in the total power ~2% and some interannual variability.

POLAR STRUCTURE

During northern winter, both poles exhibited compact spots in the upper troposphere, associated with cyclonic vortices, with subsidence and adiabatic heating [Fletcher et al. 2008]. At the southern (summer) pole, the warm structure persisted into the stratosphere near 1 mbar, where the warm region was slightly broader in extent. In the north, the warm pole was less compact and intense in the stratosphere. Evidence for polar subsidence was further supported by the depletion in PH_{3}¬, a disequilibrium compound thought to be transported upward from the deeper atmosphere. CIRS observations also detected the cold anticyclonic zone (warm cyclonic belt) poleward (equatorward) of the jet at 77° N, associated with the polar hexagon. (The hexagonal shape actually represents the orthographic projection of a wavenumber 6 sinusoidal variation of the amplitude in latitude with longitude.) As Saturn's seasons moved from northern winter to northern summer, the hexagon retained its structure in the thermal infrared and the north polar stratosphere developed a well-defined warm region that is broader than in the troposphere [Fletcher et al. 2015; Sayanagi et al. 2018]. On the other hand, the warm stratosphere over the south pole has weakened considerably. More recently, the recent Grand Finale orbits have provided observations of the poles with the highest spatial resolution of the mission. Tropopause temperatures over the north pole, now in

summer, increase sharply between 89° and 90° N [Achterberg et al. 2018]. The average subsidence velocity in this region, assuming a balance between adiabatic heating and radiative damping, are modest, ~0.05 mm/s. However, the circulation appears to be deeply rooted, still depressing the isentropes over the pole at the deepest levels probed by CIRS, ~600 mbar.

Temporal behavior

SATURN STORM

One of the key advantages of having a long-term orbiting spacecraft about a planet is the ability to map the fourth dimension—time—in addition to the three spatial dimensions. Geophysical systems are inherently nonlinear, and their temporal behavior is often not easily predictable. This is particularly true of meteorology. Our terrestrial experience has taught us that continued observation is critical to understanding an atmosphere's dynamical behavior.

One of the key advantages of having a long-term orbiting spacecraft about a planet is the ability to map the fourth dimension—time . . .

An intriguing phenomenon is the outbreak of the great Saturn storms. These originate as the appearance of a white compact spot that quickly spreads and encircles the planet with clouds within a latitude band. The storms recur in the northern hemisphere roughly every 30 years (approximately Saturn's orbital period) generally in northern summer, when Saturn is near periapsis—see, for example, the review by Sánchez-Lavega et al. [2016]. However, storms prior to the last one, which erupted in December 2010, were observed by Earth observatories, and this may have introduced some bias in the detections because of obscuration by the rings. The last storm, which was observed by Cassini, was unexpected in that it erupted early, just after the northern spring equinox. For the first time, an observatory was in hand to observe the storm evolution, not only up close, but with a full array of instruments spanning much of the electromagnetic spectrum as well as obtaining in situ data.

CIRS observations were critical in characterizing the effect of the storm on atmospheric structure. Current thinking attributes the storm outbreak as driven by a moist convective instability associated with Saturn's water clouds. Retrievals from CIRS spectra, obtained over the course of 18 months after the outbreak, indicated that tropospheric temperatures in the latitude band encircled by the clouds were elevated and the para ratio of H_2 was lower, relative to the ambient atmosphere at adjacent latitudes [Achterberg et al. 2014a]. This is broadly consistent with the notion of a rapid convectively unstable updraft that transports a higher fraction of ortho H_2, in equilibrium with the higher temperatures at depth. If, as on Earth, the convective updrafts are confined to narrow towers, surrounded by compensating downdrafts, which occupy most of the horizontal surface area in the perturbed latitude band, the adiabatic compression and warming would produce the higher temperatures observed, rather than lateral mixing of latent released in the updrafts. The mean zonal winds and temperatures are coupled via the thermal wind equation.

The warmer tropospheric temperatures at the storm latitude band means that winds become more westward with altitude equatorward of the band and eastward with altitude poleward, hence increasing the mean zonal anticyclonic vorticity with altitude. This is roughly consistent with the behavior inferred from cloud tracking studies using various filters [Sayanagi et al. 2013].

Li et al. [2015] examined the effect of the storm on Saturn's radiant power. The storm increased the total power near 45° by 9%, causing the globally emitted power to increase by 2%.

For the first time, the effects of the storm on the stratosphere was observed. CIRS observations indicated that initially two warm spots were observed near 2 mbar at the same latitude as the storm [Fletcher et al. 2012]. It was quickly realized that these could not have resulted directly from updrafts, because, with the sharp increase in static stability above the tropopause, any updraft would quickly become negatively buoyant. Instead, the effect of any updrafts hitting the tropopause region would be analogous to tossing a stone into a pond, generating waves that would propagate upward. The waves would likely be nonlinear, with the warm spots resulting from local subsidence and adiabatic heating. There were no accompanying colder regions at other longitudes, perhaps because of the presumed nonlinearity. It should be appreciated that Cassini observations, because they had been pre-programmed several months in advance, were not optimally configured to track the storm. Therefore, ground-based observations were brought to bear to fill in the gaps. VLA observations tracked the evolution of the two warm spots initially detected [Fletcher et al. 2012]. Because zonal pressure gradients were relatively weak in the troposphere, application of hydrostatic balance implied that the warm regions were high pressure centers, hence anticyclonic vortices with clockwise flow, with wind velocities ~200 m/s. Both anticyclonic vortices moved slowly westward at different speeds with respect to the background zonal flow. Eventually, in May 2011, they merged, with the vortex increasing in strength. At that time, the vortex temperature at 2 mbar was 80 K warmer than the ambient atmosphere at this isobaric level, unheard of in the normally quiescent Saturn stratosphere. CIRS observations indicated that not only were temperatures elevated, but there was a 100-fold enhancement of ethylene (C_2H_4) [Hesman et al. 2012]. The cause of this enhancement is not understood, but it may result from the release of condensed C_2H_4 bound onto aerosols that was released by the higher temperatures in the merged vortex.

The tropospheric disturbances associated with the storm dissipated over eight months. In contrast the stratospheric disturbance lasted nearly three years after the storm began [Fletcher et al. 2017]. The persistence of the stratospheric disturbance shows evidence of interfering with the descending phase of the equatorial oscillation (see next sectional paragraph below).

EQUATORIAL OSCILLATION

One of the remarkable phenomena on Jupiter and Saturn is the occurrence of equatorial oscillations in the planets' stratospheres. Equatorial oscillations on Earth—the quasi-biennial oscillation (QBO), with an irregular period ranging from 22–34 months, and the semi-annual oscillation (SAO) with a well-defined periodicity—have been extensively studied. The zonally symmetric structure in the equatorial middle atmosphere (stratosphere and mesosphere) is

characterized by an alternating series of warmer and colder layers with height. Because of Earth's rapid rotation, temperatures and zonal winds are in thermal wind balance, and the warm and cold regions are associated with decreasing and increasing zonal wind shear, respectively. The alternating shears are large enough that the zonal winds alternate between eastward and westward with altitude. Associated with the temperature and wind structure are a series of stacked meridional circulation cells. At equatorial levels where there is subsidence (ascent), adiabatic warming (cooling) produces warmer (colder) temperatures. These meridional cells close at higher latitudes in each hemisphere, and thus affect the structure of temperatures and winds at higher altitude. Indeed, there is evidence that the strength of the winter polar vortices on Earth, is correlated with the phase of the QBO. The terrestrial equatorial oscillations are thought to be mechanically driven, from the absorption of upwardly propagating atmospheric waves with both eastward and westward zonal phase velocities.

Ground-based observations [Orton et al. 2008] have indicated an oscillatory behavior in Saturn's equatorial stratosphere for decades, but they did not spatially resolve the vertical structure. Cassini CIRS observations resolved this structure for the first time. Fouchet et al. [2008] found the analogous warm and cold anomalies at the equator from limb-viewing spectra. The warm and cold anomalies were spaced apart by approximately two pressure scale heights. The zonal winds implied by the thermal wind equation did not reverse, as on Earth, but remained eastward. However, the peak-to-peak variation between the largest and smallest eastward winds was roughly 200 m/s, compared to the characteristic value between 400 and 500 m/s for the cloud-top winds. Some evidence for the extratropical extent of the implied meridional circulations associated with the equatorial oscillation was seen in the enhancement of C_2H_6 near 20° N. Since ethane increases with altitude, this suggested that subsidence was transporting it downward. The CIRS limb observations were limited and did not provide direct evidence that the observed undulatory structure in the temperatures and winds was indicative of the zonal mean structure, like on Earth. The evidence for that came from Cassini radio occultations [Schinder et al. 2011a]. Occultations at several different longitudes over the course of a few months indicated larger-scale undulations in the retrieved temperature profiles that agreed with those found with CIRS and which did not differ markedly with longitude. In addition, there was much smaller-scale structure that did vary from profile to profile, that could be indicative of atmospheric wave structure, perhaps of internal gravity waves.

Cassini not only provided close-up viewing of Saturn, but also an opportunity to observe the temporal behavior of the oscillation. Guerlet et al. [2011] compared CIRS limb observations 4–5 years apart of the equatorial regions. They observed that the pattern reported by Fouchet et al. [2008] had descended. The descent rate of warm and cold layers was consistent with the ~15-year period—approximately half of Saturn's year—that had been inferred from the ground-based observations by Orton et al. [2011]. Cassini radio occultations [Schinder et al. 2011a] also indicated a roughly comparable descent rate. During the descent the pattern is not rigid, and the vertical structure undergoes some modulation. The Earth's QBO and SAO also exhibit descending patterns that modulate. This behavior is linked to the deposition of zonal momentum of the absorbed vertically propagating waves that drive the oscillation—see, for example, Baldwin

et al. [2001]. More recent limb observations of Saturn, from 2015 [Guerlet et al. 2018] have shown the descent continues.

Li et al. [2011a] have combined cloud-tracking of Cassini imaging data and application of the thermal wind equation to CIRS temperature retrievals from nadir-viewing observations to assess the temporal variation of the zonal winds near the equator. Although they cannot access the higher altitudes associated with limb-sounding observations, they can probe the tropopause region better. They find variations in the zonal winds consistent with the previously cited work, but with the amplitude reduced near the tropopause.

The question arises whether the Saturn equatorial oscillation is really semi-annual, like the SAO on Earth. Comparison of temperatures retrieved from Voyager measurements in 1980–1981 with Cassini observations one Saturnian year later in 2009–2010 by Sinclair et al. [2014] and Li et al. [2013] at 2.1 mbar and 50–100 mbar, respectively, indicated that the later temperatures were noticeably warmer than expected if the oscillation were strictly periodic [see also the review by Fletcher et al. 2018]. More recently, Fletcher et al. [2017] found that the descent of the equatorial oscillation was significantly affected by the great northern storm, described earlier, at the beginning of 2011, when the equatorial region at pressures less than 5 mbar cooled by 10–12 K. This disruption persisted until at least 2014, after which the normal phasing of descending warm and cold equatorial anomalies appears to have resumed. Recent observations of Earth's QBO have revealed a disruption in the phase of the descending pattern in 2016. The origin of this disruption is not known, although zonal momentum transport from the northern hemisphere by mid-latitude planetary waves has been suggested. There have been a few analyses of Saturn's temperatures to characterize wave structure, from the Voyager Infrared Interferometer Spectrometer—IRIS—measurements [Achterberg and Flasar 1996] and from Cassini CIRS [Li et al. 2008; Guerlet et al. 2018], and these have suggested the presence of planetary waves with low to intermediate zonal wavenumbers. More effort is warranted.

Rings

This section contains an introduction which outlines the nature of ring thermal emission, a brief overview of Saturn's rings and their key characteristics, and a brief discussion of CIRS ring data analysis. Following the introduction is a discussion of CIRS ring models, the key CIRS ring results, the modeling of those results organized by the CIRS science objectives and the science assessments, and conclusions and future work. Thermal measurements of Saturn's rings by ground-based or spacecraft-based observations are summarized in book chapters by Cuzzi et al. [1984]; Cuzzi et al. [2009]; and Spilker et al. [2018]. The CIRS ring material in the following sections is taken primarily from Flasar et al. [2004] and Spilker et al. [2018], and a multitude of CIRS ring papers.

Introduction

The thermal response of a ring is determined by the way particles absorb, transfer heat in their interior and re-radiate it through the ring. The radiation source functions depend upon the ring structure. Energy sources include direct, reflected and scattered solar light, mutual heating by neighboring ring particles, and thermal and visible radiation from Saturn. Because of mutual shading and heating between particles, the thermal emission is determined not only by the physical properties of the particles, but also by the structural and dynamical properties of the ring disk itself. Friction in mutual dissipative collisions between particles, due to their possibly irregular surfaces, transforms orbital kinetic energy into spin. The particle surface temperature and its thermal emission are expected to vary on the surface along the rotation axis and azimuthally. Ring particles, as they collide into each other, are tumbling around the ring mid-plane with a vertical excursion governed by the local ring dynamics. The thermal history of a particle along its orbit is then an indicator of vertical dynamics. The particle is conditioned by the time it spends in sunlight and in the planetary shadow. At the exit of the shadow, its thermal inertia scales its ability to warm up as a function of time. Any difference in the heating curves between the lit and unlit sides should reveal the time each particle spends on each side.

Friction in mutual dissipative collisions between particles, due to their possibly irregular surfaces, transforms orbital kinetic energy into spin.

The thermal emission of planetary rings is thus expected to be a complex function of ring particle properties, ring disk structure, and observed geometry. Individual particle properties include size, regolith characteristics, Bond albedo, thermal emissivity and inertia, spin rate, and spin axis orientation. Ring structural and dynamical properties include optical depth, particle size distribution, vertical thickness and excursion, filling factor, and thermal inertia, too [Spilker et al. 2003a; Ferrari and Leyrat 2006; Morishima et al. 2009; Ferrari and Reffet 2013]. The emission observed from Saturn's rings also depends on the illumination and viewing conditions and to the position of the targeted ring segment relative to those two. Phase angle, solar elevation angle, observer elevation angle, local hour angle, and radial location in the rings are thus parameters of variable impact on that thermal emission.

SATURN RINGS OVERVIEW

The major ring features, from closest to farthest from Saturn, are the D-ring, C-ring, B-ring, Cassini Division, A-ring, narrow F-ring, faint G-ring and extended, and faint E-ring. The main rings (D through A) range from ~67,900 km to 136,800 km from the center of Saturn, and lie in a thin disk that is typically less than 10 meters thick [Tiscareno et al. 2007]. The C-ring and Cassini Division optical depths are lowest; 0.05–0.35 and 0–0.1, respectively. The B-ring optical depth is highest, 0.4 to >5, while the A-ring optical depth is intermediate, 0.4 to 1. Some gravitational wakes—temporary clumping of particles—have been detected in these to rings. Such a diversity in

the opacity of the rings versus distance is expected to play a role in the temperatures measured by CIRS and allowed us to address additional key questions such as: how does clumping affect the thermal radiation from the rings, and what does this tell us about the nature of these aggregates? Are the rings organized in a multi-particle-layer or mono-particle-layer, and how does the clumping affect this structure? How does the thermal inertia of the rings vary with the disk structure (thickness, filling factor, particle vertical excursion, etc.) or with particle properties such as albedo, surface roughness, porosity, or spin?

CIRS was indeed able to observe all but the faint and optically thin D-ring, G-ring, and E-ring, with optical depths ranging from ~10^{-5} to 10^{-6}. CIRS results from Saturn's F-ring, with the best data taken during the ring-grazing orbits near the end of the mission, are still under study.

CIRS RING DATA ANALYSIS

The ring spectra (Figure CIRS-1) delivered by the FP1 focal plane have been predominantly used for obtaining information about the ring temperatures because they contain the peak of the Planck function for typical ring temperatures (50–100 K). This allows a determination of the characteristic temperature within the FOV. Nearly every uncontaminated FP1 spectrum taken during the mission is well fit by a Planck function such that [Spilker et al. 2006; Pilorz et al. 2015]

$$I(\nu) = \beta B(\nu, T)$$

where $I(\nu)$ is the spectral intensity in W cm^{-2}sr^{-1}cm, $B(\nu, T)$ is the Planck function dependent on the wavenumber ν, T the effective temperature in the FOV. The β-factor is scalar, and stands for the product of the geometric filling factor β_{geo}, the infrared emissivity ε_{IR}, and the factor β_{therm} that arises due to a distribution of temperatures within the FOV [Altobelli et al. 2007]:

$$\beta = \beta_{geo}\varepsilon_{IR}\beta_{therm}$$

The expected deviations from the single-temperature fit resulting from the presence of multiple temperatures within the FOV are relatively small [Spilker et al. 2005].

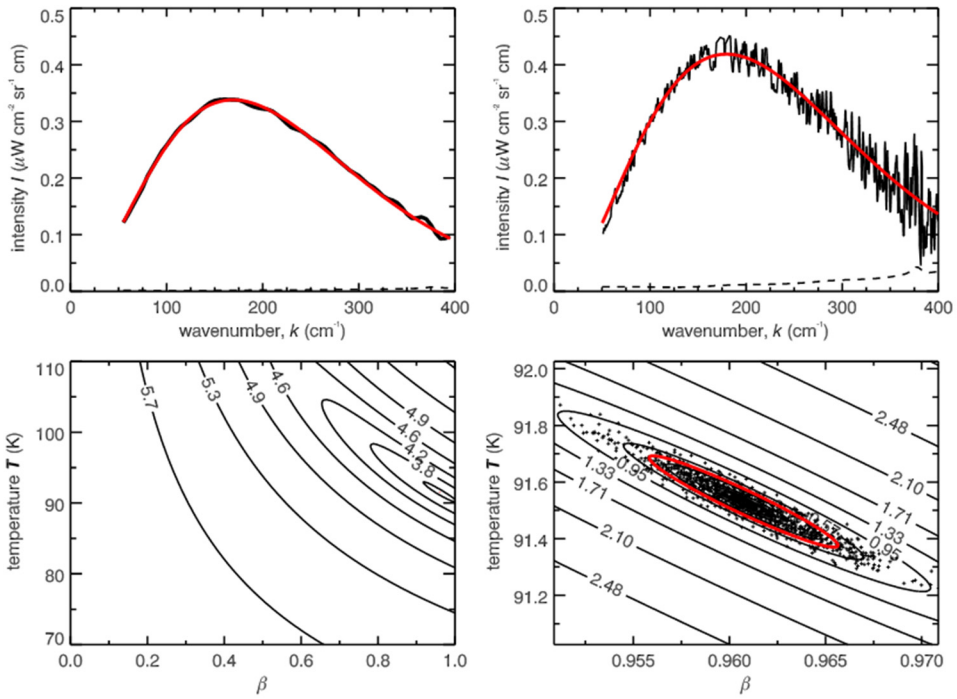

Figure CIRS-1. *Top panels*: show examples of low and high spectral resolution spectra used in the fitting process. We show two spectra selected from the B-ring at 105,000 km from Saturn. *Top left panel*: is from the lit, high-phase low-resolution (15.5 cm^{-1}) scan. *Top right panel*: is from the lit, low-phase high-resolution (1 cm^{-1}) scan. Noise spikes have been removed from these spectra. Each spectrum is plotted with the best fit to the single-temperature Planck function. The NESR at these wave numbers are shown as dashed lines. *Bottom panels*: show an example of the chi-square fitting procedure for the high-resolution spectrum. *Bottom left panel*: contours of the chi-square are shown over a large range of possible values. These contours are typical, and there are no local minima other than around the best fit (shown as a red dot). *Bottom right panel*: is an expanded plot of the contours in the vicinity of the best fit. Here, the theoretical 1 σ contour that we use in our error analysis is highlighted in red; the crosses represent the temperature and beta values derived from 1000 perturbations to the best fit spectrum, using uncorrelated, randomly generated noise with a standard deviation equal to the NESR at any wavenumber. In this realization 672 of the 1000 points lie within the theoretical contour, in close agreement with the expected 68%. Figure from Spilker et al. [2006], Figure 2.

Ring thermal structure

The main result obtained on the way the thermal emission, first as a function of the distance from the planet and of optical depth, then as a function of the solar elevation about the ring plane or as a function of the spacecraft position relatively to the Sun and finally with local hour angle, are presented below.

TEMPERATURE VARIATION WITH DISTANCE AND RING OPTICAL DEPTH

The effective temperature of Saturn's rings, as defined above, varies with radial distance from the planet. Radial temperature variations (Figure CIRS-2) are observed across both the lit and unlit

rings at both low and high phase angles [Spilker et al. 2006]. On the lit side of the rings, at low phase angle, the dominant trend across the ring system is a rough anti-correlation between optical depth and temperature. The optically thin C-ring and Cassini Division are considerably warmer than the optically thick A-ring and B-ring. However, within the A-ring and B-ring, the correlation between optical depth and temperature is distinctly positive and stronger at low phase angles (phase angle dependence will be discussed in more detail below). At high enough optical depth, the sunlight does not penetrate so deeply into the ring. The C-ring and Cassini Division also have lower albedos than the A-ring and B-ring. The lower albedos, lower optical depth and reduced mutual shadowing in these rings all contribute to their higher temperatures.

The temperatures of the A-ring and B-ring are correlated with their optical depths when viewed from the lit side of the rings and are anti-correlated when viewed from the unlit side. On the unlit side of the B-ring the lowest temperatures correlate with the largest optical depths and are also the same at both low and high phase angles, indicating that very little sunlight penetrates to the unlit side of the densest ring region. This also suggests that vertical mixing of ring particles is not very efficient in the optically thickest part of the rings. In the densest part of the unlit B-ring the phase variation nearly vanishes, indicating that direct sunlight does not play a significant role in heating these particles.

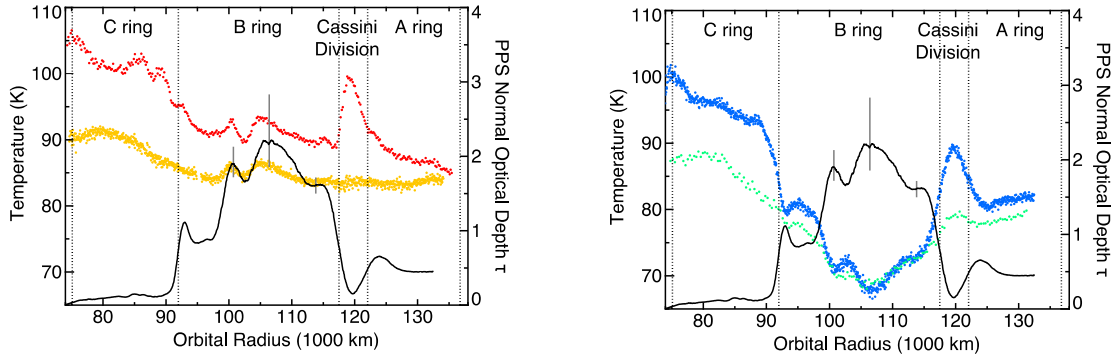

Figure CIRS-2. Radial temperature variations. *Left*: Radial temperature variation across the lit rings at both low and high phase angle. The ring temperatures at low phase (red symbols) and high phase (gold symbols) are shown as a function of ring radius, with boundaries between rings indicated by dashed lines. Both scans were taken at afternoon local times. The Voyager PPS optical depth profile is superposed, smoothed to the CIRS FP1 resolution. Vertical gray bars indicate the calibration uncertainty (1σ) in the PPS-derived B ring optical depths. Elsewhere the uncertainties are narrower than the width of the plotted line. *Right*: Same as the left, but for the ring temperatures at low phase (blue symbols) and high phase (green symbols). Figures from Spilker et al. [2006].

TEMPERATURE VARIATION WITH SOLAR ELEVATION AND THE EQUINOX CASE

One of the strongest effects observed in the ring thermal data is the decrease of temperature with decreasing solar elevation [Flandes et al. 2010]. The solar insolation is therefore, to first order, the main driver of the ring temperature. This effect is observed in all ring regions. Regions with low optical depth, the C-ring and Cassini Division, appear to have more limited amplitudes in

temperature variations. In contrast, larger differences are found between solar solstice and equinox in the B-ring and A-ring. The measurements of ring temperature with solar elevation (Figure CIRS-3) now cover a full seasonal cycle. The analytical model from Froidevaux [1981] assuming a monolayer with only slow rotators was fit to each ring data set using the visible bond albedo as the only model parameter—see Flandes et al. [2010] for model details—and can reproduce the observed temperature changes.

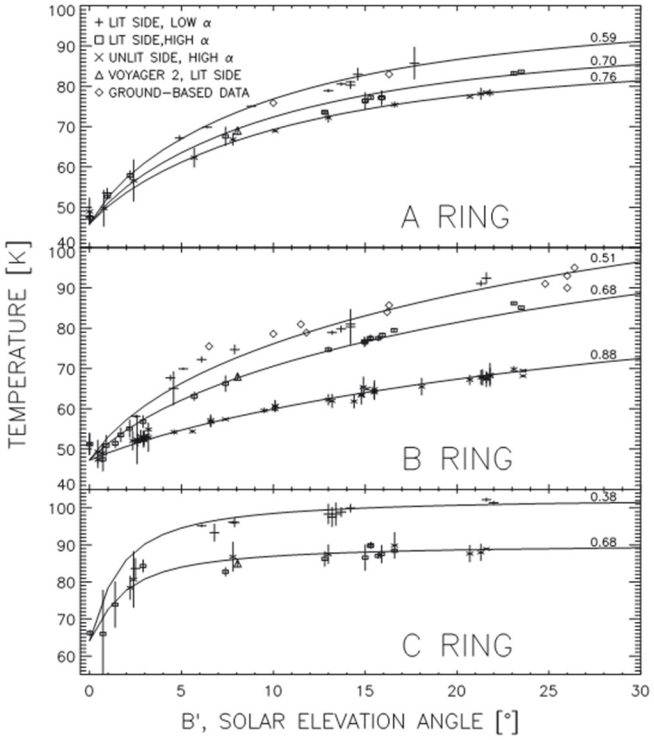

Figure CIRS-3. Saturn's ring temperatures as a function of solar elevation angle for the A-ring, B-ring, and C-ring. Observational data from Cassini CIRS (plus mark, cross and square), ground-based (diamond) and Voyager 2 (triangle) are shown. Data are presented at low (α ~ 30 deg) and high (α > 120 deg) phase angles for lit and unlit sides of the rings. The error bars represent the observed standard deviation. The analytical model from Froidevaux [1981] was used to fit the CIRS data assuming a mono-particle-layer of a ring and only slowly rotating particles. Figure from Flandes et al. [2010].

The solar equinox occurred on August 11, 2009. During the equinox period (August 11–13), CIRS obtained 15 radial scans [Spilker et al. 2013]. These observations took place when the solar elevation was between 0° and 0.036° above the ring-plane, mostly after the equinox. The very low solar elevation angle guarantees that the direct solar illumination is negligible. The absolute spacecraft elevation angle was about 20° for all the scans. Assuming that the heat source at the equinox is simply the infrared flux from Saturn, the simplest zeroth-order model gives the expected particle temperatures (Figure CIRS-4) [Spilker et al. [2013]. Saturn infrared emission is definitely structuring the radial variations of ring temperatures at equinox. The anti-correlation between the

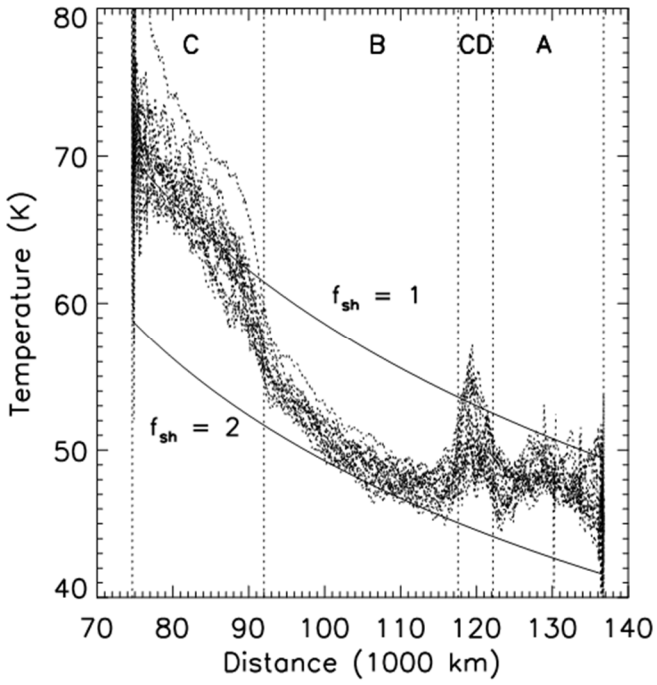

Figure CIRS-4. Ring temperature versus saturnocentric distance at the solar equinox (dotted curves). The temperature and the optical depth are anticorrelated and the temperature decreases with distance, as expected for the case of central heating. The temperature profiles from a simple model are also shown for optically thin (f_{sh} = 1) and thick (f_{sh} = 2) rings. See Spilker et al. [2013] for details.

ring temperature and the optical depth strongly supports the idea that nearby particles partially block Saturn's radiation depending on their optical depth.

The local observed temperature variations from scan to scan are caused by a change in observer geometry if the particles are not isotropic emitters. We found that the leading hemisphere of the particle is warmer than the trailing hemisphere at least for the C-ring and probably for the A-ring and B-ring too, although the temperature differences are as small as the error bars. This asymmetry indicates that some fraction of particles has spin rates lower than the synchronous rotation rate, provided that their thermal inertia is not zero. Spins slower than synchronous are indeed expected for the largest particles in N-body simulations [Salo 1987; Ohtsuki and Toyama 2005; Morishima and Salo 2006].

A multi-particle-layer model of Morishima et al. [2009] can reproduce the observed equinox temperatures for the C-ring and B-ring. C-ring temperatures were being well reproduced by the mono-particle-layer model of Ferrari and Leyrat [2006] while the multi-particle-layer model significantly underestimated the A-ring temperatures. This, in fact, indicates that the A-ring was not completely cooled down at the equinox and that it is possible to give constraints on the size and seasonal thermal inertia of A-ring particles. For further detail see the section entitled Seasonal Thermal Inertia and Particle Size, and the paper by Morishima et al. [2016].

TEMPERATURE VARIATION WITH PHASE ANGLE

The analysis of the temperature variations with phase angle across the main rings (Figure CIRS-5) reveals a variable dependence on optical depth and solar elevation [Altobelli et al. 2007, 2009; Morishima et al. 2017]. A surge in temperature is observed at low phase angles, if the solar elevation is low enough and the (normal) optical depth of the ring region observed (high enough) typically above ~0.3.

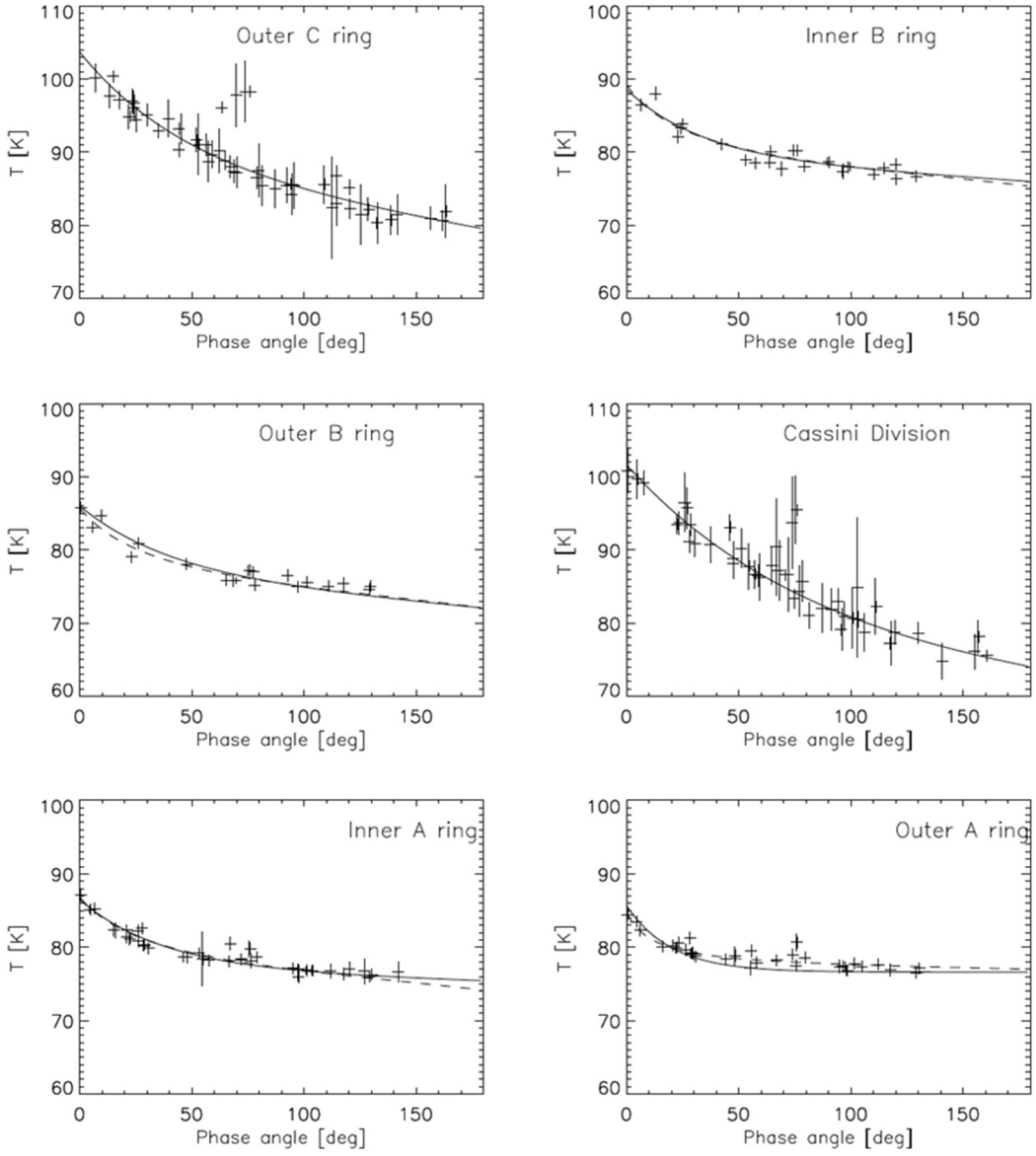

Figure CIRS-5. Temperature versus phase angle obtained at different ring locations. In all ring regions, an exponential-linear fit is applied (plain curve). In the A-ring and B-ring only, a fit based on the shadowing function of Hapke [1993] is also plotted (dashed curve).

The shape of thermal phase curves does not vary with solar elevation in the optically thin portions of the C-ring and Cassini Division. However, the shape does vary in the optically thicker regions of the B-ring, with an opposition surge at low solar elevation [Altobelli et al. 2007]. A similar behavior is observed in the C-ring plateaus [Altobelli et al. 2009] which are optically thicker than the surrounding background. The temperature surge is more pronounced for the plateaus than the C-ring background at low phase angle while similar phase curves are seen for both the plateaus and background at large phase angle.

The morphology of the phase curve, in particular the thermal surge in optically thicker regions for combinations of low phase angles and low solar elevation, can be explained by mutual shadowing between particles. Lower solar elevations obviously favor mutual shadowing by increasing the length of shadows projected on the ring-plane. (For futher detail see the section entitled Modeling of Opposition Surge for Packed Particulate Medium.)

AZIMUTHAL DEPENDENCE

CIRS executed azimuthal scans (Figure CIRS-6) of the lit and unlit rings at constant radial distance from the planet to measure ring temperature variations with local hour angle [Leyrat et al. 2008a]. Some scans investigated eclipse cooling, from which the thermal inertia of the rings and possibly of wake structures within dense rings were inferred.

Temperature scans of A-ring, B-ring, and C-ring versus local hour angle all exhibit a large drop in temperature from the entry into the shadow to a few hours after the shadow exit. This eclipse event is the major source of azimuthal temperature variations. The thermal gradient between entry

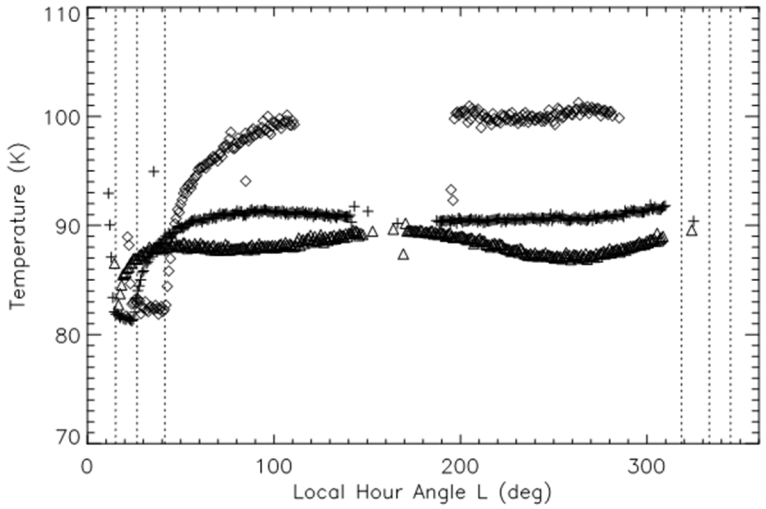

Figure CIRS-6. Typical azimuthal scans of ring temperatures versus local hour angle: C-ring (diamond), B-ring (cross), and A-ring (triangle). The vertical dotted lines mark the shadow boundaries for each ring. At this epoch, the Sun is relatively high above the ring plane (*B'*=-21.4 deg) and the shadow sector is significantly smaller for the A-ring. The phase angle ranges between 14 deg and 25 deg.

and exit from the shadow increases with solar elevation and decreases with phase angle [Leyrat et al. 2008a]. The shadow crossing is not detectable on the unlit side of the thick B-ring [Leyrat et al. 2008a; Reffet et al. 2015], which is consistent with the expectation that no direct sunlight reaches this side.

The temperature of the A-ring exhibits a quadrupole azimuthal modulation of 2–3 K on top of the eclipse drop, which is about 5–6 K [Leyrat et al. 2008a]. This modulation appears to vary with viewing and lighting geometry [Morishima et al. 2014]. Ferrari et al. [2009] showed that the model fit for the A-ring azimuthal variations of the scaling factor β at different solar elevations were improved using the regularly spaced, infinitely long, opaque elliptical cylinders, first introduced by Hedman et al. [2007] (Figure CIRS-7).

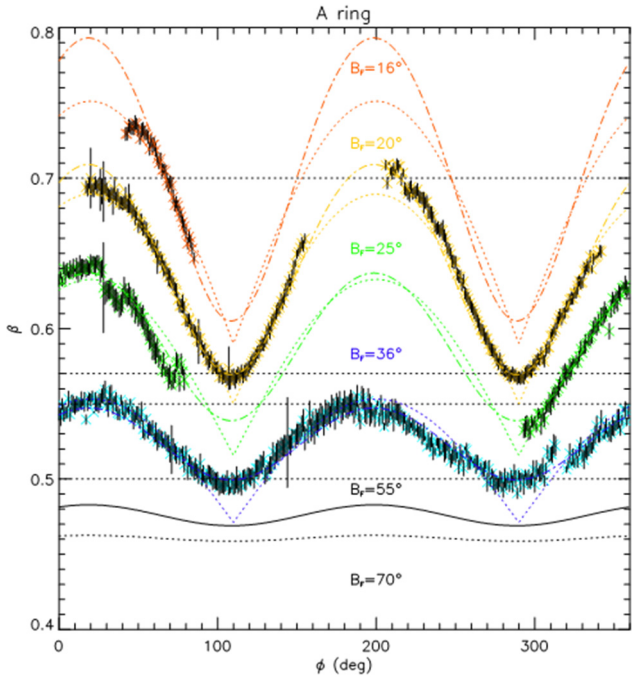

Figure CIRS-7. Averaged azimuthal profiles of the A-ring filling factor as a function of S/C azimuthal angle in the rotating frame ϕ at various spacecraft elevation *B* (shown as B_F in the figure). Best fit for elliptical cylinders wake model (dash-dot) or rectangular bars wake model (dot) are superimposed with the same color. Expected profiles at elevation *B* = 55 deg and *B* = 70 deg are also plotted. Figure from Ferrari et al. [2009].

Ring optical depth at mid-IR wavelengths

Differences between radial profile of optical depths at different wavelengths provide information on changes in the size distribution versus distance. Such profile was definitely missing at infrared wavelengths. Several CIRS ring occultations of the bright stars Eta Carinae and CW Leo were observed using the CIRS FP3 10-pixel array, with the objective of obtaining such mid-infrared (MIR) optical depths of Saturn's main rings (Figure CIRS-8). Since the rings also emit thermal photons at these wavelengths, the FP3 array was aligned along the occultation track. The stars and their

extended dust clouds were observed across two pixels, and the remaining pixels were used for background subtraction of the rings. CIRS optical depths were compared to UVIS optical depths from a high-resolution UVIS occultation of the star β Persei. It was expected that the cross-sections in the UV and MIR would behave similarly, but a linear fit of the observed MIR power to the UVIS-derived line of sight filling factor for a UV occultation indicates that the observed MIR filling factor is approximately 4% smaller than that predicted from the ultraviolet occultation of Saturn's rings [Pilorz et al. 2018a]. The optical depths agree well in the C-ring and A-ring, but in the B-ring the CIRS derived optical depth is smaller. This could result from the simplistic calibration, or be due to details related to the saturation of the CIRS signal in that region due to strong B-ring emission in the MIR. Additional CIRS Eta Carinae occultations obtained late in the mission are still to be processed.

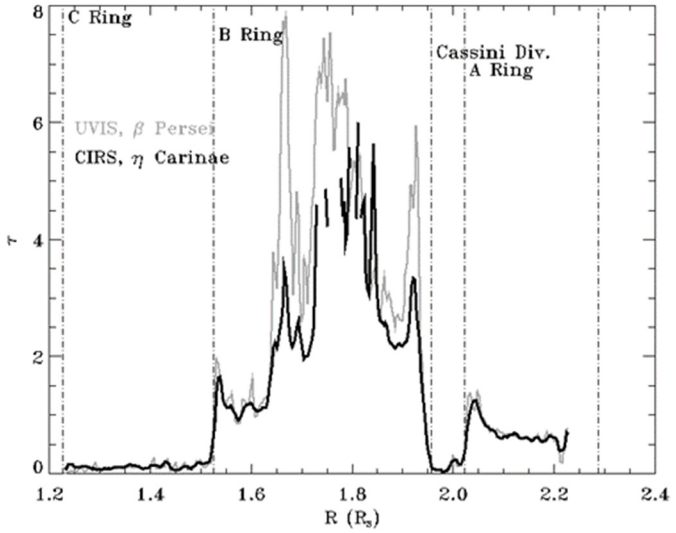

Figure CIRS-8. MIR optical thickness. This is an estimate obtained from the Eta Carini occultation, which may change pending ongoing work to correct for the response of the FP3 detectors, the location of the star within the FOV, the thermal signal from the rings, and the maximum signal received. Figure from Pilorz et al. [2018a].

Ring thermal models

Saturn's rings offer a wide diversity of optical depths and dynamical contexts. Particle properties are expected to be more easily probed in optically thin rings or in rings with very low volume filling factor *D*. As the volume filling factor increases or as tidal effects diminish, particles may interact dynamically to form wakes, gravitational instabilities of any form, like typically suggested for Saturn's A-ring and B-ring. The thermal behavior of the ring depends on the structure of group ensembles or on the dynamics of colliding particles, which is still not well known. If *D* is low, particle-based models are generally used. In case of high volume filling factor, the ring can be treated either as infinitesimally long elliptical or rectangular cylinders or as a slab or static packed bed with limited excursion of ring particles. These latter slab-based models do not usually consider individual particles but can eventually treat heat transfer both at the particle scale and

the scale of the ring itself. They may be suitable for the thick A-ring and B-ring and for the wake structures seen in these rings.

Various models have recently been developed to tentatively reproduce the observed thermal behaviors of Saturn's rings. They rely on different a priori hypotheses and produce various observables to be fitted to data. At this stage, none of these models is able to reproduce all observed thermal behaviors at once. We describe here models for the ring geometric filling factor and temperatures that have been developed in the past decade. These thermal models are classified into particle-based models and slab-based models.

Heat transfer

The particle-based models solve the heat diffusion equation at the scale of the particle and its facets, whereas the slab models solve it at the scale of the ring. Both ring and particle can be considered as porous media. In order to follow the change of the temperature T with time in such media, the thermal diffusion equation needs to be solved with appropriate boundary conditions, i.e., energy balance, assuming effective thermal properties of a mixture of voids and matter.

The temporal variation of the incoming flux at the chosen scale occurs due to the particle spin, to azimuthal motion around the planet, or to vertical motion of particles in optically thick rings. While some models explicitly take into account these variations by solving the thermal diffusion equation, the heat conduction term is often ignored in simple models. On a long timescale, seasonal variation occurs due to the obliquity of Saturn. It is reasonable to ignore the heat conduction term for the seasonal effect as the thermal relaxation time is much shorter than the Saturn's orbital period. An exception is at equinox, at which the rings may not completely cool down to the equilibrium temperatures that are determined in the absence of direct solar illumination.

The total radiation flux consists of the sum of the direct solar radiation, the thermal radiation from Saturn, the sunlight reflected by Saturn, the thermal radiation from nearby particles, and the radiation of visible light multiply scattered by neighboring particles. Methods to calculate these fluxes vary among models but the direct solar radiation term dominates other terms except near solar equinox.

Particle-based models

The two extreme examples of the particle-based models are the mono-particle-layer model [Froidevaux et al. 1981; Ferrari and Leyrat 2006] and the multi-particle-layer model [Kawata 1983; Morishima et al. 2009]. The particle-based thermal models that have been recently developed [Ferrari and Leyrat 2006; Morishima et al. 2009] calculate temperature distribution over the surfaces of individual particles. The ring temperature is derived by integrating the emitted spectrum averaged over the particle surfaces. Therefore, these models are applicable to any observational geometries while the early models are practically applicable only to ground-based observations. Particles may oscillate around the ring mid-plane and exhibit spin. Their properties are characterized by various

parameters such as bolometric Bond albedo, distribution of spins, thermal inertia, infrared emissivity, or surface roughness.

Monolayer Model: Ferrari and Leyrat [2006] proposed a standard spin model that calculates the temperature of a monolayer ring of spinning particles with finite thermal inertia. It calculates exactly the surface temperature pattern as a function of spin rate, obliquity and thermal inertia. The surface temperature map of a particle is calculated over time along its specified orbit, taking into account the periodic crossing of the planetary shadow and the changing directions of the heating sources in the particle rotating frame.

For each particle facet the heat diffusion equation is solved in 1D-spherical coordinates over several times the larger one of the skin depth associated with the particle spin or that with the rotation around Saturn. The energy balance is applied at the scale of a facet of a particle. It takes into account mutual shadowing between particles, visible light scattered and infrared heating by nearby particles or by the planet. The effective temperature of the unresolved particle is calculated from its integrated thermal spectrum as seen from the spacecraft position. Model parameters are the probability density functions for spin rates and orientations, the particle Bond albedo, emissivity, and thermal inertia.

Ferrari and Leyrat [2006] showed that the spin rate, orientation and thermal inertia significantly modulate the ring temperature along local hour angle L and that the longitude of the peak temperature mainly depends on the spacecraft local hour angle, as it alternatively observes the morning, noon, afternoon, or night-time face of particles. The distribution in spin rates or obliquities, prograde or retrograde, the thermal inertia affects this modulation to a lesser extent.

Multilayer Model: In the multi-particle-layer model of Morishima et al. [2009], the vertical thickness of a ring is assumed to be much larger than the particle size or equivalently the ring's volume filling factor $D = 0$. The model numerically solves the classical radiative transfer equation [Chandrasekhar 1960; Modest 2003] using the multi-stream method. The model adopts the plane-parallel approximation so rings are horizontally homogeneous.

The model takes into account heat transport due to particle motion in the vertical and azimuth directions by following temporal thermal evolution of thousands of ring particles. The model employs two different types of vertical motion of particles: sinusoidal motion without collision and cycloidal motion that mimics bouncing at the mid-plane. The model assumes, instead of an actual continuous size distribution, a bimodal size distribution consisting of fast and slow rotators. Fast rotators are small rapidly spinning particles having spherically symmetric thermal structure whereas slow rotators are large non-spinning Lambertian particles. The areal fraction of fast rotators and the ratio of the scale height of fast rotators to that of slow rotators are the input parameters. The ring effective temperature is derived by summing up the thermal emission of all ring particles toward the observer, taking into account the attenuation factor due to other particles on the line of sight.

MODELING OF OPPOSITION SURGE FOR PACKED PARTICULATE MEDIUM

Models for packed particulate medium [Lumme and Bowell 1981a; Hapke 1993], which were originally derived to explain reflectance measurements of atmosphereless bodies, was used by Altobelli et al. [2007, 2009]. These models envision Saturn's rings as a packed particulate medium. In this approach, the drop-off in temperature with increasing phase angle is related to a net reduction of the particles' illuminated cross-section as a result of mutual shadowing. In addition, particles must be big enough and far enough apart with respect to the wavelength so that diffraction effects are negligible, which is certainly the case for Saturn's rings at visible and thermal infrared wavelengths. For a given optical depth, the relevant physical parameter for particles to cast shadow is their volume filling factor *D*.

SLAB-BASED RING STRUCTURE MODELS

Current slab-based ring thermal models follow diverse objectives. They aim at predicting ring lit side temperatures with no attempt to implement the physical processes at the origin of the thermal emission [Altobelli et al. 2014], at reproducing the thermal opposition surge with a varying degree of surface roughness [Morishima et al. 2017], or at estimating the thickness of rings from thermal gradients between lit and unlit sides [Ferrari et al. 2005; Ferrari and Reffet 2013; Pilorz et al. 2015]. The slab-based models that reproduce the diurnal or seasonal temperature variations of lit and unlit sides help us understand how heat transfers from one side to the other and why the thermal inertias observed are so low.

Empirical modeling of lit side ring temperatures: Altobelli et al. [2014] attempted to fit the entire CIRS data set using a slab-based model with correction factors due to variations of observation geometries defined empirically. They focused on only the lit side, non-shadowed by the planet. This analytical model has proven to be a good predictor of temperature variations for most of the viewing geometries. The model has been tested over the whole ring radial extent, using radial slices 1500–4000 km wide. The radial resolution is constrained by requiring at least one hundred individual measurements with an error below 2 K within each ring slice. The resulting full parameter values are provided in Altobelli et al. [2014].

Particle scale properties

The models cited below have been compared to CIRS ring temperatures to provide constraints on ring and particle properties. They share some basic common parameters like albedo, spin or thermal inertia, which can be defined at both the scales of the particle and the ring. Some models include unique parameters.

BOLOMETRIC BOND ALBEDO

The bolometric albedo A_V (Figure CIRS-9) is the albedo averaged over ultraviolet to near-infrared wavelengths, weighted by the solar intensity. It controls the overall temperature level at any

observational geometry: the temperature increases with decreasing A_V. From Morishima et al. [2010] the albedo A_V derived from CIRS data is lowest, ~0.1, at the innermost C-ring and increases with increasing saturnocentric distance up to 0.6 at the mid B-ring. Through the mid B-ring to the outer B-ring, A_V is nearly constant. The Cassini division shows $A_V \sim 0.4$. The A-ring has a nearly constant A_V of ~0.5. The values of A_V derived from this thermal model can be compared with those from photometric observations and models. Although overall agreements are good, the thermal data generally give lower values of A_V than those from the photometric data, particularly for the C-ring. One possible explanation for the deviation is that the infrared emissivity ε_{IR} is less than unity while the thermal model assumes $\varepsilon_{IR} = 1$. Other studies (see the section entitled Scalar Thermal Emissivity for particle and ring emissivity) derive values for ε_{IR} of ~0.9 across all rings.

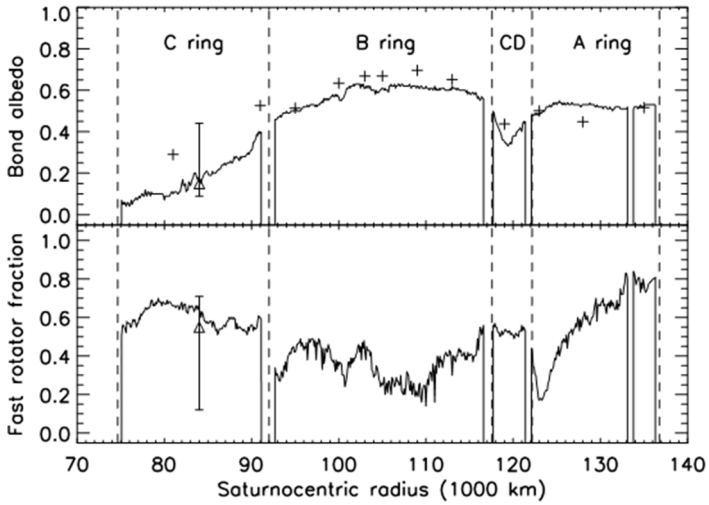

Figure CIRS-9. Bolometric Bond albedo A_V and areal fraction of fast rotators f_{fast} estimated from CIRS radial scans and the multi-particle-layer model. [Morishima et al. 2009, 2010]. The triangles are A_V and f_{fast} estimated from Voyager IRIS data and the mono-particle-layer model [Leyrat et al. 2008a]. *Top panel*: plus marks are the values of A_V calculated using visible and near-infrared albedos [Poulet et al. 2003; Porco et al. 2005].

SPIN RATE

The phase dependence and first-order azimuthal variations of ring temperatures can be interpreted as being caused by spherical spinning particles, as demonstrated by particle-based models. Slowly spinning particles emit predominantly toward the heat source, while fast spinning particles emit more isotropically.

The multi-particle-layer model of Morishima et al. [2009] employs a bimodal spin distribution consisting of slow rotators and isotropic emitters fast rotators with fraction f_{fast} which is roughly half for the all rings although some regional variations, such as smaller particles and more fast rotators in the outer A-ring, are seen. Roughly speaking, fast rotators are defined so that their spin periods are shorter than the thermal relaxation time [Morishima et al. 2011]. The spin periods of the largest particles are about the orbital period while the orbital periods of smaller particles are proportional

to particle sizes [Salo 1987; Ohtsuki 2006a, 2006b; Morishima and Salo 2006]. Therefore, f_{fast} increases with increasing particle-size distribution width and with increasing thermal inertia. Morishima et al. [2011] found good agreements between the size distribution width suggested from f_{fast} and thermal inertia and those estimated from stellar occultations [French and Nicholson 2000]. The analysis with Ferrari and Leyrat [2006] model of the temperatures of the C-ring at equinox epoch implied that both population are indeed present [Spilker et al. 2013].

DIURNAL THERMAL INERTIA

The thermal inertia Γ is a measure of the thermal responsiveness of a material to variations in the incoming flux. When Γ is small enough the particle temperature quickly reaches the equilibrium value determined by the instantaneous flux. Morishima et al. [2011] applied their multi-particle-layer model to CIRS azimuthal scans (Figure CIRS-10) that include data in Saturn's shadow and estimated the diurnal thermal inertia (diurnal here represents a variation due to rotation around Saturn).

The values of Γ are estimated from individual CIRS azimuthal scans at different solar phase angles. The values are about 10–20 $Jm^{-2}\ K^{-1}\ s^{-1/2}$ for all the rings. The Cassini division shows the lowest values. These are comparable to or slightly higher than those estimated with the mono-layer spin model both for pre-Cassini studies [Leyrat et al. 2008b] or Cassini observations of the C-ring at 10 $Jm^{-2}\ K^{-1}\ s^{-1/2}$ [Ferrari 2006; Spilker et al. 2013].

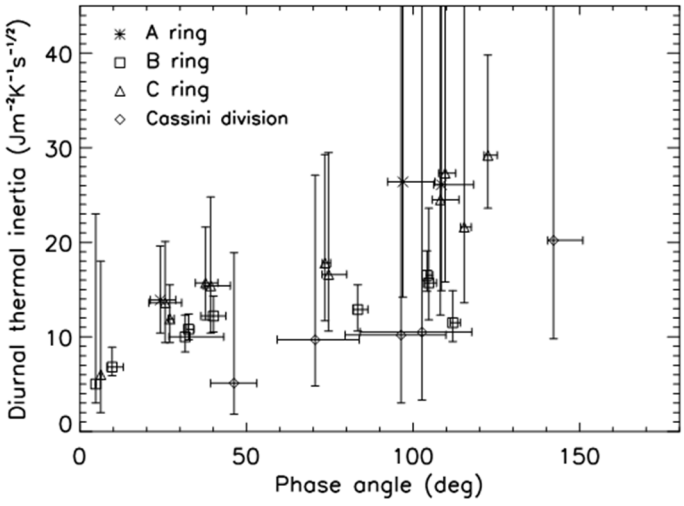

Figure CIRS-10. Diurnal thermal inertia estimated from CIRS azimuthal scans. The multi-particle-layer model [Morishima et al. 2009, 2011] is used. Thermal inertias of the B-ring and C-ring at the lowest phase angles (~5 deg) are those estimated by Ferrari et al. [2005] who applied their mono-particle-layer model to the ground-based data.

However, it was found that Γ increases with solar phase angle for all the rings. Morishima et al. [2011] interpreted this trend as caused by the size-dependent thermal inertia; large slow rotators have lower thermal inertia values than those for small fast rotators because the thermal emission

of slow rotators is relatively stronger than that of fast rotators at low phase and vice versa. Their additional parameter fits, which assume that slow and fast rotators have different thermal inertia values, showed the thermal inertia of fast rotators are 30–80 $Jm^{-2}\ K^{-1}\ s^{-1/2}$ and that of slow rotators are 5–9 $Jm^{-2}\ K^{-1}\ s^{-1/2}$. A probable reason for the large thermal inertia of fast rotators is that they cannot hold very fluffy regolith layers because of their fast spins while the slow rotators can accumulate a thicker, porous regolith layer leading to smaller thermal inertias.

SEASONAL THERMAL INERTIA AND PARTICLE SIZE

Morishima et al. [2016] applied both the multi-particle-layer model [Morishima et al. 2009] and the wake model [Morishima et al. 2014] to the equinox data of the A-ring. They found that the observed equinox temperatures are much higher than model predictions as long as only the flux from Saturn is taken into account. In addition, the post-equinox temperatures are lower than the pre-equinox temperatures at the same absolute solar elevation angle. These facts indicate that the A-ring was not completely cooled down at the equinox and that it is possible to give constraints on the size and seasonal thermal inertia of ring particles.

A simple seasonal model based on the monolayer model (Figure CIRS-11) was used to estimate the seasonal thermal inertia and the particle size for the A-ring [Morishima et al. 2016]. If the internal density and the thermal inertia of a ring particle are assumed to be uniform with depth, the seasonal thermal inertia is found to be 30–50 $Jm^{-2}\ K^{-1}\ s^{-1/2}$ in the middle A-ring, whereas it is ~10 $Jm^{-2}\ K^{-1}\ s^{-1/2}$ or as low as the diurnal thermal inertia in the inner and outermost regions of the A-ring. The particle size is estimated to be 1–2 m. Another internal structure model, in which a particle has a high-density core surrounded by a fluffy regolith mantle with Γ of 10 $Jm^{-2}\ K^{-1}\ s^{-1/2}$ shows that

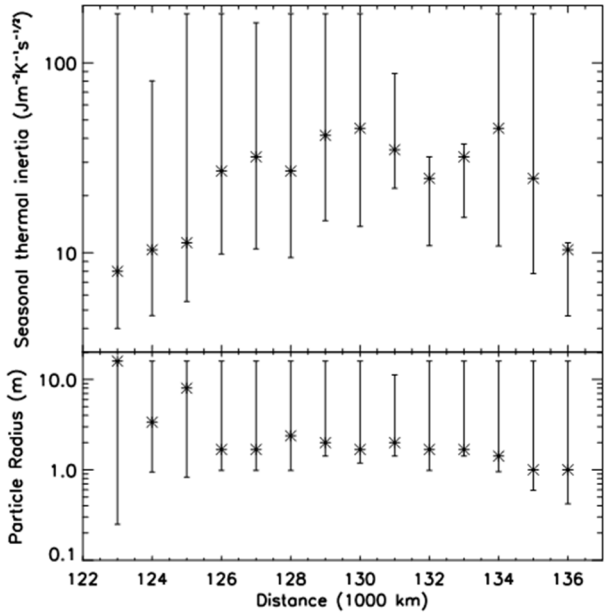

Figure CIRS-11. Seasonal thermal inertia and size of particles for the A-ring [Morishima et al. 2016].

the core radius relative to the particle radius is about 0.9 for the middle A-ring and is much less for the inner and outer regions of the A-ring [Morishima et al. 2016]. This means that the radial variation of the internal density of ring particles exists across the A-ring. Some mechanisms may be confining dense particles in the middle A-ring against viscous diffusion. Alternatively, the middle A-ring might have recently formed ($<10^8$ yr) by destruction of an icy satellite, so that dense particles have not yet diffused over the A-ring and regolith mantles of particles have not grown thick.

Scalar Thermal Emissivity

Since the thermal infrared emission of the particle is proportional to the scalar emissivity ε_{IR}, the temperature increases with decreasing ε_{IR}. A degeneracy between A_V and ε_{IR} is expected, as the particle temperature is proportional to $((1 - A_V)/\varepsilon IR)^{1/4}$ with a single heat source emitting visible light (e.g., the Sun).

It is possible to constrain ε_{IR}, if the ring temperature and the geometric filling factor are known [Altobelli et al. 2008]. For optically thin rings, the geometric filling factor is well represented by the formulation of the multi-particle-layer model. Using the formulation, Altobelli et al. [2008] derived $\varepsilon_{IR} = 0.9$ for the C-ring. For the thickest part of the B-ring, the geometric filling factor is almost unity, and $\varepsilon_{IR} = 0.9$ is derived, too [Spilker et al. 2005; Altobelli et al. 2008]. Morishima et al. [2016] applied the wake model of Morishima et al. [2014] to the A-ring equinox data and estimated the lower limit of ε_{IR} to be ~0.9. The most recent work by Pilorz et al. [2018b] supports the previous results (Figure CIRS-12).

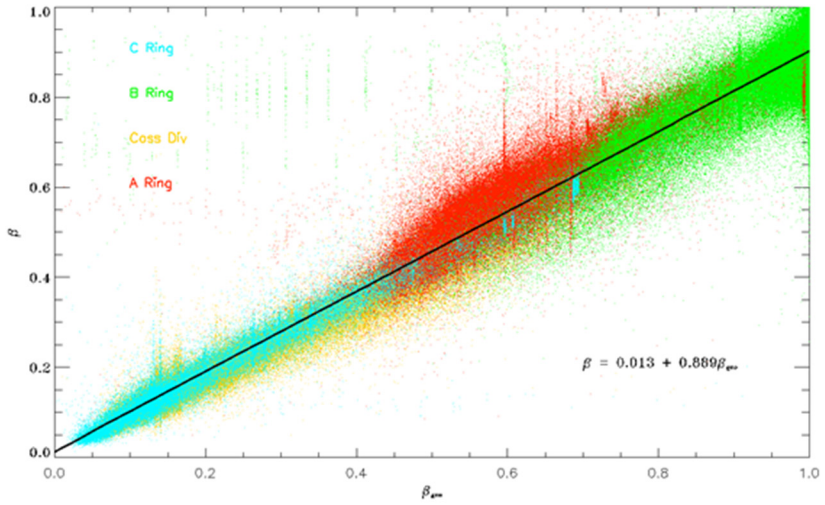

Figure CIRS-12. Scaling factor β versus convolved geometric filling factor β_{geo}. Figure from Pilorz et al. [2018b].

Ring-scale properties

When compared with the orbital and seasonal temperature variations of the lit and unlit sides, slab-based thermal models have provided new insights into the structure of dense rings, their volume filling factor, thickness, mass and thermal properties. The observed correlation of the vertical thermal gradient between both sides with optical depth proved useful in this regard.

VOLUME FILLING FACTORS OF A-RING AND B-RING

Both the thermal opposition effect model [Altobelli et al. 2009] and the multi-scale slab model favor a relatively high volume filling factor for the dense central B-ring. For a mono-disperse population of spherical particles, the half-width-half-maximum (HWHM) of the thermal opposition peak $h \approx -(3/8)\ \ln(1-D)$ yields $0.3 < D < 0.4$ in the B-ring. In the outer A-ring, $D < 0.2$. The C-ring background and Cassini division thermal phase curves could hardly be reproduced by this model, suggesting that, as expected, the thermal emission is not modulated by mutual shadowing in these thin rings. The C-ring plateaus, on the other hand, show strong opposition surge and Altobelli et al. [2007] yielded $D = 0.001–0.01$.

Reffet et al. [2015] also demonstrated that, in the frame of a multi-scale slab approach, the correlation between the lit-unlit face temperature difference and the optical depth seen in the B-ring [Spilker et al. 2006] could not be explained by an increasing compaction D but rather by an increasing slab thickness. The fit of this model to orbital and seasonal temperatures all along the Prime Mission in the central B-ring (across the B2 and B3 thickest regions of the B-ring yielded a volume filling factor $D = 0.34 \pm 0.01$, remarkably consistent with the value derived from the opposition surge [Altobelli et al. 2009] and with expectations from numerical simulations of ring dynamics [Salo and Karjalainen 2003; Salo and French 2010].

ENERGY BUDGET AND HEAT TRANSFER IN B-RING

The optically thick B-ring is a good region for a slab-based modeling approach because the ring particles are expected to be close together, as confirmed by its measured filling factor. The slab approach allows the heat transfer to be quantified through such a dense ring structure and provides an effective thermal inertia or thermal conductivity through a vertical slab from the lit to the unlit side of the B-ring. The heat transfer can be by conduction through the solid phase of particles, by radiation through voids or by the vertical particle motion.

Ignoring vertical particle motion in the thick B-ring, Ferrari and Reffet [2013] proposed a model for the B-ring slab, including both heat transport by radiation and conduction and being able to disentangle ring and particle thermal inertias thanks to a multi-scale approach (Figure CIRS-13). This model was successfully fitted to more than 600 temperature measurements of both lit and unlit sides of the B-ring and spread all along the Cassini Prime mission (2004–2009) [Reffet et al. 2015]. Only mid-phase angle data were used to avoid the low-phase angle thermal hotspot, which the model cannot account for, assuming particles are isothermal. Self-gravity wakes have been

observed in the B-ring and the reduced width of the inter-wake gap allows them to be considered as a continuous slab. This is not the case for these structures observed in the A-ring.

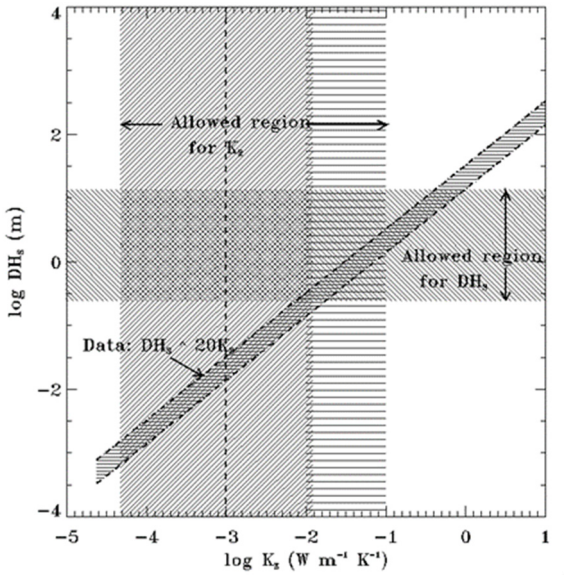

Figure CIRS-13. Diagram of the allowed values of effective ring thickness, DH_S, and effective heat conductivity, K_E, for the B-ring. These values are consistent with the ratio K_E/DH_S constrained in Pilorz et al. [2015]. The diagonal hashed region indicates combinations of values of DH_S and K_E such that ratio K_E/DH_S agrees with observations of the seasonal variation of heat throughput. The horizontal and vertical hashed regions indicate ranges of values for DH_S and K_E, respectively that are currently accepted as reasonable for ring thickness and the conductivity of icy moon regoliths or ring models.

THERMAL PROPERTIES, THICKNESS, AND SURFACE MASS DENSITY OF B-RING

Fitting of the model of Ferrari and Reffet [2013] to the central B-ring at the distance of 105,000 km from Saturn, where most data on the transient thermal regime about the planetary shadow were focused, Reffet et al. [2015] found a slab Bond albedo of A_V = 0.402 ±0.005 for an emissivity nearly unity, in total agreement with the energy balance studied by Pilorz et al. [2015].

Assuming no heat transport by the vertical motion of particles, but solely by conduction through the particles and radiation through voids, the particles have to be relatively conductive to ensure vertical heat transport through the slab. The effective slab conductivity estimated by Reffet et al. [2015] is on the order of 0.06–0.08 W m^{-1} K^{-1} at 80 K. Despite very different approaches but fitted on similar data sets, Reffet et al. [2015] and Pilorz et al. [2015] yield similar slab effective conductivity. The seasonal thermal inertia for the B-ring was found to be 30–35 Jm^{-2} K^{-1} s$^{-1/2}$, comparable to the seasonal thermal inertia of particles measured in the A-ring by Morishima et al. [2016].

The empirical model of Altobelli et al. [2014], using the entire CIRS data set to that date, and including radial scans near the shadow boundaries, yields a thermal relaxation time of 15–25

minutes, almost radially constant for the A-ring and B-ring. Since the thermal relaxation time is expected to be linearly proportional to the slab thermal inertia [Morishima et al. 2011], the radial variation of the slab thermal inertia is likely to be small for these rings.

Assuming that the vertical thermal gradient in the B-ring mainly fluctuates with the slab thickness and that ring and particle properties across the whole ring are similar to the one derived at 105 000 km distance, Reffet et al. [2015] have derived two radial profiles of the B-ring thickness $H_S(R)$ at two different epochs, where B_0 = −15.7° and B_0 = −4.5°. They happen to be highly consistent and exhibit variations in between 1 m and 3 m in the highest optical depth regions of the B-ring (Figure CIRS-14). If this thickness is assumed to be the same as the thickness of self-gravity wakes in the B-ring, it can be combined with their aspect ratios to derive a surface mass density across the thickest regions (B_2 to B_4) of the B-ring. It is found that the surface mass density is about 400 kg m^{-2} in the B_2 region, about 500 kg m^{-2} in the B_4 region and larger than 1000 kg m^{-2} in the B_3 region as self-gravity wakes are observed with difficulty in this dense region.

The resulting minimum mass of the B-ring derived by this method is $M_B = 8.7 \pm 1.7 \times 10^{18}$ kg [Reffet et al. 2015]. The minimum total mass of Saturn's rings, given the estimates of the C-ring, CD-ring, A-ring, and B_1-ring, for a total mass of 5.3×10^{18} kg [Baillié et al. 2011; Colwell et al. 2009; Tiscareno et al. 2007; Esposito et al. 1984], would then be $M_R = 1.4 \pm 0.2 \times 10^{19}$ kg. It is consistent with larger estimates provided by Esposito et al. [1983] and Robbins et al. [2010]. The minimum mass of the B-ring estimated by this method compares rather well to the residual mass of a viscous ring which has evolved over the age of the solar system, i.e., $M_R = 1.5 \times 10^{19}$ kg, whatever the initial (larger) mass is [Salmon et al. 2010].

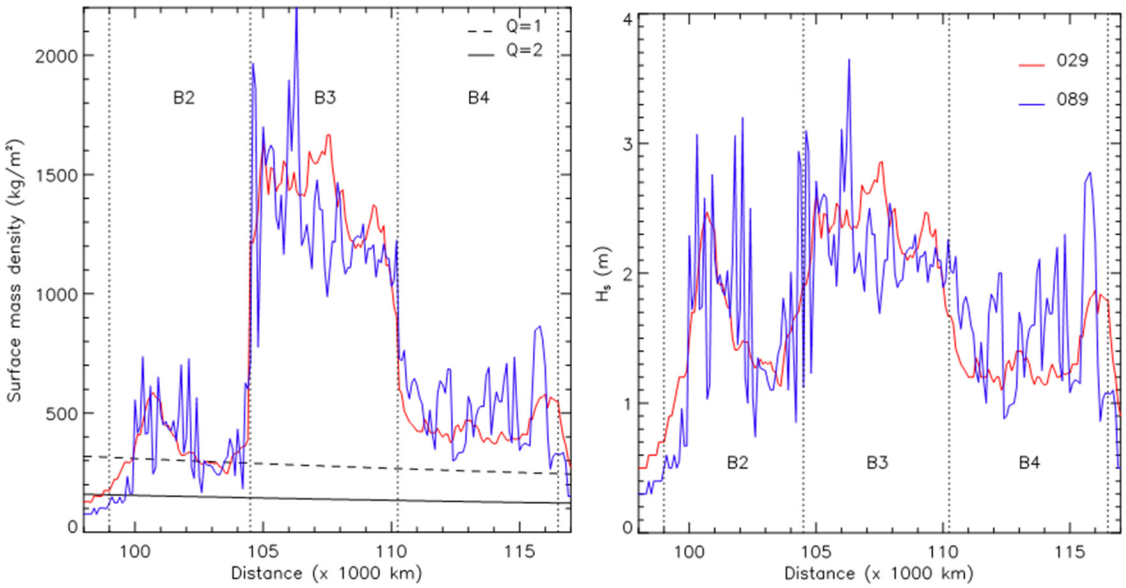

Figure CIRS-14. *Left*: Vertical thickness of the B-ring slab as a function of distance to Saturn. Both profiles have been estimated from vertical gradient measured at B_0 = -15.7 deg (rev. 29) and B_0 = −4.5 deg (rev. 89). *Right*: Radial variations of surface mass density of the B-ring as derived from ring thickness H_S. See Reffet et al. [2015] for details.

SELF-GRAVITY WAKES IN THE A-RING

The quadrupole azimuthal asymmetry first discovered in the A-ring in visible light from the ground [Lumme and Irvine 1976; French et al. 2007] has been since observed with the Cassini remote sensing instruments [Colwell et al. 2006; Hedman et al. 2007; Thomson et al. 2007]. It is caused by the presence of self-gravity wakes forming in this ring close to the Roche limit. As trains of gravitationally bounded particles, separated by gaps of low optical depth [Salo 1995; Robbins et al. 2010], self-gravity wakes are expected to modulate both the filling factor of the instrument field of view and the ring observed temperature along azimuth. These structures were satisfactorily modeled as rectangular bars or elliptical cylinders mainly after the analysis of occultation data [Colwell et al. 2006; Hedman et al. 2007].

Ferrari et al. [2009] showed that the fit with azimuthal variation of the beta factor at different solar elevations was improved using the regularly spaced, infinitely long, opaque elliptical cylinders using the geometric filling factor from Hedman et al. [2007]. In the wake model of Morishima et al. [2014], the temperature distribution over the wake surface is calculated instead of considering the temperatures of individual particles. Wakes are approximately represented by opaque elliptical cylinders as adopted in Hedman et al. [2007] and Ferrari et al. [2009]. The model ignores inter-wake particles for simplicity. The surface of an elliptical cylinder is divided into multiple facets and interactions between facets (inter-wake mutual heating and multiple scattering of photometric light) are calculated using a radiosity method. The ring effective temperature is calculated by summing up the thermal emission from facets that can be seen from the observer.

SURFACE ROUGHNESS OF THE B-RING

Morishima et al. [2017] reanalyzed the seasonal variation of thermal phase curves for the B-ring, first found by Altobelli et al. [2009]. Morishima et al. [2017] approximated the B-ring as a slab covered by craters and the surface roughness of the B-ring was found to be moderate. The modeled phase curves of optically thick rings are shallow if the phase angle change is primarily due to change of observer azimuthal angle. On the other hand, the phase curves are steep if the phase angle change is due to change of observer elevation angle, as inter-particle shadows become visible at higher observer elevation. In addition, the area of shadowed facets increases with decreasing solar elevation angle. These combined effects explain the large seasonal change of the phase curve steepness observed for the B-ring.

Regolith properties deduced from CIRS emissivity roll-off

Ring particles are often assumed to be covered by tiny regolith grains. In rings with low volume filling factor *D*, ring properties can be relatively easily related to the particle and grain properties. Under this assumption, rings are clouds of particles and their thermal emission is a function of the individual particle properties. The ring emissivity can be retrieved from observations and compared to a model which links it to the average emissivity of individual particles and then regolith grains. Rings then are multi-scale worlds made of cm-to-m-sized particles themselves covered by μm-to-

cm-sized grains. Morishima et al. [2012] after the work of Spilker et al. [2005] in the earlier stages of the Cassini mission propose a model to interpret the ring emissivity in terms of regolith grain size and chemical composition.

THERMAL EMISSIVITY ROLL-OFF AT SUBMILLIMETER WAVELENGTHS

The infrared spectrometer provides the thermal radiance *I* (ν) of the ring as a function of wavenumber, ν. If the emissivity ε(ν) is assumed constant over a footprint, using a single temperature approximation, Spilker et al. [2005] derived the ring emissivity as:

$$\varepsilon(\nu) = I(\nu) / \left(\beta_{geo} B(\nu, T_0)\right)$$

where they obtained β_{geo} using Voyager Power & Pyrotechnics Subsystem (PPS) occultation data and the multilayer approximation. The spectral roll off occurs for $\nu < 50$ cm^{-1} for all rings.

While Spilker et al. [2005] analyzed a limited number of CIRS spectra measured in the very early stage of the Cassini mission from relatively large distances, Morishima et al. [2012] analyzed a much larger number of spectra more comprehensively. In their emissivity model, two warm and cold portions, with temperatures T_w and T_c, are considered where f_w is the fraction of the warm portion. A superposition of spectra with two different temperature portions produces a downward convex function of the emissivity when applied to a Planck fit with a single temperature. On the other hand, the emissivity spectrum of water ice has a downward convex function in far-infrared wavelengths. Because these two effects cancel each other out to some degree, degeneracy is generated between the retrieved emissivity spectrum and the temperature distribution. To avoid this issue, Morishima et al. [2012] applied simultaneous fits of the emissivity model parameters (grain sizes) and of hot and cold temperature distributions. They also derived β_{geo} using Cassini UVIS data, taking into account the spacecraft elevation dependence on the photometric optical depth.

The emissivity of Saturn's rings at far-infrared wavelength (Figure CIRS-15) is high basically because of absorption caused by intermolecular vibrations of water ice. A dip seen at 230 cm^{-1} corresponds to the maximum of the imaginary part of the refractive index of the water ice (transverse-optical mode). As found by Spilker et al. [2005], the emissivity decreases with decreasing wavenumber for $\nu < 50$ cm^{-1} because water ice becomes increasingly transparent at longer wavelengths (thus opening a view into the deeper ring particle). The exact wavelength of the roll-off is a strong function of the size of an individual particle, with larger particles having flatter emissivity as the geometric optics limit is approached. No one particle or grain size fits any spectrum and the emissivity is reflective of the collective distribution of ring particle and their regolith grain sizes.

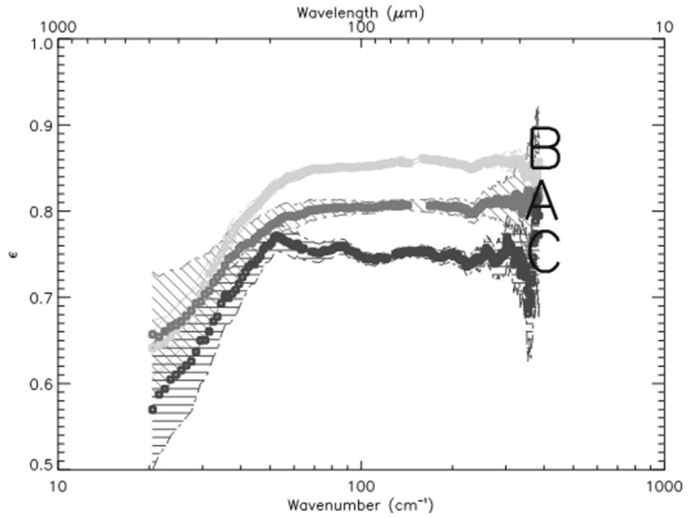

Figure CIRS-15. Emissivity spectra for the A-ring, B-ring, and C-ring. Figure from Spilker et al. [2005].

REGOLITH GRAIN SIZES INFERRED BY EMISSIVITY MODELING

A ring emissivity model was proposed by Morishima et al. [2012] to interpret the ring emissivity in terms of regolith grain size and chemical composition. The single scattering albedos of regolith grains are calculated using the Mie theory [Mie 1908; Bohren and Hoffman 1983], diffraction is removed with the delta-Eddington approximation [Joseph et al. 1976], and the hemispherical emissivities for macroscopic particles are calculated using Hapke's isotropic scattering model [Hapke 1993]. The composition of regolith grains is assumed to be pure water ice *Ih*. The intra-grain porosity of 0.7 is introduced to reproduce the shallow 230 cm^{-1} feature seen in the ring spectra in Morishima et al. [2012]. The maximum ring particle size that CIRS is sensitive to is estimated to be 1–100 cm in most of the rings, although the C-ring shows very different values of maximum grain size, and is dependent on the temperature of the ring. The median size is typically between 100 and 1000 μm. The reason for the temperature dependence of the estimated size distributions, particularly seen in the C-ring, is not clearly understood. Morishima et al. [2012] suggested that it is caused by the effect of eclipse cooling; only small grains are heated to very high temperatures.

The retrieved grain sizes are larger than those estimated from UVIS [Bradley et al. 2010, 2013] and VIMS [Nicholson et al. 2008; Cuzzi et al. 2009; Filacchione et al. 2012; Hedman et al. 2013] reflectances. An interpretation of this discrepancy is that large regolith grains are covered by small grains. At short wavelengths, the incoming light is primarily reflected by these small grains while at longer wavelengths the light can penetrate deeper into the regolith layers.

Exploring possible contaminants using CIRS spectra remains for future work, although the range of wavelengths covered by CIRS is not very suitable for this purpose due to strong water absorptions. Preliminary work [Edgington et al. 2008, unpublished] looked for the presence of silicates, carbon monoxide, and several other simple ices to no avail. This work also sought to determine the relative amounts of amorphous versus crystalline water ice. During Cassini's Solstice

Mission, a great many additional observations at high spectral and higher spatial resolution were acquired. Given this additional data, along with improved calibration of the CIRS data set, a proper statistical analysis and spatial trend analysis is warranteed to look for spatial variations in particle sizes and the presence of contaminant ring material. Another potential area of investigation would couple analysis of the longest wavelengths of the roll-off region with Titan Radar Mapper (RADAR) observations of the rings which probe the deeper particle cores.

Possible polarization effects have been studied. A few CIRS observations where designed to make use of the polarization nature of the FP1 interferometer (accomplished by rotating the spacecraft to three distinct orientations separated by 60°) to look for polarization effects in the far-IR. Theoretically possible with non-spherical thermal emitters, the data were inconclusive as observed patterns could be explained by other physical effects such as thermal opposition surges. These individual observations do not take into account the advantage that the entire CIRS FP1 data set picks off a particular polarization direction. The possibility that there is a polarization signal hidden in the global data set remains to be seen.

Conclusions and future work

Considering the Cassini CIRS data set in its entirety showed us that the ring can be characterized as a thermal system whose properties result from multi-scale phenomena, including the physical properties of individual particles as well as large-scale interactions, resulting in shadowing and thermal transport across the ring. Future analysis will aim at combining the global approach yielding empirical models of the ring thermal behavior, with the forward modeling of individual particles, such as to reject solutions possibly acceptable at one scale but not at the other. The key CIRS ring results are discussed in the next several paragraphs.

The global modeling of all measurements obtained over the illuminated rings yields radial profiles of the ring emissivity and albedo with the highest spatial resolution ever achieved in the thermal infrared. The anisotropy of the temperature distribution with viewing geometry, and in particular the effect of mutual shadowing between particles in regions with higher optical depth, is directly inferred from the global empirical modeling. Thermal surges at low phase angle, most likely resulting from shadow hiding, have been observed in all ring regions, except those with the lowest optical depth like the C-ring background. A contribution to shadow hiding from the particle's regolith cannot be excluded, in particular if regolith properties are driven by the frequency of particle collision, correlated with the ring optical depth. Combining the empirical model of the ring, constrained by all measurements, with dynamical simulations and with realistic temperature distributions on irregular, regolith covered icy surfaces, is the next logical step to disentangle the large-scale properties of the rings from those of its individual constituents.

There is a correlation between the bolometric Bond albedo and the ring optical depth. This is also found by photometric observations and is probably produced by meteoritic bombardment. The areal fractions of fast and slow rotators are similar to each other, although the fast rotator's fraction is larger for thin rings. This produces large range of size distributions for thin rings. A large fraction

of fast rotators is seen in the outer A-ring, suggesting enhanced impact velocities in this region, possibly due to satellite perturbations or strong self-gravitational wakes.

The diurnal thermal inertia is estimated to be about 10 J m^{-2} K^{-1} $s^{-1/2}$ for all the main rings from eclipse cooling data, although the Cassini division shows the lowest values. The low diurnal thermal inertia may indicate a very fluffy surface regolith layer. The thermal skin depth associated with eclipse cooling is on the order of 1 mm. The seasonal temperature variations can provide constraints on thermal inertia of deep interiors of particles, if they do not completely cool down at equinox to their equilibrium temperatures that are determined by the flux from Saturn only. The equinox temperature of the middle A-ring is found to not completely cool down. The seasonal thermal inertia of the middle A-ring particles is estimated to be 30–50 J m^{-2} K^{-1} $s^{-1/2}$, while it is as low as the diurnal thermal inertia for the outer and inner parts of the A-ring. The ring particles in the middle A-ring are likely to have a dense core under a thin fluffy regolith mantle. This indicates that unknown mechanisms confine dense particles in the middle A-ring or that the A-ring has been recently formed (~100 million years) by destruction of a pre-existing icy satellite. The seasonal thermal inertia of the thick B-ring is also found to be of the order of 30–50 J m^{-2} K^{-1} $s^{-1/2}$, assuming no heat transport by the vertical motion of particles. The seasonal inertia of particles in this multi-scale approach is found to be much larger, about 160–200 J m^{-2} K^{-1} $s^{-1/2}$, and the difference is due to the ring porosity that limits heat transfer through the solid phase. At this stage more effort is needed to understand why the thermal inertia of particles is so low, how heat transfer actually happens at their scale, and how deep the thermal waves are actually penetrating and sounding the particles on short and long timescales. Seasonal thermal effects should be able to probe particle interiors. But current thermal models, which attempt to explore them, are still facing an abnormally high porosity which yields a very low bulk density.

The ring particles in the middle A-ring are likely to have a dense core under a thin fluffy regolith mantle.

The particle properties are mostly derived using the multi-particle-layer model of Morishima et al. [2009], which ignores any effects of particle clumping (i.e., finite volume filling factor of a ring). Although this model can reproduce temperatures observed at various observational geometries, it does not accurately model the data in some cases. These failures are most likely all related to effects of particle clumping. Models that handle the effects of particle clumping are also discussed. In models of geometric filling factor and temperature of the A-ring, wakes are represented by elliptical or rectangular cylinders. These models can reproduce azimuthal modulations of geometric filling factor or temperature. The ratio of the vertical thickness to the horizontal width of wakes estimated from CIRS data at the middle A-ring is found to be slightly larger than those from stellar occultations.

Thermal opposition surges are seen in the dense A-ring and B-ring, and C-ring plateaus, but not in C-ring backgrounds. The volume filling factors estimated from the phase curves near the opposition are 0.2 and 0.4 for the A-ring and B-ring and 0.001–0.01 for the C-ring plateaus. The

temperature difference between the lit and unlit faces of the B-ring suggests very efficient heat transport is taking place from the lit face to the unlit face. The multilayer model can reproduce the lit–unlit face temperature difference if ring particles have vertical motion. In the densest part of the B-ring, particles likely bounce near the mid-plane. The lit–unlit face temperature can also be reproduced by a slab-type model in which vertical heat transport is taking place primarily by radiation and conduction, provided ring particles are isothermal. This model also yields a volume filling factor for the B-ring consistent with that estimated from opposition effects, i.e., on the order of 0.3.

The models that take into account the effects of particle clumping are only applicable to rather specific data sets. Universal models that are applicable to various geometries are required. A possible new model is one that directly uses the outputs of *N*-body simulations. Ray-tracing models that are applicable to photometric observations of packed particulate mediums have been developed by several authors [Salo and Karjalainen 2003; Porco et al. 2008; Ciarniello et al. 2015]. Modeling of thermal infrared emission using packed particulate mediums is much more complicated because various heat sources need to be included such as mutual heating. In addition, since the problem is time-dependent (particle spins and particle motion), radiative transfer needs to be solved at every time-step. Full modeling is very challenging and some approximations may be necessary for the first step.

Analysis of CIRS data using currently existing models also have not been fully conducted. For example, we do not clearly know the radial variation of the diurnal thermal inertia. The spatial resolution of the data that we have used were also limited. A part of the issue may be resolved by using FP3 data in addition to FP1 data. FP3 data have so far been used only for the opposition surge of the outer C-ring. During the final phase of the Cassini mission, the spacecraft's orbit carried it high above the planet's north pole and then sent it plunging between the planet and the innermost edge of its rings. In this orbital geometry, the Cassini spacecraft flew closer to some of Saturn's rings than ever before, and this encounter provided unprecedentedly high spatial resolution data. The CIRS instrument resolved some fine structures such as the F-ring, Cassini division, and C-ring plateau region, even with FP1. Future work will also include multi-analysis of data from multiple instruments, combining other temperature indicators provided by the VIMS for the top surface layer, and microwave radiometry for the interior of the particles.

CIRS emissivity spectra give constraints on sizes of regolith grains. The deduced sizes range from 1 μm to 10 cm and are on average larger than those estimated from data at short wavelengths. This may suggest that large grains are covered by small grains or that regolith structure is fractal. Modeling of such structures remains for future work, as does the effect of possible contaminants on CIRS spectra.

Other studies that are related to thermal emission but have not been covered by the present review are orbital migration of ring particles due to thermal effects that include the Yarkovsky effect, the Yarkovsky–Schach effect, and the Pointing–Robertson effect [Rubincam 2006; Vokrouhlický et al. 2007]. Vokrouhlický et al. [2007] found that the total torques on ring particles due to these effects are negative for all rings with a plausible range of thermal parameters that

are consistent with those reviewed in Spilker et al. [2018]. CIRS data of Saturn's rings will be analyzed for decades to come.

Titan

This section contains an introduction which outlines the broad nature of Titan's atmosphere and crust and the nature of thermal emissions from the gases, particulates and surface. Following the introduction is a discussion describing the typical means of modeling Titan spectra to retrieve information, the CIRS Titan science results and their implications organized by the CIRS science objective, the science assessments, and the conclusions and future work. See also book chapters and reviews that include CIRS results [Bézard 2009; Bézard et al. 2013; Flasar et al. 2009, 2014; Lebonnois et al. 2014; Lorenz et al. 2009; Strobel et al. 2009].

Introduction

Titan is the second-largest moon in the solar system (diameter 5150 km), the largest moon of Saturn, and the only moon with a significant atmosphere. The atmosphere is now known to have a bulk composition of ~94.5–98.5% nitrogen (N_2) and 5.5–1.5% methane (CH_4) [Niemann et al. 2010]. With a surface pressure of ~1.5 bar and temperature of ~90 K, and a similar molecular weight to Earth's air, the surface atmospheric density is almost 5× denser than Earth's according to the ideal gas equation. However due to the lower gravity, the scale height (*RT/Mg*) is much greater than Earth (~45 km versus 11 km) leading to a greatly extended atmosphere (~1500 km to the exobase [Yelle et al. 2008]). Titan is tidally locked to Saturn, orbiting with a 15.95-day period, and a substantial eccentricity of 3%. Titan's obliquity relative to Saturn is near-zero, leading to identical solar insolation cycle and seasons.

Titan is the second-largest moon in the solar system (diameter 5150 km), the largest moon of Saturn, and the only moon with a significant atmosphere.

ATMOSPHERIC STRUCTURE

Titan has a mild greenhouse (21 K) and anti-greenhouse effect (9 K) [McKay et al. 1991] leading to a surface temperature of 94 K, considerably warmer than the predicted effective temperature (82 K) for an airless body at 9.5 AU. The greenhouse effect arises from the long-wavelength opacity at ~25–200 μm from collisions primarily of N_2 and CH_4 molecules. The anti-greenhouse effect is due to the high-altitude hazes and condensates that absorb and reflect sunlight in the visible and UV, while being almost transparent in the thermal infrared. Due to these effects, Titan has a similar atmospheric structure to the Earth although caused by different gases. Convection in the lower atmosphere leads to decreasing temperatures up to the tropopause (~45 km, 70 K) with temperatures increasing again in the stratosphere, due to solar heating from methane and aerosols,

up to a well-defined stratopause at ~300 km. Above this altitude the temperature falls through the mesosphere (300–550 km) due to enhanced gas and aerosol cooling, and rises through the thermosphere (550–850 km) due to non-local thermodynamic equilibrium (non-LTE) processes. Above this homopause altitude gases begin to separate and have different scale heights, and ionization has a major effect up to the exobase (1500 km) where gases may escape to space due to Jeans escape [Hunten 1973], sputtering [De La Haye et al. 2007] and possibly slow hydrodynamic escape [Strobel 2008; Yelle et al. 2008].

Titan's global circulation in the stratosphere is dominated by single or dual cell meridional circulations. Following the solstices, warm air in the summer hemisphere rises (to 400–500 km) and circulates to the winter pole, where it cools and descends. Adiabatic compression leads to a hot, elevated stratopause, and a much cooler stratosphere beneath. Near to the equinoxes, a two-cell circulation is briefly in existence, with rising warm air at the equator forming two high-altitude circulation branches towards either pole.

ATMOSPHERIC CHEMISTRY

The dual action of solar UV (primarily Lyman α) and charged particle bombardment (primarily electrons) from Saturn's magnetosphere photolyzes the major atmospheric gases—N_2 and CH_4—leading to radicals of N, C, CH, CH_2, and CH_3 and associated ions. These react and recombine forming larger molecules—primarily hydrocarbons (C_xH_y) and nitriles ($C_xH_y(CN)_z$). The primary photolysis product of methane is ethane (40%, [Wilson and Atreya 2009]):

$$2\,CH_4 + 2\,h\nu \rightarrow C_2H_6 + H_2,$$

leading to escape and permanent loss of hydrogen. Other major photolysis products are acetylene (C_2H_2) and HCN. Small amounts of oxygen reaching Titan mostly from Enceladus lead to trace amounts of CO_2 and H_2O, and a larger amount of CO (50 ppm), which is very long-lived and accumulates over time.

These chemicals diffuse or are transported downwards, creating a vertical concentration gradient that is normally positive upwards. In the cold lower stratosphere, most gases reach saturation and condense onto haze particles (next section), using these as condensation nuclei, and falling out of the atmosphere towards the surface (some re-evaporation may occur). The tropopause thus acts as a cold trap for both methane in the upward sense, and other gases in the downward sense. The few non-condensing gases are: N_2, H_2, CO, and C_2H_4, plus light noble gases (Ne, Ar).

Due to the Hadley circulation (previous section) the minor gases are entrained, and become decaying tracers of atmospheric motions with lifetimes varying from hours to decades or longer. Many minor gas species are highly enriched in the stratosphere over the winter pole, as first detected by Voyager.

PARTICULATES

Two types of particulates are common in Titan's atmosphere: 1) aerosols, defined for our purposes as photochemically-produced microscopic organic particles and assumed to be agglomerations of macromolecules bonded by Van Der Waals forces as seen in terrestrial smog, smoke and laboratory simulations (tholins); and 2) condensates (liquid and solids) formed by condensation of trace gases (methane, ethane, etc.) into small droplets (liquid) or grains (ice) similar to terrestrial tropospheric and stratospheric clouds. Condensates can be, and likely are, mixtures of several molecular types with similar freezing/boiling points. Further grain-surface photochemistry may change the composition (see the section entitled Surface).

SURFACE

Titan's surface was only coarsely imaged as late as 1996 [Smith et al. 1996] using the Hubble Space Telescope (HST), and subsequently with ground-based telescopes employing adaptive optics. Detailed imaging awaited the Huygens probe, which descended to Titan's surface in 2005 [Tomasko et al. 2005]. The Cassini orbiter followed up with mapping at visible (ISS), near-IR (VIMS) and RADAR wavelengths; the latter providing the most detailed morphological picture. RADAR was the key to discovering Titan's dune fields [Lorenz et al. 2006], polar lakes and seas [Stofan et al. 2007], and surface cratering [Neish and Lorenz 2011]. Overall, Titan's topography remains low in relief [Lorenz et al. 2013], with the tallest surface prominences reaching only 1.4 km [Lopes et al. 2013]. Proposed geologic activity remains controversial [Nixon et al. 2018]. Key goals for CIRS included measurement of an expected equator-to-pole thermal gradient and diurnal variation due to insolation effects, and any possible local differences over the seas, dunes and impacted terrain (Xanadu) due to differences in altitude and thermal inertia, related to porosity and composition.

Spectral modeling and inversion

Once CIRS spectra have been calibrated, and usually averaged together (co-added) to increase the signal-to-noise (S/N) ratio, they are modeled using a radiative transfer program to retrieve atmospheric quantities such as temperature, gas abundances, and particle column densities. The CIRS team used multiple radiative programs—for example, ARTT Coustenis et al. [2007], NEMESIS Irwin et al. [2008]—and other modeling codes developed at the University of Maryland, Paris Observatory, NASA Goddard Space Flight Center (GSFC), and elsewhere, to retrieve atmospheric and surface information.

The process of modeling a spectrum usually follows these principal steps:

1. Define a reference atmospheric profile of vertical temperature, gas abundances, and particle sizes and number densities.

2. Run a forward model for the reference atmosphere and compare to the CIRS spectrum.

3. Adjust model parameters (reference atmosphere) iteratively and rerun forward model, until a fit to the spectrum is obtained, usually defined as reaching the noise threshold, or some other pre-determined measure of convergence.

In many cases, atmospheric gas abundances are obtained in a two-step process: (i) model the emission of a well-mixed gas of known (or assumed) abundance (often methane) to retrieve atmospheric temperatures; and (ii) fix the temperature profile and model other parts of the spectrum to obtain gas abundances. However, this paradigm is often modified by assuming or ingesting temperatures from other sources such as the Huygens probe, or radio occultation measurements. In other cases, gas or particle abundances and temperatures are obtained simultaneously.

Steps of the model process are described in the following section.

REFERENCE ATMOSPHERE

The first step is to construct an initial model atmosphere that includes temperature profiles and vertical profiles of gases and aerosols. An excellent starting point is the vertical profile data recorded by the Huygens probe, which provided in situ measurements at the landing site coordinates (10.3° S, 192.3° W) of Titan's temperature profile, gas abundances, and an aerosol altitude profile below 150 km [Fulchignoni et al. 2005; Niemann et al. 2010; Tomasko et al. 2005]. Further reference temperatures profiles are available from Cassini CIRS [Achterberg et al. 2008a, 2011] and radio occultations [Schinder et al. 2011a, 2012]. The temperature profiles are combined with trial gas abundances based on previous measurements or photochemical model predictions to create an a priori (initial-guess) profile for Titan's atmosphere.

FORWARD MODEL

The outgoing spectral radiance along a single atmospheric path is obtained by evaluating the Schwarzchild integral for emission:

$$I_{\tilde{\nu}} = \int_0^{z_\infty} \frac{\partial \tau_{\tilde{\nu}}(z_\infty, z)}{\partial z} B_{\tilde{\nu}}\big(T(z)\big) dz, \qquad \text{(Eq. 1)}$$

where $I_{\tilde{\nu}}$ is the outgoing radiance, $\tau_{\tilde{\nu}}$ is the transmittance from height z to the top of the (sensible) atmosphere at height z_∞, $B_{\tilde{\nu}}(T)$ is the Planck function (local thermodynamic equilibrium, or LTE, as assumed), and the subscript $\tilde{\nu}$ indicates wavenumber. Including the surface with an emissivity ε_s, and dropping the wavenumber subscripts for convenience, the outgoing intensity is:

$$I = \int_0^{z_\infty} \frac{\partial \tau(z_\infty, z)}{\partial z} B\big(T(z)\big) dz + \varepsilon_s B(T_s)\tau_s + (1-\varepsilon_s)\tau_s \int_{z_\infty}^{0} \frac{\partial \tau(0,z)}{\partial z} B\big(T(z)\big) dz, \qquad \text{(Eq. 2)}$$

where τ_s is the transmittance evaluated from the surface to the top of the atmosphere. Note that the third term accounts for the down-welling radiation which is reflected from the surface and suffers extinction on return; this term vanishes when the surface emissivity is unity. The transmittance is defined as: $\tau_{\tilde{\nu}} = \exp(-\chi_{\tilde{\nu}})$ where $\chi_{\tilde{\nu}}$ is the spectral opacity due to all sources in the atmosphere

integrated over the path. The radiative transfer program evaluates the discretized form, replacing the integral by a summation over *N* atmospheric layers, e.g., for unit surface emissivity:

$$I_\infty = B_s\tau_{N_L} + \sum_{l=1}^{N_L}\left[B_l exp\left(-\sum_{i=1}^{l}\Delta\chi_i\right)\right]. \quad \text{(Eq. 3)}$$

The opacity increment at each layer $\Delta\chi_i$ is typically the sum of three sources: $\Delta\chi_i = \Delta\chi_{L,i} + \Delta\chi_{C,i} + \Delta\chi_{P,i}$, which are the opacities due to spectral lines, collision-induced absorption (CIA) and particles, respectively. These are:

$$\Delta\chi_{L,i}(\tilde{\nu}) = \sum_{j=1}^{N_g}\left[k_j(\tilde{\nu})q_{ij}\right]\rho_i\,\Delta z_i \quad \text{(LINES)} \quad \text{(Eq. 4)}$$

$$\Delta\chi_{C,i}(\tilde{\nu}) = \sum_{j=1}^{N_g}\sum_{k=1}^{N_g}\alpha_{jk}\,(\tilde{\nu})q_{ij}q_{ik}\left(\frac{p_i}{p_0}\right)^2\left(\frac{T_0}{T_i}\right)^2\Delta z_i \quad \text{(CIA)} \quad \text{(Eq. 5)}$$

$$\Delta\chi_{P,i}(\tilde{\nu}) = \sum_{j=1}^{N_P}\sigma_j\,(\tilde{\nu})n_{ji}\Delta z_i \quad \text{(PARTICLES)} \quad \text{(Eq. 6)}$$

where *kj* is the absorption co-efficient (per unit mass) due to spectral lines for the j^{th} of N_q gases in the atmosphere, q_{ij} is the volume mixing ratio of each gas at each level, ρ_i is the total atmospheric mass density of the layer, Δz_i is the thickness of the layer, α_{jk} is the spectral CIA coefficient for the (*j,k*) gas pair normalized to nominal pressure p_0 and temperature T_0, p_i and T_i are the pressure and temperature of the layer respectively, σ_j is the extinction cross-section of the j^{th} particle type and n_{ji} is the number density of each particle type in the layer. The exact method of computing the spectral line absorption coefficient *k* varies: it may be a line-by-line model, or more usually a band model of correlated-k technique, which preserves accuracy but at much shorter computational time.

SPECTRAL LINE DATA

Infrared spectral line data are taken from the standard line atlases: GEISA [Jacquinet-Husson et al. 2016] and/or HITRAN [Rothman and Gordon 2013], supplemented by additional line lists provided by colleagues for some gases and bands that have been measured recently, but not yet included in the standard atlases. The CIA coefficients of are those of Borysow and colleagues as detailed in [Teanby et al. 2006b]. Extinction cross-sections for stratospheric aerosols are often based on laboratory tholin coefficients measured by Khare et al. [1984a, 1984b], but more recent laboratory work and CIRS-derived coefficients are now available [Khare et al. [1984a, 1984b]. A list of principal detected infrared bands is given in Table CIRS-5. See also Figure CIRS-16.

Table CIRS-5. Principal gases in Titan's stratosphere, and infrared spectral bands seen by Cassini CIRS.

	Gas Name	Chemical Formula	Emission Bands Detected in Mid-/Far-IR (center or range in cm^{-1})	VMR (equator at 5 mbar)
Major Species	Nitrogen	N_2	~100 (collision-induced opacity)	9.85×10^{-1}
	Methane	CH_4	60–140 (pure rotations); 1304 (n4)	1.40×10^{-2}
	Argon	*Ar*	*none*	
	Hydrogen	H_2	355 and 585 (dimers)	1.00×10^{-3}
Hydrocarbons	Acetylene	C_2H_2	729 (n5)	3.00×10^{-6}
	Ethylene	C_2H_4	949 (n7)	1.50×10^{-7}
	Ethane	C_2H_6	822 (n9), 1379 (n6), 1468 (n8)	1.00×10^{-5}
	Propyne	C_3H_4	328 (n10), 633 (n9)	7.00×10^{-9}
	Propene	C_3H_6	913 (n19)	$2{:}00 \times 10^{-9}$
	Propane	C_3H_8	748 (n21), 870 (n8), 922 (n16), 1054 (n15), 1158 (n7), 1376 (n13), 1472 (n19)	5.00×10^{-7}
	Diacetylene	C_4H_2	220 (n9), 628 (n6)	1.40×10^{-9}
	Benzene	C_6H_6	674 (n4)	5.00×10^{-10}
Nitriles	Hydrogen Cyanide	HCN	40–100 (pure rotations), 712 (n2)	1.00×10^{-7}
	Cyanoacetylene	HC_3N	499 (n6), 663 (n5)	4.00×10^{-10}
	Cyanogen	C_2N_2	233 (n5)	(north only)
Oxygen Species	Carbon Monoxide	CO	50–100 (pure rotations)	4.50×10^{-5}
	Carbon Dioxide	CO_2	667 (n2)	1.40×10^{-8}
	Water	H_2O	80–300	1.00×10^{-10}

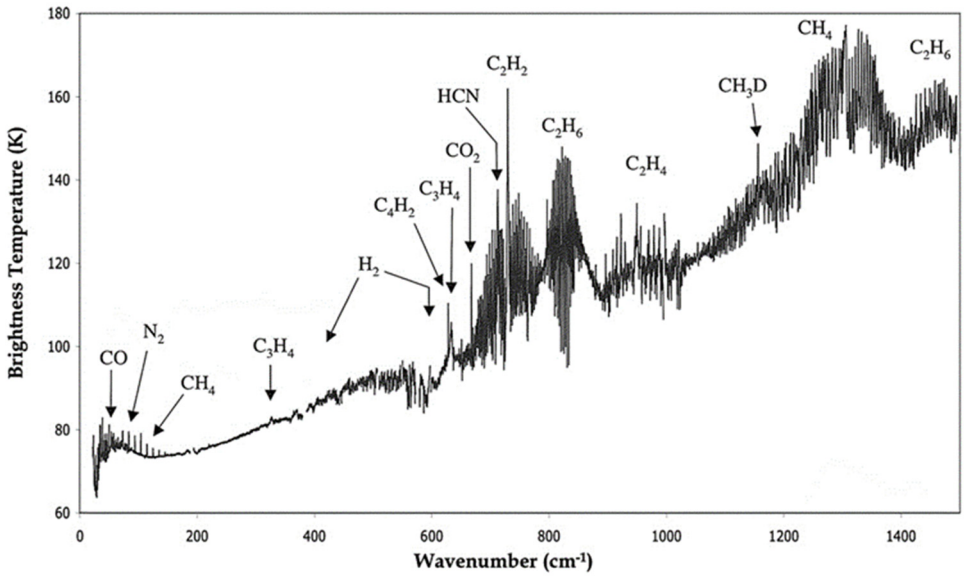

Figure CIRS-16. A complete composite unapodized CIRS spectrum in brightness temperature taken during TB at medium resolution (1.7 cm^{-1}) at mid-latitudes. Figure from Coustenis et al. [2007].

RETRIEVAL/INVERSION

Coupled to the forward model, many radiative transfer models also include a retrieval (or inversion) methodology—for example, Rodgers [2000], which attempts to find the set of model parameters $\underline{x}$ which best fits the spectral data, $\underline{y}$. The measurement process may be written as: $F(\underline{x}) = \underline{y} + \varepsilon$, where F is the physics and ε is the measurement error. The inverse problem is therefore to find a self-consistent atmospheric state $\underline{\hat{x}}$ such that $F(\underline{\hat{x}}) = \underline{y} \pm \varepsilon$. The retrieval proceeds by defining a goodness of fit metric similar to a chi-squared test, and sometimes called the cost function, that is minimized to achieve a best fit atmospheric state $\underline{\hat{x}}$; e.g., the cost function ϕ used by NEMESIS:

$$\phi = \left(\underline{y} - F(\underline{\hat{x}})\right)^T \underline{S}_{\varepsilon}^{-1} \left(\underline{y} - F(\underline{\hat{x}})\right) + (\underline{\hat{x}} - \underline{\hat{a}})^T \underline{S}_a^{-1} (\underline{\hat{x}} - \underline{\hat{a}}), \quad \text{(Eq. 7)}$$

is comprised of two terms, the first being the traditional χ^2 difference between the model and data spectra, while the second is a constraint term that is proportional to the square of the deviation between the solution vector and the a priori (best-guess) vector $\underline{\hat{a}}$, required to obtain a solution to the ill-posed problem. The retrieval procedure iterates to solve the non-linear problem, until the cost function or other fitness measure ceases to decrease appreciably (converges). This combination of forward model and retrieval scheme is a powerful tool to retrieve values and error estimates for the temperature, gas abundance profiles, and haze opacities from CIRS spectral data.

Titan's surface

Titan's surface temperature can be directly sensed in the far-infrared through a window of low opacity near 530 cm^{-1} (19 μm), as discovered by Voyager 1 [Flasar et al. 1981; Hanel et al. 1981; Samuelson et al. 1981]. This wavelength is sensed by CIRS FP1, which being a single pixel of relatively large angular diameter, places some limits on resolution and mapping capability. Nevertheless, CIRS was able to significantly expand on the science of Voyager, giving global context for the Huygens measurements, and comparison for RADAR temperature measurements at longer wavelengths [Janssen et al. 2009].

LATITUDINAL VARIATION

The first surface temperature results from CIRS were published by Jennings et al. [2009], who averaged data from 43 flybys of the prime mission (2004–2008). They found T = 93.7 ±0.6 K at the Huygens landing site, in good agreement with the in situ measurements, and also the maximum recorded at any latitude. The temperature decreased to 90.5 ±0.8 K at 87° N and 91.7 ±0.7 K at 88° S, in broad agreement with the season (late northern winter).

TEMPORAL CHANGES

Jennings et al. [2011] followed up on the earlier work, showing the first time-resolved measurements covering two time periods: 2006–2008 (L_S = 335°) and 2008–2010 (L_S = 0°), the latter coinciding with northern spring equinox (NSE) in 2009. By the time of NSE, the temperature distribution had become symmetric, with polar temperatures in both hemispheres leveling off at ~91 K, and an equatorial maximum of 93.4 K. A slight phase lag relative to solar insolation of ΔL_S ~9° was recorded, consistent with the observations of Voyager 1, and general circulation modeling (GCM).

Cottini et al. [2012b] followed up with a comprehensive analysis of data from 2004–2010, this time dividing the data temporally into three two-year periods. Agreement with HASI was again noted at the Huygens landing site, and changes of several degrees near the poles were in good agreement with Jennings et al. [2011]. Cottini et al. [2012b] were also able to detect diurnal variations in surface temperature, based on data from −20° to +20° latitude. A slow warming of ~1 K was observed from daybreak to late afternoon, followed by a plateau, and then a more rapid cooling from midnight to dawn. By comparing to models from Tokano [2005], the authors found consistency with a thermal inertia of 300–600 J m^{-2} $s^{-1/2}$ K^{-1} and albedo 0.3, in agreement with a surface crust of porous icy material.

A surface temperature update was published by Jennings et al. [2016], who divided the period 2004 to 2014 into five two-year periods (Figure CIRS-17). During this time the north polar temperature rose by about 1 K from 90.7 ±0.5 to 91.5 ±0.2 K, while that at the south pole dropped by a larger amount from 91.7 ±0.3 to 89.7 ±0.5 K. The low latitude temperature maximum stayed constant at 93.65 ±0.15 K, while moving northwards from 19° S to 16° N. In general, temperature changes were in agreement with GCM models, excepting in the north polar regions from 2014 onwards, where the rise was about 1 K less than expected. This anomaly was tentatively attributed to surface cooling through increased precipitation and methane evaporation. Recently Jennings et al. [2019] extended the analysis to the end of mission in September 2017.

VARIATION WITH TOPOGRAPHY AND TERRAIN

A search for localized temperature differences has been made by members of the CIRS team including V. Cottini and D. E. Jennings, including over the northern lakes/seas, and over low-latitude albedo features such as Xanadu with no conclusive evidence to date—unlike the thermal anomalies seen by RADAR [Janssen et al. 2009]. This has been attributed to the much lower S/N and larger spatial resolution footprint of CIRS that may not be sufficient to see small temperature contrasts over small features, including lakes and seas.

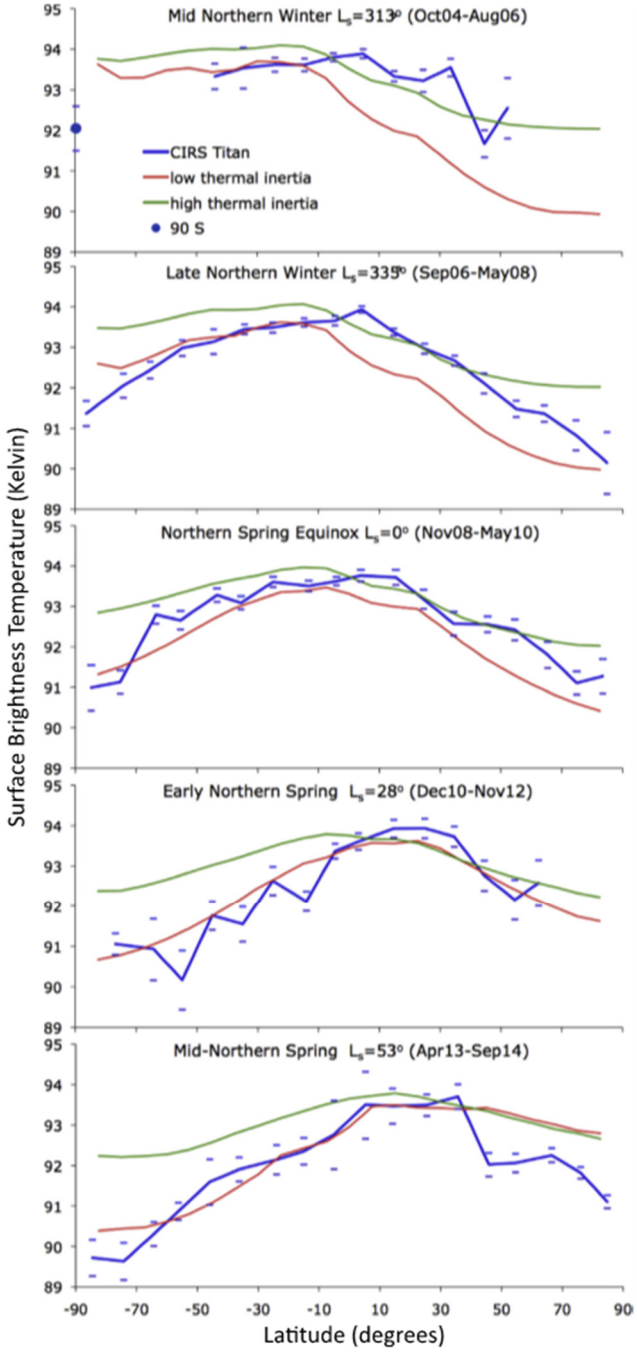

Figure CIRS-17. Measured surface brightness temperatures (blue) on Titan compared with GCM predictions, for five approximately two-year periods during the Cassini mission. The error bars are two standard deviations, calculated from the average that produced each data point. Variation in the size of the error bars is due primarily to differences in the number of spectra averaged. The two GCM curves [Tokano 2005] correspond to low thermal inertia (red) and high thermal inertia (green). Two of the periods, L_S = 313° and 28°, did not have sufficient data to completely map the high latitudes. The single data point at 90° S for L_S = 313°, added here to extend the coverage to the south pole, was from June 6, 2005. Figure from Jennings et al. [2016].

Atmospheric dynamical state

CIRS has mapped Titan's atmospheric temperatures primarily through two spectral regions: the ν_4 band of methane centered on 1305 cm^{-1} (visible on FP4) that sense the stratosphere, and the far-infrared (100–400 cm^{-1}) that gives temperatures in the troposphere. By assuming abundances of CH_4 and H_2, typically from Huygens Gas Chromatograph Mass Spectrometer (GCMS), the temperatures may be retrieved. Temperature (and gas abundance) retrievals use either one of two observing geometries: nadir viewing, where the sightline intercepts the surface, although not necessarily normal (90° to surface); and limb, where the line of sight passes above the surface (tangential). Limb viewing is often preferable for two reasons: (i) the emission is usually strongly localized at the tangent point altitude, allowing for more precise altitude sensing; and (ii) the longer path length compared to nadir viewing increases S/N, allowing retrievals to proceed to higher altitudes.

Limb viewing on Titan encounters a problem not usually significant on the Earth: the larger scale height of the atmosphere causes the depth of the sensible atmosphere to be greatly extended relative to the solid body diameter. This means that the weighting function extends significantly to either side of the tangent point, and therefore latitudinal/longitudinal variations in composition and temperature are important. This causes problems for 1-D radiative transfer models (such as NEMESIS), which cannot capture the 2-D nature of the problem (Figure CIRS-18), although at least one full 2-D temperature retrieval model has now been developed [Achterberg et al. 2008a].

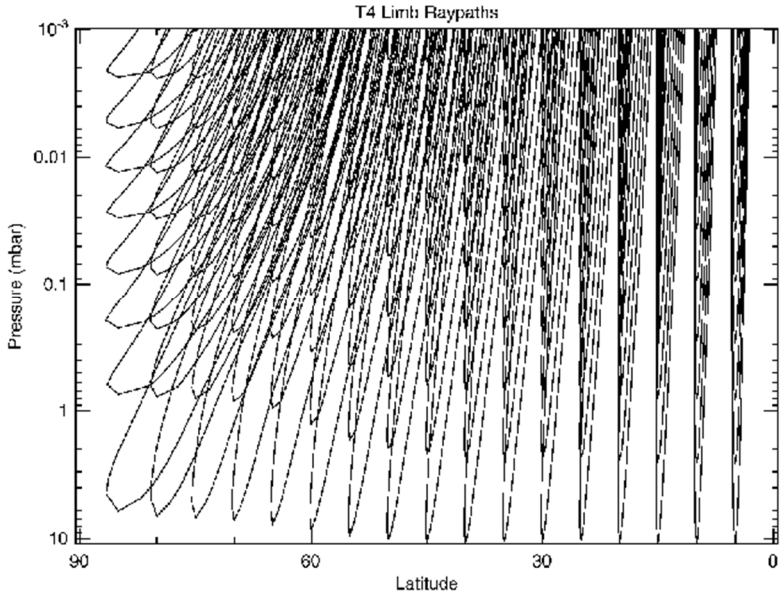

Figure CIRS-18. Ray paths for limb measurements acquired on the T4 Titan flyby, illustrating the nature of the 2-D retrieval problem. Tangent views towards high latitudes traverse a significant range of latitudes. The equatorward branch of each trajectory extends from the spacecraft to the tangent point of the ray, while the poleward branch is the extension of the ray path beyond the tangent point. Figure from Achterberg et al. [2008a].

GLOBAL TEMPERATURE MAPPING

The first maps of Titan's global temperatures were published by Flasar et al. [2005a], showing the first Titan results from Cassini CIRS. The stratopause was distinct at ~310 km (186 K) at low latitudes, and showed a cooling of 4–5 K towards the south pole. The northern hemisphere above 60° N was not measured. Shortly thereafter, Huygens HASI results [Fulchignoni et al. 2005] were to show disagreement with the CIRS low latitude stratopause altitude, a discrepancy that has long persisted, although may recently have been resolved [Lellouch et al. 2014].

The first and so-far only model to successfully retrieve the 2-D atmospheric structure on Titan was devised by Achterberg et al. [2008a]. The authors showed the significant errors that can occur in 1-D models, by comparing to a fully 2-D model (Figure CIRS-19). Temperatures were retrieved from 90° S to 60° N and 5 to 0.2 mbar from nadir mapping data, and from 75° S and 85° N and 1 to 0.005 mbar from limb data. The higher-altitude limb data allowed the stratopause to be fully captured, and showed that it was 20 K warmer in the northern polar atmosphere than at low latitudes (<40° N) and higher by about 100 km (0.01 mbar N polar, versus 0.1 mbar low latitudes) (Figure CIRS-20). This is in agreement with GCM models [Lebonnois et al. 2009, 2012] that predict subsidence in the stratosphere over the winter pole and consequent adiabatic warming.

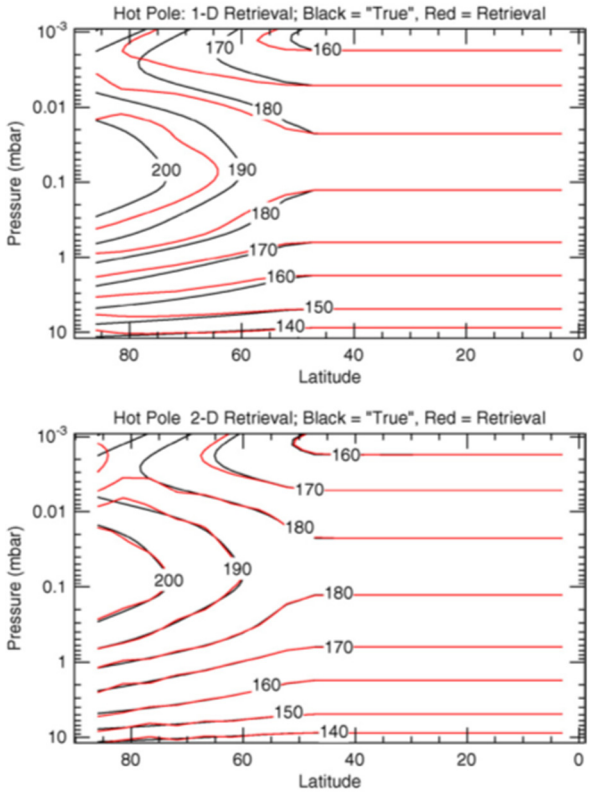

Figure CIRS-19. One- and two-dimensional retrieval results on synthetic data with a warm pole. The one-dimensional retrieval does not recover the polar warm spot well. Figure from Achterberg [2008a].

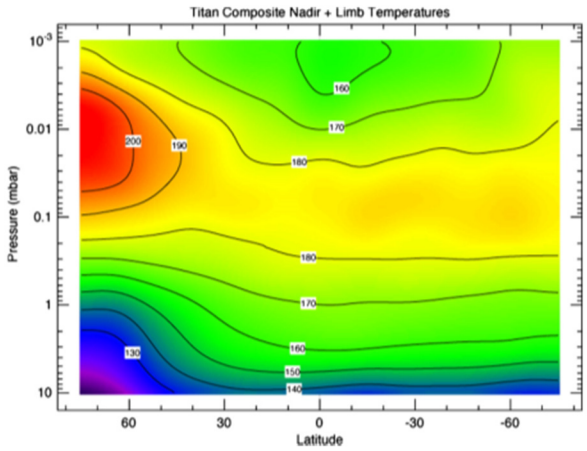

Figure CIRS-20. Zonal mean temperatures from all limb and nadir maps. Retrieved temperatures were averaged in 5° latitude bins, then smoothed with a 10° boxcar function applied three times. Contours are labeled in K. Figure from Achterberg et al. [2008a].

Winds and Jets

The first CIRS derivation of the stratospheric wind was shown in Flasar et al. [2005a], with zonal winds reaching 160 m/s in mid-northern latitudes above 200 km (1 mbar). Achterberg et al. [2008a] also applied the thermal wind equation to derive zonal winds, finding a jet of 190 ms^{-1} at 30–60° N, and peaking near 1 mbar (Figure CIRS-21).

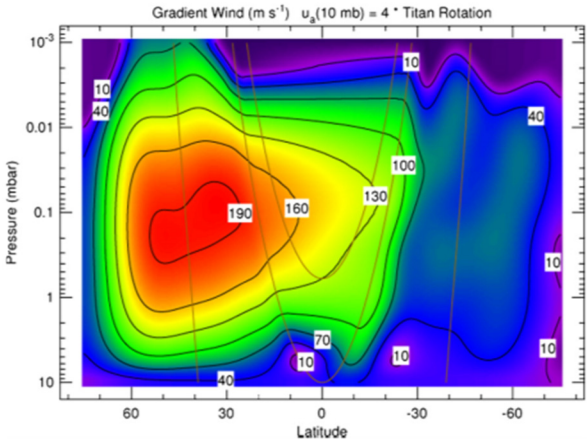

Figure CIRS-21. Zonal winds calculated from the temperatures in Figure CIRS-19 from the gradient wind equation, assuming solid-body rotation at the 10 mbar level at four times Titan's rotation rate. Wind speed contours (black lines) are labeled in ms^{-1}. The gray lines indicate cylindrical surfaces parallel to the rotation axis along which the gradient wind equation is integrated. Equatorward and above the gray line tangent to the equator at 10 mbar, the winds are unconstrained by the gradient wind equation, and have been linearly interpolated on constant pressure surfaces. Figure from Achterberg et al. [2008a].

ATMOSPHERIC ROTATION AXIS

A curious and hitherto unknown phenomenon was observed at the end of the prime mission by Achterberg et al. [2008b]—that isotherm contours plotted in a polar frame are not concentric about the solid body pole, but offset by ~3.5° (Figure CIRS-22). This axial offset was observed most clearly in the north due to the steeper temperature contours, but was also observed in the opposite sense in the south. The atmospheric tilt was later confirmed in other datasets, including an analysis of Titan's brightness banding in ISS images [de Kok et al. 2010b; Roman et al. 2009] and in composition contours of HCN gas from CIRS [Teanby et al. 2010a].

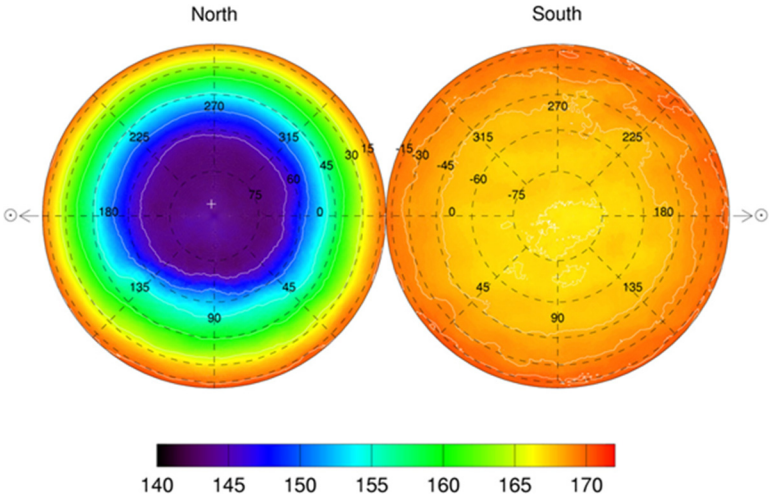

Figure CIRS-22. Polar projection maps of retrieved temperatures at the 1 mbar level. The northern hemisphere is shown on the *left* and the southern hemisphere on the *right*. The color-coded temperature scale in kelvins is shown at the bottom. The superposed grid represents latitude and west longitude in a Sun-fixed frame with the longitude of the subsolar point at 180° W, such that the Sun direction is towards the left and right edges of the figure. Temperature contours are plotted at intervals of 5 K in the northern hemisphere, and 1 K in the southern hemisphere. The fitted axis of symmetry is indicated by a white cross (+). Figure from Achterberg et al. [2008b].

In 2008, it was unclear whether this axis was fixed in a solar frame, or a sidereal (inertial) frame, and Achterberg et al. [2008b] suggested that the observed pole tilt might represent a compromise between two competing effects. The first is the need to maintain Titan's global super-rotation, which requires the upward transport of angular momentum. For an axisymmetric circulation the most favorable configuration for achieving this with upwelling at the equator. The second is the transport of heat by a Hadley circulation, which is most efficient when the upwelling is centered about the subsolar latitude. If this hypothesis were correct, the axial tile should remain fixed in the solar frame. However, more recent, unpublished work by the same authors, which includes observations from the remainder of the Cassini mission, indicates that the axial tilt, remains fixed in the inertial frame. The origin of the tilt still lacks an explanation.

GLOBAL ENERGY BALANCE

Li et al. [2011b] considered whether Titan is in overall thermal equilibrium: as it should be if there is no significant internal energy source. One the strengths of CIRS is the very broad spectral coverage, which includes almost the entire Planck function of cold outer solar system bodies. By carefully integrating across the entire spectrum and accounting for emission angle, Li and colleagues found a global power emission of (2.84 ±0.01) × 10^{14} watts. This compares very closely to the global absorbed solar energy of (2.89 ±0.12) × 10^{14}, which has a significantly larger associated error due to the bond albedo, and places any possible thermal imbalance at ≤ 6%.

In a follow-up paper, Li [2015] searched for temporal variability of the emitted power. In the northern hemisphere, the radiant energy dropped from 2007–2009, then increased 2009–2013, whereas in the southern hemisphere, the power continuously dropped by eventually 5% from 2.40 to 2.28 W/m^2 (Figure CIRS-23). This drop was attributed to seasonal variation. Taken together, the overall global power drop was 2.5%: much less than the decrease (13%) in the solar constant at Titan in the same period, showing the significant thermal inertia of Titan's atmosphere.

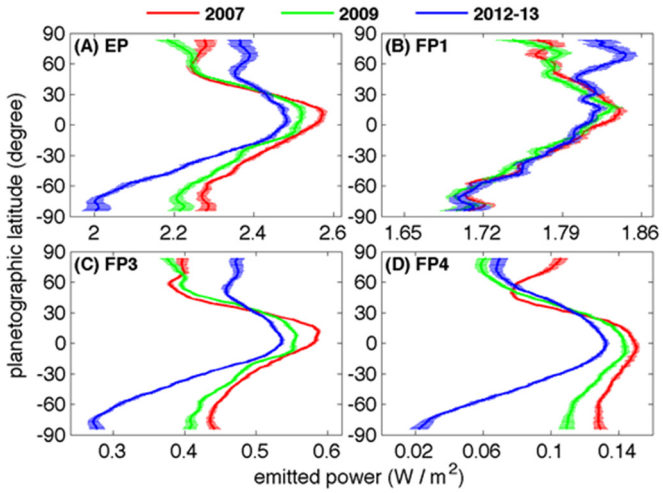

Figure CIRS-23. Meridional distribution of Titan's emitted power. Panel (A): total emitted power. *Panels (B), (C), and (D):* are thermal radiance recorded by the focal planes FP1, FP3, and FP4, respectively. The thick line is the profile of the emitted power and horizontal lines represent the uncertainties. The estimated uncertainty is combined by the uncertainty related to the filling observational gaps and the uncertainty related to the CIRS data calibration. Figure from Li [2015].

A more detailed picture of the global energy balance was presented by Bézard et al. [2018], who developed a seasonal radiative-dynamical model. Constrained by gas and haze data from CIRS and Huygens Descent Imager/Spectral Radiometer (DISR), the model was capable of investigating the net heating and cooling rates at varying latitudes as a function of time. A significant revision downward of the radiative relaxation time in the stratosphere was proposed, and the change in the solar flux due to Saturn's orbital eccentricity was found to be enough to explain a 4 K drop in equatorial temperature at 1 mbar noted between 2009 and 2016. At mid-latitudes on the other hand, the model predicted changes in temperature much larger than observed, which put new constraints on the vertical mixing.

SEASONAL CHANGE

Achterberg et al. [2011] followed up on the original work of [Achterberg et al. 2008a], showing time variation in the stratospheric temperatures from 2004–2009 (L_S 293° to 4°, from late northern winter to just after equinox). Significant cooling (20 K) of the northern stratopause had occurred, consistent with a weakening of the descending branch of the stratospheric circulation cell. Smaller changes were noted elsewhere in the atmosphere.

Teanby et al. [2012a] reported rapid changes in the south polar temperature field shortly after equinox (Figure CIRS-24). They measured elevated mesospheric temperatures in early 2010, which were indicative of south polar subsidence. This is opposite to the south polar upwelling inferred at the start of the mission and was the first observation of Titan's circulation reversing. The reversal was extremely rapid and was evident in both temperature and composition 2-D cross-sections.

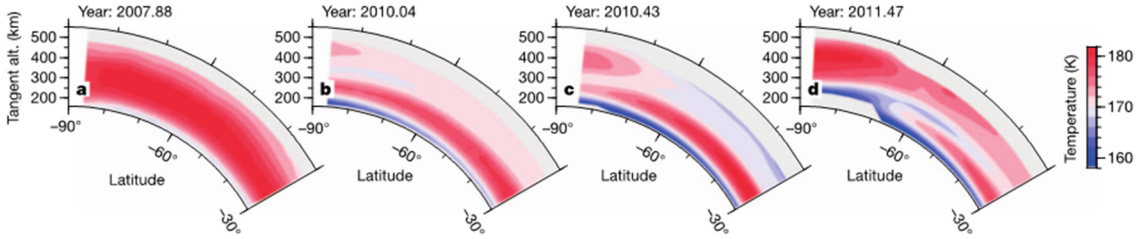

Figure CIRS-24. South polar seasonal temperature changes. Cross-sections were derived from low-spectral-resolution limb-mapping sequences and cover pre-equinox (a) and post-equinox (b–d) periods. Substantial stratospheric (300 km) cooling occurs after the equinox, consistent with reduced total solar flux during this time, as Titan moves towards southern winter. After the equinox (after mid-2009), there is evidence for high-altitude (450 km) polar warming relative to more equatorial latitudes. This is initially present as a small (2 K) temperature anomaly almost immediately proceeding the equinox (b), which increases to 6 K (c) and then to 8 K (d) in subsequent sequences. This implies that the mesospheric circulation has reversed and is now subsiding at the south pole. The strongest polar warming occurs in the most recent observation, indicating the fastest subsidence speeds. The gray regions indicate latitudes and altitudes where observations exist but have insufficient signal-to-noise ratios for an accurate temperature determination. Contour spacing is 2 K, which is the maximum uncertainty for this altitude range. These changes are confirmed by additional single-latitude observations at both high and low spectral resolution. Figure from Teanby et al. [2012a].

Teanby et al. [2017] reported another new discovery about Titan's winter polar vortex, this time in the south, during the early winter time period that Cassini had not been able to observe in the north (happening in 2002 just prior to arrival of the spacecraft). Previously, a hot elevated stratopause had been seen in the late winter vortex in the north, and also in the early winter vortex in the south. Abruptly however, in 2012 three years post-equinox, the mesosphere in southern winter vortex cooled dramatically, and did not recover its previous temperature until 2015. This phenomenon, not seen elsewhere in the solar system, was interpreted as being due to the huge enrichment occurring in trace gases, which were efficiently cooling the mesosphere. This observation provided a unique glimpse at the interplay between thermodynamic and radiative effects on controlling atmospheric temperature (Figure CIRS-25).

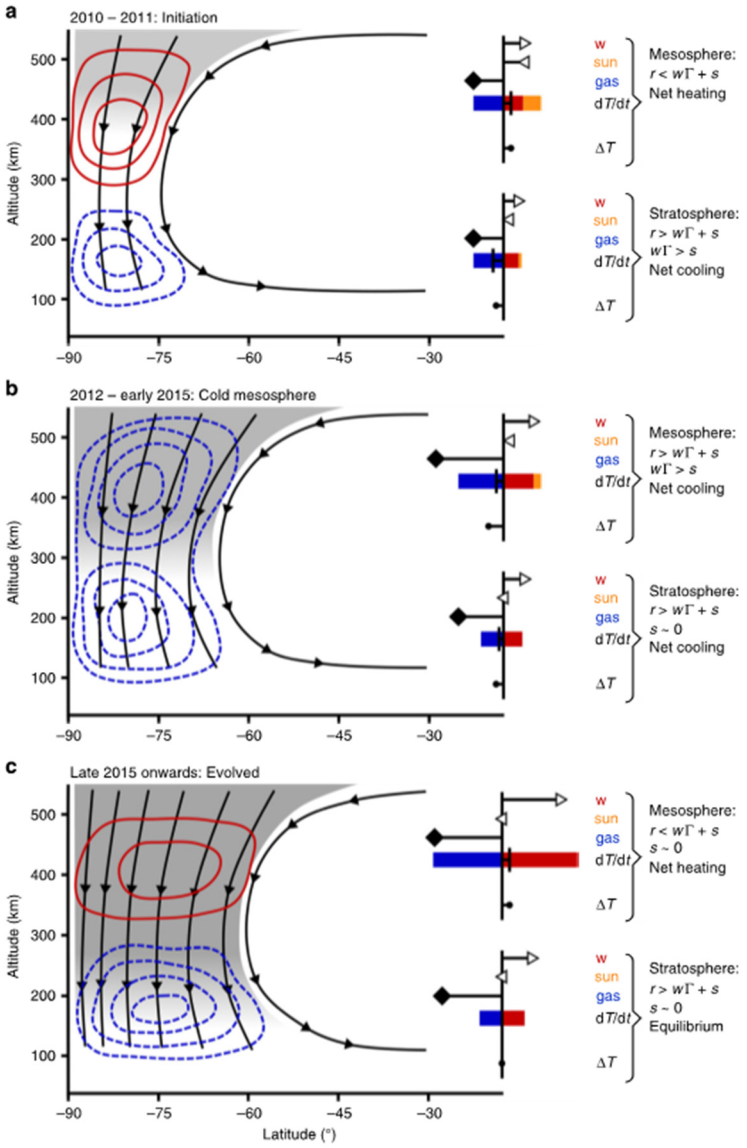

Figure CIRS-25. Schematic of the three stages of Titan's vortex evolution. Shaded areas represent trace gas abundance, which increases with time due to the subsiding flow (black streamlines). Red contours indicate hot anomalies and blue-dashed contours represent cold anomalies. Inset bar plots in each panel represent mesospheric and stratospheric heating and cooling processes; right-pointing triangles indicate subsidence speed w, which drives adiabatic heating rate wΓ (red bar); left-pointing triangles indicate solar heating rate s (orange bar); and diamonds indicate trace gas relative abundance, which drives long-wave radiative cooling rate r (blue bar). The overall net heating rate ∂T/∂t = −r + wΓ + s (vertical line) produces either a hot or cold temperature anomaly ΔT (filled circle). Estimated long-wave cooling rates range from 0.75 to 3.3 K per day in the mesosphere (~0.01 mbar, 400 km) and 0.04–0.17 K per day in the stratosphere (~1 mbar, 175 km). The three stages are: *Panel a*: vortex initiation, with a hot mesosphere driven by modest subsidence-induced adiabatic heating combined with weak cooling from trace gases; *Panel b*: cold mesosphere, caused by enhanced net cooling from increased trace gas opacity; and *Panel c*: evolved vortex, with a hot mesosphere driven by strong subsidence-induced adiabatic heating that exceeds enhanced cooling from trace gas enrichment. Figure from Teanby et al. [2017].

Gas composition and chemistry

The gas composition of Titan's atmosphere is highly informative in many respects: it yields information on the chemistry, it acts as a tracer of dynamical motions, and informs about the possible composition of aerosols and condensates. As previously mentioned, measurement of the gas abundances through thermal infrared emissions is contingent on first knowing the temperature profile, either through external (non-CIRS) measurements or models, or through CIRS modeling based on a prior well known/well mixed gas such as CH_4, CO, or H_2. However, in some instances these well-known gas abundances are instead the object of study, necessitating a joint retrieval which complicates the analysis.

GLOBAL GAS DISTRIBUTION

The first latitudinal trends in Titan's gases from CIRS data were published in Flasar et al. [2005a], showing similar qualitative trends in the lower stratosphere to those seen in Voyager flyby data 24 years earlier, i.e., short-lived trace gases (HCN, HC_3N, C_4H_2) showed sharp increases towards the north pole by 1–2 orders of magnitude, while longer-lived gases (such as CO_2 and C_3H_4) showed smaller increases or none at all. C_2H_4 showed an unexpected decrease from 0 to 60° N, which remains unexplained. Shortly thereafter, a focused follow-up study of the latitudinal variation of nitriles by Teanby et al. [2006] using medium resolution nadir spectra confirmed the trends reported in the 2005 paper.

The year 2007 was a watershed year for CIRS Titan results, with publications by Coustenis, Teanby, Vinatier and de Kok describing gas composition measurements.

Coustenis et al. [2007] modeled observations encompassing the first half of the Cassini prime mission (2004–2006), and including medium (2.5 cm^{-1}) and high (0.5 cm-) spectral resolution observations. All previous gases seen by Voyager IRIS and the Infrared Space Observatory (ISO) were detected, including a robust confirmation of benzene, tentatively detected by ISO [Coustenis et al. 2003]. Latitudinal variations of all species were mapped (Figure CIRS-26), showing the greatest polar increases for HCN, HC_3N, C_4H_2, C_3H_4, and C_6H_6. The D/H ratio was measured from CH_3D, and found to be $(1.17 \pm 0.25) \times 10^{-4}$.

The first results from analysis of CIRS limb observations, yielding vertical-latitudinal profiles of HCN, HC_3N, and C_2H_2, were shown in the paper of Teanby et al. [2007], and was also the first to include CIRS data covering 60–90°N. It clearly revealed for the first time the 2-D structure of the atmospheric trace gas concentrations, and dramatically showed the difference in distributions between the three decaying tracers of differing lifetimes (Figure CIRS-27). The longest-lived species, C_2H_2 showed only marginal polar enhancement, while the shortest-lived species, HC_3N showed the steepest vertical gradient at low latitudes, and the most intense enhancement over the northern (winter) pole where the descending branch of stratospheric global circulation was occurring. The intermediate lifetime species, HCN, showed the most interesting and unexpectedly distribution, with a tongue of enriched air reaching from the lower N polar stratosphere back

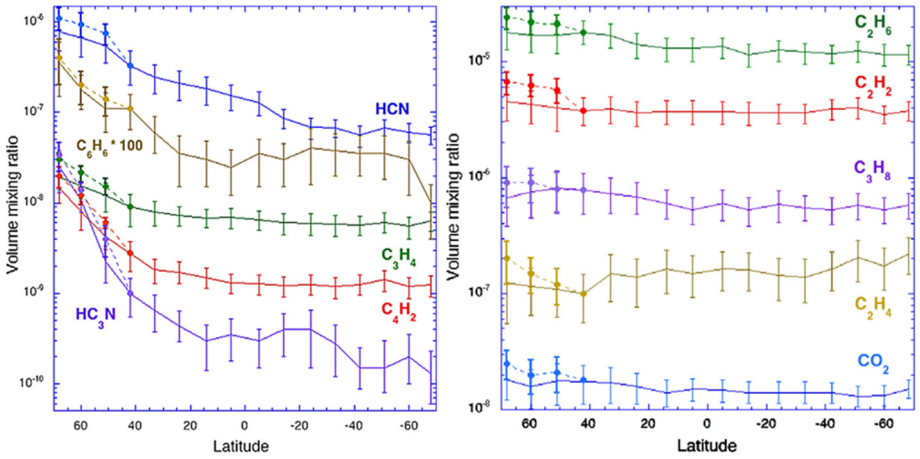

Figure CIRS-26. Meridional variations in the composition of trace gases in Titan's stratosphere and associated error bars. The latitudes indicated take into account the latitude smearing effect. The abundances shown are the averages of the results from fitting tours TB–T10. In dotted lines are shown the results at high northern latitudes when using the limb-based profiles instead of the nadir-based ones, highlighting the uncertainty on the higher northern inferences. Figure from Coustenis et al. [2007].

equatorwards. This was interpreted as the returning branch of the stratospheric circulation, seen clearly for the first time outside of GCM models.

Vinatier et al. [2007a] retrieved temperatures and vertical profiles for a wider array of gases at two latitudes on Titan—15° S and 80° N—from early flybys in 2004–2005. The temperature profiles confirmed the existence of a well-defined stratopause on Titan that was elevated (380 km versus 310 km) and hotter (207 K versus 183 K) in the north, in agreement with model expectations. The gas distributions largely confirmed the predicted picture from photochemical and dynamical models, however, there were unexpected details. Two of the heavier gases (C_3H_4 and C_4H_2) showed a minimum at 300 km in the north, perhaps related to haze formation. C_2H_4 showed a decreasing profile with altitude in the south: the opposite trend to other species, and possibly indicative of a secondary formation peak at low altitudes.

Oxygen-containing molecules were the focus of work by de Kok et al. [2007a], who retrieved a global mean abundance of CO equal to 47 ±8 ppm, and an upper limit for H_2O of 0.9 ppb, from CIRS FP1 far-IR spectra. CO_2 was found to have a typical abundance of 15 ppb in the lower stratosphere (100–200 km) with little latitude variation, in agreement with its expected long photochemical lifetime.

Teanby et al. [2008a] made a more detailed study of the northern polar vortex, this time using limb observation data to find the vertical gas distributions. A primary focus was to infer dynamical information from the distribution of trace gas species. A clear mixing barrier was detected at the edge of the northern vortex, preventing the enriched air from mixing laterally into the mesosphere at lower latitudes. However, at the base of the vortex, a tongue of tracer-enriched was spotted extending to lower latitudes, suggesting cross-vortex mixing and a residual polar circulation:

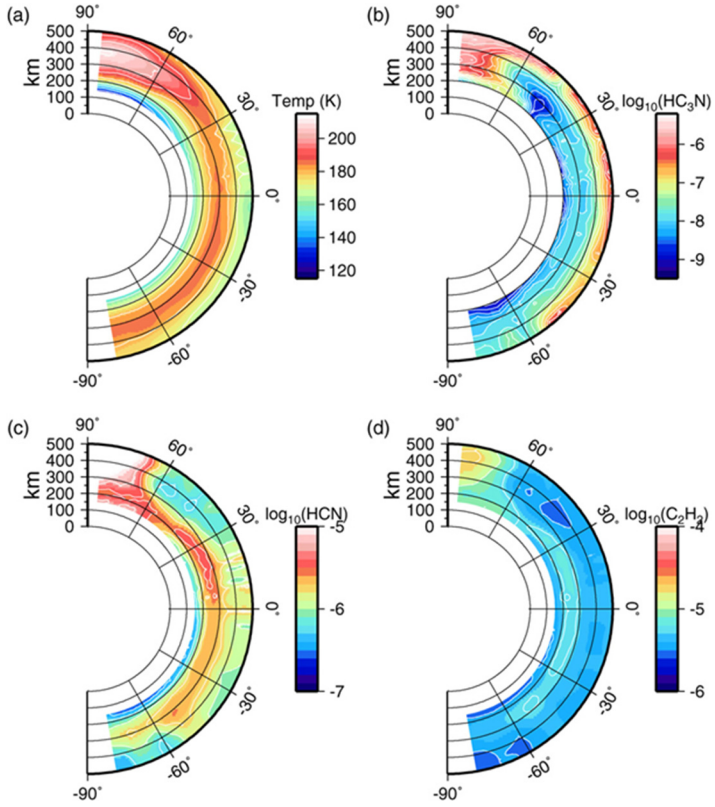

Figure CIRS-27. Cross-sections through Titan's atmosphere obtained using the three low resolution mapping sequences displaying temperature, HC_3N, HCN, and C_2H_2 abundance. Temperature is increased over the northern winter pole in the upper stratosphere and mesosphere and the stratopause is elevated with respect to the equator. The stratopause in the south also appears to be slightly higher than at the equator. The lower stratosphere in the north is much colder than at the equator. HC_3N shows a massive enrichment over the north pole, which appears to be confined to latitudes above 60° N. There is a suggestion of a tongue of enriched air extending from the north to the south at 200 km and 60° N. Note that HC_3N retrievals are not reliable southward of 50° N as the signal from HC_3N is too small. HCN is also enriched in the north, but the most striking feature is the layer of HCN enriched air at 200–250 km extending from the north pole to lower latitudes, which is suggestive of entrainment of enriched air in a meridional circulation cell. C_2H_2 appears to be well mixed throughout the atmosphere and does not vary significantly with latitude. There appears to be some slight enrichment over the north pole, which may be an artifact due to the correlation between HCN and C_2H_2 retrievals. Figure from Teanby et al. [2007].

features not reproduced in contemporary GCM models. Evidence was also seen for possible polymerization of C_2H_2 to C_4H_2.

A 2-D circulation model (CM) appeared soon thereafter, due to the work of Crespin et al. [2008] at the Institute Pierre-Simon Laplace, and with extensive collaboration from CIRS investigators. This model attempted to replicate the temperature fields measured by Achterberg, and vertical gas distributions retrieved by Vinatier and Teanby, especially. This represented an important step forward in modeling the new Cassini data, and provided an explanation for some of the observed phenomena. For example, the low-altitude increase in C_2H_2 was explained as the

presence of a long-lived, non-condensing gas species in the returning branch of the global circulation cell. However, some difficulties were encountered, such as the inability of the model to replicate a well-defined stratopause, and to reproduce the amplitude of the residual (previous season) winter polar enhancement in the south. These model deficiencies were important in pointing the way to further future work.

Hydrocarbon and nitrile composition from CIRS far-infrared spectra were first reported by Teanby et al. [2009c], who aggregated data from the first four years of the Cassini mission, encompassing the entirety of the prime mission (2004–2008). Three gases previously seen in this spectral region (200–400 cm^{-1}) by Voyager IRIS were detected: C_3H_4, C_4H_2, and C_2N_2, the last of which (cyanogen) is not seen in the mid-infrared spectrum of CIRS (600–1400 cm^{-1}). The abundance of C_3H_4 was about 2× greater than inferred from mid-infrared data, suggesting that coefficients for one or other of the bands were incorrect. For the first time, C_2N_2 was detected at low latitudes, where its abundance ($5.5 \pm 1.4 \times 10^{-11}$) is amongst the lowest of any gas detections by CIRS. Like other nitriles (HCN, HC_3N), cyanogen showed a greater polar enhancement than hydrocarbons with similar lifetimes, suggesting that chemical processes were missing from contemporary models.

In a study by Coustenis et al. [2010], the 2007 survey was expanded to include nadir data from all flybys of the Cassini prime mission (2004–2008), and including latitudes 90° S to 90° N, and also using revised spectroscopic parameters for C_2H_2, C_2H_6, and HCN to improve accuracy of results. By and large, the results were in agreement with GCM predictions [Crespin et al. 2008], but discrepancies were noted, such as lack of observational support for a secondary circulation cell.

Vinatier et al. [2010b] provided a comprehensive look at vertical profiles of a nearly-complete suite of Titan gases in the CIRS spectrum (C_2H_2, C_2H_4, C_2H_6, C_3H_8, CH_3C_2H, C_4H_2, C_6H_6, HCN, HC_3N, and CO_2) including first-ever maps of the 2-D distribution of C_2H_4, C_2H_6, C_3H_8, C_6H_6 and CO_2 at nine latitudes from 56° S to 80° N (Figure CIRS-28). This confirmed earlier results [Vinatier et al., 2007a], such as the decreasing abundance of C_2H_4 with altitude, in contrast to other gas species. Other previously unknown details of the gas distribution emerged, including depleted regions of C_2H_2, HCN, and C_4H_2 at 400 km (0.01 mbar) and 55° N. In contrast an enhanced region of CO_2 was seen at 30–40° N between 2–0.7 mbar. Finally, nearly all molecules showed a local minimum in abundance at (300 km, 80° N) in contrast with GCM models that predicted vertically constant profiles inside the vortex.

Far-infrared spectral lines of HCN were modeled by Teanby et al. [2010b] to confirm the earlier polar enhancement derived from mid-infrared spectral emissions [Teanby et al. 2007]. The data also supported the conclusion of Teanby et al. [2009c] that nitriles were missing a chemical sink in current photochemical schemes, since the emission versus lifetime distribution did not match that of hydrocarbons. In addition, the abundance of CO was re-derived and found to be: 55 ±6 ppm at 20 mbar, in good agreement with de Kok et al. [2007a].

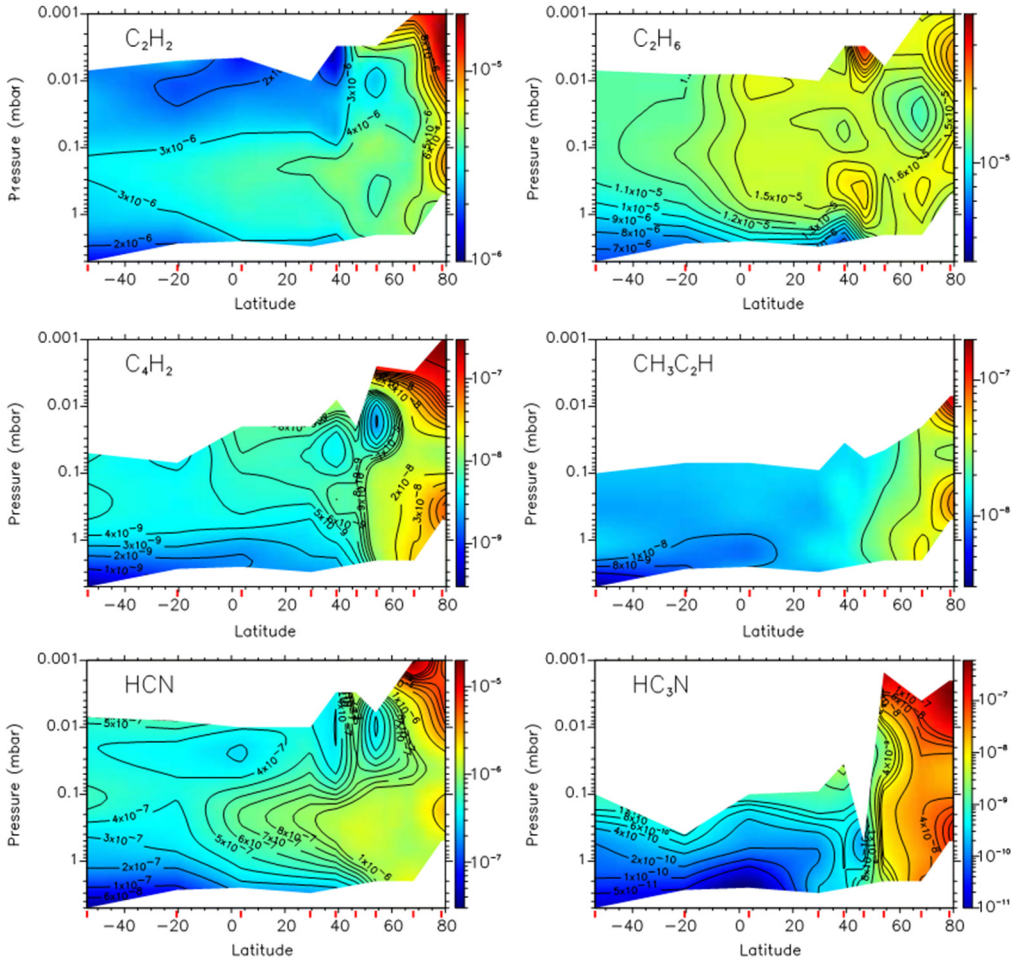

Figure CIRS-28. Latitude/pressure map of mixing ratios of C_2H_2, C_2H_6, C_4H_2, CH_3C_2H, HCN, and HC_3N. The regions of insufficient information content appear in white. Latitudes of the observed spectra are displayed as red vertical bars on the latitude axis. Figure from Vinatier et al. [2010b].

The global abundance of H_2 was the objective of a study by Courtin et al. [2012], who modeled the H_2–N_2 dimer S_0 (0) feature around 355 cm^{-1} seen on CIRS FP1 using data from 2006–2007. The mean abundance found was (9.6 ±2.4) × 10^{-4}, in good agreement with the Huygens GCMS value of (1.01 ±0.16) × 10^{-3} [Niemann et al. 2010]. This value is however some 4× lower than the ionospheric value: (4.05 ±0.03) × 10^{-3} at ~1200 km [Waite et al. 2005], which causes significant difficulty for modeling to explain. Interestingly, the CIRS measurements of the hydrogen abundance showed some evidence of increase towards the poles (Figure CIRS-29), by 30–70%, which would only make sense if it was due to downward transport in the presence of a vertically increasing hydrogen profile, as implied by the joint CIRS-GCMS-INMS results. Whether or not such a large hydrogen gradient is consistent with photochemical timescales from modeling remains an open question.

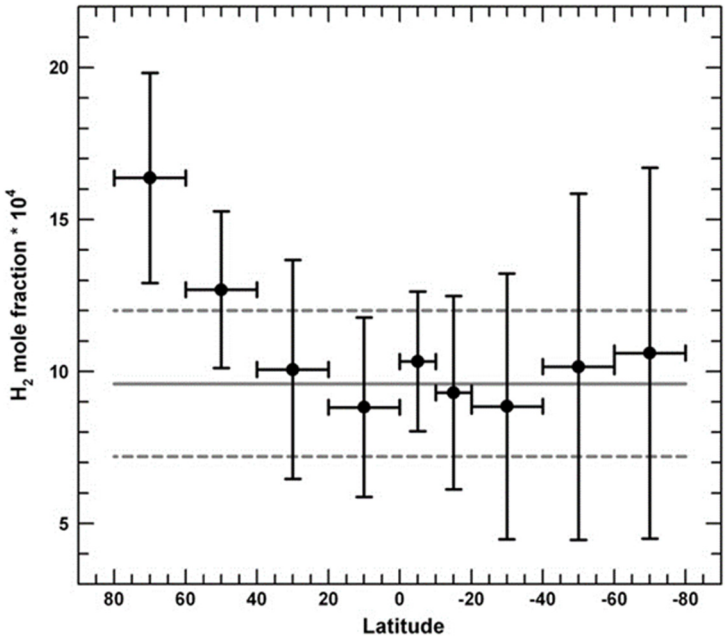

Figure CIRS-29. Values of the H_2 mole fraction (in unit of 10^4) derived from the CIRS average spectra in the nine latitude bands. The horizontal lines represent the global average value we derived, $(9.6 \pm 2.4) \times 10^{-4}$. Figure from Courtin et al. [2012].

Cottini et al. [2012a] made the first measurement of water latitude distribution from Cassini CIRS far-IR data, following the upper limit published by de Kok et al. [2007a] and a southern hemisphere average by Teanby et al. [2009b]. Globally, nadir measurements yielded an abundance of 0.14 ±0.05 ppb for an altitude of 97 km for a well-mixed vertical profile, somewhat lower than previously inferred from ISO (0.4 ppb). Two vertical profile points were also retrieved (Figure CIRS-30), showing a steep gradient that was in agreement with some photochemical models. No latitude variation was noted in the data.

In 2014, an interesting result emerged from the work of Lellouch et al. [2014] to constrain the abundance of methane, normally assumed to be constant with latitude in CIRS analysis, and fixed to the Huygens probe GCMS values [Niemann et al. 2010]. Lellouch and colleagues sought instead to retrieve the atmospheric temperature and the abundance of CH_4, via simultaneous modeling of mid-infrared rovibrational lines and far-infrared pure rotational lines. The result was unexpected, showing a variation in the abundance of methane from 1.0 to 1.5% at 85 km (15 mbar) in the lower stratosphere, a large fluctuation that was difficult to explain. Intriguingly, the low value (1.0%) near the equator allowed a temperature profile that agreed for the first time with Huygens HASI measurements, at the cost of losing agreement with GCMS. An explanation was offered for the mid-latitude increases in methane abundance as being due to tropospheric convection events percolating and persisting into the stratosphere.

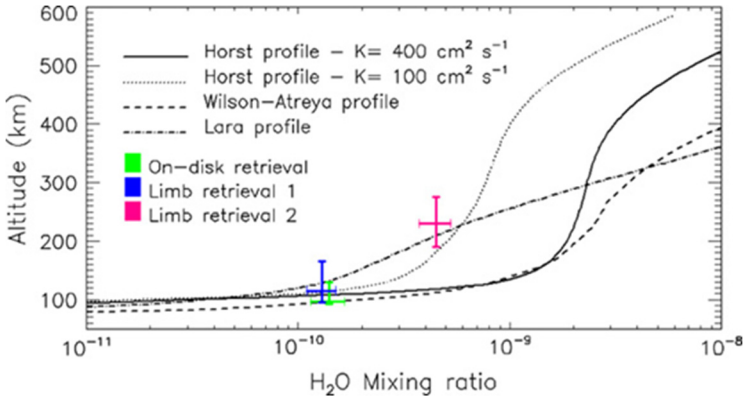

Figure CIRS-30. Water vapor mole fraction retrieved from CIRS on-disk and two limb observations assuming a water profile constant with altitude over the condensation level. Water profiles from three photochemistry models are also shown for comparison. The Hörst et al. [2008] water vapor profile was derived assuming two different eddy diffusion coefficients—100 cm^2 s^1 and 400 cm^2 s^1 (the second being the one recommended in their model; dotted curve plus solid curve). Also the profiles in Wilson and Atreya [2004] (dashed curve) and in Lara et al. [1996] (dot-dash curve). Figure from Cottini et al. [2012a].

Titan's water abundance was further constrained by the work of Bauduin et al. [2018], who analyzed a unique set of distant (~10^6 km) observations of Titan by CIRS, taken so that the entire moon was contained inside the FP1 pixel. This was done for intercomparison purposes with earlier studies using ISO and Herschel data, where Titan was similarly unresolved from the Earth-orbiting telescopes. Bauduin and colleagues found that the original discrepancy of a factor ~5 between Herschel (0.023 ppb at 12.1 mbar) and CIRS (0.14 ppb at 10.7 mbar) was sustained in the reanalysis, opening the possibility of seasonal change in the water abundance.

Lombardo et al. [2019] used a new line list for propene, first detected by Nixon et al. [2013a] to make the first spectral retrievals for this gas species. The results indicate that propene has a significantly different latitudinal profile from the other C_3H_x species: propyne and propane. Instead of being concentrated over the winter pole, the greatest abundance was found at the equator. Differences from photochemical model predictions were also found.

SEASONAL CHANGES

The paper of Teanby et al. [2008b] marked the start of papers focused on a new dimension of the dataset: seasonal changes in the gas distributions, from (L_S = 293°–328°). Teanby and colleagues used nadir spectra at medium (2.5 cm^{-1}) and high spectral resolution (0.5 cm^{-1}) to elucidate spatial and temporal changes in the abundances of C_2H_2, C_3H_4, C_4H_2, HCN, and HC_3N. A major new result was the gas distribution for the north polar region, showing that abundances continued to increase right up to 90° N (Figure CIRS-31). No secondary circulation cell was seen at the south pole, in contrast to GCM models predictions. A decline in southern gases was noted, as the residual southern winter enhancement faded.

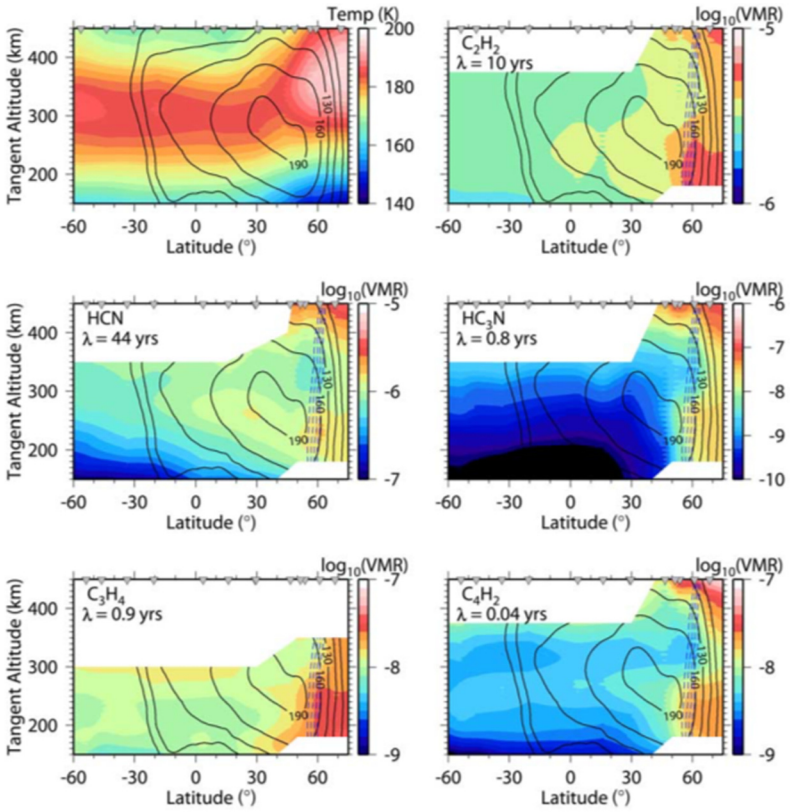

Figure CIRS-31. Cross-sections of temperature and composition through Titan's atmosphere. Composition is given as a volume mixing ratio, and the positions of the observed profiles are denoted by inverted triangles at the top of each plot. Contours indicate the vortex zonal wind speeds (in m s^{-1}) derived by Achterberg et al. [2008a], and blue dashed lines show the region with the steepest horizontal potential vorticity gradient, which indicates a dynamical mixing barrier (see Figure CIRS-5 and the section entitled Jupiter). Altitudes with low signal to noise or where the atmosphere becomes opaque are not plotted. VMR is the volume mixing ratio, and lambda is the photochemical lifetime at 300 km. Figure from Teanby et al. [2008b].

Teanby et al. [2009b] elaborated on the previous work, and showed that nitriles have different enhancements over the winter pole compared to hydrocarbons of similar photochemical lifetimes, which suggests some missing reactions in chemical models. A further update to seasonal and temporal trends in gas abundances was published by Teanby et al. [2010c], enlarging the dataset to include the six-year period from 2004–2010. Post-equinox (August 2009), increases in gases at both poles was seen, the first tentative evidence that Titan was transitioning to a two-cell circulation.

Seasonal changes in temperature and composition were also reported by Bampasidis et al. [2012], who modeled CIRS high resolution (0.5 cm^{-1}) nadir spectra from 50° S to 50° N, and spanning a time range from 2006–2012. At northern latitudes, the temperature profile evolved during the time period from a strong positive gradient to a more isothermal profile, with a cooling mesosphere and warming stratosphere. A maximum in the polar trace gas enrichment was found at the time of northern spring equinox (August 2009), followed by a sharp decrease as the polar descending circulation weakened and gases began to dissipate.

The first clear evidence for reversal of the stratospheric circulation was reported by Teanby et al. [2012a], who reported a build-up in trace gases over the south pole, some two years after equinox. A primary result was that the transition was very rapid, taking less than six months. The gas enrichments were used to estimate subsidence velocities within the vortex. Furthermore, gas and temperature distributions showed that upper atmosphere circulation must extend too much higher altitudes than previously thought: 600 km or more. This placed an imperative for revision of GCM models that did not at the time reach to such altitudes. In addition, the data suggested that the detached haze layer at ~500 km could not be solely generated by the circulation.

Coustenis et al. [2013] tackled the important question of intercomparison of findings from Cassini CIRS and Voyager IRIS, spanning a full Titan year, albeit with incomplete coverage. Temperature profiles and gas abundances in the lower stratosphere were measured and compared between 1980 and 2010, one Titan year apart. The results indicated little inter-annual variability, although the detailed distributions of the shortest-lived molecules C_3H_4 and C_4H_2 did exhibit differences.

Most recently, Vinatier et al. [2015] provided an update on the vertical profiles for the majority of Titan gas species seen in the CIRS data (Figure CIRS-32), using data from 2006–2013, focusing on seasonal changes. This provided a clear picture of the changes occurring in seasonal circulation, most especially around equinox, when the two-cell system persisted for just six months (January 2010–June 2010). By 2011, the single-cell winter circulation pattern had become established, reversing the direction of the circulation seen at the start of the mission. A sudden unexpected temperature drop was seen soon afterwards above the south pole, hypothesized to be due to enrichment in trace gases acting as coolants. In late 2012, a detached haze layer was seen in the CIRS data at 320–330 km, corresponding to the altitude of the detached haze layer seen by Cassini's cameras in the UV.

Seasonal change in Titan's temperatures and gases at high latitudes was studied by Coustenis et al. [2016], focusing especially on the comparison of ±50° and ±70° from 2010–2014, following Coustenis et al. [2010] (Figure CIRS-33). For the longest-lived hydrocarbons there was minimal change at all latitudes prior to 2013, with a small trend for increase in the south thereafter. At 70° S there was a strong enhancement in heavier hydrocarbons from late 2011 (equinox), including the appearance of HC_3N and C_6H_6 that were undetectable at this latitude at earlier times. A possible link between the gases and haze formation was postulated.

Sylvestre et al. [2018] followed up on the work of Teanby et al. [2009c], this time searching for seasonal changes in Titan's gases via the far-infrared spectrum. The heavy molecules C_3H_4, C_4H_2, and C_2N_2 were measured, showing a dramatic increase in abundance over the south pole in a short period from 2012–2013, while north polar abundances remained nearly unchanged. However, at northern mid-latitudes the shorter-lived species C_4H_2 and C_2N_2 did exhibit a decrease, while C_3H_4 did not. These results provide further constraint on photochemical and dynamical models.

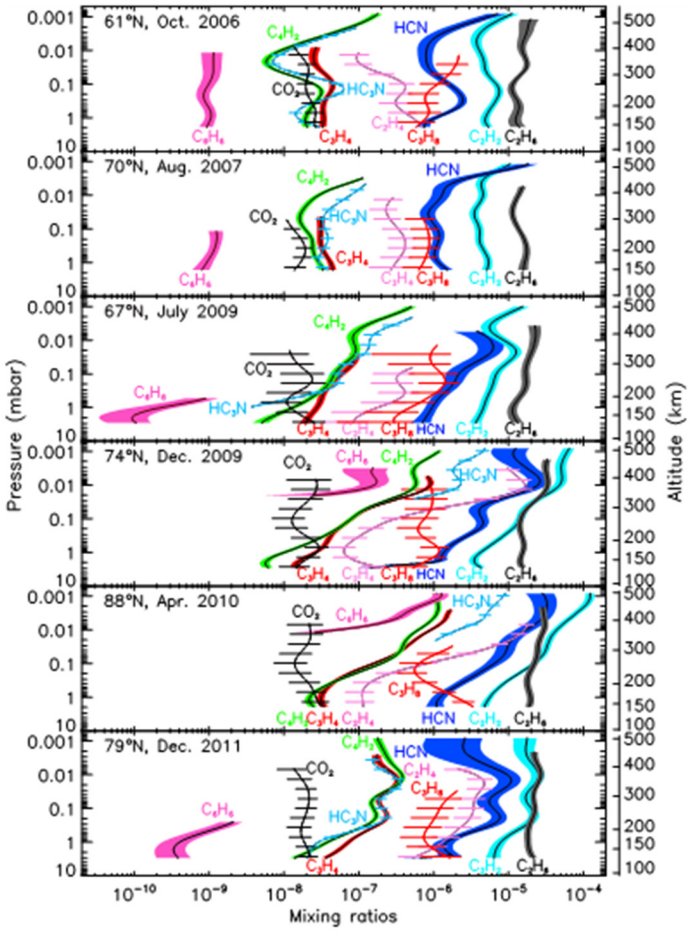

Figure CIRS-32. Seasonal variations of the mixing ratio profiles of C_2H_2 (cyan), C_2H_4 (pink with horizontal bars), C_2H_6 (gray), C_3H_8 (red with horizontal bars), C_3H_4 (red envelope), C_4H_2 (green), C_6H_6 (pink envelope), HCN (dark blue), HC_3N (blue with horizontal bars), and CO_2 (black with horizontal bars) at the north pole, derived from 0.5 cm^{-1} resolution limb spectra. Envelops and horizontal bars give the 1 r error bars. Figure from Vinatier et al. [2015].

A follow-up to the trends in seasonal changes of trace gases reported by Coustenis and colleagues in 2010 and 2016 was made by Coustenis et al. [2018], who focused on the polar regions 60°–90° north and 60°–90° south from CIRS nadir data. Notably different behavior was found for the onset of southern winter gas enhancement, which began in 2012, versus the decline in northern winter enhancement, beginning in 2015. The asymmetry in heating was dramatically evidenced in lower stratospheric temperatures: from 2013–2016 the north, entering spring, showed a mild temperature increase of 10 K, while the south, tending towards winter showed a more dramatic decrease of 25 K in the same period.

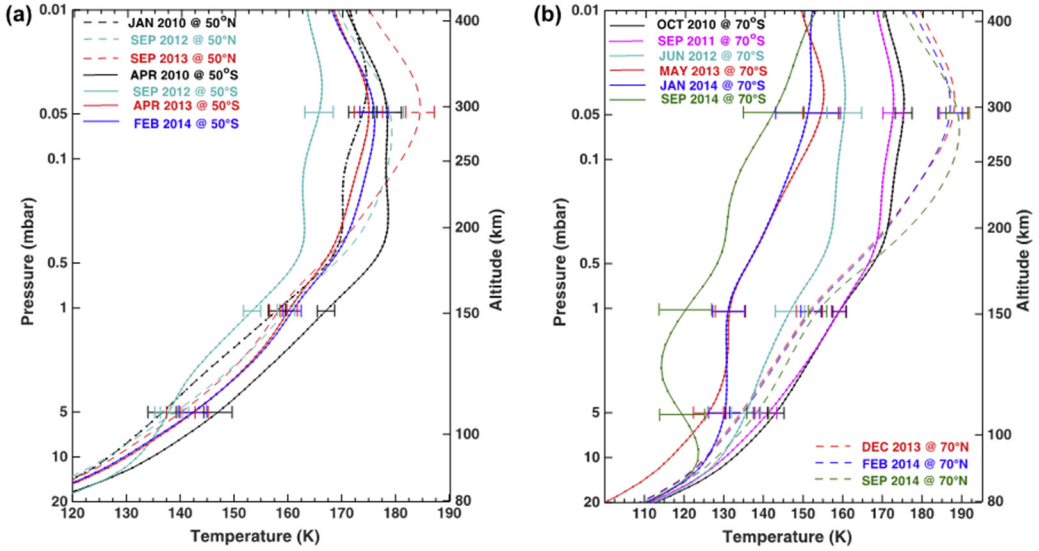

Figure CIRS-33. Seasonal change in Titan's temperatures and gases at high latitudes. (a): temperature variations at 50° S (solid lines) and 50° N (dashed lines) in Titan's stratosphere from January 2010 until February 2014; (b): temperature profiles of Titan at 70° S (solid lines) and 70° N (dashed lines) with dates ranging from October 2010 to September 2014 (in different colors).The pressure/altitude ranges probed by these profiles vary with latitude, but are generally in the 0.1–20 mbar region. The 3-r error bars on the temperature are plotted at 0.05, 1, and 5 mbar (see text for details). As can be seen, the stratospheric temperatures in the 0.1–1 mbar pressure range dropped by about 40 K near the southern pole within the past four years. At the same time, the temperatures in the north had not indicated similar dramatic changes, but rather an increase in temperature is found since February 2014, as the north moves into summer. The dashed lines, thus, show that within about seven months since December 2013, the NORTH POLE had warmed up by about 6 K. Figure from Coustenis et al. [2016].

SEARCH FOR NEW GAS SPECIES

Nixon et al. [2009a] made a detailed survey of the CIRS mid-infrared spectrum of Titan, searching for previously unseen gas species, and focusing especially on the region from 850–1050 cm^{-1} where there are few strong emissions. While a null result was obtained, numerous weak bands of propane (C_3H_8) were seen clearly for the first time that were not present in existing line lists used by the team, prompting a renewed round of laboratory work to provide line parameters.

In a follow-up paper, Nixon et al. [2010b] computed upper limits for several of gases expected to be found on Titan, from dedicated search observations (FP3/4 pair mode) at latitudes 25° S and 75° N. By comparing the results to photochemical model predictions they concluded that NH_3 and CH_3OH are likely present at levels far below the CIRS detection threshold, while CH_3CN, CH_2CCH_2 and H_2CO are closer to detection limits. In a later paper, Nixon et al. [2013b] added upper limits for biologically important sulfur and phosphorus-bearing compounds: H_2S and PH_3.

The first, and to this date only, new gas species detection on Titan from Cassini CIRS data was announced by Nixon et al. [2013a], following the availability of new propane line parameters from

several sources. This enabled the isolation of a propene (C_3H_6) emission at 912 cm^{-1} from stronger over-lying propane and ethylene bands (Figure CIRS-34), with an abundance of 2–4 ppb depending on altitude. This detection marked the completion of the triad of C_3H_x hydrocarbons, although the search for isotopologues such as allene (CH_2CCH_2) and cyclopropane (c-C_3H_6) continues.

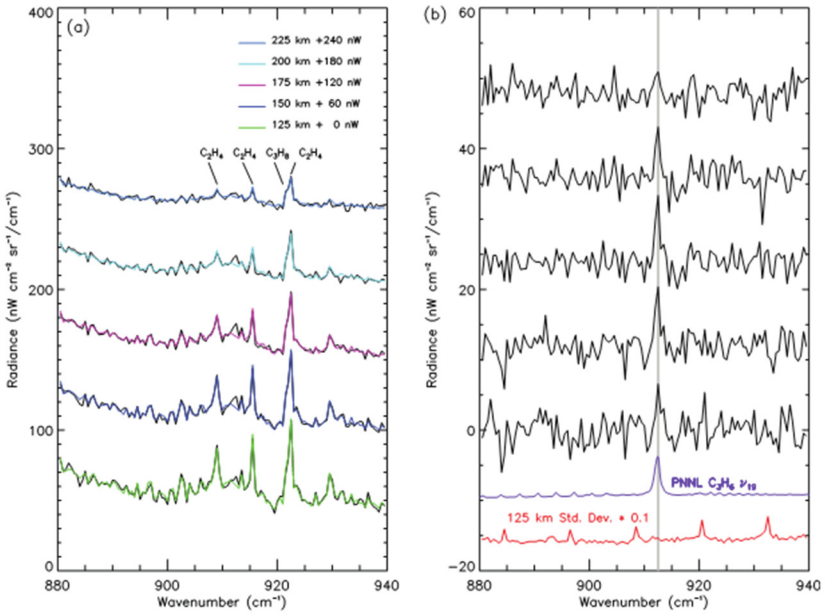

Figure CIRS-34. New gas species detection on Titan from Cassini CIRS data. (a) Co-added data spectrum (black) from weighted average of lowest (125 km), middle (175 km), and topmost (225 km) vertical bins. Also shown are the model spectra with propane (red) and without propane (blue) from the JPL pseudo-line list. (b) Residuals from subtracting data–model: blue line is model without propane and red line is with propane. The purple line shows the smoothed laboratory absorbance spectrum of propene recorded at PNNL, scaled by 1 × 10^4 and offset by −10. The detection significance is ~5 σ. Figure from Nixon et al. [2013a].

A detailed study was made by Jolly et al. [2015] to search for dicyanoacetylene (C_4N_2) in the far-infrared spectrum of CIRS, based on both theoretical expectations for its presence, and also the tentative identification of the ice at 478 cm^{-1} from Voyager IRIS data. Previous searches for the v8 band gas emissions at 472 cm^{-1} had been unsuccessful, causing a dilemma: how could there be ice clouds without vapor? New laboratory work indicated that the ν_9 band at 107 cm^{-1} was in fact stronger than ν_8, and a better candidate for detection given the better S/N in this part of the spectrum. However, only an upper limit on non-detection of 5–7 × 10^{-10} at the 1 σ level was found, leaving the question open about the origin of C_4N_2 ice.

ISOTOPIC RATIOS

Bézard et al. [2007] made a distinguished first detection of the first known double isotopologue on Titan: $^{13}CH_3D$ (Figure CIRS-35). By modeling the emission to measure the gas abundance they were able to estimate isotopic ratios of: $^{12}C/^{13}C$ = 82 (+27/−18) and D/H = (1.32 +0.15/−0.11) × 10^{-4}.

The carbon ratio was in good agreement with the terrestrial ratio (89), however the D/H appeared slightly lower than terrestrial (1.56×10^{-4}), though still substantially higher than in the giant planets, in accordance with expectations.

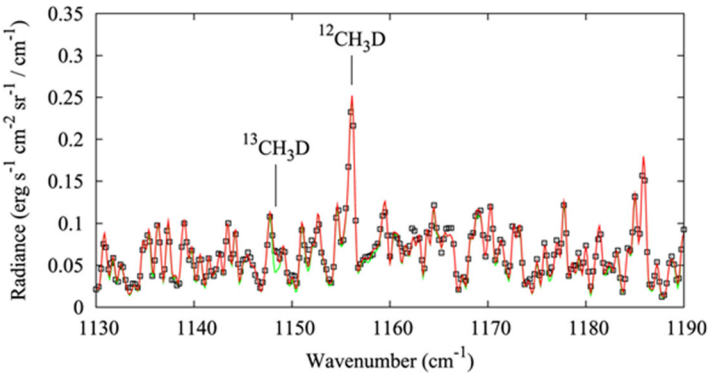

Figure CIRS-35. Comparison between a CIRS spectral selection centered at 15° S (symbols) and synthetic spectra calculated with (red line) and without (green line) $^{13}CH_3D$ line opacity, assuming a $^{12}C/^{13}C$ ratio of 89. Spectral resolution is 0.52 cm^{-1} (apodized). Both calculations use the same haze model, a CH_4 mole fraction of 1.4% and a CH_3D mole fraction corresponding to D/H = 1.34°ø 10^{-4}. Figure from Bézard et al. [2007].

Isotopic ratios in HCN were presented by Vinatier et al. [2007b] from CIRS limb spectra near 700 cm^{-1} on two early flybys. Abundances of HCN, $H^{13}CN$ and $HC^{15}N$ were individually measured, yielding isotopic ratios: $^{13}C/^{12}C = 75 \pm 12$, consistent with the current GCMS measurement at the time (82 ±1); and $^{14}N/^{15}N = 56 \pm 8$, lower than the value measured by GCMS in N_2 (183 ±5), but consistent with previous determinations in HCN from ground-based submillimeter investigations, and confirming that nitrogen-15 is preferentially depleted from the atmospheric reservoir in N_2 and incorporated into HCN.

The year 2008 proved to be a bumper year for new isotopic measurements, with four papers based on CIRS data. Coustenis et al. [2008] made the first detection of C_2HD, enabling for the first time the measurement of D/H in this chemical species. The modal value of $(2.09 \pm 0.45) \times 10^{-4}$ was significantly lower than the D/H in methane found by Bézard et al. [2007]: 1.56×10^{-4}, indicating possible fractionation from the parent (CH_4) to daughter molecule via photolysis or chemical selection.

Jennings et al. [2008] provided the first detection of carbon isotopes of HC_3N, most especially the strong detection of $H^{13}CCCN$ at 658.7 cm^{-1}, well separated from the main gas at 663.3 cm^{-1}. The derived isotopic ratio $^{12}C/^{13}C = 79 \pm 17$ was in good agreement with the terrestrial inorganic standard (89), and confirmed the growing body of evidence that carbon does not incur photochemical fractionation in Titan's atmosphere.

In a companion paper, Nixon et al. [2008b] showed the first detection of CO_2 isotopes on Titan, including both $^{13}CO_2$ and $CO^{18}O$. The carbon ratio ($^{12}C/^{13}C$) was 84 ±17, again in agreement with terrestrial levels, while the oxygen ratio ($^{16}O/^{18}O$) showed some evidence for enrichment: 346 ±110, versus the terrestrial 506. This value was later revised upwards to 380 ±142 by Nixon et

al. [2009b] using a more sophisticated and accurate model for the detector responses, moving the oxygen ratio closer to consistency with terrestrial values.

First remote-sensing measurements of the $^{12}C/^{13}C$ ratio in prominent hydrocarbons: methane, ethane, and acetylene were made by Nixon et al. [2008a], using CIRS high-resolution limb spectra. The results were: 76.6 ±2.7, 84.8 ±3.2, and 89.8 ±7.3 for CH_4, C_2H_2, and C_2H_6, respectively. While the acetylene and ethane values were close to terrestrial, the methane value was markedly lower: a perplexing result, lower even than the GCMS value (at the time) of 82.3 ±1 [Niemann et al. 2005]. Possible explanations were offered in terms of line strength errors or else some strong fractionation effect, however, unknown systematic errors may have contributed.

Following small irregularities in the modeling of the strong ν_8 band of diacetylene (C_4H_2), Jolly et al. [2010] were able to identify the carbon-13 isotopologue: $H^{13}CCCCH$ at 622.3 cm^{-1} (Figure CIRS-36). By modeling emission and comparing to the main isotopologue, a ratio $^{12}C/^{13}C$ = 88 ±7 was derived. This is in good agreement with the ratio in C_2H_2 [Nixon et al. 2008] and also the terrestrial and giant planet values, confirming an emerging picture that carbon undergoes very little isotopic fractionation across the solar system, in comparison to hydrogen and nitrogen.

Nixon et al. [2012] attempted a more accurate measurement of $^{12}CH_4/^{13}CH_4$ to resolve the uncertainty, this time including the other known methane isotopologues: $^{12}CH_3D$ and $^{13}CH_3D$. The

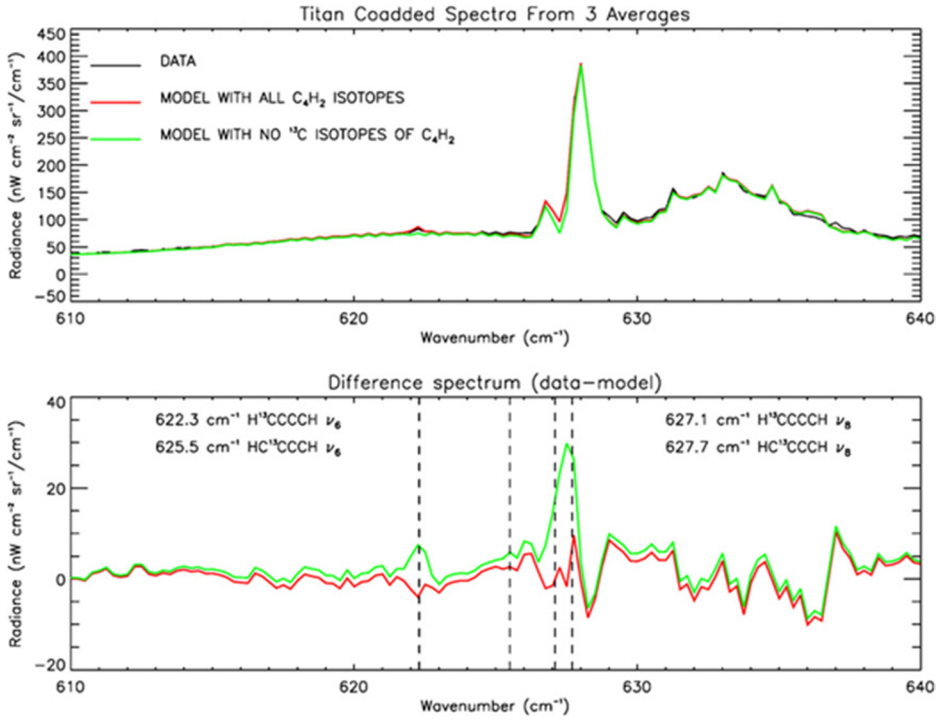

Figure CIRS-36. Modeling emission and comparing to the main isotopologue. *Top*: mean observed spectrum of Titan, compared to model spectra with and without the contribution of ^{13}C isotopologues of C_4H_2. *Bottom*: residual emission obtained after subtracting the observed spectrum and both model spectra. Figure from Jolly et al. [2010].

$^{12}C/^{13}C$ from these new measurements: 86.5 ±8.2 was now in much closer agreement with Huygens GCMS, also revised upwards to 91.1 ±1.4, and both in agreement with terrestrial (89), removing any need for significant fractionation. D/H was also measured to be (1.59 ±0.33) × 10^{-4}, in good agreement with the Huygens GCMS value in H_2: (1.35 ±0.30) × 10^{-4}. By considering the limited divergence of these ratios from primordial values, the authors were able to place an upper bound on the age of Titan's atmosphere of 1600 million years.

Hazes and condensates

In this section, we discuss the rich information derived from CIRS data regarding hazes and condensates in Titan's atmosphere. Although the definitions are sometimes blurred, we will here use the term haze in a narrow sense to mean photochemically-derived, refractory organic particles that are heterogenous in size, composition, and structure at the microscopic level. We use "condensate" to refer to clouds of droplets of ice particles of relatively pure substances that have reached their condensation/freezing point. We note that haze particles are thought to act as nuclei for condensation, and would, therefore, be present in the cores of condensate cloud droplets, although at that point, undetectable. In addition, condensates may undergo photochemical reactions and change their composition, as described the following sections.

HAZE

The first paper tackling the derivation of haze properties from CIRS data was the work of de Kok et al. [2007b], who studied far-infrared (10–600 cm^{-1}) spectral limb data. The authors were able to measure the fractional scale height of the main, ubiquitous haze, in addition to identifying three specific spectral components that could be modeled with Gaussian signatures at 140, 190, and 220 cm^{-1}. These spectral features were localized in both latitude and altitude on Titan, and were in fact condensates of unknown composition, with B and C being seen preferentially in the northern (winter) hemisphere. Haze B appeared to be the re-detection of a strong feature seen by Voyager IRIS, whose composition remains uncertain (Figure CIRS-37).

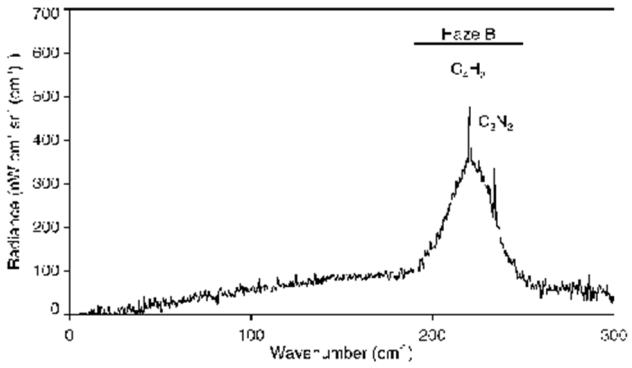

Figure CIRS-37. The average of 13 limb spectra at 85°N at 0.5 cm^{-1} resolution. The FOV centre is at 135 km and the FOV size is 135 km. This spectrum clearly shows a broad feature (Haze B) with gas emissions super-imposed on it. Figure from de Kok et al. [2007b].

A possible anti-correlation between gas and haze vertical abundances was proposed by Teanby et al. [2009a], based on joint analysis of CIRS and ISS data from 150–450 km. Periodic density enhancements were noted, with a length scale of ~50 km, and especially visible over the north pole and vortex boundary. A dynamical origin for the layering was proposed, based on cross-vortex (latitudinal) motions.

Vinatier et al. [2010a] provided the first survey of haze features in the mid-infrared regime of CIRS (600–1400 cm^{-1}), using nine limb integrations from 55° S to 80° N during the prime mission (Figure CIRS-38). Vertical profiles of haze opacity in 17 spectral bins were found, showing near-identical vertical trends, and indicating the haze composition is relatively unvarying with altitude. Distinct spectral features were found at 630 cm^{-1}, 745 cm^{-1}, and 1390 cm^{-1}. A global trend for increasing mass mixing ratio with altitude was taken as strong evidence that the haze is created at high altitudes, above the level of CIRS detection.

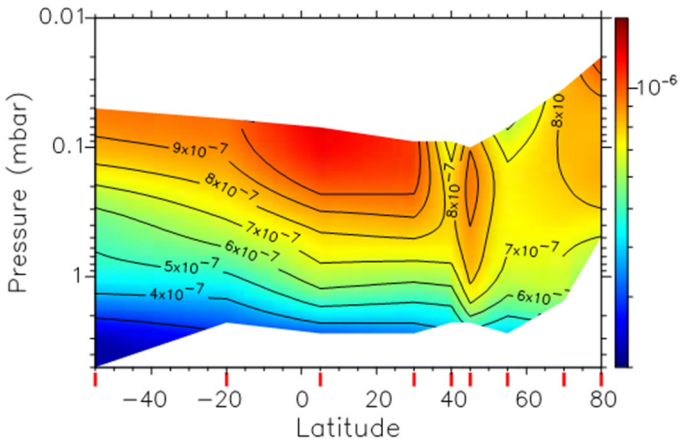

Figure CIRS-38. Latitudinal/pressure map of the haze mass mixing ratio. Latitudes of the observed spectra are displayed as red vertical bars on the latitude axis. Figure from Vinatier et al. [2010a].

A multi-instrument study of the haze banding on Titan was presented by de Kok et al. [2010b], using data from Cassini's ISS and VIMS instruments as well as CIRS. The imagery showed a prominent tropical haze band, and its orientation confirmed the tilt of the atmospheric rotation axis suggested by Achterberg et al. [2008b]. Haze profile retrievals from CIRS data at 640–670 cm^{-1} also reinforced the result.

A comprehensive follow-study by Vinatier et al. [2012] derived the optical properties of Titan's haze from the far-IR to mid-IR (70–1500 cm^{-1}), by modeling the haze particles as aggregates of ~3000 spherical monomers (0.05 micron radius) with fractal dimension n = 2. Real and imaginary refractive indices were derived across the entire range, and several distinct spectral features were found corresponding to vibrations of methyl and methylene. The same features were found across a wide array of altitudes and latitudes, indicating that Titan's haze is relatively uniform in composition.

The notorious, unidentified haze feature at 220 cm^{-1} in the CIRS far-IR was the subject of a study by Jennings et al. [2012b], who observed its seasonal change over the northern (polar) winter pole. From 2004–2012, the intensity of the feature decreased by a factor four, and the authors speculated that this could be due to either: (i) increased photolytic destruction of source chemicals, (ii) decreased condensation due to warmer temperatures, or (iii) a weakening of the subsiding branch of the seasonal circulation. In a follow-up paper [Jennings et al. 2012a] the authors reported the rapid appearance of the 220 cm^{-1} haze in the south (Figure CIRS-39), in July 2012, following non-detection in February the same year. In a 2015 paper on the same feature, it was definitively attributed to a cloud instead of a haze, as described in the following paragraph.

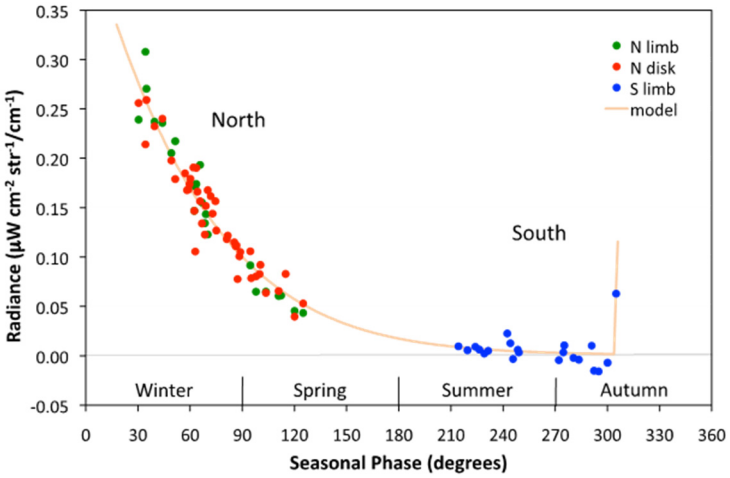

Figure CIRS-39. North and south polar radiances of the 220 cm^{-1} feature plotted on the same seasonal scale. Data from Titan's north represents winter–spring behavior and the data from the south represents summer–autumn behavior. The northern values were adapted from Jennings et al. [2012b], with the addition of a data point in the north from July 24, 2012. The southern values are from Figure CIRS-2 in this report. The seasonal phase scale begins at winter solstice and each 30° increment equals one Titan month. The model is described in the text. Figure from Jennings et al. [2012b].

CONDENSATES

Samuelson et al. [2007] provided the first update on condensates (ices) from CIRS data, comparing the spectral features seen in the far-infrared by CIRS to those seen previously by Voyager. Two definite ice/condensate features were identified in north polar (winter) spectra: the large emission feature at 220 cm^{-1}, previously seen by Voyager IRIS, and also called Haze B by de Kok the same year; and a weaker signature at 160 cm^{-1}. This latter feature was attributed to HCN ice particles of r < = 5 μm at altitudes less than 160 km, while the former was compared to pure crystalline water ice, and also ice of propionitrile (C_2H_5CN), and both candidates found to be produce insufficient spectral fits.

de Kok et al. [2008] further considered gases that might be condensing at Titan's winter (north) pole, especially the open question of C_4N_2 ice first raised by Khanna et al. [1987], and the

origin of Haze B. As with Samuelson et al. [1997], the authors found an upper limit for C_4N_2 gas based on the absence of the gas feature at 471 cm^{-1}, and therefore found the case for the ice identification to be uncertain. Likewise, an upper limit for propionitrile (C_2H_5CN) gas was found to be too low to support the large emission at 220 cm^{-1}, and an alternative explanation in terms of a mixed condensate including an HCN component was postulated instead.

A search for evidence of a tropospheric methane cloud was conducted by de Kok et al. [2010a], using CIRS far-infrared nadir and limb spectra. The authors concluded that the CIRS data were consistent with a cloud at 30 km, however this explanation was in conflict with findings from Cassini VIMS and Huygens DISR. A strong conclusion however was that the collision-induced opacity coefficients for N_2-CH_4 should be in increased by 50%, pending laboratory reevaluation.

The first confirmation for an HC_3N ice cloud on Titan was found by Anderson et al. [2010] at 62° N and 70° N, based on analysis of far-infrared spectral data (Figure CIRS-40). HC_3N ice (506 cm^{-1}) was clearly separated from HC_3N gas (499 cm^{-1}) for the first time, confirming earlier hints of its existence from Voyager IRIS [Samuelson 1985]. Cloud top altitudes were determined for HC_3N ice as 165 km (70° N) and 150 km (62° N), while upper limits for cloud abundances were measured at latitudes of 85° N, 55° N, 30° N, 10° N, and 15° S.

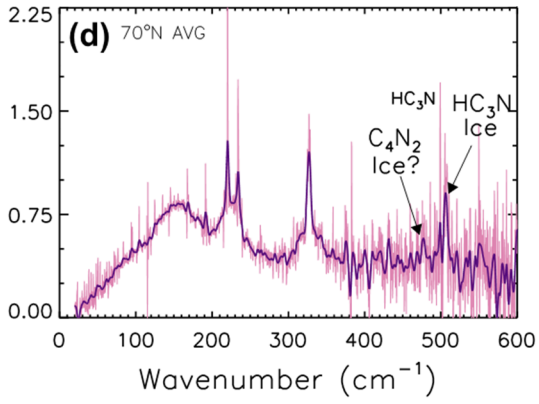

Figure CIRS-40. Weighted vertical average of both sit-and-stares at 70° N. Light pink curves are the data at the original spectral resolution (Dm) of 0.5 cm^1 and the dark purple curves represent the data smoothed by a Gaussian kernel to Dm = 3.0 cm^1. Condensed HC_3N and possibly C_4N_2 emission features are indicated by the arrows. Figure from Anderson et al. [2010].

Anderson and Samuelson [2011] derived the vertical and spectral properties of hazes and condensates at four latitudes (62° N, 15° N, 15° S, 58° S) using CIRS data at both high (0.5 cm^{-1}) and low (15 cm^{-1}) spectral resolution. While haze abundance was comparable, ices were found to be 3× more abundant at 62 °N compared to 15° S. A nitrile (HCN, HC_3N) ice cloud was inferred from a spectral signature at 160 cm^{-1}, 90 km and a second ice cloud was tentatively inferred at 80 cm^{-1}, 60 km. Aerosols were found to be uniformly mixed from the surface to the top of the stratosphere, with a broad emission feature at 140 cm^{-1} possibly due to PAHs.

In de Kok et al. [2014] looked for evidence in the CIRS data to explain the curious high-altitude (300 km) cloud seen by Cassini ISS above Titan's south polar in May 2012. The CIRS data showed

a strong cooling at this altitude (Figure CIRS-41), in contrast with previously observed warming during winter stratospheric subsidence. In addition, the saturation vapor pressure profile of HCN was found to reach 100% at this temperature minimum, providing a strong explanation for the ISS images in terms of an HCN ice cloud.

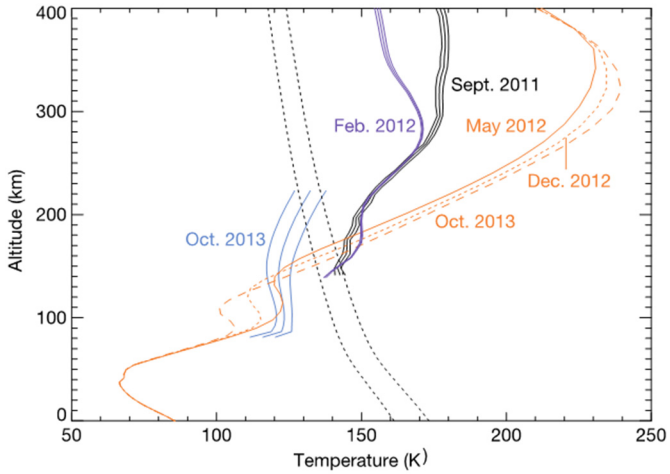

Figure CIRS-41. South-polar temperatures from models and retrievals. Retrieved temperatures and their 1 s errors at 86 u S in September 2011 (black solid line) and February 2012 (purple) from CIRS limb measurements and at 87u S in October 2013 from CIRS nadir measurements (blue). We plot only regions where the observations provide reliable temperature information. Orange lines are circulation model output for May 2012 (solid), December 2012 (dotted), and October 2013 (dashed). Black dotted lines indicate saturation temperatures for HCN volume mixing ratios of 10^{26} (*left*) and 10^{25} (*right*), which cover the measured concentrations of HCN in the south polar vortex. A cloud at 300 km would require temperatures of 125 K there [de Kok et al. 2014].

Anderson et al. [2014] proposed the existence of subsidence-induced methane clouds (SIMCs) over Titan's north pole, based on an analysis of far-infrared rotational lines of methane. By ingesting a radio science (RS) temperature profile and then deriving the vertical profile of methane, the authors showed that methane could exceed its saturation vapor pressure between 20–48 km, and that subsidence in the winter polar vortex could therefore induce condensation. A near-infrared counterpart and possible identification of this cloud was found in Cassini VIMS data.

Jennings et al. [2015] further studied the 220 cm^{-1} feature seen in the far-infrared spectrum of CIRS, and previously referred to as a haze in papers by de Kok et al. [2007b] and Jennings et al. [2012a, 2012b]. The 2015 paper showed the evolution of the condensate cloud at both poles, which was seen to be different. The northern cloud was decreasing in intensity since the start of the mission, with a half-life of 3.8 years. The southern cloud was doubling in intensity every year from 2012, confined to a ring centered on 80° S. In contrast, south polar trace gases had a bi-modal structure with a peak abundance at 90° S, minimum at 80° S, and ring of increased emission at 70° S. The authors concluded that the condensate and gases exhibited an anti-correlation, possibly due to condensation.

Chemical changes on grains of Titan's polar ice clouds were the subject of a 2016 paper by Anderson et al. [2016]. The authors proposed that the previously observed ice signature of C_4N_2 at 478 cm^{-1} (Figure CIRS-42) could arise naturally without condensation from the vapor phase, due to the action of sunlight acting on existing HCN-HC_3N mixed condensates. This process has a counterpart in terrestrial polar stratospheric clouds, where solid state photochemistry leads to condensed nitric acid trihydrate (NAT) particles and loss of ozone.

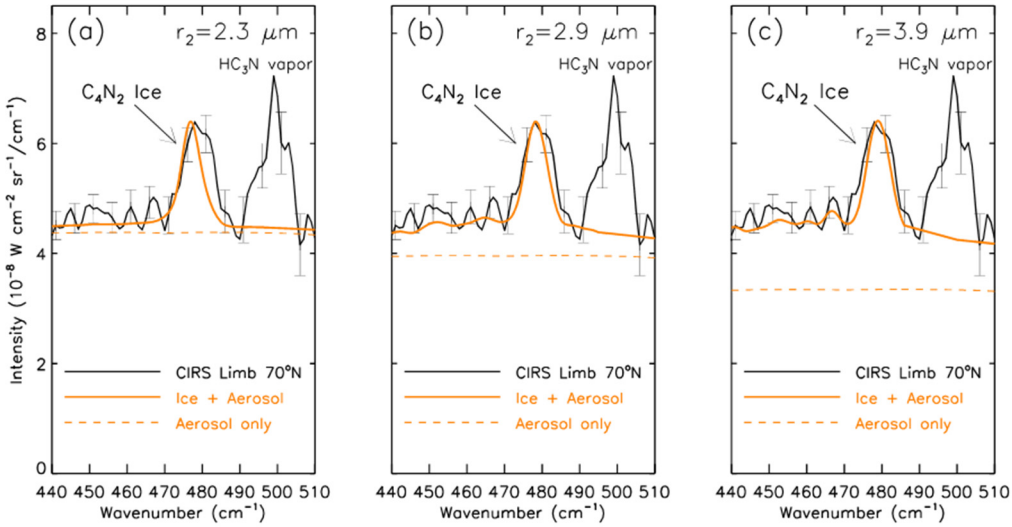

Figure CIRS-42. Radiative transfer fits (solid orange curves) to the continuum of CIRS limb-tangent spectral averages at 70° N (solid black curve). The spectral range is limited to 440–510 cm^{-1}, and the C_4N_2 ice feature at 478 cm^{-1} is included in the fits. A simplified two-stream plane-parallel model, patterned after the one by Hanel et al. [2003], is used to include effects due to anisotropic multiple scattering. Single-scattering parameters are calculated for various C_4N_2-HCN abundance ratios and mean particle radii: (a) pure C_4N_2 ice, r_2 = 2.3 μm; (b) 50:50 C_4N_2-HCN ice mixture, r_2 = 2.9 μm; and (c) 20:80 C_4N_2-HCN ice mixture, r_2 = 3.9 μm. Orange dashed curves show aerosol contributions. The 1σ error bars are spaced every 5 cm^{-1}. Figure from Anderson et al. [2016].

The south polar winter stratosphere again featured in the research of Vinatier et al. [2018], who investigated condensate signatures in the mid-infrared spectral region of CIRS. A weak feature isolated for the first time at 682 cm^{-1} was attributed to benzene ice, and a feature at 695 cm^{-1} was tentatively attributed to C_2H_3CN ice. Mass mixing ratios of both ices were determined, and it was shown that the cloud top for benzene was 300 km at the pole, decreasing to lower latitudes. An upper size limit of 1.5 micron was determined for the benzene ice particles.

Anderson et al. [2018] described their laboratory work dedicated to unraveling the spectral signatures of Titan ices, by deposition and spectroscopy of thin ice films. Pure condensates and co-condensates of HCN, HC_3N, and C_4N_2 were investigated, and the application to modeling and interpretation of CIRS spectra discussed.

Conclusions and further work

The Cassini CIRS instrument in general, and CIRS Titan science in particular, have been hugely successful relative to mission goals, as described in the section entitled CIRS Science Assessment. The original mission was projected to last for four years: in the end Cassini and CIRS returned data for 13 years, allowing an undreamt level of insight into Titan's atmospheric workings, and interactions with the surface. GCM and photochemical models that were largely speculative at the outset of the mission now have large, detailed and time-resolved datasets to use as constraints, providing fodder for study many years into the future.

In the absence of an active mission in the Saturn system, the focus will now turn to observations with ground and space-based observatories such as JWST [Nixon et al. 2016], ALMA, SOFIA, and large optical telescopes. However, given the difficulties of observing through Earth's atmosphere, significant sections of the infrared spectrum remain out reach (for all but JWST). It will be vital to continue monitoring seasonal changes in Titan's atmosphere to extend the time-base of Cassini observations, and prepare the way for the next generation of missions to visit this complex and fascinating world.

Icy Satellites

The key TM questions of Icy Satellite science that CIRS has helped address are:

Level 1

Changes on Enceladus (IC1a)

IC1a: Determine whether Enceladus exhibits any seasonal changes. Other temporal changes (e.g., mean anomaly) are also considered.

Enceladus' plume mass varies as a function time and of orbital position [Ingersoll and Ewald 2017], as shown in Figure CIRS-43. CIRS observations of Enceladus' active south polar region during Cassini's F-ring and proximal orbits (FRPO) were designed to investigate whether Enceladus' surface temperatures also vary with time. Preliminary results indicate that Enceladus' surface temperatures do vary with mean anomaly, but lag in time behind the plume change.

To determine whether the thermal emission of Enceladus varies with mean anomaly a series of observations were planned in the FRPO. A summary of the observations is given in Table CIRS-6.

Howett et al. [2017] presented analysis of this CIRS data at AGU 2017. They used focal plane 3 (FP3) observations since they offer the best compromise between spatial and spectral coverage of Enceladus' active region. The CIRS observations taken of Enceladus clearly show the active region. Figure CIRS-44 shows the original plane of sky data. The figure clearly shows the higher surface emissions from the active south polar terrain.

Table CIRS-6. Summary of the CIRS FP3 observations of Enceladus' south polar terrain. Those in bold have the best SNR, and therefore have been focused upon.

Orbit (Rev)	Date	# FP3 Observations	Mean Anomaly Range
250	**11/27/16**	**5**	**244 to 265**
251	12/4/16	9	8 to 46
254	**12/26/16**	**13**	**247 to 300**
255	1/2/17	5	1 to 18
259	**1/30/17 to 1/31/2017**	**19**	**303 to 24**
263	**2/28/2017 to 3/01/2017**	**21**	**272 to 50**
267	3/29/17	11	215 to 278
286	**8/1/17**	**17**	**280 to 252**

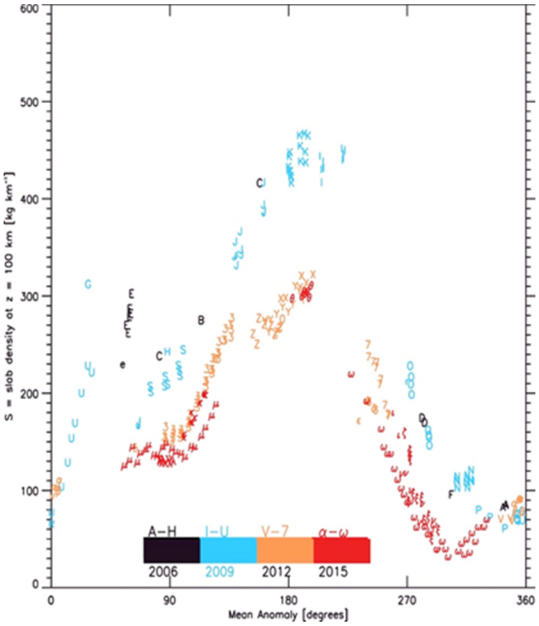

Figure CIRS-43. Enceladus' plume mass vis. Orbital position (mean anomaly). Figure from Ingersoll and Ewald [2017].

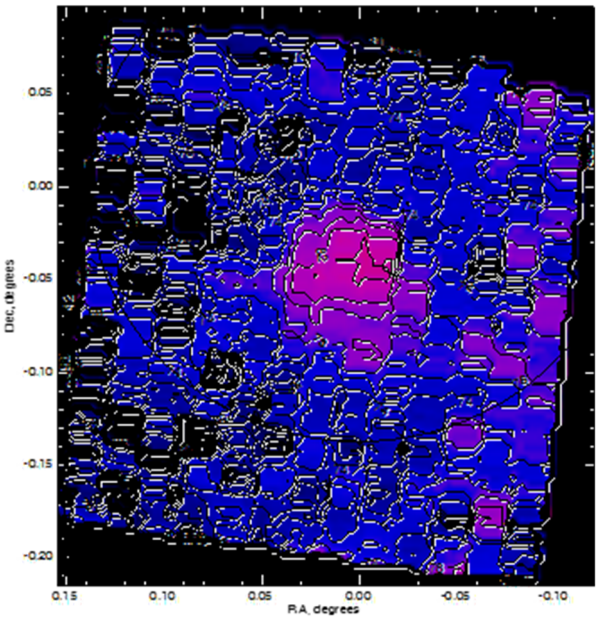

Figure CIRS-44. Typical FP3 scan shown in the plane of sky. Enceladus' active south polar terrain is clearly visible as the warmer purple region.

To properly account for the poles these data were binned into triangles, which are tessellated across the sphere. The area of each triangle is almost constant. The triangles are much smaller than the size of a single FP3 field of view, but since CIRS scans FP3 slowly across the disk subpixel resolution is achieved. Example of the resulting binned total integrated flux between 610 and 800 cm^{-1} are shown in Figure CIRS-45, at the start or end of each observation sequence.

The integrated radiances of all the high SNR observations were totaled for all bins inside of 70° S. The results are shown in Figure CIRS-46. As the figure shows only mean anomalies between ~270 and 10° are covered by these observations, but they appear to show the flux from Enceladus' surface decreasing by about a factor of two during that time.

This is smaller than the 3–5× decrease observed in the plume mass, and occurs at slightly higher mean anomalies. However, the difference is notable and tentatively implies that the temperature of Enceladus' surface in its active region does vary with its orbital location, but the change lags the plume emission change. More work is required to firm up this preliminary result, and analyze the lower signal-to-noise observations to fill in the mean anomaly coverage.

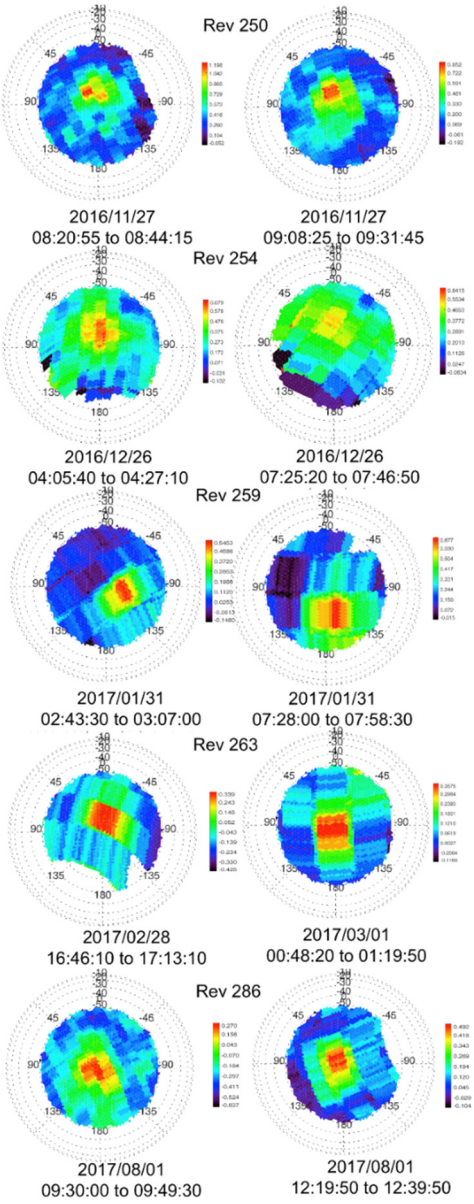

Figure CIRS-45. Binned integrated radiances (610 to 800 cm^{-1}) at the start and end of every rev considered.

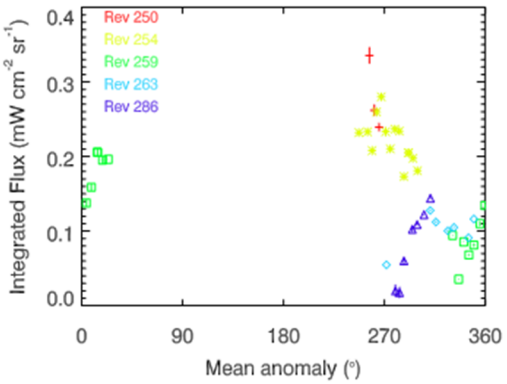

Figure CIRS-46. Total integrated flux (from 610 to 800 cm^{-1}) observed inside of 70° S for all high S/N observations.

CONCLUSIONS

Preliminary analysis indicated that Enceladus' surface emission could be varying with its orbital position, but perhaps lags behind changes in the plume emission. More work is required to firm-up this result, and increase the mean anomaly coverage.

Enceladus' interior (IN1a)

IN1a: Determine the surface temperature in active regions and constrain Enceladus' heat flow, to better constrain models of its activity.

INTRODUCTION

Much work has been done on this subject. An overview of the major results is provided chronologically.

SPENCER ET AL. [2006]

Initial analysis of mid-infrared data (600 to 1100 cm^{-1}) taken by CIRS FP3 onboard Cassini indicated that the endogenic power of Enceladus' south polar region was 5.8 ±1.9 GW [Spencer et al. 2006], much higher than the expected radiogenically produced power of 0.3 GW [Porco et al. 2006; Schubert et al. 2007]. Dissipation of tidally produced energy, most likely from the Dione and Enceladus 2:1 resonance, has been suggested as a possible production mechanism of the observed endogenic power [Spencer et al. 2006; Porco et al. 2006; Yoder 1979; Ross and Schubert 1989].

The Spencer et al. [2006] calculation of Enceladus' endogenic power found that blackbody emission at 133 ±12K over an area of 345 (−160, +320) km^2 matched the total >600 cm^{-1} CIRS FP3 spectrum of the south polar region. However, at this temperature only 10% of the blackbody spectral energy falls within the FP3 wave number range, while the remaining 90% of it falls within the 10 to 600 cm^{-1} wave number range of CIRS' FP1. The percentage of the spectral energy in the FP3 wave number range decreases further with decreasing temperature, rendering FP3 insensitive to low temperature emission, and it was noted by Spencer et al. [2006] that additional power might be radiated at lower temperatures.

HOWETT ET AL. [2011A]

Since the Spencer et al. [2006] analysis used FP3 data it was unable to quantify low-temperature endogenic emission. So another attempt was made to determine Enceladus' heat flow, this time using FP1 data [Howett et al. 2011a]. Long integrations (known as stares) were targeted at Enceladus' south polar region on March 12, 2008 (orbit or revolution, rev 61), and October 31, 2008 (rev 91). The signal to noise of each data set is increased by averaging the stares together. These stares are the only FP1 observations that will be made over the entire Cassini mission which both cover the entire south polar terrain and are sensitive to the wave number region where the bulk of

the endogenic power is radiated. Figure CIRS-47 shows the stare locations: each of the 73 integrations in rev 61 and the 48 integrations in rev 91 has comparable geometry.

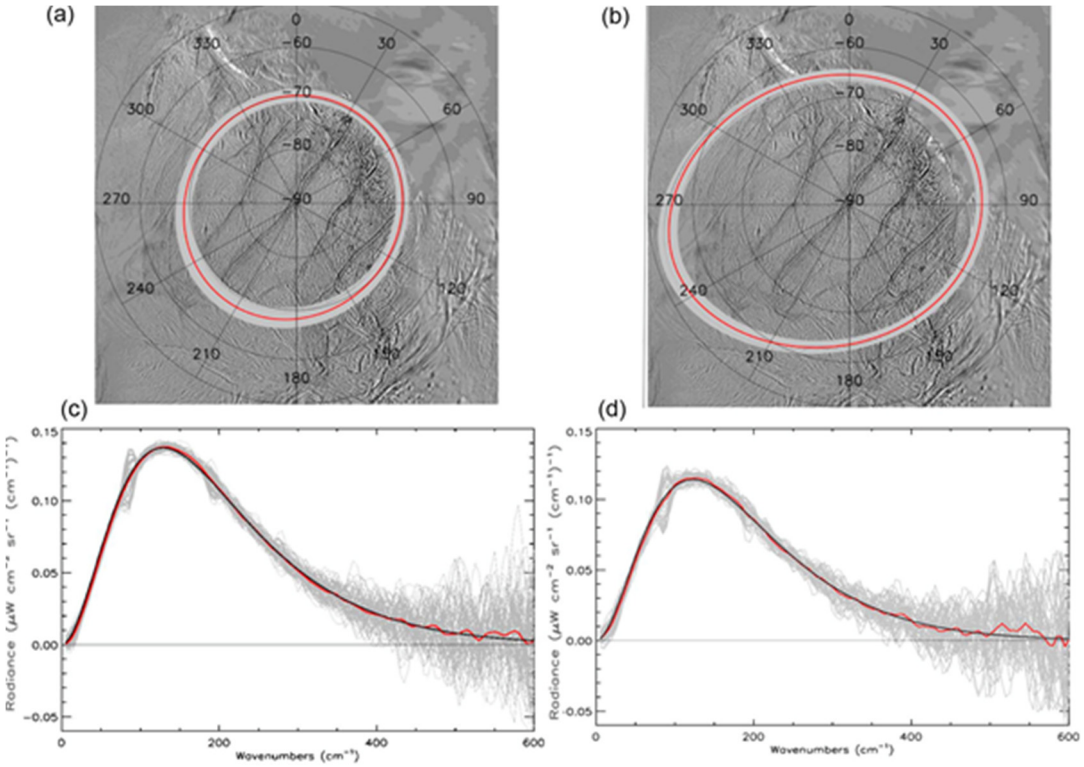

Figure CIRS-47. The range of locations of the FP1 field of view during the stare observations of rev 61 *Panel (a)*, and rev 91 *Panel (b)* over Enceladus' south pole (shown in gray). The field of view at the observation mid-time is also shown (red). The four prominent fractures within the rev 61 field of view are the active tiger stripes. The base map used is the 2006 ISS mosaic PIA 08342. In *Panel (c)* and *Panel (d)*, the spectra of each stare observation (gray), the mean spectrum (red), and the best fit two-temperature to this mean value (black) for revs 61 (*panel c*) and 91 *Panel (d)*.

FP1 is sensitive to the passive emission from the solar-heated surface, which has temperatures in the 35–80 K range [Spencer et al. 2006]. Thus, to obtain the endogenic component of the spectra this passive emission must first be removed. Passive emission is modeled for each epoch and observational geometry using a seasonal and diurnal 1-D numerical thermal model [Spencer et al. 1989]. The model determines surface temperatures by calculating conductive heat flow into and out of the subsurface through every diurnal cycle of an entire Saturnian year, accounting for insolation variations resulting from the 29° tilt of Enceladus' rotation axis relative to the sun, and the concurrent changes in heliocentric distance (9.03–10.05 AU) resulting from Saturn's orbital eccentricity. The model assumes that albedo does not vary with incidence angle, and does not initially account for the effects of heating by radiation from Saturn, or solar eclipses by Saturn, though these are discussed in the section entitled Characterize the Surfaces of Saturn's Small Satellites (IN2d) below. The thermal inertia values it uses are based on previous observations but require assumptions about the thermophysical properties at depth.

For each observation the temperatures predicted by this model are used to calculate the passive background across the FP1 field of view, assuming blackbody emission. These temperatures are weighted by the spatial sensitivity pattern of the FP1 detector, which is approximated as a 2-D Gaussian with a FWHM of 2.42 mrads [Flasar et al. 2004a]. The results from this model were validated by demonstrating the good agreement between the modeled spectrum produced, and CIRS data taken within Enceladus' south polar terrain but away from the tiger stripes themselves. For each observation, this passive thermal background is subtracted from the CIRS spectra leaving a residual, the spectrum of the endogenic emission. The residual is then weighted to correct for the assumed spatial distribution of the endogenic emissions. Three possible scenarios are considered: (i) that emission from the tiger stripes is uniform along their length, (ii) that the emission from the stripes varies in the same way as previously observed by higher spatial resolution higher wave number observations by the CIRS FP3 detector and, (iii) to set a lower limit on the endogenic power, a scenario which all emission arises from the most sensitive central 10% of the field of view is also considered. The effects these scenarios have on the endogenic emission determination are discussed further in the section entitled Tethys and the E-ring (IN2b) below. In the case of the stare observation the corrected residuals for each rev are averaged to increase the signal to noise. The final corrected residual is then fitted by a blackbody temperature curve with a filling factor, which allows the residual to be fitted by emission from only a fraction of the field of view if required. The endogenic power of that residual is then derived using the Stefan-Boltzmann law, the fitted temperature, filling factor and area of the projected FP1 field of view.

Since the response of the FP1 detector is non-uniform we also had to consider the spatial distribution of the endogenic emission. To estimate the dependence of the derived endogenic emission on its spatial distribution we evaluated three different scenarios: (i) that the tiger stripes are the sole source of the power and have uniform emission along their lengths, (ii) that the tiger stripes are the sole source of the power but that the emission intensity varies along each stripe, and (iii) finally that the emission is independent of the tiger stripes location but arises instead from an area within the most sensitive central 10% of the FP1 field of view. The last scenario is unrealistic, but is designed to determine a lower limit to the endogenic emission. The FP1 detector is most sensitive to emission from its central region and thus concentration of the emission in this region would minimize the true power required to produce the observed signal. Under the second scenario the variation in brightness along the length of the tiger stripes is assumed to be the same as that determined from high spatial resolution 600–1100 cm^{-1} FP3 observations made on rev 61 (Figure CIRS-48) from 1922:00 to 1944:00 UT. These observations had a spatial resolution of 4.1-9.6 km, sufficient to resolve the tiger stripes and the spatial distribution of emission along their lengths (Figure CIRS-48). Almost the entire tiger stripe region was covered, with the exception of the Saturn-facing end of Alexandria Sulcus, for which we have included approximate brightness values based on other CIRS observations [Spencer et al. 2006]. For the uniform case, we assigned equal brightness to all spatial bins with nonzero normalized brightness.

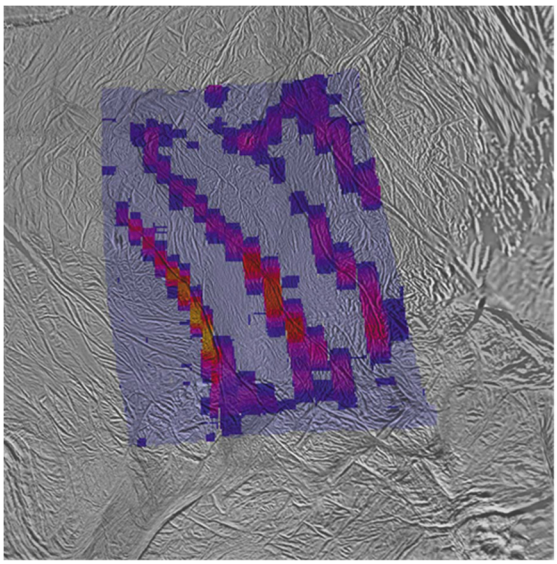

Figure CIRS-48. CIRS FP3 map of the spatial distribution of radiated 600–1100 cm^{-1} brightness along the four tiger stripes, as observed on March 12, 2008 (rev 61). Relative brightness is shown by colors ranging from blue (faintest) to yellow (brightest). The pale blue area shows regions that were mapped, but showed negligible radiated power. The data used in this scan was taken between 1922:00 and 1944:00UT on March 12, 2008.

Finally, the emission from a surface also depends on its albedo and thermal inertia. These properties are not known for Enceladus' active south polar terrain, although they are known for regions close to it [Howett et al. 2010]. By modeling FP1 observations close to, but not over the active part of Enceladus south polar terrain, it was possible to narrow down the range of albedo to ~0.80. Since constraining thermal inertia was not possible three scenarios are considered: (i) a constant thermal inertia of 27 MKS at all depths, (ii) two scenarios both of which have a thermal inertia of 27 MKS from the surface to a depth of 1 cm, but have higher thermal inertias of 100 MKS, and (iii) 1000 MKS below 1 cm. A near- surface thermal inertia of 27 MKS was derived for the latitude bin 60° S to 50° S [Howett et al. 2010], this is the closest location to the south polar terrain (SPT) for which thermal inertia has been determined. The lower deep layer thermal inertia value of 100 MKS was selected using results from 2005 Cassini CIRS observations of Enceladus' winter north pole that showed the north polar thermal inertia to be less than 100 MKS to a depth of ~1 m [Spencer et al. 2006]. The higher deep layer thermal inertia value of 1000 MKS was selected to be close to that of solid water ice [Paige et al. 1994]. The results are shown in Figure CIRS-49, and a summary of the endogenic emission predicted using these different scenarios is given in Table CIRS-7.

The maximum and minimum endogenic emission values given in boldface in Table CIRS-7, excluding the extreme and unlikely scenario where all emission is concentrated at the center of the FP1 field of view, are used as our estimate of the uncertainty range of the total endogenic emission. Thus, it is estimated that Enceladus' south polar endogenic emission of 14.8 ±1.9 GW for rev 61 and 16.9 ±2.4 GW for rev 91, which agree within error and give a combined value of 15.8 ±3.1 GW.

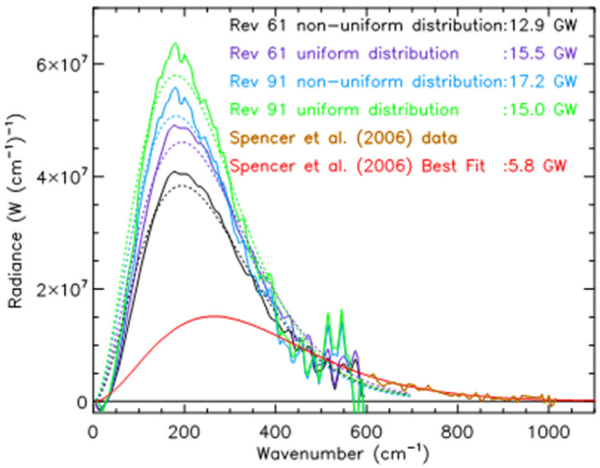

Figure CIRS-49. The mean endogenic emission of the FP1 stare observations taken during revs 61 and 91, assuming both uniform and nonuniform emission along the tiger stripes (see the section entitled Tethys and the E-ring (IN2b)). The best fitting blackbody temperature fits are given by the dotted lines, which are correspondingly colored. Temperatures of 99.1 K and 92.4 K provide the best fit to rev 61 and 91 for both of the assumed spatial distributions. However, the total surface area of the emission decreases from 2657 km^2 to 2211 km^2 for rev 61 and from 4121 km^2 to 3609 km^2 for rev 91 as the assumed spatial distribution varies from uniform to nonuniform. The 2005 FP3 endogenic emission spectrum used by Spencer et al. [2006] to determine the previous lower estimate of endogenic power is also shown, along with the extrapolation of a blackbody fit to that spectrum over the wave number range of the FP1 detector.

Table CIRS-7. Summary of the predicted endogenic emission from Enceladus under a variety of reasonable assumptions about the thermophysical properties of Enceladus' surface. See text for a full description.

Assumed Subsurface Conditions for Thermal Model	Rev 61 Endogenic Power Uniform Spatial Distribution (GW)	Rev 61 Endogenic Power FP3-like Spatial Distribution (GW)	Rev 61 Endogenic Power Central Spatial Distribution (GW)	Rev 91 Endogenic Power Uniform Spatial Distribution (GW)	Rev 91 Endogenic Power FP3-like Spatial Distribution (GW)	Rev 91 Endogenic Power Central Spatial Distribution (GW)
Scenario 1	16.6	13.8	8.2	**19.3**	16.9	11.9
Scenario 2	15.5	**12.9**	7.6	17.2	15.0	10.6
Scenario 3	**16.6**	13.8	8.1	16.6	**14.5**	10.2

SPENCER ET AL. [2012]

The previous heat flow estimates were based on observations that did not resolve the tiger stripes from their surroundings, so passive emission from the surroundings had to be modeled and subtracted to determine endogenic heat. In this work, Spencer et al. [2012] used higher spatial resolution observations to spatially separate the tiger stripe emission, which must be endogenic, from background emission, which is expected to be partly or entirely passive.

They model the surfaces radiating the endogenic emission as continuous ribbons of material of temperature T (l) and width W (l) which vary smoothly with distance l along the tiger stripes and associated warm fractures. T and W are adjusted to match the spatial and wavelength dependence

of the emission seen in specific CIRS observations, using a forward model. The most extensive FP3 map of the tiger stripes, obtained on orbit 61 in March 2008 (Figure CIRS-48 and Figure CIRS-50), can be matched with a single relatively high temperature endogenic component, denoted by subscript H , with TH (I) varying spatially between 120 and 165 K, and WH (I) varying between 60 and 330 meters. The best spatially resolved constraint on lower-wavenumber emission, an FP1 scan across the tiger stripes Damascus, Baghdad, and Cairo from orbit 136 in August 2010 (Figure CIRS-50) shows that an additional lower temperature component is also needed (Figure CIRS-51). However the limited spatial coverage of this and other FP1 scans does not allow unique constraints on the spatial distribution of the low temperature component. To estimate the contribution of this component (denoted by subscript L), we constrain TL and WL from the wavelength-dependent FP1signature where the rev 136 scan crosses the tiger stripes (Figure CIRS-51), and extrapolate to the rest of the system by assuming that both TL and WL /WH are independent of location. We then re-fit all parameters using these assumptions.

The resulting total heat flow is 2.7 GW and 1.5 GW from the high and low temperature components respectively, for a total of 4.2 GW. Enceladus' power output also includes the latent heat of the escaping plume (~0.5 GW [Ingersoll and Pankine 2010]), giving a total output of ~4.7 GW. There may be additional endogenic heat from the regions between the tiger stripes, included in previous estimates but excluded here, which may account for some of the discrepancy with earlier estimates. It is also possible that previous models under-estimated the passive contribution to the integrated south polar emission (e.g., due to spatial variability of thermophysical properties), and thus, over-estimated of the endogenic component.

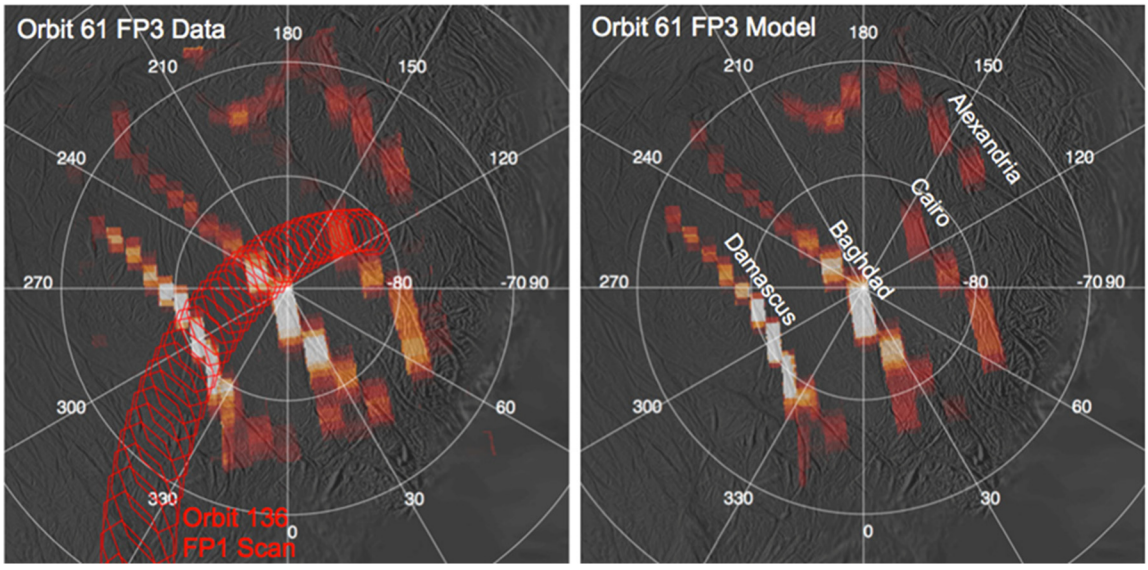

Figure CIRS-50. Constraining the tiger stripe emission distribution model using the orbit 61 CIRS FP3 scan of the tiger stripe system. *Left*: shows observed 600–850 cm^{-1} radiance. *Right*: shows the simulated observation derived from the best-fit model. *Left*: also shows (red) the location of the orbit 136 FP1 scan used to constrain the longer wavelength emission from the tiger stripes (Figure CIRS-51).

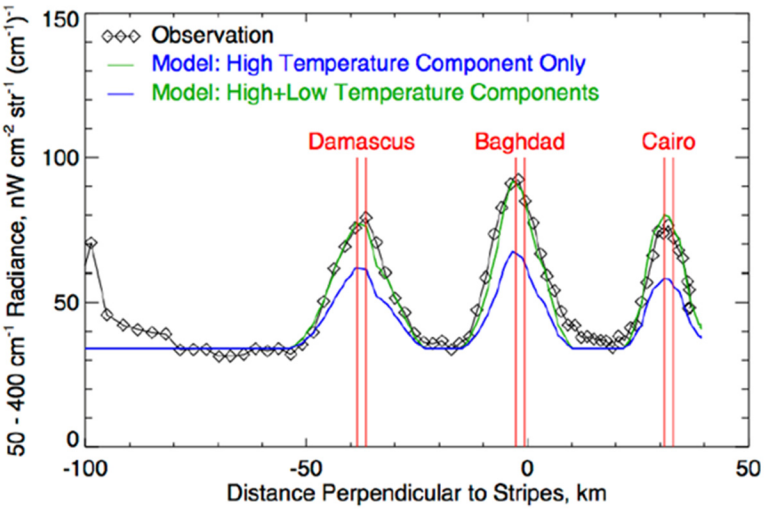

Figure CIRS-51. Profile of low-wavenumber FP1 radiation across three of the tiger stripes (Figure CIRS-50) from orbit 136, compared to predictions from our best-fit model of tiger stripe temperatures, with and without the inclusion of a low-temperature component. The model also includes a constant background radiance, assumed here to be passive re-radiated sunlight. This FP1 scan reveals that the high-temperature component fitted to the FP3 observations (Figure CIRS-50) does not account for all the radiated power at low wavenumbers, and an additional low temperature component is need to match the data.

The inconsistency of heat flows derived from different techniques highlights the difficulty of these measurements, indicating that all heat flow estimates should be treated with caution. However, all estimates are much larger than the expected maximum steady-state tidal heating of 1.1 GW [Meyer and Wisdom 2007].

CURRENT WORK

To minimize the effect of passive emission observations of Enceladus were made with FP1 late in the Cassini mission, when Enceladus' active south pole was in winter. During such time, the effect of low-temperature passive emission is minimized (Figure CIRS-52). Observations taken during rev 250 by FP1 offer one of the best opportunities for determining Enceladus' heat flow. In this rev, a scan of Enceladus entire south polar terrain was made by FP1. Preliminary analysis has been performed using two methods and provides similar results.

The first method was to look at individual spectra taken over Enceladus' active region, remove the (small) expected passive emission, and assume the remaining emission is endogenic (Figure CIRS-52). The resulting endogenic emission is ~9 GW.

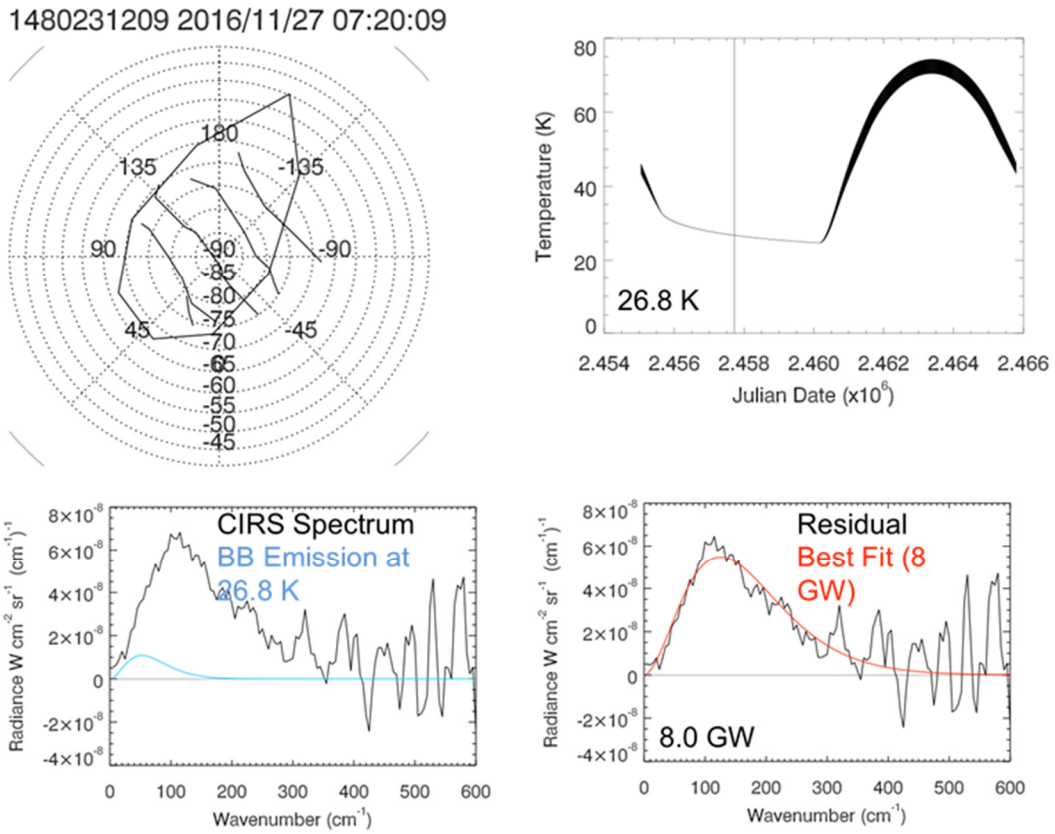

Figure CIRS-52. Individual spectra taken over Enceladus' active region. *Top left*: location of the observation analyzed, spacecraft event time (SCET) relative to Earth time, it was taken. The position of the tiger stripes is indicated. *Top right*: Seasonal model for a surface with an albedo of 0.80 and a constant thermal inertia with depth of 27 MKS. The temperature this model predicts for Enceladus' passive emission at the time the observation was taken is 26.8 K. *Bottom left*: calibrated CIRS FP1 spectrum taken, compared to the predicted passive emission. *Bottom right*: residual CIRS spectrum and the best fit.

The second technique is to use observations close to the tiger stripe but away from the activity as a proxy for the expected passive emission (see Figure CIRS-53). These results imply that the total south polar power (in one FP1 FOV) is ~6–8 GW. However, further work is required to determine to what extent power spills into multiple field of views.

Conclusions

Determining the heat flow of Enceladus' active region is a particularly difficult thing to do, since in order to determine the low-temperature heat flow Enceladus passive emission must be removed (particularly early on in Cassini's mission when the south pole was not in winter). This modeling effort is hampered by a somewhat chicken-and-egg problem: in order to model the passive emission the thermophysical properties of Enceladus' surface are needed to be accurately known, but it is difficult to determine these properties because of the activity.

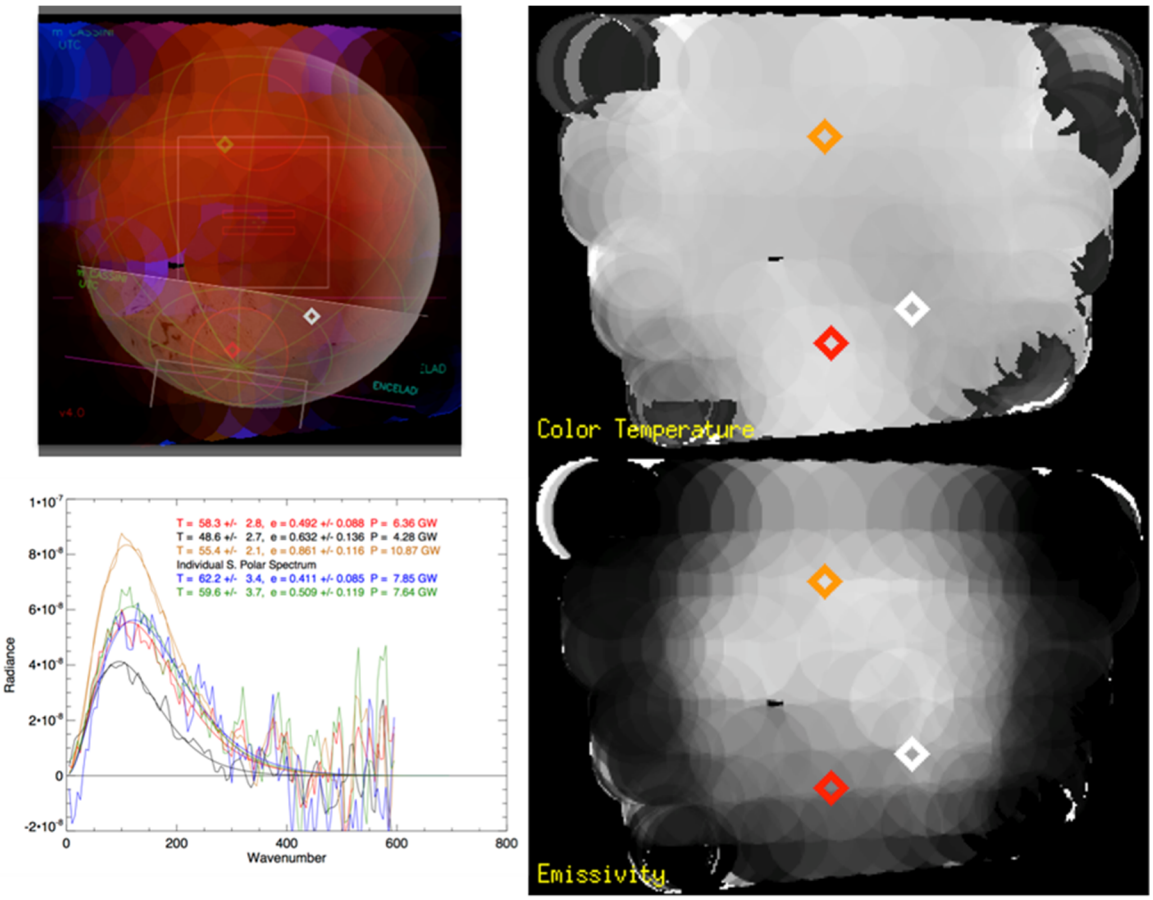

Figure CIRS-53. Observations close to the tiger stripe but away from the activity as a proxy for the expected passive emission. *Top Left*: Temperature map of Enceladus, with geometry overlaid. The position of three reference points are indicated: one away from the tiger stripes (orange), another close but not in the active south polar terrain (white) and another in the heart of the active region (red). *Bottom Left*: calibrated CIRS FP1 spectra and their best fits at the reference points. *Top/Bottom Right*: The radiance map plotted as a function of color temperature and emissivity variations. The plots show the temperature highest over the south polar terrain, which also displays the lowest emissivity.

Early attempts set a limit based on the high-temperature endogenic emission: 5.8 ±1.9 GW [Spencer et al. 2006]. Later attempts characterized both the high- and low-temperature emission: 15.8 ±3.1 GW [Howett et al. 2011a]. Continued modeling of the high- and low-temperature emission from only the stripes themselves pointed to a lower value of ~4.7 GW [Spencer et al. 2018]. New and ongoing work trying to characterize Enceladus' heat flow while the southern polar region is in winter (i.e., has a reduced passive emission) provides an estimate between 6 and 8 GW, but more work is required to fully characterize this emission.

So, more work is required! And even then, there will always be some ambiguity over this number—particularly if it is varying, as preliminary results from Howett et al. [2017] suggest. However, what is certain is that Enceladus' activity is continuing and impressive.

Compare Saturn's mid-sized satellites (IN1b)

IN1b: Compare the surface characteristics of Saturn's mid-sized satellites, including the thermally anomalous Pac-Man regions.

INTRODUCTION

Observations returned by CIRS and ISS showed a thermal and color anomaly at low latitudes on Mimas and Tethys' leading hemisphere (see Figure CIRS-54). This anomaly, dubbed Pac-Man (because its shape mimics that of the 1980s' video icon), displays warmer nighttime and cooler daytime temperatures than its surroundings and appears darker in IR/UV color ratio maps [Howett et al. 2011b, 2012; Schenk et al. 2011]. The color and thermal anomalies are believed to be the result of surface alteration by high-energy electrons, which preferentially bombard this region, altering its surface and increasing its thermal inertia. These high-energy electrons, in Saturn's magnetosphere, drift in a retrograde direction relative to corotation. Recent modeling efforts, supported by the Low Energy Magnetospheric Measurement System (LEMMS) on Cassini's Magnetospheric Imaging Instrument (MIMI), have shown that these electrons preferentially bombard low latitudes on Mimas, Tethys, and Dione's leading hemisphere [Paranicas et al. 2012, 2014; Howett et al. 2011b; Schenk et al. 2011].

COMPARISON OF THE SURFACE PROPERTIES OF THE SATELLITES, HOWETT ET AL. [2010]

We measure surface temperatures by determining the temperature that best match the observed thermal radiation, on the assumption of blackbody radiation. Nighttime temperatures provide the strongest constraints on thermal inertia, and of the icy satellites only Phoebe (due to its low ABB and rapid rotation) has nighttime temperatures warm enough to be detectable by FP3 Flasar et al. [2005a]. The higher wavenumbers detected by FP4 are insensitive to all of the Saturnian icy satellite's passive daytime and nighttime temperatures. This investigation therefore solely uses FP1 data, which is sensitive to both daytime and nighttime radiation from Saturn's icy moons. The

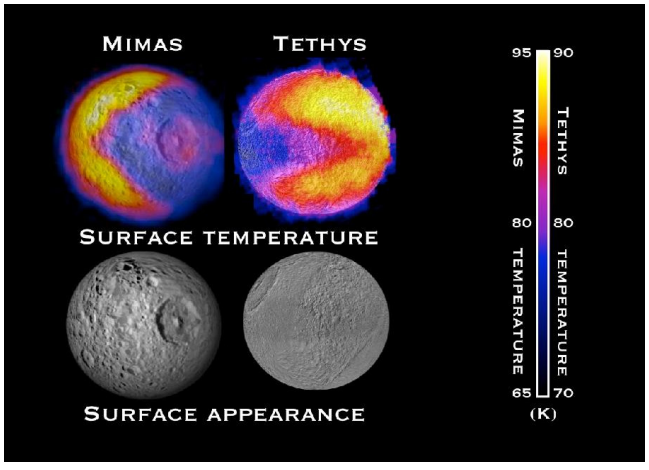

Figure CIRS-54. Summary of the two Pac-Man.

consistency of temperatures derived from FP1 and FP3 observations were spot-checked using selected daytime observations of Rhea and Dione that included near-simultaneous measurements with both detectors. Derived temperature were consistent to within 2–3 K.

The best fitting values for each of Saturn's icy moons is summarized in Table CIRS-8. For Enceladus, the local time coverage of each 10° latitude bin was good enough to constrain the thermal inertia and albedo as a function of latitude between latitude 60° S and 70° N.

Table CIRS-8. Summary of the CIRS derived thermal inertia and albedo for icy satellites in the Saturn system. Table data from Howett et al. [2010].

Target	Bolometric albedo	Thermal inertia (MKS)	Skin Depth (cm)	References
Jovian Satellites				
Io	0.52	70	0.39[c]	Rathbun et al. [2004]
Europa	0.55	70 14 ± 5	0.55[c] 0.01[d]	Spencer et al. [1999] Hansen [1973]
Ganymede	0.32 ± 0.04	70 ± 20 12 ± 3 14 ± 3	0.78[c] 0.01[d] 0.01[d]	Spencer [1987] Hansen [1973] Morrison and Cruikshank [1973]
Callisto	0.2 ± 0.4	50 ± 10 10 ± 1	0.86[c] 0.01[d]	Spencer [1987] Morrison and Cruikshank [1973]
Saturnian Satellites				
Mimas	$0.49^{+0.05}_{-0.14}$	19^{+57}_{-9}	0.54	
Enceladus	0.81 ±0.04	15^{+24}_{-9}	0.51	
Tethys	0.67 ±0.11	9^{+10}_{-4}	0.36	
Dione	0.63 ±0.15	11^{+18}_{-6}	0.53	
Rhea trailing	$0.57^{+0.20}_{-0.26}$	8^{+12}_{-5}	0.50	
Rhea leading	$0.63^{+0.11}_{-0.12}$	9^{+9}_{-5}	0.56	
Iapetus trailing	$0.31^{+0.15}_{-0.17}$	20^{+13}_{-8}	5.22	
Iapetus leading	0.10[a]	$14^{+7^{a}}_{-8}$	3.66	
Phoebe	0.1	20/25[b]		

Latitude bin	Bolometric Bond albedo	Thermal inertia (MKS)
60° N to 70° N	0.76 ±0.06	16^{+17}_{-13}
40° N to 50° N	$0.74^{+0.06}_{-0.04}$	9^{+5}_{-4}
30° N to 40° N	0.77 ±0.05	10^{+10}_{-6}
20° N to 30° N	$0.78^{+0.05}_{-0.04}$	12^{+15}_{-7}
10° N to 20° N	0.75 ±0.03	17^{+10}_{-7}
0° to 10° N	$0.79^{+0.04}_{-0.05}$	25^{+25}_{-14}
10° S to 0°	$0.78^{+0.03}_{-0.02}$	25^{+22}_{-12}
20° S to 10° S	$0.81^{+0.03}_{-0.05}$	18^{+21}_{-9}
30° S to 20° S	$0.81^{+0.05}_{-0.06}$	20^{+19}_{-12}
40° S to 30° S	$0.82^{+0.02}_{-0.03}$	26^{+12}_{-13}
50° S to 40° S	$0.79^{+0.02}_{-0.01}$	40^{+10}_{-18}
60° S to 50° S	$0.80^{+0.03}_{-0.04}$	27^{+13}_{-20}

Accurate determination of the endogenic south polar heat flow from Enceladus [Spencer et al. 2006] requires subtraction of the passive component from the total thermal emission, making knowledge of the thermophysical properties of Enceladus, and their latitudinal variation, particularly important. The CIRS observations previously used to determine the global surface properties between 60° S and 70° N were separated into 10° latitude bins and the same analysis techniques as previously described were applied to each bin. The number of high resolution spectra available between 50° N and 60° N and north of 70° were not high enough to allow the albedo and thermal inertia to be adequately constrained.

However, the bolometric Bond albedos and thermal inertias of Mimas, Enceladus, Tethys, Dione, the leading and trailing hemisphere of Rhea, and the trailing hemisphere of Iapetus have been determined. The diurnal curves derived using these values provide good fits to the calculated black body temperatures fits to the CIRS spectra. The bolometric Bond albedo of the leading side of Iapetus is too low to accurately determine a value; however, an upper limit is found and the local time coverage is adequate to determine its thermal inertia. The thermal inertia of all of Saturn's icy satellites is shown to be less than half that of the Galilean satellites, implying less consolidated and more porous surfaces, perhaps partially due to the limited mobility of water ice on the Saturnian satellites due to their low temperatures compared with the Galilean satellites, or to a surface coating of E-ring particles. The latitudinal variation in the thermal inertia of Enceladus implies the surface becomes more consolidated towards the southern pole, whereas the higher albedo in the southern hemisphere implies a cleaner surface, perhaps due to plume fallout. Further work investigating the hemispheric bolometric Bond albedo asymmetries of Dione would be valuable, as although the globally averaged values derived here provide a good fit to the CIRS data, observations of viable wavelength have observed notable differences between the leading and trailing hemispheres [Buratti and Veverka 1984].

MIMAS, HOWETT ET AL. [2011B]

CIRS day- and nighttime observations of Mimas taken in rev 126 and 139 are shown in Figure CIRS-55. Both the orbit 126 and 139 maps show a V-shaped boundary, sharp at CIRS resolution, separating warmer and cooler temperatures. The apex of the V is at 0° N and 180° W, and the boundary extends in a northeasterly and southeasterly direction, during orbit 144 indicates the eastern edge of the thermal anomaly is near 0_ longitude. The region east of the boundary, on Mimas' leading hemisphere, is colder than its surroundings in the orbit 126 daytime observations, but is warmer than its surroundings in the orbit 139 nighttime and early morning data. This region thus displays much smaller-amplitude diurnal temperature variations than regions to the west, north, and south, which show thermal behavior more typical of other Mimas longitudes and most of the surfaces of Mimas' neighboring satellites, Tethys, Dione, and Rhea [Howett et al. 2010]. Thus, we refer to the region east of the boundary, on the anti-Saturn hemisphere, as the thermally-anomalous region.

Overlaid on Figure CIRS-55 are new estimates of the energy flux of MeV electrons bombarding Mimas, updating those given in Schenk et al. [2011]. Because energetic electrons in Saturn's magnetosphere drift in a retrograde direction relative to corotation they preferentially

bombard Mimas' leading hemisphere. Notable improvements in the new model include the use of additional data from the LEMMS on Cassini's MIMI (several-year averages were used) and the introduction of data from the channel E7 on LEMMS. The E7 channel is the highest energy electron channel on LEMMS and adding these data modifies the spectral slope at high energies, which turns out to be very important for the behavior of the contours particularly away from the equator. Further details on the mission averaged electron data are given in Paranicas et al. [2012, 2014].

The thermal anomaly is closely correlated spatially with an IR/UV (0.930/0.338 lm) color ratio anomaly previously observed in global maps of Mimas using Cassini ISS data. An updated version of the global IR/UV map of Mimas, originally given in Schenk et al. [2011], is shown in Figure CIRS-55. Though there are some inconsistencies in the latitudes and longitudes of features on the two maps, the location of the thermal and color anomalies can be compared by reference to craters near the anomaly boundaries appearing on both maps (red circles, Figure CIRS-55).

Figure CIRS-55 boundaries of the thermal and color anomalies appear to be nearly identical, although the apex of the thermal anomaly appears sharper. In the absence of endogenic emission, surface temperatures are controlled by surface bolometric Bond albedo and thermal inertia. A surface's thermal inertia describes how well it is able to store and release thermal energy. To investigate the cause of the anomalous temperatures seen by CIRS we determine albedo and thermal inertia for two representative regions, one outside and another inside the anomaly (shown by the boxes in Figure CIRS-55). The surface temperature for each of the two regions in orbits 126 and 139 was determined by fitting a single blackbody curve to the mean CIRS FP3 spectra of all the observations taken of that region. Following the example of Spencer et al. [2006], the spectral noise was estimated using the difference between a blackbody emission spectra. These two steps are repeated numerous times and the temperature error estimate is given by the standard deviation of the temperatures whose best able to fit the created spectra.

The ranges of bolometric Bond albedos capable of fitting the data outside and inside of the anomaly overlap: 0.49–0.70 and 0.56–0.62 respectively. This is consistent with the lack of a noticeable albedo boundary in visible-wavelength images. These albedos are comparable in value with those observed on Tethys, Dione and Rhea. As expected, it is the thermal inertias that vary significantly: <16 J m^2 K^{-1} $s^{-1/2}$ outside the anomaly (these units henceforth referred to as MKS) and 66 ±23 MKS within it. The low thermal inertias outside of the anomaly are similar to those observed on Tethys, Dione and Rhea [Howett et al. 2010], whilst those inside the anomaly are greater than but more comparable with values observed on the icy Galilean satellites. The higher thermal inertias inside the anomalous region indicate that the surface there is less porous and/or has a higher thermal conductivity.

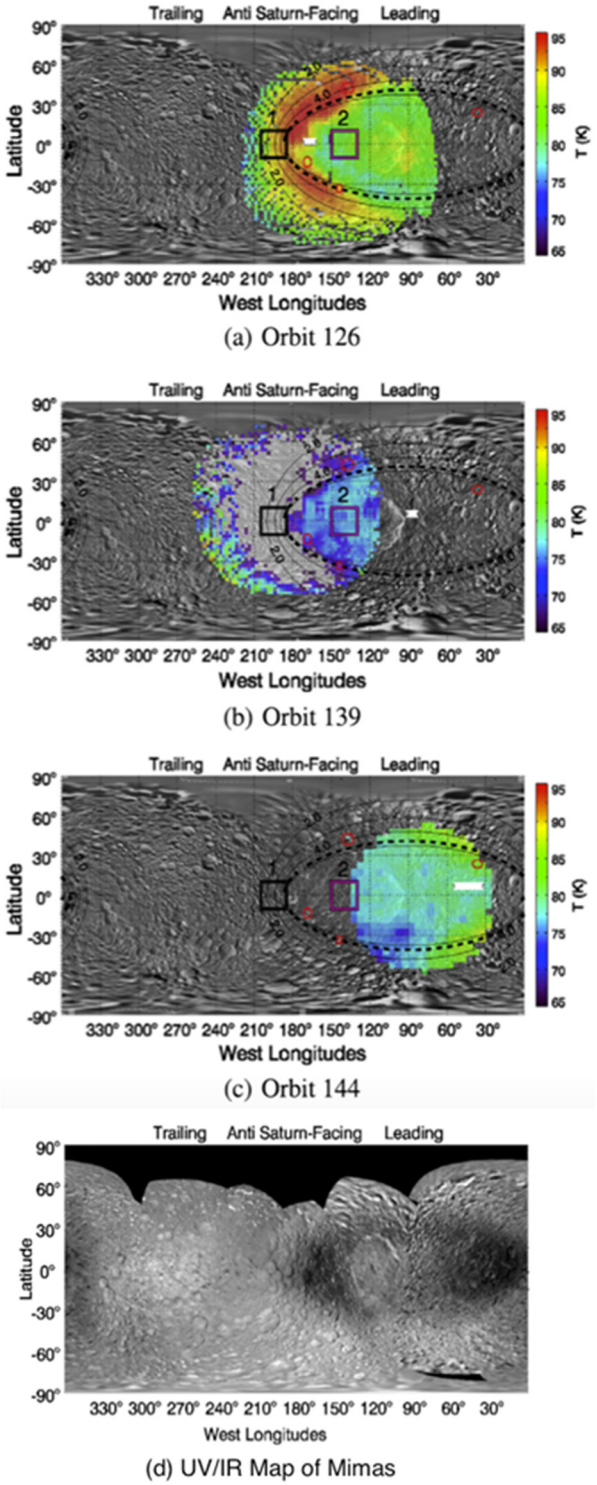

Figure CIRS-55. CIRS day- and nighttime observations of Mimas. *Panel (a)*: Orbit 126 daytime surface temperatures. *Panel (b)*: Orbit 139 nighttime surface temperatures of Mimas. *Panel (c)*: Orbit 144 daytime surface temperatures. *Panel (d)*: IR/UV (0.930/0.338 lm) color ratio map of Mimas' surface determine from Cassini ISS data.

The close spatial correlation of the thermal and IR/UV color ratio anomalies suggests a common origin. It has been proposed that high-energy (MeV) electron bombardment of Mimas' surface is responsible for the observed IR/UV color ratio variation [Schenk et al. 2011]. Plasma corotates with the planet and thus flows around Saturn in a prograde sense, overtaking Mimas in its orbit and impacting its trailing hemisphere. However, electrons with energies above about 1 MeV flow retrograde with respect to Mimas. Their north–south motion is much faster than their longitudinal motion and these electrons therefore bombard the moon close to its leading equator. The impact patterns are represented by lens-shaped contours of energy deposition very similar in shape to the color and thermal boundary (Figure CIRS-55). The color boundary at Mimas corresponds to an electron energy deposition rate contour of about 5.6×10^4 MeV cm^2 s^{-1} [Schenk et al. 2011]. The contour corresponding to the boundary of the thermal anomaly is harder to determine due to its poorer spatial correlation, however it appears to be similar to that of the color anomaly.

TETHYS, HOWETT ET AL. [2012]

In September 2011 (during Cassini's orbit 153) CIRS obtained a daytime medium-spatial resolution observation (the average resolution was 84 km/pixel) of Tethys' leading hemisphere. FP3 was used for these observations since it provides the best compromise between sensitivity to thermal radiation and spatial resolution for daytime observations of icy satellites. These observations were at a significantly better spatial resolution than the previous best thermal map of this hemisphere, a nighttime map obtained in June 2007 (Cassini's orbit 47; 150 km/pixel) using FP1. The lower spatial resolution FP1 is the only CIRS detector sensitive to the cool nighttime surface emission of Saturn's icy satellites; therefore, spatial resolution differences in the night-day-time coverage with CIRS are common. Combination of the orbit 47 and orbit 153 observations provides sufficient local time coverage to constrain surface albedo and thermal inertia.

The results, given in Figure CIRS-56, clearly show a thermally anomalous region exists on Tethys' leading hemisphere at low latitudes in both the daytime and nighttime temperatures. The region appears to be ~10 K cooler during the day and ~10 K warmer at night than its surroundings, quite unlike the pattern expected if surface properties were spatially uniform (also shown in Figure CIRS-56), with largest thermal contrast occurring at the northern anomaly boundary, particularly towards the east. The thermally anomalous region is lens-shaped with apexes at 0° W and 180° W, and is widest in the center of the leading hemisphere (90° W) reaching latitude ±20°. This anomalous region spatially coincides with a dark (low) albedo region at low latitudes on Tethys' leading hemisphere was first observed in Voyager data [Stooke 1989, 2002]. Photometry applied to Cassini ISS images showed the band to be 2–3% brighter in the NAC CL1-UV3 filter (338 nm) and 8% darker in the NAC CL1-IR3 (930 nm) filter [Elder et al. 2007].

The best-fit bolometric Bond albedo for all three of these regions is remarkably constant: 0.67 ±0.02, whilst the best-fit thermal inertia increases from 5 ±1 MKS outside the anomaly, to 11 ±1 MKS at the western boundary and 25 ±3 MKS inside the anomaly. The values outside the thermal anomaly are comparable to those seen on other Saturnian satellites [Howett et al. 2010]. The derived albedo is also consistent with previous estimates.

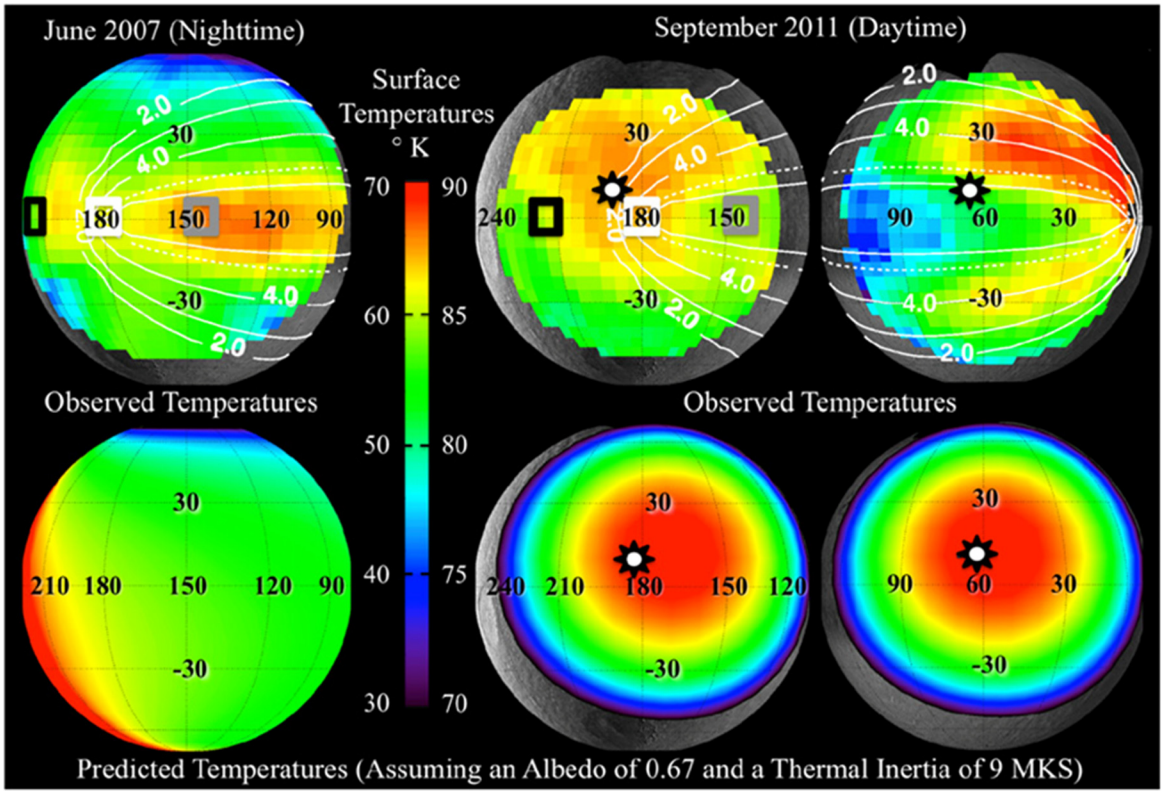

Figure CIRS-56. Tethys' thermal anomaly can be seen by comparing the observed and predicted surface temperatures of Tethys at night (June 2007) and during the day (September 2011). Contours overlaid on the observed temperatures show the predicted electron energy flux onto Tethys' surface, in units of log10(MeV cm^{-2} s^{-1}), with the white dashed line contour representing the best fit electron energy flux contour to the observed surface color alteration (18 GeV cm^{-2} s^{-1}) [Schenk et al. 2011]. The black stars-shapes with the white centers indicate the location of the subsolar point.

The maximum electron energy flux bombarding Tethys is nearly six times lower than that on Mimas and is constrained to a smaller latitudinal extent, consistent with the relative amplitude and shape of the thermal anomaly on the two bodies [Paranicas et al. 2012; Schenk et al. 2011]. The discovery of Tethys' thermal anomaly, which as Figure CIRS-56 shows has a boundary corresponding to an 18 GeV cm^{-2} s^{-1} electron flux (compared to 56 GeV cm^{-2} s^{-1} on Mimas), greatly strengthens the case that energetic electrons are able to significantly alter an icy satellite surface, and also proves that the threshold electron energy flux able to do so is lower than previously thought. A lower energy flux threshold increases the probability that such alteration occurs on other satellite surfaces. Why high-energy electron bombardment would decrease the IR/UV surface color ratio and why the thermal anomalous region appears darker in visible light images of Tethys, but not on Mimas, remains a mystery.

DIONE, HOWETT ET AL. [2014]

Maps of variations in albedo and thermal inertia were derived for Dione, using eight separate CIRS observations taken from 2005 until 2012, which provided both day and nighttime coverage. Figure CIRS-57 shows the thermally-derived bolometric Bond albedo variation across Dione. The map shows that the bolometric Bond albedo of Dione's trailing hemisphere (0.39 ±0.13) is much darker than its leading hemisphere (0.49 ±0.11). The disk-integrated value (0.44 ±0.13) is consistent (to within error) of previously determined values: 0.52 ±0.08 Pitman et al. [2010] and 0.63 ±0.15 Howett et al. [2010]. The trailing/leading hemisphere albedo trend has been previously observed on Dione from visible-wavelength observations (e.g., in the geometric albedo map by Blackburn et al. [2012]) and, as noted in the introduction, is thought to be due to the preferential bombardment of Dione's leading hemisphere by E-ring particles [Hamilton and Burns 1994], which plausibly cause surface brightening [Verbiscer et al. 2007].

Dione displays a different trend in its thermal inertia, which is highest at low latitudes on its leading hemisphere. Between 30° S and 30° N, 180° W and 360° W, the mean thermal inertia is 8 MKS, while between the same latitudes and 30°–150° W, the mean thermal inertia is 11 MKS.

As noted above, Mimas and Tethys display similar anomalies [Howett et al. 2011b, 2012]. However, on Dione the magnitude of the thermal inertia increase is too subtle for its effect to be easily observed in maps of the surface temperature (unlike on Mimas and Tethys). Nonetheless, the inference of high thermal inertia in these regions becomes clear when diurnal temperature curves are compared with Dione's observed surface temperatures; the lower thermal inertia value (8 MKS) is unable to fit Dione's leading hemisphere's higher nighttime temperatures. Diurnal temperatures probe thermophysical properties over a range given by the thermal skin depth, which for these thermal inertias is 0.4–0.6 cm (assumptions as in Howett et al. [2010]). The location of Dione's higher thermal inertia region is spatially correlated with the region preferentially bombarded by high energy electrons. This is the same trend that is observed on Mimas and Tethys. On Mimas E-ring grain particles bombard opposite hemispheres, while on Tethys (and Dione) they both bombard the leading hemisphere. The similarity between Mimas' and Tethys' thermal anomalies (their location on the leading hemisphere and strong spatial correlation to the region preferentially bombarded by high-energy electrons) provides a compelling argument for them having the same formation mechanism, which on Mimas cannot be E-ring grain bombardment. Thus, it is concluded that surface alteration by high-energy electrons is the dominant process on Tethys, and by extension, the same is likely on Dione.

The magnitude of the thermal inertia difference between the background and inside the thermal anomaly is greatest on Mimas and then decreases from Tethys to Dione. However, on Dione the thermal anomalous region does not appear to be spatially correlated with a decrease in the IR/UV albedo ratio as it is on Mimas and Tethys, which suggests either that the surface alteration on Dione is below the threshold for UV darkening to occur or that the color change is too subtle to be detected. No such anomaly is observed on Enceladus, presumably due to its high resurfacing rates.

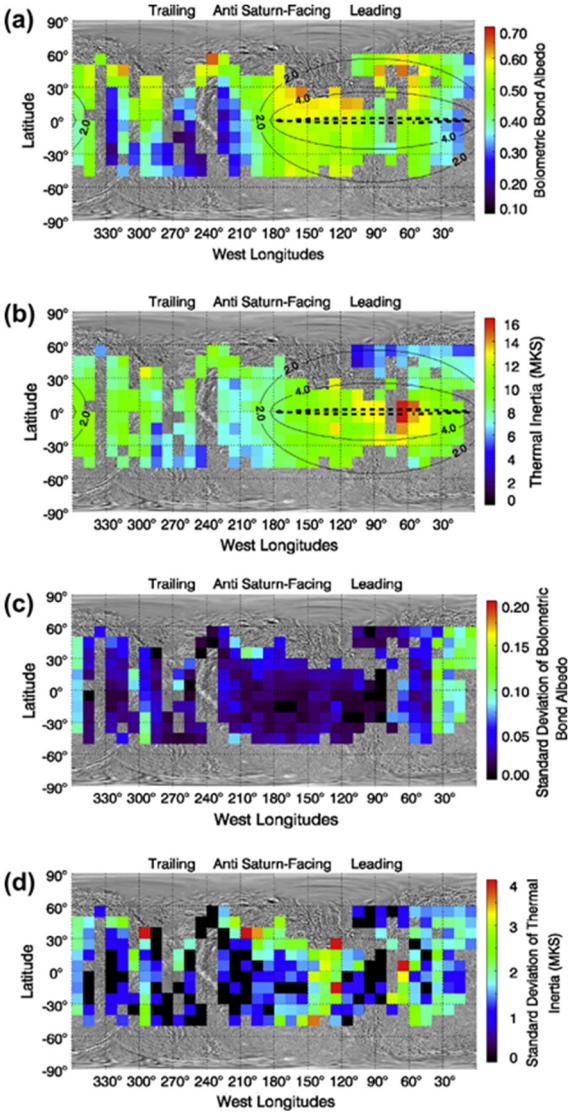

Figure CIRS-57. Maps of derived thermophysical properties for Dione. *Panel (a)*: Bolometric Bond albedo map of Dione. Overlaid are contours of energetic electron power deposited into the surface per unit area (log10 MeV cm^2 s_1). *Panel (b)*: Thermal inertia map of Dione. Overlaid are contours of high-energy electron flux, see the description in *Panel (a)* for details. *Panel (c)*: The standard deviation of the bolometric Bond albedo values given in *Panel (a)*. *Panel (d)*: The standard deviation of the thermal inertia values given in *Panel (b)*.

RHEA, HOWETT ET AL. [2014]

Maps of variations in albedo and thermal inertia were derived for Rhea, using eight separate CIRS observations taken from 2005 until 2012, which provided both day and nighttime coverage. The bolometric Bond albedo and thermal inertia maps of Rhea are given in Figure CIRS-58. Two trends are obvious in the maps: the trailing hemisphere of Rhea is somewhat darker and there is a region of high thermal inertia centered on 110° W, 20° S. Rhea's hemispherical albedo pattern has been previously observed directly at visible wavelengths—for example, Verbiscer and Veverka [1989] and via thermal observations [Howett et al. 2010]. The bolometric Bond albedo maps give a disk-integrated value of 0.58 ±0.12, and leading and trailing hemisphere value of 0.59 ±0.11 and 0.56 ±0.13, respectively. Within error these results agree with the literature values: 0.48 ±0.09 disk-integrated Pitman et al. [2010]; 0:63 (+0.11, −0.12) leading hemisphere Howett et al. [2010]; 0:57 (+0:20, −0:26) trailing hemisphere Howett et al. [2010].

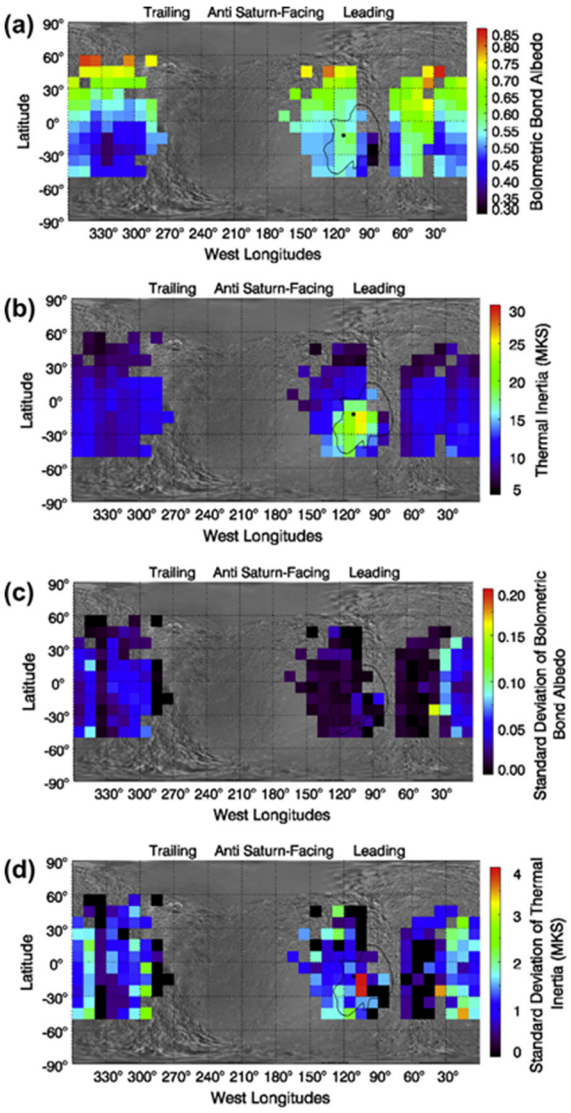

Figure CIRS-58. Maps of derived thermophysical properties for Rhea. The black solid contour shows the approximate edge of the Inktomi ejecta blanket, while the dark circle at 14.1° S and 112.1° W shows the location of the Inktomi crater. *Panel (a)*: Bolometric Bond albedo map of Rhea. *Panel (b)*: Thermal inertia map of Rhea. *Panel (c)*: The standard deviation of the albedo values given in *Panel (a)*. *Panel (d)*: The standard deviation of the thermal inertia values given in *Panel (b)*.

The high thermal inertia region in the southern hemisphere of Rhea's leading hemisphere is a new discovery. The anomalous region does not bear the characteristics of the high thermal inertia regions observed on Mimas, Tethys, and Dione (described in Howett et al. [2011b, 2012, 2014] for Mimas, Tethys and Dione respectively), and Rhea does not display a darkening on this hemisphere in the IR/UV associated with Mimas and Tethys' thermally anomalous region. Rather the thermally anomalous region on Rhea appears to be spatially correlated with the ejecta blanket of Rhea's bright ray crater, Inktomi. Here the thermal inertia increase is more dramatic than on Dione: the background value (the mean value from 30° to 60° W and 10° to 30° S) is 10 MKS, whilst the value on the Inktomi crater ejecta blanket (the mean value between 100° and 120° W, and 10° and 30° S) is 19 MKS. Craters floors with a high thermal inertia compared to the background value have been observed on Mars—for example, Edwards et al. [2013], and the Moon [Bauch et al. 2011], but this is the first time such change in thermal inertia has been observed over a crater on an icy saturnian satellite. This range of thermal inertias corresponds to a thermal skin depth of 0.7–1.3 cm.

Activity on Dione (IN1c), Howett et al. [2018]

IN1c: Determine whether Dione is currently active, or has been so on recent geological timescales.

There are hints that maybe activity does occur on Dione: Dione has smooth plains (indicative of recent resurfacing). Plasma was detected flowing from Dione, which could have been caused by recent geological activity [Burch et al. 2007], although this can also be explained without activity.

FP1 Cassini CIRS data to make nighttime temperature maps of Dione's surface, and model temperature maps were produced by modeling Dione's seasonal temperature change (using previously published thermal inertia and albedo values from Howett et al. [2014]): thermal inertia: 5, 11, and 29 MKS, and albedo values: 0.48, 0.63, and 0.78. Then observed versus modeled temperatures were compared, and temperatures outside of the expected range were looked for. The results are shown in Figure CIRS-59, which shows that for this preliminary example no temperatures are observed outside of those predicted by a passive emission model. When this is repeated for all nighttime CIRS FP1 and FP3 observations of Dione no evidence for activity was found. Therefore, we conclude that there is no evidence in CIRS observations of Dione for activity, and upper-limits of undetected activity have been placed. These results were published in Howett et al. [2018].

The maximum temperature of a 50, 100 and 200 km^2 hot spot is then derived using the highest resolution observation at a given location. The results are shown in Figure CIRS-60.

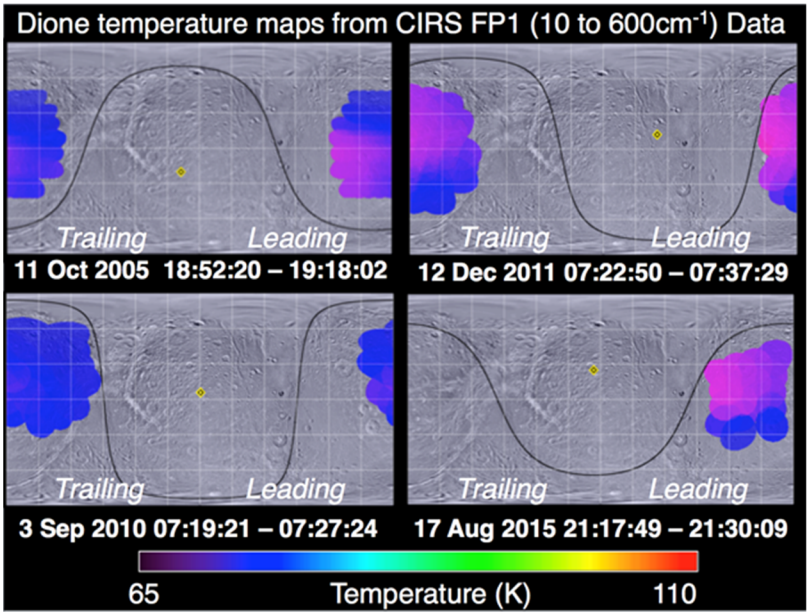

Figure CIRS-59. Comparison of surface temperatures derived from Cassini CIRS FP1 observations to those predicted by a passive emission model.

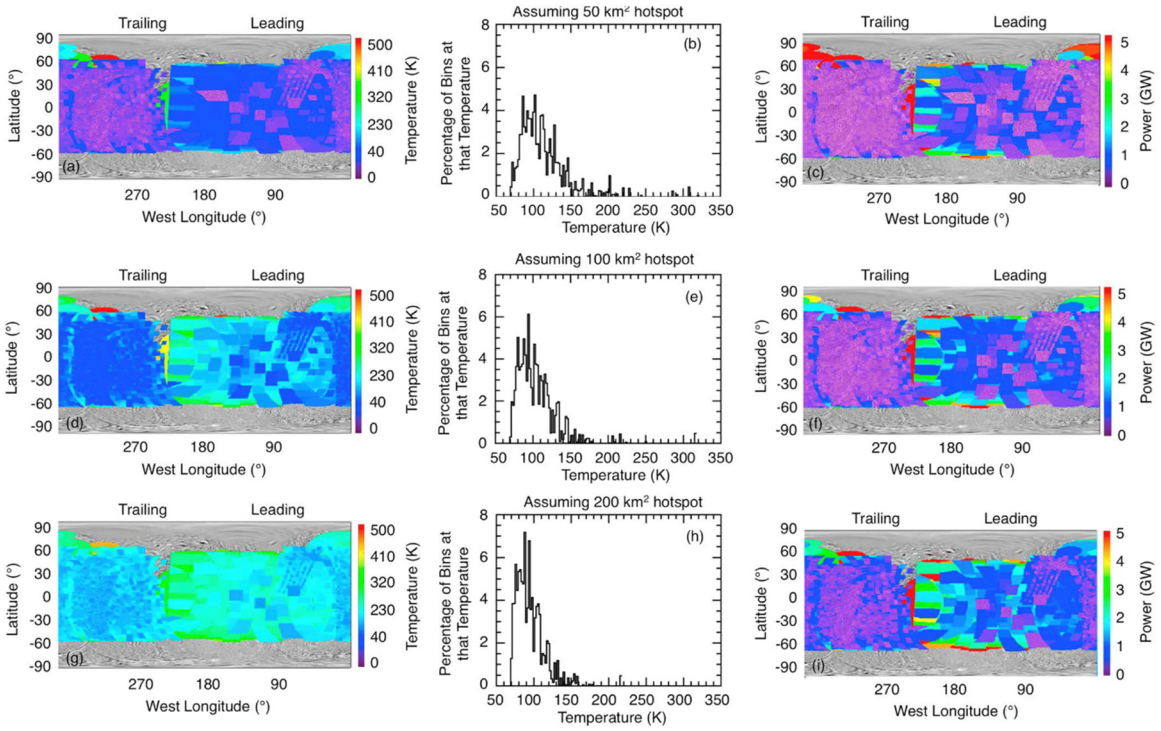

Figure CIRS-60. Details of the upper limits for a 50, 100, and 200 km2 hot spot that could exist on Dione and not be detected in this work. *Panels (a), (d), (g)*: The maximum temperature of a hot spot that could exist on Dione and have remained undetected in this work. *Panels (b), (e), (h)*: The maximum power of a hot spot that could exist on Dione and have remained undetected in this work. *Panels (c), (f), (i)*: Histograms of the maximum temperature a hot spot could have and remain undetected in this study.

Level 2

Rhea's ring (IN2a)

IN2a: Determine if there is a ring (or debris disk) around Rhea, and if so, characterize the spatial and particle size distribution.

ALTERATION OF RHEA'S SURFACE BY INFALL FROM AN ANCIENT RING

Schenk et al. [2011] found blue patches along Rhea's equator, which they believe are evidence for infall from a ring around Rhea. This is because the patches are not associated with any obvious, endogenic tectonic process, as no linear or other tectonic fabric is apparent. Furthermore, a thin ring (or halo) around Rhea was tentatively discovered by Jones et al. [2008] (although this has not been upheld by further observations) [Pitman et al. 2008; Tiscareno et al. 2010].

These patches are small (<1 km), and often well-below the spatial resolution of CIRS thus making them hard to detect. The best estimate of how the surface properties of Rhea vary was

given by Howett et al. [2014], and is shown in Figure CIRS-58. As the figure shows, no obvious change in albedo or thermal inertia is observed along Rhea's equator. We conclude CIRS is unable to contribute to whether infall from an ancient ring around Rhea has altered its surface.

Tethys and the E-ring (IN2b)

IN2b: Determine whether Tethys is geologically active, and thus could be contributing to the E-ring.

Nighttime observations of Tethys have been investigated—see Howett et al. [2012] and this section—and show no evidence for high temperatures expected from activity. Further work is required to set explicit limits on such activity.

Characterize the surfaces of Saturn's small satellites (IN2d)

IN2d: Derive the surface thermophysical properties of Saturn's small satellites, including (but not limited to) Epimethys, Janus, Methone, and Promethus.

CIRS made positive detections of two moons: Epimetheus and Atlas. These results have been submitted as part of a multi-instrument paper [Buratti et al. 2018].

Detections of both Epimetheus and Atlas were made using dedicated CIRS scans bracketed by ISS observations. Epimetheus was detected on January 30, 2017, during a scan that occurred between 19:54:20 to 20:05:50 UTC, at a distance that decreased from 80,179 to 67,237 km. During this time, the sub-spacecraft position changed from 345.0° W / 73.5° N to 346.5° W / 73.7° N, the local time at the sub-spacecraft point increased from 271° to 276° and the phase increased slightly from 68.0° to 68.5°.

Atlas was detected a few months later on April 12, 2017, during a scan that ran from 13:16:39 to 13:24:40 UTC, at a distance that decreased from 33,572 km to 24,580 km. During that time, the phase at the sub-spacecraft point decreased from 51.2° to 47.2°, the sub-spacecraft position changed from 141.9° W / 60.1° N to 149.8° W / 52.1° N, and the local time at the sub-spacecraft point decreased from 226° to 221°.

In both detections, CIRS used its focal plane 3 (FP3, which covers 570–1125 cm^{-1}) to scan the target and background sky. The results are given in Figure CIRS-61, which shows the temperature that has a blackbody emission curve best able to fit the observed radiance over all wavelengths. Both Epimetheus and Atlas are clearly visible above the background dark sky. The mean surface temperature observed on Epimetheus is 90.1 ±2.7 K, and 82.4 ±4.7 K on Atlas.

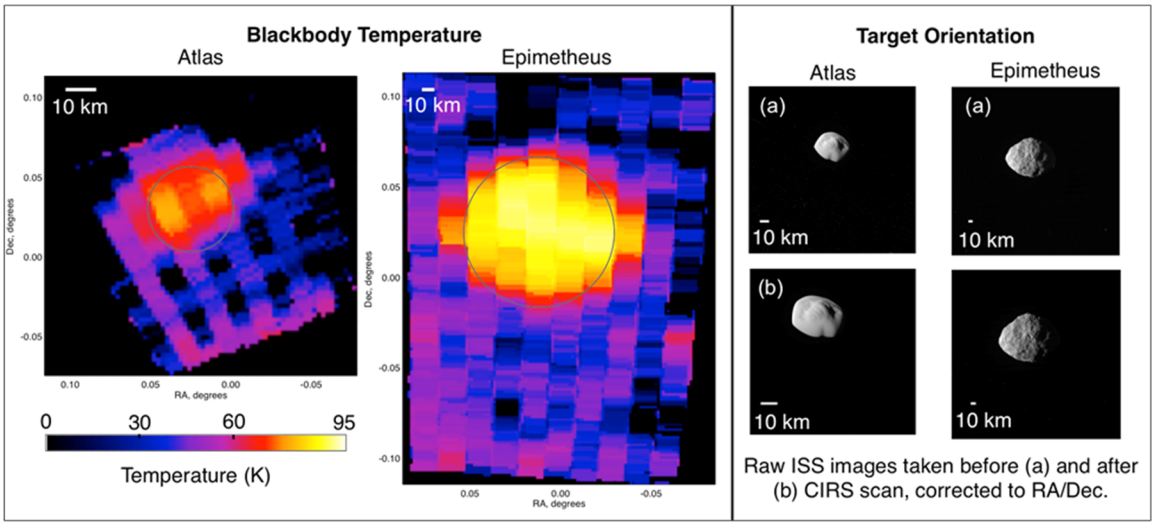

Figure CIRS-61. CIRS and ISS observations of Atlas and Epimetheus. *Left*: The blackbody temperature of the two targets, as determined by fitting a blackbody curve to the full CIRS radiance spectrum at each location. The results are shown in Right Ascension/Declination (RA/Dec) space, which has been corrected so the center of the target lies at 0°/0°. *Right*: Raw ISS observations of both targets taken before and after the CIRS scan, the images have been rotated so they are also in RA/Dec coordinates. However, the scale of the CIRS data and the ISS images is notably different, as indicated by the 10 km scale bar given in every image. Images of Atlas *Panel (a)*: ISS image N00279648 taken using CL1 and CL2 filters on April 12, 2017, at 1:15 UT; *Panel (b)*: ISS image N00279649 taken using CL1 and CL2 filters on April 12, 2017, 1:27 UT. Images of Epimetheus *Panel (a)*: ISS image N00275708 taken using CL1 and CL2 filters on January 30, 2017, 7:53 UT; *Panel (b)*: ISS mage N00275709 taken using CL1 and UV3 filters on January 30, 2017, 8:07 UT.

Open Questions

Saturn

- Exactly how does tropospheric eruption of the great storms perturb the stratosphere so strongly? Presumably by waves generated near the tropopause, but what is the nature of these nonlinear waves?
- What are the waves driving the equatorial oscillation, compared to those identified as drivers for Earth's equatorial oscillations?
- What are the systematic errors affecting the different estimates of the helium abundance from remote sensing techniques (thermal infrared spectra, thermal infrared and radio occultations, thermal infrared and ultraviolet stellar occultations)?
- How important is interannual variability?
- Geophysical systems are complex, nonlinear, and their behavior can be difficult to understand or predict. Cassini, given its proximity and duration, provided us a unique 4-dimensional slice of Saturn. When can we go back?

Rings

Some key open questions on rings are listed below. Other CIRS-specific questions are discussed in the Conclusions and Future Work.

- Why is the ring thermal inertia so low?
- What is the internal structure of ring particles?
- How does the thermal inertia vary with radial distance from Saturn?
- What will even higher spatial resolution data tell us about radial and azimuthal thermal variations in Saturn's rings?
- At higher spatial resolution, which ring regions exhibit a thermal surge and which do not?
- Are there spectral signatures of compounds other than water ice in infrared spectra?
- What are the thermal properties of the faint rings (D-ring, E-ring, G-ring, Phoebe ring) and ringlets (A-ring/Encke gap, F-ring)?
- Do the thermal properties of rings with clumps (A-ring/Encke gap, F-ring, G-ring, E-ring) vary with time?

Titan

- What is the nature of the 220 cm^{-1} absorber?
- How high in altitude does the stratospheric/mesospheric circulation extend?
- Does Titan have a well-defined mesopause?
- Are the nitriles CH_3CN, C_2H_3CN and C_2H_5CN, already seen at sub-mm wavelengths, detectable in the infrared with sufficiently high resolution?
- What functional groups are causing the aerosol absorption features in the mid-IR?
- What is mechanism driving the tilted stratospheric pole?
- How is stratospheric super-rotation generated and maintained?
- What is the link between gas chemistry and aerosol production, and are the abundances anti-correlated?
- Are there condensate clouds of homogenous composition, or are all clouds co-condensates?
- Can we make inferences about Titan's methane history from isotopic ratios?
- Why is the $^{15}N/^{14}N$ much higher in HCN than in N_2?

- Do the abundances of H_2 and CH_4 vary with latitude?
- Are there oxygen bearing molecules beyond CO, CO_2 and H_2O?

Icy satellites

Mimas

- Is there evidence on Mimas' trailing hemisphere for surface alteration due to (low) energy electron bombardment?

Enceladus

- Does the thermal emission of Enceladus' tiger stripes increase over the jet positions predicted by Helfenstein and Porco [2015]?
- Does the thermal emission of Enceladus' tiger stripes show any temporal variability, both in the short-term (with mean anomaly) and long-term (decadal)?
- Are there any more small-scale hot spots?
- Is there any evidence for a thermal anomaly in the location of the radar ones—for example, Le Gall [2017]; Ries et al. [2015]?
- Is there any evidence for a change in thermophysical properties in plume fallout regions?

Tethys

- How does the thermophysical properties vary across Tethys' trailing hemisphere?

Dione

- What is the lower limit of activity on Dione?
- Does the Creusa on Dione show a lower thermal inertia than its surroundings (like Inktomi on Rhea)?
- How do the thermophysical properties of Dione's surface change across its wispy terrain?

Rhea

- What are the thermophysical properties of Rhea's anti-Saturn hemisphere?

Iapetus

- How does the thermal inertia of Iapetus' dark and light terrain vary?

Other Questions

- Can we say anything useful about the surface properties of Saturn's other icy moons?
- What can we learn by combining data sets?
- Is there other evidence of emissivity signatures in the CIRS data?

CIRS Non-Saturn Science Results

Jupiter

Formation and evolution

D/H

See the section entitled Saturn isotopes.

N^{15}/N^{14}

Fouchet et al. [2004a] used large averages of mid-infrared CIRS spectra at the highest apodized resolution (0.5 cm^{-1}) to isolate the weak $^{15}NH_3$ lines from the forest of strong $^{14}NH_3$ lines. The averages were segregated into latitude bins. They found no measurable variation with latitude. The mean global value ($(2.22 \pm 0.52) \times 10^{-3}$) agreed with previous measurements obtained from the Infrared Space Observatory and from the Galileo Probe Mass Spectrometer. They interpreted these values as representative of the proto-solar value. The terrestrial value is a factor nearly 1.7 larger, which they interpreted as originating in a reservoir isolated from the main reservoir of the proto-solar nebula. Abbas et al. [2004] independently analyzed comparable data sets and obtained essentially the identical result for the global average.

Atmospheric gas composition

Disequilibrium Tropospheric Compounds

Phosphine. As noted earlier for Saturn, PH_3 is generally believed to be a product of rapid vertical mixing from deep atmospheric levels, and the observed abundances in the upper troposphere

represent the quenched equilibrium conditions deeper down. Irwin et al. [2004] analyzed CIRS mid-IR spectra over the ranges 600 and 700 cm^{-1} and 1000–1200 cm^{-1} to retrieve jointly the temperature profile, the deep phosphine abundance (~1 bar), the deep ammonia abundance and fractional scale height, and the total cloud (or haze) opacity. They found PH_3 to be greatest within the equatorial zone, indicating upward transport, and smaller within the north and south equatorial belts. The mid latitudes seem to be asymmetric, with PH_3 larger near 40° N at the corresponding latitude in the south. The cause of this is not understood. PH_3 was also enhanced over the Great Red Spot, consistent with upwelling there. Using a more extended spectral range and consideration of tropospheric clouds and aerosols, Fletcher et al. [2009] verified the equatorial enhancement and hemispheric asymmetry. They found Jupiter's mid-IR spectrum is best reproduced by a dual-cloud model, with a compact 10 μm NH_3 ice layer existing at the predicted condensation altitude, and a deeper source of gray opacity (possibly due to NH_4SH clouds). They also found that Jupiter's infrared aerosol opacity is elevated at the equator and within other zones.

Halides. Fouchet et al. [2004b] analyzed CIRS far-infrared spectra to place upper limits on the abundances of HF, HCl, HBr, and HI. The upper limits on the first two were sufficiently small to lie well below solar abundances and support the notion of the halogens' condensation in ammonium salts predicted by thermochemical models for the upper Jovian troposphere.

DISEQUILIBRIUM STRATOSPHERIC COMPOUNDS

Ethane and Acetylene. The thermal infrared spectrometers (IRIS) on the Voyager spacecraft provided meridional profiles of C_2H_6 and C_2H_2, but with limited sensitivity and spatial resolution. Even at a swing-by distance ~138 RJ CIRS vastly improved the latter, and had much better sensitivity. Kunde et al. [2004] found that the latitude profile of C_2H_6 was relatively flat, whereas that of C_2H_2 followed the insolation pattern. The former pattern could be explained if the meridional transport is much faster than the loss of C_2H_6 by vertical mixing (~100 years). That of C_2H_2 suggested that its distribution is mostly governed by local photochemistry with a lifetime of ~1 year. Kunde et al. [2004] concluded that the different distributions would be expected if the dynamical timescale for horizontal transport was between the lifetimes of these two gases, ~10 years.

Kunde et al. [2004] used the emission intensities of C_2H_6 and C_2H_2, relative to the adjacent continuum, as surrogates for the abundances. They corrected for airmass variations using a model of limb brightening. Nixon et al. [2007] noted that the assumption that relative abundance variations with latitude will not, in general, proportionally follow the relative variations of the line intensities, because it ignores the saturation that can occur in the stronger emission lines. As a result, the actual abundance variations are somewhat greater than the intensity analysis would suggest. Nixon et al. [2007] retrieved C_2H_6 and C_2H_2 from the CIRS mid-infrared spectra using a rigorous inversion scheme. They found that the observed spectral emission from C_2H_6 and C_2H_2 was the combination of stratospheric emission, with a peak contribution at ~5 mbar, and tropospheric absorption at 100-400 mbar. For acetylene, they found: (i) the stratospheric volume mixing ratio (VMR) at 5 mbar decreases sharply from a peak around 20° N towards both poles, by a factor ~4; (ii) the northern hemisphere stratosphere is apparently enriched compared to the southern hemisphere at the time

of observation; (iii) in the upper troposphere at 200 mbar the abundance is near constant at ~3 × 10^{-9}. For ethane, the VMR in the equatorial stratosphere at 5 mbar is around 4 × 10^{-6}, in line with previous findings; and increases by factors of ~1.75 to 70° N and ~2.0 to 70° S. The tropospheric VMR at 200 mbar shows similar increases. Nixon et al. [2010a] redid their retrievals using improved modeling of the instrument spectral resolution, and a more recent and improved line list for C_2H_6. They found little change in the meridional distribution of C_2H_2, but found observable changes in the C_2H_6, mainly attributable to the newer line list used. They then analyzed Voyager IRIS spectra from the Jupiter flyby in 1979 (northern fall equinox) and compared the resulting distributions with those from CIRS in 2000 (northern summer solstice). They found the 2-D distribution of ethane was quite similar for the two epochs, although the Cassini distribution was more symmetric than that of Voyager, where C_2H_6 was somewhat depleted in the north relative to the south. Also, the Cassini abundances were mostly higher overall, perhaps because the solar distance was smaller. Acetylene exhibited a much more dramatic change, having a uniform meridional profile at equinox, but strong depletions towards both poles at solstice. The solstice distribution seemed to match the annual-mean picture that would be predicted by a 1-D photochemical model.

HCN and CO_2. The Cassini swing-by also facilitated the mapping of HCN and CO_2 [Kunde et al. 2004]. Both species were thought to be products of the impact of the comet SL9 in 1994, near 45° S. However, observed distributions in latitude were markedly different. HCN exhibited a broad distribution with a maximum near 45° S, a steep fall-off poleward, and a smooth decrease northward to 60° N. The CO_2 profile, however, was much narrower, and its maximum lay southward of 60° S, decreasing abruptly northward of 50° S. Kunde et al. [2004] suggested that the sharp decrease in HCN could result from the inhabitation of horizontal wave-induced diffusion by the south polar vortex. The difference in the meridional distribution of CO_2, compared to that of HCN, particularly at southern latitudes, indicated that it might have other sources in addition to the SL9 impact, and the authors suggested that the precipitation of energetic oxygen ions in the southern auroral regions might be important. Another possibility is that HCN and CO_2 are located at different altitudes. The abundances of both species are so low that their emission features are optically thin; that only restricts their altitude range to be in the stratosphere. Lellouch et al. [2006] revisited the issue, considering various scenarios for transport by eddies and mean meridional circulations. They suggested that the meridional distributions were consistent with HCN and CO_2 residing at different altitudes, with the latter being at the 5-mbar level or lower, and HCN ~3 scale heights higher. However, this possibility is not exclusive, and the enigma remains.

Auroral compounds: C_4H_2 and CH_3. Two new stratospheric species were discovered on Jupiter by CIRS during the 2000-2001 flyby: methyl (CH_3) and diacetylene (C_4H_2) [Kunde et al. 2004]. Diacetylene had previously been detected on Titan, but the detection of the methyl radical marked a first for the solar system. These were detected at 606 cm^{-1} (methyl) and 628 cm^{-1} (diacetylene) on FP3 in both northern and southern hotspots using unapodized data at a resolution of 0.26 cm^{-1}. Simulations were able to replicate the spectral detections, but due to uncertainties in the non-LTE temperatures of the emissions, abundances were not determined.

Clouds and aerosols

Ammonia ice. Thermochemical models suggest that Jupiter's visible cloud deck is composed of ammonia but spectroscopic proof has been difficult to obtain. Ammonia ice can be identified by two infrared absorption features: the ν_3 absorption band (N–H stretch) at 2.96 μm (3376 cm^{-1}) and the ν_2 absorption band (N–H bend) at 9.46 μm (1057 cm_{-1}). The NH_3 ice features cannot be detected from the ground because of telluric CO_2 and H_2O absorption at 3 μm, and terrestrial ozone absorption at 10 μm. Attempts to use mid-infrared spectra from the Voyager IRIS to detect the ν_2 NH_3 ice feature were unsuccessful. Wong et al. [2004] did identify the feature in CIRS spectra, by taking the difference in brightness temperatures, T1040–T1060. They found the highest concentrations of ice at the equator and near 23° N. At the latter location, their spectral fit required at least two types of cloud particles. The NH_3 ice feature at 1060 cm^{-1} required ~1 μm particles in an extended cloud with a scale height equal to the total gas scale height, while the spectrum from 1125 to 1200 cm^{-1} can be matched by a more compact gray cloud with a scale height 20% of the gas scale height and an optical depth of 5.

A good candidate for the deeper cloud layer is NH_4SH, since it could easily form clouds at pressures lower than the predicted condensation pressure level.

Matcheva et al. [2005] used a narrow spectral window centered at 1392 cm^{-1} to map cloud opacities. At this wavenumber atmospheric absorption from ammonia gas is very weak and uncertainties in the ammonia abundance do not impact the cloud retrieval results. In the absence of clouds, the atmospheric transmission is limited by absorption of H_2 and CH_4, and the optical depth is unity near 1200 mbar. The authors found a large variation in latitude, more or less correlated with the zone-belt structure. Their results imply two distinct cloud layers: (i) an optically thick cloud layer of ammonia ice with a base pressure at about 900 mbar or larger; and (ii) a thinner cloud layer with a cloud base at about 1100 mbar that is seen through the gaps of the ammonia ice cloud layer. A good candidate for the deeper cloud layer is NH_4SH, since it could easily form clouds at pressures lower than the predicted condensation pressure level.

Gaseous NH_3. Achterberg et al. [2006] mapped the zonal-mean NH_3 gas abundance between 400 and 500 mbar as a function of latitude. They found the Equatorial Zone is rich in ammonia, with a relative humidity near unity. The North and South Equatorial Belts are depleted relative to the Equatorial Zone by an order of magnitude. The Great Red Spot shows a local maximum in the ammonia abundance. They found NH_3 abundance to be highly correlated with temperature perturbations at the same altitude. Under the assumption that anomalies in ammonia and temperature are both perturbed from equilibrium by vertical motion, they concluded that the adjustment time constant for ammonia equilibration is about one third of the radiative time constant.

Atmospheric structure and circulation

GLOBAL AND ZONAL MEAN STRUCTURE

The 138 RJ swing-by of Jupiter in December 2000–January 2001 provided the best opportunity to map the temperatures of its stratosphere and upper troposphere since the Voyager flybys in 1979. Despite the large distance, the smaller detectors in the mid-infrared focal planes enabled CIRS to achieve a spatial resolution (2.4° latitude near the equator), exceeding the global-mapping resolution obtained by IRIS on Voyager. Application of the thermal wind equation to the retrieved zonal-mean temperatures provided a meridional cross-section of the mean zonal winds [Flasar et al. 2004b]. As expected from the Voyager IRIS observations, the winds decayed with altitude above the visible clouds. However, near the equator, they began to increase with altitude above the ~20 mbar level, reaching a maximum of ~140 m/s near 4 mbar. This stratospheric jet is comparable to the winds lower in the troposphere, obtained from cloud-feature tracking. The undulating structure in altitude is reminiscent of an equatorial oscillation similar to that on Earth. Orton et al. [1991]—see also Simon-Miller et al. [2006]—had observed a temporal oscillation in equatorial brightness temperatures that was not strictly periodic, but cyclic over 4–5 years. Leovy et al. [1991] pointed out that this was reminiscent of the terrestrial quasi-biennial oscillation in the stratosphere. This is mechanically forced by the absorption of atmospheric waves, and they suggested that a similar mechanism operates on Jupiter. A similar phenomenon exists on Saturn (see the section entitled Equatorial Oscillation).

Potential vorticity (PV) has been extensively used in studies of geophysical fluid flows, because under many conditions it is approximately conserved and can serve as a tracer of motion. Moreover, it figures in several stability criteria. Read et al. [2006] used velocity measurements, obtained from tracking cloud features in Voyager and Cassini images, and thermal measurements obtained from Voyager IRIS and Cassini CIRS observations, to derive the PV associated with Jupiter's zonal-mean atmospheric flow. The profiles show some evidence for a step-like pattern suggestive of local PV homogenization, separated by strong PV gradients in association with eastward jets, though on differing scales in the northern and southern hemispheres. The northward gradient of PV is found to change sign in several places in each hemisphere, and the relationship between PV and the mean zonal flow indicate that the northern hemisphere may be closer to marginal stability with respect to Arnol'd's second stability theorem (see the section entitled Internal Rotation) than the southern hemisphere.

The zonal-mean meridional motion can be inferred from the meridional distribution of hydrocarbons discussed earlier.

Li et al. [2012] analyzed the global thermal emission from Jupiter and its meridional distribution from CIRS and VIMS observations. They found Jupiter's mean effective temperature to be 125.6° K. The hemispheric distribution of emitted power was asymmetric, with the emitted power in the north 3.0% larger than in the south. The distribution in the Voyager epoch was more symmetric. Moreover, the Cassini total power was 4% higher than that from Voyager. The authors

suggest that this difference is attributable to the warming of atmospheric layers around 200 mbar, but the cause of this is not understood.

Waves

Flasar et al. [2004b] examined the zonal structure in the 2000–2001 Jupiter swing-by data to search for planetary-scale waves in the troposphere and stratosphere. They observed structure near the equator, which conceivably could be related to the forcing of the equatorial oscillation, but they also observed a variety of thermal features well away from the equator. In the troposphere long trains of regularly spaced features were observed, and they appeared to be quasi-stationary relative to Jupiter's internal rotation. These types of waves had been observed earlier in Voyager and ground-based observations. The stratospheric thermal perturbations also exhibit regularly spaced zonal features, but they were less confined in latitude. Moreover, there was a tendency for many of the features to drift westward relative to the ambient zonal flow, consistent with Rossby waves, although an unambiguous identification could not be made. At many latitudes, the connection between the tropospheric and stratospheric disturbances was not conclusive, either in wavenumber or in zonal phase velocity.

In a later study, Li et al. [2006] compared wave structure in both the CIRS and Cassini imaging data sets. They identified a quasi-stationary wave in the north equatorial belt as a Rossby wave in both data sets that had a slow westward drift.

Aurora

Flasar et al. [2004b] detected an intense warm region at 1 mbar at high northern latitudes, centered near 65° N, 180° W. This had been extensively observed in infrared ground-based observations; however, the morphology of the spot differs from that of the Jovian aurorae described at ultraviolet, visible, and near infrared wavelengths. Because the spectra were of necessity obtained in the nadir-viewing mode (138 RJ), Flasar et al. [2004b] could not place limits on how much higher in altitude the hot spot extended. They were, however, able to place a lower limit on the altitude, because the hot spot was not visible at the 4 mbar level. From the thermal wind equation, strong anticyclonic winds would be expected to bound the hot spot, with vertical shears ~30 m/s per scale height. Kunde et al. [2004], observed enhanced emission from several hydrocarbons within the northern auroral hot spot, for example, from the Q branch of C_2H_2 at 729 cm^{-1}. They also detected enhanced emission from C_2H_2, albeit weaker, at 75°–85° S (higher latitudes were not well observed) over longitudes spanning 0° to 70° W. They estimated the excess thermal emission from the northern spot to be ~1013 W, about an order of magnitude larger than that expected from far-ultraviolet spectra from precipitating particles. They suggested that Joule heating could be a viable alternative source.

Sinclair et al. [2017] analyzed Jupiter's auroral hot spots, using spectra from IRIS on Voyager 1 and CIRS on Cassini. They attempted to separate the effects of temperature from concentration in the observed enhanced emission from C_2H_2 and C_2H_6 within the spot at mid-

infrared wavelengths. To do this, they retrieved vertical profiles of temperature for the upper troposphere and tropopause region from the 600–625 cm^{-1} and 640–665 cm^{-1} portions of the spectrum (both collision induced absorption regions associated with the S(1) line of H_2 but with the emission features of C_3H_4, C_4H_2 and C_6H_6 omitted) and stratospheric temperatures from 1230-1380 cm^{-1} (CH_4 emission) regions. This leaves a range from ~50 mbar to ~5 mbar where the information content of nadir-viewing spectra is minimal, and temperature profiles must be interpolated. However, as noted above, most of the lateral contrast associated with the aurora occurs above the 4 mbar level. The vertical profiles of C_2H_2 and C_2H_6 were retrieved from their respective emission features at 710–750 cm^{-1} and 770–890 cm^{-1}. The authors conclude that the vertical temperature profiles retrieved from CIRS spectra covering the auroral-related spots indicate the presence of two discrete vertical regions of heating, at the 1 mbar level and at pressures of 10 µbar and lower. They argued that the temperatures at 10 µbar and lower pressures were likely indicative of joule heating, ion drag, and/or electron precipitation, ion-drag and energy released from exothermic ion-chemistry. On the other hand, they concluded that the heating at the 1 mbar level is the result of either a layer of aurorally-produced haze particles, which are heated by incident sunlight and/or adiabatic heating by subsidence within the auroral hot-spot region. Retrievals of indicated that C_2H_2 is enriched but C_2H_6 is depleted in auroral regions relative to quiescent regions. They suggested that the contrast between C_2H_2 and C_2H_6 can be explained by a coupling of auroral-driven chemistry and horizontal advection. Ion-neutral and electron recombination chemistry in the auroral region enriches all C_2 hydrocarbons but in particular, the unsaturated C_2H_2 and C_2H_4 hydrocarbons. Once advected outside of the auroral region, the unsaturated C_2 hydrocarbons are converted into C_2H_6 by neutral photochemistry thereby enriching C_2H_6 in quiescent regions, which gives the impression it is depleted inside the auroral region.

Open Questions

- What is the descending pattern of Jupiter's equatorial oscillation? Is it similar to Saturn's? What are the waves driving the oscillation, compared to those identified as drivers for Earth's?
- What is the nature of the physical process causing the apparent discrepancy of stratospheric HCN and CO_2? Is ion chemistry involving exogenic H_2O important, or are the meridional circulations in the high stratosphere multi-layered?
- Why does Jupiter not exhibit the intense storms disrupting broad latitude bands that are observed on Saturn?

ACRONYMS

Note: For a complete list of Acronyms, refer to Cassini Acronyms – Attachment A.

AO	Announcement of Opportunity
CIA	collision-induced absorption
CIRS	Composite Infrared Spectrometer
CM	circulation model
DISR	Descent Imager/Spectral Radiometer
FOV	field of view
FRPO	F-ring and proximal orbits
FTS	Fourier Transform Spectrometer
GCM	general circulation modeling
GCMS	Gas Chromatograph Mass Spectrometer
GSFC	Goddard Space Flight Center
HCN	hydrogen cyanide
HST	Hubble Space Telescope
HWHM	half-width-half-maximum
IR	infrared
IRIS	infrared spectrometers
ISO	Infrared Space Observatory
ISS	Imaging Science Subsystem
LEMMS	Low Energy Magnetospheric Measurement System
LTE	local thermodynamic equilibrium
MIMI	Magnetospheric Imaging Instrument
MIR	mid-infrared
mrad	microradians
NAC	narrow-angle camera
NAT	nitric acid trihydrate
NSE	northern spring equinox
PPS	Power & Pyrotechnics Subsystem
PV	potential vorticity
QBO	quasi-biennial oscillation
RA/Dec	Right Ascension/Declination
RADAR	Titan Radar Mapper
RS	radio science
SAO	semi-annual oscillation
SCET	spacecraft event time
SNR	signal to noise ratio
SPT	South polar terrain
TM	Traceability Matrix

UV	ultraviolet
UVIS	Ultraviolet Imaging Spectrograph
UVIS	Ultraviolet Imaging Spectrometer
VIMS	Visual and Infrared Mapping Spectrometer
VMR	volume mixing ratio
VMR	volume mixing ratio
WAC	wide-angle camera

REFERENCES

Disclaimer: The partial list of references below correspond with in-text references indicated in this report. For all other Cassini references, refer to Attachment B – References & Bibliographies; Attachment C – Cassini Science Bibliographies; the sections entitled References contributed by individual Cassini instrument and discipline teams located in Volume 1 Sections 3.1 and 3.2 Science Results; and other resources outside of the Cassini Final Mission Report.

Abbas, M. M., A. LeClair, E. Woodard, M. Young, M. Stanbro, F. M. Flasar, V. G. Kunde, et al., (2013), Distribution of CO_2 in Saturn's atmosphere from Cassini/CIRS infrared observations, The Astrophysical Journal, 776, 2, doi: 10.1088/0004-637X/776/2/73.

Abbas, M. M., A. LeClair, T. Owen, B. J. Conrath, F. M. Flasar, V. G. Kunde, et al., (2004), The nitrogen isotopic ratio in Jupiter's atmosphere from observations by the Composite Infrared Spectrometer on the Cassini spacecraft, The Astrophysical Journal, 602, 2, 1063–1074, doi: 10.1086/381084.

Achterberg, R. K., F. M. Flasar, G. L. Bjoraker, B. E. Hesman, N. J. Gorius, A. A. Mamoutkine, L. N. Fletcher, M. E. Segura, S. G. Edgington, S. M. Brooks, (2018), Thermal emission from Saturn's polar cyclones, Geophysical Research Letters, vol. 45, Issue 11, pp. 5312–5319, Geophysical Research Letters, doi: 10.1029/2018gl078157.

Achterberg, R. K., P. J. Schinder, et al., (2016), CIRS team meeting notes.

Achterberg, R. K., P. J. Gierasch, B. J. Conrath, L. N. Fletcher, B. E. Hesman, G. L. Bjoraker, F. M. Flasar, (2014a), Changes to Saturn's zonal-mean tropospheric thermal structure after the 2010–2011 northern hemishere storm, The Astrophysical Journal, 786, 2, doi: 10.1088/0004-637X/786/2/92.

Achterberg, R. K., et al., (2014b), CIRS team meeting notes.

Achterberg, R. K., P. J. Gierasch, B. J. Conrath, F. M. Flasar, C. A. Nixon, (2011), Temporal variations of Titan's middle-atmospheric temperatures from 2004 to 2009 observed by Cassini/CIRS, Icarus, 211, 1, 686–698, doi: 10.1016/j.icarus.2010.08.009.

Achterberg, R. K., B. J. Conrath, P. J. Gierasch, E. M. Flasar, C. A. Nixon, (2008a), Titan's middle-atmospheric temperatures and dynamics observed by the Cassini Composite Infrared Spectrometer, Icarus, 194, 1, 263–277, doi: 10.1016/j.icarus.2007.09.029.

Achterberg, R. K., B. J. Conrath, P. J. Gierasch, F. M. Flasar, C. A. Nixon, (2008b), Observation of a tilt of Titan's middle-atmospheric superrotation, Icarus, 197, 2, 549–555, doi: 10.1016/j.icarus.2008.05.014.

Achterberg, R. K., B. J. Conrath, P. J. Gierasch, (2006), Cassini CIRS retrievals of ammonia in Jupiter's upper troposphere, Icarus, 182, 1, 169–180, doi: 10.1016/j.icarus.2005.12.020.

Achterberg, R. K. and F. M. Flasar, (1996), Planetary-scale thermal waves in Saturn's upper troposphere, Icarus, 119, 2, 350–369, doi: 10.1006/icar.1996.0024.

Altobelli, N., D. Lopez-Paz, S. Pilorz, L. J. Spilker, R. Morishima, S. Brooks, C. Leyrat, E. Deau, S. Edgington, A. Flandes, (2014), Two numerical models designed to reproduce Saturn ring temperatures as measured by Cassini-CIRS, Icarus, 238, 205–220.

Altobelli, N., L. Spilker, S. Pilorz, et al. (2009). Thermal phase curves observed in Saturn's main rings by Cassini-CIRS: Detection of an opposition effect? Geophysical Research Letters, vol. 36, Issue 10, doi: 10.1029/2009GL038163.

Altobelli, N., L. Spilker, C. Leyrat, S. Pilorz, (2008), Thermal observations of Saturn's main rings by Cassini CIRS: Phase, emission and solar elevation dependence, Planetary and Space Science, 56, 134–146.

Altobelli, N., L. Spilker, S. Pilorz, et al., (2007), C-ring fine structures revealed in the thermal infrared, Icarus, 191, 691–701.

Anderson, C. M., R. E. Samuelson, D. Nna-Mvondo, (2018), Organic Ices in Titan's Stratosphere, Space Science Reviews, 214, no. 8, 125.

Anderson, C. M., R. E. Samuelson, Y. L. Yung, J. L. McLain (2016), Solid-state photochemistry as a formation mechanism for Titan's stratospheric C4N2 ice clouds, Geophysical Research Letters, 43, 7, 3088–3094, doi: 10.1002/2016gl067795.

Anderson, C. M., R. E. Samuelson, R. K. Achterberg, J. W. Barnes, F. M. Flasar, (2014), Subsidence-induced methane clouds in Titan's winter polar stratosphere and upper troposphere, Icarus, 243, 129–138, doi: 10.1016/j.icarus.2014.09.007.

Anderson, C. M. and R. E. Samuelson (2011), Titan's aerosol and stratospheric ice opacities between 18 and 500 μm: Vertical and spectral characteristics from Cassini CIRS, Icarus, 212, 2, 762–778, doi: 10.1016/j.icarus.2011.01.024.

Anderson, C. M., R. E. Samuelson, G. L. Bjoraker, R. K. Achterberg, (2010), Particle size and abundance of HC_3N ice in Titan's lower stratosphere at high northern latitudes, Icarus, 207, 2, 914–922, doi: 10.1016/j.icarus.2009.12.024.

Baillié, K., J. E. Colwell, J. J. Lissauer, L. W. Esposito, M. Sremčević, (2011), Waves in Cassini UVIS stellar occultations: 2. The C ring, Icarus, 216, no. 1, 292–308.

Baldwin, M. P., L. J. Gray, T. J. Dunkerton, K. Hamilton, P. H. Haynes, W. J. Randel, J. R. Holton, et al., (2001), The quasi-biennial oscillation, Reviews of Geophysics, vol. 39, Issue 2, pp. 179–229, doi: 10.1029/1999rg000073.

Bampasidis, G., A. Coustenis, R. K. Achterberg, S. Vinatier, P. Lavvas, C. A. Nixon, D. E. Jennings, et al., (2012), Thermal and chemical structure variations in Titan's stratosphere during the Cassini Mission, The Astrophysical Journal, 760, 2, doi: 10.1088/0004-637x/760/2/144.

Bauch, K. E., H. Hiesinger, M. S. Robinson, F. Scholten, (2011), Thermophysical properties of selected lunar study regions determined from LROC and diviner data, 42nd Lunar and Planetary Science Conference, 2278pdf.

Bauduin, S., P. G. J. Irwin, E. Lellouch, V. Cottini, R. Moreno, C. A. Nixon, N. A. Teanby, T. Ansty, F. M. Flasar, (2018), Retrieval of H_2O abundance in Titan's stratosphere: A (re) analysis of CIRS/Cassini and PACS/Herschel observations, Icarus, 311, 288–305.

Bézard, B., S. Vinatier, R. K. Achterberg, (2018), Seasonal radiative modeling of Titan's stratospheric temperatures at low latitudes, Icarus, 302, 437–450.

Bézard, B., R. V. Yelle, C. A. Nixon (2013), The composition of Titan's atmosphere, Titan: Interior, Surface, Atmosphere, and Space Environment, 14, 158–189.

Bézard, B., (2009), Composition and chemistry of Titan's stratosphere, Philosophical Transactions of the Royal Society a-Mathematical Physical and Engineering Sciences, 367, 1889, 683–695, doi: 10.1098/rsta.2008.0186.

Bézard, B., C. A. Nixon, I. Kleiner, D. E. Jennings (2007), Detection of $^{13}CH_3D$ on Titan, Icarus, 191, 1, 397–400, doi: 10.1016/j.icarus.2007.06.004.

Blackburn, D. G., B. J. Buratti, E. G. Rivera-Valentin, (2012), Exploring the impact of thermal segregation on Dione through a bolometric bond albedo map, 43rd Lunar Planetary Science Conference, 1536pdf.

Bohren, C. F. and D. R. Huffman, (1983), Absorption and scattering of light by small particles, Wiley-Interscience, NY.

Bradley, E. T., J. E. Colwell, L. W. Esposito, (2013). Scattering properties of Saturn's rings in far ultraviolet from Cassini UVIS spectra, Icarus, 225, 726–739.

Bradley, E. T., J. E. Colwell, L. W. Esposito, et al., (2010), Far ultraviolet spectral properties of Saturn's rings from Cassini UVIS, Icarus, 206, 458–466.

Buratti, B. J., T. Momary, R. N. Clark, et al., (2018), First results from five fabulous flybys of Saturn's ring moons, Science, submitted February 6, 2018.

Buratti, B. and J. Veverka, (1984), Voyager photometry of Rhea, Dione, Tethys, Enceladus and Mimas, Icarus, 258, 254–264.

Burch, J. L., J. Goldstein, W. S. Lewis, D. T. Young, A. J. Coates, M. K. Dougherty, N. André (2007) Tethys and Dione as sources of outward-flowing plasma in Saturn's magnetosphere, Nature, 447, 833–835, doi: 10.1038/nature05906.

Ciarniello, M., F. Capaccioni, G. Filacchione, A. Raponi, F. Tosi, M. C. De Sanctis, M. T. Capria, et al., (2015), Photometric properties of comet 67P/Churyumov-Gerasimenko from VIRTIS-M onboard Rosetta, Astronomy & Astrophysics, 583, A31, doi: 10.1051/0004-6361/201526307.

Chandrasekhar, S., (1960), Radiative Transfer, Dover Publications, https://books.google.com/books?id=CK3HDRwCT5YC.

Charnoz, S., J. Salmon, A. Crida, (2010), The recent formation of Saturn's moonlets from viscous spreading of the main rings, Nature, 465, 752–754.

Colwell, J. E., J. H. Cooney, L. W. Esposito, M. Sremčević, (2009), Density waves in Cassini UVIS stellar occulations: 1, The Cassini division, Icarus, 200, 574–580.

Colwell, J. E., L. W. Esposito, M. Sremčević, G. R. Stewart, W. E. McClintock, (2007), Self-gravity wakes and radial structure of Saturn's B-ring, Icarus, 190, 127–144.

Colwell, J. E., L. W. Esposito, M. Sremčević, (2006), Self-gravity wakes in Saturn's A-ring measured by stellar occultations from Cassini, Geophysical Research Letters, vol. 33, Issue 7, doi: 10.1029/2005GL025163.

Cottini, V., C. A. Nixon, D. E. Jennings, C. M. Anderson, N. Gorius, G. L. Bjoraker, A. Coustenis, et al., (2012a), Water vapor in Titan's stratosphere from Cassini CIRS far-infrared spectra, Icarus, 220, 2, 855–862, doi: 10.1016/j.icarus.2012.06.014.

Cottini, V., C. A. Nixon, D. E. Jennings, R. de Kok, N. A. Teanby, P. G. J. Irwin, F. M. Flasar, (2012b), Spatial and temporal variations in Titan's surface temperatures from Cassini CIRS observations, Planetary and Space Science, 60, 1, 62–71, doi: 10.1016/j.pss.2011.03.015.

Courtin, R., C. K. Sim, S. J. Kim, D. Gautier, (2012), The abundance of H_2 in Titan's troposphere from the Cassini CIRS investigation, Planetary and Space Science, 69, 1, 89–99, doi: 10.1016/j.pss.2012.03.012.

Coustenis, A., D. E. Jennings, R. K. Achterberg, G. Bampasidis, C. A. Nixon, P. Lavvas, V. Cottini, F. M. Flasar, (2018), Seasonal evolution of Titan's stratosphere near the poles, The Astrophysical Journal Letters, 854, no. 2, L30, doi: 10.3847/2041-8213/aaadbd.

Coustenis, A., D. E. Jennings, R. K. Achterberg, G. Bampasidis, P. Lavvas, C. A. Nixon, N. A. Teanby, C. M. Anderson, V. Cottini, F. M. Flasar, (2016), Titan's temporal evolution in stratospheric trace gases near the poles, Icarus, 270, 409–420, doi: 10.1016/j.icarus.2015.08.027.

Coustenis, A., G. Bampasidis, R. K. Achterberg, P. Lavvas, D. E. Jennings, C. A. Nixon, N. A. Teanby, S. Vinatier, F. M. Flasar, R. C. Carlson, G. Orton, (2013), Evolution of the stratospheric temperature and chemical composition over one Titanian year, The Astrophysical Journal, 779, 2, doi: 10.1088/0004-637x/779/2/177.

Coustenis, A., D. E. Jennings, C. A. Nixon, R. K. Achterberg, P. Lavvas, S. Vinatier, N. A. Teanby, et al. (2010), Titan trace gaseous composition from CIRS at the end of the Cassini-Huygens prime mission, Icarus, 207, 1, 461–476, doi: 10.1016/j.icarus.2009.11.027.

Coustenis, A., D. E. Jennings, A. Jolly, Y. Bénilan, C. A. Nixon, S. Vinatier, D. Gautier et al., (2008), Detection of C_2HD and the D/H ratio on Titan, Icarus, 197, 2, 539–548, doi: 10.1016/j.icarus.2008.06.003.

Coustenis, A., R. K. Achterberg, B. J. Conrath, D. E. Jennings, A. Marten, D. Gautier, C. A. Nixon, et al. (2007), The composition of Titan's stratosphere from Cassini/CIRS mid-infrared spectra, Icarus, 189, 1, 35–62, doi: 10.1016/j.icarus.2006.12.022.

Coustenis, A., A. Salama, B. Schulz, S. Ott, E. Lellouch, T. Encrenaz, D. Gautier, H. Feuchtgruber, (2003), Titan's atmosphere from ISO mid-infrared spectroscopy, Icarus, 161, no. 2, 383–403.

Crespin, A., S. Lebonnois, S. Vinatier, B. Bézard, A. Coustenis, N. A. Teanby, R. K. Achterberg, P. Rannou, F. Hourdin, (2008), Diagnostics of Titan's stratospheric dynamics using Cassini/CIRS data and the 2-dimensional IPSL circulation model, Icarus, 197, 2, 556–571, doi: 10.1016/j.icarus.2008.05.010.

Cuzzi, J. N., R. Clark, G. Filacchione, R. French, R. Johnson, E. Marouf, L. Spilker, (2009), Ring particle composition and size distribution, Chapter 15, In Saturn from Cassini-Huygens, (eds.) M. K. Dougherty, L. W. Esposito, S. M. Krimingis, Springer, Dordrecht, pp. 459–509, doi: 10.1007/978-1-4020-9217-6_15.

Cuzzi, J. N. and P. R. Estrada, (1998), Compositional evolution of Saturn's rings due to meteoroid bombardment, Icarus, 132, 1–35.

Cuzzi, J. N., J. J. Lissauer, L. W. Esposito, J. B. Holberg, E. A Marouf, G. L. Tyler, A. Boischot, (1984), Saturn's rings - Properties and processes, In International Astronomical Union (IAU) Colloquia 75: Anneaux des Planetes (Planetary Rings), University of Arizona Press. Tucson, AZ, pp. 73–199.

de Kok, R. J., N. A. Teanby, L. Maltagliati, P. G. J. Irwin, S. Vinatier, (2014), HCN ice in Titan's high-altitude southern polar cloud, Nature, 514, 7520, 65–67, doi: 10.1038/nature13789.

de Kok, R., P. G. J. Irwin, N. A. Teanby, (2010a), Far-infrared opacity sources in Titan's troposphere reconsidered, Icarus, 209, 2, 854–857, doi: 10.1016/j.icarus.2010.06.035.

de Kok, R., P. G. J. Irwin, N. A. Teanby, S. Vinatier, F. Tosi, A. Negrao, S. Osprey, A. Adriani, M. L. Moriconi, A. Coradini (2010b), A tropical haze band in Titan's stratosphere, Icarus, 207, 1, 485–490, doi: 10.1016/j.icarus.2009.10.021.

de Kok, R., P. G. J. Irwin, N. A. Teanby (2008), Condensation in Titan's stratosphere during polar winter, Icarus, 197, 2, 572–578, doi: 10.1016/j.icarus.2008.05.024.

de Kok, R., P. G. J. Irwin, N. A. Teanby, E. Lellouch, B. Bézard, S. Vinatier, C. A. Nixon, et al., (2007a), Oxygen compounds in Titan's stratosphere as observed by Cassini CIRS, Icarus, 186, 2, 354–363, doi: 10.1016/j.icarus.2006.09.016.

de Kok, R., P. G. J. Irwin, N. A. Teanby, C. A. Nixon, D. E. Jennings, L. Fletcher, C. Howett, et al., (2007b), Characteristics of Titan's stratospheric aerosols and condensate clouds from Cassini CIRS far-infrared spectra, Icarus, 191, 1, 223–235, doi: 10.1016/j.icarus.2007.04.003.

De La Haye, V., J. H. Waite Jr, R. E. Johnson, R. V. Yelle, T. E. Cravens, J. G. Luhmann, et al., (2007), Cassini Ion and Neutral Mass Spectrometer data in Titan's upper atmosphere and exosphere: Observation of a suprathermal corona, Journal of Geophysical Research: Space Physics, 112, A7, doi: 10.1029/2006ja012222.

Del Genio, A. D., R. K. Achterberg, K. H. Baines, F. M. Flasar, P. L. Read, A. Sánchez-Lavega, A. P. Showman, (2009), Saturn Atmospheric Structure and Dynamics, Chapter 6, In Saturn

from Cassini-Huygens, (eds.) M. K. Dougherty, L. W. Esposito, S. M. Krimigis, Springer, Dordrecht, pp. 113–159, doi: 10.1007/978-1-4020-9217-6_6.

Dyudina, U. A., A. P. Ingersoll, S. P. Ewald, A. R. Vasavada, R. A. West, K. H. Baines, T. W. Momary, et al., (2009), Saturn's south polar vortex compared to other large vortices in the Solar System, Icarus, 202, 1, 240–248, doi: 10.1016/j.icarus.2009.02.014.

Dyudina, U. A., A. P. Ingersoll, S. P. Ewald, A. R. Vasavada, R. A. West, A. D. Del Genio, J. M. Barbara, et al., (2008), Dynamics of Saturn's south polar vortex, Science, 319, 5871, 1801–1801, doi: 10.1126/science.1153633.

Edgington, S. G., et al., (2008), unpublished.

Edwards, C. S., J. L. Bandfield, P. R. Christensen, A. D. Rogers, (2013), The formation of infilled craters by impact induced decompression melting of the martian mantle, 44th Lunar Planetary Science Conference, 2153pdf.

Elder, C., P. Helfenstein, P. Thomas, J. Veverka, J. A. Burns, T. Denk, C. Porco, (2007), Tethys'mysterious equatorial band, Bulletin American Astronomical Society, 39, 429.

Esposito, L. W., J. N. Cuzzi, J. B. Holberg, et al., (1984), Saturn's rings - Structure, dynamics, and particle properties, Saturn, pp. 463–545.

Ferrari, C. and E. Reffet, (2013), The dark side of Saturn's B-ring: Seasons as clues to its structure, Icarus, 223, 28–39.

Ferrari, C., S. Brooks, S. Edgington, et al., (2009), Structure of self-gravity wakes in Saturn's A-ring as measured by Cassini CIRS, Icarus, 199, 145–153.

Ferrari, C. and C. Leyrat, (2006), Thermal emission of spherical spinning ring particles, Astronomy & Astrophysics, 447, 745–760.

Ferrari, C. (2006), Cassini-CIRS observations of Saturn's rings, Asia Oceania Geosciences Society 3rd Annual Meeting.

Ferrari, C., P. Galdemard, P. O. Lagage, E. Pantin, C. Quorin, (2005), Imaging Saturn's rings with CAMIRAS: thermal inertia of B and C rings, Astronomy & Astrophysics, 441, 379–389.

Ferrari, C., P. Galdemard, P. O. Lagage, E. Pantin, (1999), Thermal inertia of Saturn's ring particles. Bulletin of the American Astronomical Society, 31, 1588–1588.

Filacchione, G., F. Capaccioni, M. Ciarniello, R. N. Clark, J. N. Cuzzi, P. D. Nicholson, D. P. Cruikshank, et al., (2012), Saturn's icy satellites and rings investigated by Cassini-VIMS: III – Radial compositional variability, Icarus, 220, 1064–1096.

Flandes, A., L. Spilker, R. Morishima, S. Pilorz, C. Leyrat, N. Altobelli, S. Brooks, S. G. Edgington, et al., (2010), Brightness of Saturn's rings with decreasing solar elevation, Planetary and Space Science, 58, 1758–1765.

Flasar, F. M., R. K. Achterberg, P. J. Schinder, (2014), Thermal structure of Titan's troposphere and middle atmosphere, Chapter 3, In Titan: Interior, Surface, Atmosphere, and Space

Environment, (eds.) I. Müller-Wodarg, C. A. Griffith, E. Lellouch, T. E. Cravens, Cambridge University Press, New York, NY, pp. 102–121.

Flasar, F. M. and R. K. Achterberg, (2009), The structure and dynamics of Titan's middle atmosphere, Philosophical Transactions of the Royal Society a-Mathematical Physical and Engineering Sciences, 367, 1889, 649–664, doi: 10.1098/rsta.2008.0242.

Flasar, F. M., K. H. Baines, M. K. Bird, T. Tokano, R. A. West, (2009), Atmospheric Dynamics and Meteorology, Chapter 13, In Titan from Cassini-Huygens, (eds.) R. H. Brown, J.-P. Lebreton, J. H. Waite, Springer, Dordrecht, pp. 323–352, doi: 10.1007/978-1-4020-9215-2_13.

Flasar, F. M., R. K. Achterberg, B. J. Conrath, P. J. Gierasch, V. G. Kunde, C. A. Nixon, G. L. Bjoraker, et al., (2005a), Titan's atmospheric temperatures, winds, and composition, Science, 308, 5724, 975–978, doi: 10.1126/science.1111150.

Flasar, F. M., R. K. Achterberg, B. J. Conrath, J. C. Pearl, G. L. Bjoraker, D. E. Jennings, P. N. Romani, et al., (2005b), Temperatures, winds, and composition in the Saturnian system, Science, 307, 5713, 1247–1251, doi: 10.1126/science.1105806.

Flasar, F. M., V. G. Kunde, M. M. Abbas, R. K. Achterberg, P. Ade, A. Barucci, B. Bézard, et al., (2004a), Exploring the Saturn system in the thermal infrared: The composite infrared spectrometer, Space Science Reviews, 115, 169–297, doi: 10.1007/s11214-004-1454-9.

Flasar, F. M., V. G. Kunde, R. K. Achterberg, B. J. Conrath, A. A. Simon-Miller, C. A. Nixon, P. J. Gierasch, et al. (2004b), An intense stratospheric jet on Jupiter, Nature, 427(6970), 132–135, doi: 10.1038/nature02142.

Flasar, F. M., R. E. Samuelson, B. J. Conrath, (1981), Titans atmosphere - temperature and dynamics, Nature, 292, 5825, 693–698, doi: 10.1038/292693a0.

Fletcher, L. N., T. K. Greathouse, S. Guerlet, J. I. Moses, R. A. West, (2018), Saturn’s Seasonally Changing Atmosphere - Thermal Structure, Composition, and Aerosols, Chapter 10, In Saturn in the 21st Century, (ed.) K. H. Baines, F. M. Flasar, N. Krupp, T. Stallard, Cambridge University Press, pp. 251–294, doi: 10.1017/9781316227220.010.

Fletcher, L. N., S. Guerlet, G. S. Orton, R. G. Cosentino, T. Fouchet, P. G. J. Irwin, L. Li, F. M. Flasar, N. Gorius, R. Morales-Juberias, (2017), Disruption of Saturn's quasi-periodic equatorial oscillation by the great northern storm, Nature Astronomy, 1, 11, 765–770, doi: 10.1038/s41550-017-0271-5.

Fletcher, L. N., P. G. J. Irwin, R. K. Achterberg, G. S. Orton, F. M. Flasar, (2016), Seasonal variability of Saturn's tropospheric temperatures, winds and para-H_2 from Cassini far-IR spectroscopy, Icarus, 264, 137–159, doi: 10.1016/j.icarus.2015.09.009.

Fletcher, L. N., P. G. J. Irwin, J. A. Sinclair, G. S. Orton, R. S. Giles, J. Hurley, N. Gorius, R. K. Achterberg, B. E. Hesman, G. L. Bjoraker, (2015), Seasonal evolution of Saturn's polar temperatures and composition, Icarus, 250, 131–153, doi: 10.1016/j.icarus.2014.11.022.

Fletcher, L. N., T. K. Greathouse, G. S. Orton, P. G. J. Irwin, O. Mousis, J. A. Sinclair, R. S. Giles (2014), The origin of nitrogen on Jupiter and Saturn from the N15/N14 ratio, Icarus, 238, 170–190, doi: 10.1016/j.icarus.2014.05.007.

Fletcher, L. N., B. E. Hesman, R. K. Achterberg, P. G. J. Irwin, G. Bjoraker, N. Gorius, J. Hurley, et al., (2012), The origin and evolution of Saturn's 2011–2012 stratospheric vortex, Icarus, 221, 2, 560–586, doi: 10.1016/j.icarus.2012.08.024.

Fletcher, L. N., B. E. Hesman, P. G. J. Irwin, K. H. Baines, T. W. Momary, A. Sanchez-Lavega, F. M. Flasar, et al. (2011), Thermal structure and dynamics of Saturn's northern springtime disturbance, Science, 332, 6036, 1413–1417, doi: 10.1126/science.1204774.

Fletcher, L. N., R. K. Achterberg, T. K. Greathouse, G. S. Orton, B. J. Conrath, A. A. Simon-Miller, N. Teanby, S. Guerlet, P. G. J. Irwin, F. M. Flasar, (2010), Seasonal change on Saturn from Cassini/CIRS observations, 2004–2009, Icarus, 208, 1, 337–352, doi: 10.1016/j.icarus.2010.01.022.

Fletcher, L. N., G. S. Orton, N. A. Teanby, P. G. J. Irwin, (2009a), Phosphine on Jupiter and Saturn from Cassini/CIRS, Icarus, 202, 2, 543–564, doi: 10.1016/j.icarus.2009.03.023.

Fletcher, L. N., G. S. Orton, N. A. Teanby, P. G. J. Irwin, G. L. Bjoraker, (2009b), Methane and its isotopologues on Saturn from Cassini/CIRS observations, Icarus, 199, 2, 351–367, doi: 10.1016/j.icarus.2008.09.019.

Fletcher, L. N., G. J. Irwin, G. S. Orton, N. A. Teanby, R. K. Achterberg, G. L. Bjoraker, P. L. Read, et al., (2008), Temperature and composition of Saturn's polar hot spots and hexagon, Science, 319, 5859, 79–81, doi: 10.1126/science.1149514.

Fletcher, L. N., P. G. J. Irwin, N. A. Teanby, G. S. Orton, P. D. Parrish, S. B. Calcutt, N. Bowles, R. de Kok, C. Howett, F. W. Taylor, (2007a), The meridional phosphine distribution in Saturn's upper troposphere from Cassini/CIRS observations, Icarus, 188, 1, 72–88, doi: 10.1016/j.icarus.2006.10.029.

Fletcher, L. N., P. G. J. Irwin, N. A. Teanby, G. S. Orton, P. D. Parrish, R. de Kok, C. Howett, S. B. Calcutt, N. Bowles, F. W. Taylor, (2007b), Characterising Saturn's vertical temperature structure from Cassini/CIRS, Icarus, 189, 2, 457–478, doi: 10.1016/j.icarus.2007.02.006.

Fouchet, T., J. I. Moses, B. J. Conrath, (2009), Saturn: Composition and Chemistry, Chapter 5, In Saturn from Cassini-Huygens, (eds.) M. K. Dougherty, L. W. Esposito, S. M. Krimigis, pp. 83–112, Springer, Netherlands, doi: 10.1007/978-1-4020-9217-6_5.

Fouchet, T., S. Guerlet, D. F. Strobel, A. A. Simon-Miller, B. Bézard, F. M. Flasar, (2008), An equatorial oscillation in Saturn's middle atmosphere, Nature, 453, 7192, 200–202, doi: 10.1038/nature06912.

Fouchet, T., P. G. J. Irwin, P. Parrish, S. B. Calcutt, F. W. Taylor, C. A. Nixon, T. Owen, (2004a), Search for spatial variation in the jovian $^{15}N/^{14}N$ ratio from Cassini/CIRS observations, Icarus, 172, 1, 50–58, doi: 10.1016/j.icarus.2003.11.011.

Fouchet, T., G. Orton, P. G. J. Irwin, S. B. Calcutt, C. A. Nixon, (2004b), Upper limits on hydrogen halides in Jupiter from Cassini/CIRS observations, Icarus, 170, 1, 237–241, doi: 10.1016/j.icarus.2004.03.013.

French, R. G., H. Salo, C. A. McGhee, L. Dones, (2007), HST observations of azimuthal asymmetry in Saturn's rings, Icarus, 189, no. 2, 493–522.

French, R. G. and P. D. Nicholson, (2000), Saturn's rings II: Particle sizes inferred from stellar occultation data, Icarus, 145, no. 2, 502–523.

Froidevaux, L., K. Matthews, G. Neugebauer, (1981), Thermal response of Saturn's ring particles during and after eclipse, Icarus, 46, no. 1, 18–26, doi: 10.1016/0019-1035(81)90071-3.

Froidevaux, L., (1981), Saturn's rings: Infrared brightness variation with solar elevation, Icarus, 46, no. 1, 4–17, doi: 10.1016/0019-1035(81)90070-1.

Fulchignoni, M., F. Ferri, F. Angrilli, A.J. Ball, A. Bar-Nun, M.A. Barucci, C. Bettanini, G. Bianchini, W. Borucki, G. Colombatti, M. Coradini, et al., (2005), In situ measurements of the physical characteristics of Titan's environment, Nature, 438, 7069, 785–791, doi: 10.1038/nature04314.

Guerlet, S., T. Fouchet, A. Spiga, F. M. Flasar, L. N. Fletcher, B. E. Hesman, N. Gorius, (2018), Equatorial Oscillation and Planetary Wave Activity in Saturn's Stratosphere Through the Cassini Epoch, Journal of Geophysical Research-Planets, 123, 1, 246–261, doi: 10.1002/2017je005419.

Guerlet, S., T. Fouchet, S. Vinatier, A. A. Simon, E. Dartois, A. Spiga, (2015), Stratospheric benzene and hydrocarbon aerosols detected in Saturn's auroral regions, Astronomy & Astrophysics, 580, doi: 10.1051/0004-6361/201424745.

Guerlet, S., T. Fouchet, B. Bézard, F. M. Flasar, A. A. Simon-Miller, (2011), Evolution of the equatorial oscillation in Saturn's stratosphere between 2005 and 2010 from Cassini/CIRS limb data analysis, Geophysical Research Letters, 38, doi: 10.1029/2011GL047192.

Guerlet, S., T. Fouchet, B. Bézard, J. I. Moses, L. N. Fletcher, A. A. Simon-Miller, F. M. Flasar, (2010), Meridional distribution of CH_3C_2H and C_4H_2 in Saturn's stratosphere from CIRS/Cassini limb and nadir observations, Icarus, 209, 2, 682–695, doi: 10.1016/j.icarus.2010.03.033.

Guerlet, S., T. Fouchet, B. Bézard, A. A. Simon-Miller, F. M. Flasar, (2009), Vertical and meridional distribution of ethane, acetylene and propane in Saturn's stratosphere from CIRS/Cassini limb observations, Icarus, 203, 1, 214–232, doi: 10.1016/j.icarus.2009.04.002.

Hamilton, D.P. and J.A. Burns, (1994), Origin of Saturn’s E-ring: Self-sustained, naturally, Nature 264, 550–553, doi: 10.1126/science.264.5158.550.

Hanel, R. A., B. J. Conrath, D. E. Jennings, R. E. Samuelson, (2003), Exploration of the solar system by infrared remote sensing, Cambridge University Press.

Hanel, R., B. Conrath, F. M. Flasar, V. Kunde, W. Maguire, J. Pearl, J. Pirraglia, et al., (1981), Infrared observations of the Saturnian system from Voyager-1, Science, 212, 4491, 192–200, doi: 10.1126/science.212.4491.192.

Hansen, O., (1973), Ten-micron eclipse observations of Io, Europa, and Ganymede, Icarus, 18, 237–246, doi: 10.1016/0019-1035(73)90208-X.

Hapke, B., (1993), Theory of reflectance and emittance spectroscopy, Cambridge University Press, New York.

Hapke, B., (2012), Theory of Reflectance and Emittance Spectroscopy, Cambridge University Press, New York.

Hedman, M. M., P. D. Nicholson, J. N. Cuzzi, et al., (2013) Connections between spectra and structure in Saturn's main rings based on Cassini VIMS data, Icarus, 223, 105–130.

Hedman, M. M., J. A. Burt, J. A. Burns, M. S. Tiscareno, (2010) The shape and dynamics of a heliotropic dusty ringlet in the Cassini division, Icarus, 210, 284–297.

Hedman, M. M., P. D. Nicholson, H. Salo, B. D. Wallis, B. J. Buratti, K. H. Baines, R. H. Brown, R. N. Clark, (2007), Self-gravity wake structures in Saturn's A-ring revealed by Cassini VIMS, The Astronomical Journal, 133, 2624–2629.

Helfenstein, P. and C. C. Porco, (2015), Enceladus' geysers: relation to Geological Features, The Astronomical Journal, 150, no. 3, 96, doi: 10.1088/0004-6256/150/3/96.

Hesman, B. E., G. L. Bjoraker, P. V. Sada, R. K. Achterberg, D. E. Jennings, P. N. Romani, A. W. Lunsford, et al., (2012), Elusive ethylene detected in Saturn's northern storm region, The Astrophysical Journal, 760, 1, doi: 10.1088/0004-637x/760/1/24.

Hesman, B. E., D. E. Jennings, P. V. Sada, G. L. Bjoraker, R. K. Achterberg, A. A. Simon-Miller, C. M. Anderson, et al. (2009), Saturn's latitudinal C_2H_2 and C_2H_6 abundance profiles from Cassini/CIRS and ground-based observations, Icarus, 202, 1, 249–259, doi: 10.1016/j.icarus.2009.02.013.

Hörst, S. M., V. Vuitton, R. V. Yelle, (2008), Origin of oxygen species in Titan's atmosphere, Journal of Geophysical Research: Planets, 113, no. E10, doi: 10.1029/2008JE003135.

Howett, C. J. A., J. R. Spencer, T. Hurford, A. Verbiscer, M. Segura, (2018), Limits on Dione's activity using Cassini/CIRS data, Geophysical Research Letters, vol. 45, Issue 12, pp. 5876–5898, doi: 10.1029/2018GL078161.

Howett, C. J. A., J. R. Spencer, A. Verbiscer, (2017), Characterizing the heat flow from between Enceladus' Tiger Stripes, American Geophysical Union (AGU) Fall Meeting, abstract 272459.

Howett, C. J. A., J. R. Spencer, T. Hurford, A. Verbiscer, M. Segura, (2014), Thermophysical property variations across Dione and Rhea, Icarus, 241, 239–247, doi: 10.1016/j.icarus.2014.05.047.

Howett, C. J. A., J. R. Spencer, T. Hurford, A. Verbiscer, M. Segura, (2012), PacMan returns: An electron-generated thermal anomaly on Tethys, Icarus, 221, 1084–1088, doi: 10.1016/j.icarus.2012.10.013.

Howett C., J .R. Spencer, J. Pearl, M. Segura, (2011a), High heat flow from Enceladus' south polar region measured using 10–600 cm^{-1} Cassini/CIRS data, Journal of Geophysical Research, 116, E03003, doi: 10.1029/2010JE003718.

Howett, C. J. A., J. R. Spencer, P. Schenk, R. E. Johnson, C. Paranicas, T. A Hurford, A. Verbiscer, M. Segura, (2011b), A high-amplitude thermal inertia anomaly of probable magnetospheric origin on Saturn's moon Mimas, Icarus, 216, 221–226, doi: 10.1016/j.icarus.2011.09.007.

Howett, C. J. A., J. R. Spencer, J. Pearl, M. Segura, (2010), Thermal inertia and bolometric Bond albedo values for Mimas, Enceladus, Tethys, Dione, Rhea and Iapetus as derived from Cassini/CIRS measurements, Icarus, 206, 573–593, doi: 10.1016/j.icarus.2009.07.016.

Howett, C. J. A., P. G. J. Irwin, N. A. Teanby, A. Simon-Miller, S. B. Calcutt, L. N. Fletcher, R. de Kok (2007), Meridional variations in stratospheric acetylene and ethane in the southern hemisphere of the saturnian atmosphere as determined from Cassini/CIRS measurements, Icarus, 190, 2, 556–572, doi: 10.1016/j.icarus.2007.03.009.

Hunten, D. M. (1973), Escape of light gases from planetary atmospheres, Journal of the Atmospheric Sciences, 30, 8, 1481–1494, doi: 1 10.1175/1520-0469(1973)030<1481:TEOLGF>2.0.CO;2.

Hurley, J., L. N. Fletcher, P. G. J. Irwin, S. B. Calcutt, J. A. Sinclair, C. Merlet (2012a), Latitudinal variation of upper tropospheric NH_3 on Saturn derived from Cassini/CIRS far-infrared measurements, Planetary and Space Science, 73, 1, 347–363, doi: 10.1016/j.pss.2012.08.003.

Hurley, J., P. G. J. Irwin, L. N. Fletcher, J. I. Moses, B. Hesman, J. Sinclair, C. Merlet, (2012b), Observations of upper tropospheric acetylene on Saturn: No apparent correlation with 2000 km-sized thunderstorms, Planetary and Space Science, 65, 1, 21–37, doi: 10.1016/j.pss.2011.12.026.

Ingersoll, A. and S. P Ewald, (2017), Decadal timescale variability of the Enceladus plumes inferred from Cassini images, Icarus, 282, 260–272, doi: 10.1016/j.icarus.2016.09.018.

Ingersoll, A. and A. Pankine, (2010), Subsurface heat transfer on Enceladus: conditions under which melting occurs, Icarus, 20, 594–607, doi: 10.1016/j.icarus.2009.09.015.

Irwin, P., N. Teanby, R. de Kok, et al., (2008), The Nemesis planetary atmosphere radiative transfer and retrieval tool, Journal of Quantitative Spectroscopy & Radiative Transfer, 109, 6, 1136–1150, doi: 10.1016/j.jqsrt.2007.11.006.

Irwin, P. G. J., P. Parrish, T. Fouchet, S. B. Calcutt, F. W. Taylor, A. A. Simon-Miller, C. A. Nixon, (2004), Retrievals of jovian tropospheric phosphine from Cassini/CIRS, Icarus, 172, 1, 37–49, doi: 10.1016/j.icarus.2003.09.027.

Jacquinet-Husson, N., R. Armante, N. A. Scott, A. Chédin, L. Crépeau, C. Boutammine, A. Bouhdaoui, et al., (2016), The 2015 edition of the GEISA spectroscopic database, Journal of Molecular Spectroscopy, 327, 31–72, doi: 10.1016/j.jms.2016.06.007.

- - - - - - - - - - - - - -

Janssen, M. A., R. D. Lorenz, R. West, F. Paganelli, R. M. Lopes, Randolph L. Kirk, C. Elachi, et al., (2009), Titan's surface at 2.2-cm wavelength imaged by the Cassini RADAR radiometer: Calibration and first results, Icarus, 200, 1, 222–239, doi: 10.1016/j.icarus.2008.10.017.

Jennings, D. E., T. Tokano, V. Cottini, C. A. Nixon, R. K. Achterberg, F. M. Flasar, V. G. Kunde, et al., (2019), Titan surface temperatures during the Cassini Mission, The Astrophysical Journal Letters, 877, 1, L8, doi: 10.3847/2041-8213/ab1f91.

Jennings, D. E., F. M. Flasar, V. G. Kunde, C. A. Nixon, M. E. Segura, P. N. Romani, N. Gorius, et al., (2017), Composite infrared spectrometer (CIRS) on Cassini, Applied Optics, 56, no. 18, 5274–5294, doi: 10.1364/AO.56.005274.

Jennings, D. E., V. Cottini, C. A. Nixon, R. K. Achterberg, F. M. Flasar, V. G. Kunde, P. N. Romani, et al., (2016), Surface temperatures on Titan during northern winter and spring, The Astrophysical Journal Letters, 816, 1, doi: 10.3847/2041-8205/816/1/l17.

Jennings, D. E., R. K. Achterberg, V. Cottini, C. M. Anderson, F. M. Flasar, C. A. Nixon, G. L. Bjoraker, et al., (2015), Evolution of the far-infrared cloud at Titan's south pole, The Astrophysical Journal Letters, 804, 2, doi: 10.1088/2041-8205/804/2/l34.

Jennings, D. E., C. M. Anderson, R. E. Samuelson, F. M. Flasar, C. A. Nixon, G. L. Bjoraker, P. N. Romani, et al., (2012a), First observation in the south of Titan's far-infrared 220 cm^{-1} cloud, The Astrophysical Journal Letters, 761, 1, doi: 10.1088/2041-8205/761/1/l15.

Jennings, D. E., C. M. Anderson, R. E. Samuelson, F. M. Flasar, C. A. Nixon, V. G. Kunde, R. K. Achterberg, et al., (2012b), Seasonal disappearance of far-infrared haze in Titan's stratosphere, The Astrophysical Journal Letters, 754, 1, doi: 10.1088/2041-8205/754/1/l3.

Jennings, D. E., V. Cottini, C. A. Nixon, F. M. Flasar, V. G. Kunde, R. E. Samuelson, P. N. Romani, et al. (2011), Seasonal changes in Titan's surface temperatures, The Astrophysical Journal Letters, 737, 1, doi: 10.1088/2041-8205/737/1/L15.

Jennings, D. E., F. M. Flasar, V. G. Kunde, R. E. Samuelson, J. C. Pearl, C. A. Nixon, R. C. Carlson, et al., (2009), Titan's surface brightness temperatures, The Astrophysical Journal Letters, 691, 2, L103–L105, doi: 10.1088/0004-637X/691/2/L103.

Jennings, D. E., C. A. Nixon, A. Jolly, B. Bézard, A. Coustenis, S. Vinatier, P. G. J. Irwin, et al. (2008), Isotopic ratios in Titan's atmosphere from Cassini CIRS limb sounding: HC_3N in the north, The Astrophysical Journal Letters, 681, 2, L109–L111, doi: 10.1086/590534.

Jolly, A., V. Cottini, A. Fayt, L. Manceron, F. Kwabia-Tchana, Y. Benilan, J. C. Guillemin, C. Nixon, P. Irwin, (2015), Gas phase dicyanoacetylene (C_4N_2) on Titan: New experimental and theoretical spectroscopy results applied to Cassini CIRS data, Icarus, 248, 340–346, doi: 10.1016/j.icarus.2014.10.049.

Jolly, A., A. Fayt, Y. Benilan, D. Jacquemart, C. A. Nixon, D. E. Jennings, (2010), The v^8 bending mode of diacetylene: from laboratory spectroscopy to the detection of ^{13}C isotopologues in Titan's atmosphere, The Astrophysical Journal, 714, 1, 852–859, doi: 10.1088/0004-637X/714/1/852.

Jones, G. H., E. Roussos, N. Krupp, U. Beckmann, A. J. Coates, F. Crary, I. Dandouras, et al., (2008), The dust halo of Saturn's largest icy moon, Rhea, Science, 319, no. 5868, 1380–1384.

Joseph, J. H., W. J. Wiscombe, J. A. Weinman, (1976), The delta-Eddington approximation for radiative flux transfer, Journal of the Atmospheric Sciences, 33, pp. 2452–2459.

Kawata, Y., (1983), Infrared brightness temperature of Saturn's rings based on the inhomogeneous multilayer assumption, Icarus 56, no. 3, 453–464.

Khanna, R. K., M. A. Perera-Jarmer, M. J. Ospina, (1987), Vibrational infrared and Raman spectra of dicyanoacetylene, Spectrochimica Acta Part A: Molecular Spectroscopy, 43, no. 3, 421–425.

Khare, B. N., C. Sagan, E. T. Arakawa, F. Suits, T. A. Callcott, M. W. Williams, (1984), Optical constants of organic tholins produced in a simulated Titanian atmosphere: From soft X-ray to microwave frequencies, Icarus, 60, no. 1, 127–137.

Khare, B. N., C. Sagan, W. R. Thompson, E. T. Arakawa, F. Suits, T. A. Callcott, M. W. Williams, et al., (1984), The organic aerosols of Titan, Advances in Space Research, 4, no. 12, 59–68.

Koskinen, T. T. and S. Guerlet, (2018), Atmospheric structure and helium abundance on Saturn from Cassini/UVIS and CIRS observations, Icarus, 307, 161–171, doi: 10.1016/j.icarus.2018.02.020.

Kunde, V. G., F. M. Flasar, D. E. Jennings, B. Bézard, D. F. Strobel, B. J. Conrath, C. A. Nixon, et al., (2004), Jupiter's atmospheric composition from the Cassini thermal infrared spectroscopy experiment, Science, 305, 5690, 1582–1586, doi: 10.1126/science.1100240.

Kunde, V. G., P. A. R. Ade, R. D. Barney, D. Bergman, J.-F. Bonnal, R. Borelli, D. Boyd, et al., (1996), Cassini infrared Fourier spectroscopic investigation, In Cassini-Huygens: A Mission to the Saturnian Systems, International Symposium on Optical Science, Engineering, and Instrumentation, Denver, CO, vol. 2803, pp. 162–177, doi: 10.1117/12.253416.

Lara, L. M., E. Lellouch, J. J. López-Moreno, R. Rodrigo, (1996), Vertical distribution of Titan's atmospheric neutral constituents, Journal of Geophysical Research: Planets, 101, no. E10, 23261–23283.

Le Gall, A., C. Leyrat, M. A. Janssen, G. Choblet, G. Tobie, O. Bourgeois, A. Lucas, et al., (2017), Thermally anomalous features in the subsurface of Enceladus’s south polar terrain, Nature, Astronomy, 1, no. 4, article 0063, doi: 10.1038/s41550-017-0063.

Lebonnois, S., F. M. Flasar, T. Tokano, C. E. Newman, (2014), The general circulation of Titan's lower and middle atmosphere, Chapter 4, In Titan: Interior, Surface, Atmosphere, and Space Environment, (eds.) I. Müller-Wodarg, C. A. Griffith, E. Lellouch, T. E. Cravens, Cambridge University Press, pp. 122–157.

Lebonnois, S., J. Burgalat, P. Rannou, B. Charnay, (2012), Titan global climate model: A new 3-dimensional version of the IPSL Titan GCM, Icarus, 218, 1, 707–722, doi: 10.1016/j.icarus.2011.11.032.

Lebonnois, S., P. Rannou, F. Hourdin (2009), The coupling of winds, aerosols and chemistry in Titan's atmosphere, Philosophical Transactions of the Royal Society a-Mathematical Physical and Engineering Sciences, 367, 1889, 665–682, doi: 10.1098/rsta.2008.0243.

Lellouch, E., B. Bézard, F. M. Flasar, S. Vinatier, R. Achterberg, C. A. Nixon, G. L. Bjoraker, N. Gorius, (2014), The distribution of methane in Titan's stratosphere from Cassini/CIRS observations, Icarus, 231, 323–337, doi: 10.1016/j.icarus.2013.12.016.

Lellouch, E., B. Bézard, D. F. Strobel, G. L. Bjoraker, F. M. Flasar, P. N. Romani, (2006), On the HCN and CO_2 abundance and distribution in Jupiter's stratosphere, Icarus, 184, 2, 478–497, doi: 10.1016/j.icarus.2006.05.018.

Leovy, C. B., A. J. Friedson, G. S. Orton, (1991), The quasiquadrennial oscillation of Jupiter's equatorial stratosphere, Nature, 354, 6352, 380–382, doi: 10.1038/354380a0.

Leyrat, C., L. J. Spilker, N. Altobelli, S. Pilorz, C. Ferrari, (2008a). Infrared observations of Saturn's rings by Cassini CIRS: Phase angle and local time dependence, Planetary and Space Science, 56, 117–133.

Leyrat, C., C. Ferrari, S. Charnoz, et al., (2008b), Spinning particles in Saturn's C-ring from mid-infrared observations: Pre-Cassini mission results, Icarus, 196, 625–641.

Li, L., X. Jiang, H. J. Trammell, Y. Pan, J. Hernandez, B. J. Conrath, P. J. Gierasch, et al., (2015), Saturn's giant storm and global radiant energy, Geophysical Research Letters, 42, 7, 2144–2148, doi: 10.1002/2015GL063763.

Li, L., (2015), Dimming Titan revealed by the Cassini observations, Scientific Reports 5, article 8239, doi: 10.1038/srep08239.

Li, L., R. K. Achterberg, B. J. Conrath, P. J. Gierasch, M. A. Smith, A. A. Simon-Miller, C. A. Nixon, et al. (2013), Strong temporal variation over one Saturnian year: from Voyager to Cassini, Scientific Reports, 3, doi: 10.1038/srep02410.

Li, L. M., K. H. Baines, M. A. Smith, R. A. West, S. Pérez-Hoyos, H. J. Trammell, A. A. Simon-Miller, et al. (2012), Emitted power of Jupiter based on Cassini CIRS and VIMS observations, Journal of Geophysical Research: Planets, 117, doi: 10.1029/2012je004191.

Li, L. M., X. Jiang, A. P. Ingersoll, A. D. Del Genio, C. C. Porco, R. A. West, A. R. Vasavada, et al., (2011a), Equatorial winds on Saturn and the stratospheric oscillation, Nature Geoscience, 4, 11, 750–752, doi: 10.1038/ngeo1292.

Li, L. M., C. A. Nixon, R. K. Achterberg, M. A. Smith, N. J. P. Gorius, X. Jiang, B. J. Conrath, et al. (2011b), The global energy balance of Titan, Geophysical Research Letters, 38, doi: L2320110.1029/2011gl050053.

Li, L., B. J. Conrath, P. J. Gierasch, R. K. Achterberg, C. A. Nixon, A. A. Simon-Miller, F. M. Flasar, et al., (2010), Saturn's emitted power, Journal of Geophysical Research: Planets, 115, doi: 10.1029/2010JE003631.

Li, L., P. J. Gierasch, R. K. Achterberg, B. J. Conrath, F. M. Flasar, A. R. Vasavada, A. P. Ingersoll, D. Banfield, A. A. Simon-Miller, L. N. Fletcher, (2008), Strong jet and a new

thermal wave in Saturn's equatorial stratosphere, Geophysical Research Letters, 35, 23, doi: 10.1029/2008GL035515.

Li, L. M., A. P. Ingersoll, A. R. Vasavada, A. A. Simon-Miller, R. K. Achterberg, S. P. Ewald, U. A. Dyudina, C. C. Porco, R. A. West, F. M. Flasar, (2006), Waves in Jupiter's atmosphere observed by the Cassini ISS and CIRS instruments, Icarus, 185, 2, 416–429, doi: 10.1016/j.icarus.2006.08.005.

Lombardo, N. A., C. A. Nixon, R. K. Achterberg, A. Jolly, K. Sung, P. G. J. Irwin, F. M. Flasar, (2019), Spatial and seasonal variations in C_3H_x hydrocarbon abundance in Titan's stratosphere from Cassini CIRS observations, Icarus, 317, 454–469.

Lopes, R. M. C., R. L. Kirk, K. L. Mitchell, A. LeGall, J. W. Barnes, A. Hayes, J. Kargel, et al., (2013), Cryovolcanism on Titan: New results from Cassini RADAR and VIMS, Journal of Geophysical Research: Planets, 118, 3, 416–435, doi: 10.1002/jgre.20062.

Lorenz, R. D., B. W. Stiles, O. Aharonson, A. Lucas, A. G. Hayes, R. L. Kirk, H. A. Zebker, et al., (2013), A global topographic map of Titan, Icarus, 225, 1, 367–377, doi: 10.1016/j.icarus.2013.04.002.

Lorenz, R. D., M. E. Brown, F. M. Flasar, (2009), Seasonal change on Titan, Chapter 14, In Titan from Cassini-Huygens, (eds.) R. H. Brown, J.-P. Lebreton, J. H. Waite, Springer Netherlands, pp. 353–372, doi: 10.1007/978-1-4020-9215-2_14.

Lorenz, R. D., S. Wall, J. Radebaugh, G. Boubin, E. Reffet, M. Janssen, E. Stofan, et al., (2006), The sand seas of Titan: Cassini RADAR observations of longitudinal dunes, Science, 312, 5774, 724–727, doi: 10.1126/science.1123257.

Lumme, K. and E. Bowell, (1981a) Radiative transfer in the surfaces of atmosphereless bodies. I. Theory, The Astronomical Journal, 86, 1694–1704.

Lumme, K. and E. Bowell, (1981b). Radiative transfer in the surfaces of atmosphereless bodies. II. Interpretation of phase curves, The Astronomical Journal, 86, 1705–1721.

Lumme, K. and W. M. Irvine, (1976), Photometry of Saturn's rings, The Astronomical Journal, 81, 863–893.

Matcheva, K. I., B. J. Conrath, P. J. Gierasch, F. M. Flasar, (2005), The cloud structure of the jovian atmosphere as seen by the Cassini/CIRS experiment, Icarus, 179, 2, 432–448, doi: 10.1016/j.icarus.2005.06.020.

McKay, C. P., J. B. Pollack, R. Courtin, (1991), The greenhouse and antigreenhouse effects on Titan, Science, 253, 5024, 1118–1121, doi: 10.1126/science.11538492.

Meyer, J. and J. Wisdom (2007), Tidal heating in Enceladus, Icarus 188, 535–539, doi: 10.1016/j.icarus.2007.03.001.

Mie, G. (1908), Beiträge zur Optik trüber Medien, speziell kolloidaler Metallösungen, Annalen der physic, 330, no. 3, 377–445, doi: 10.1002/andp.19083300302.

Modest, M. F., (2003), Radiative heat transfer, Academic Press, An imprint of Elsevier Science, San Diego, CA.

Morishima, R., N. Turner, L. Spilker, (2017), Surface roughness of Saturn's rings and ring particles inferred from thermal phase curves, Icarus, 295, 74–88.

Morishima, R., L. Spilker, S. Brooks, E. Deau, S. Pilorz, (2016). Incomplete cooling down of Saturn's A-ring at solar equinox: Implication for seasonal thermal inertia and internal structure of ring particles, Icarus, 279, 2–19.

Morishima, R., L. Spilker, N. Truner, (2014), Azimuthal temperature modulations of Saturn's A-ring caused by self-gravity wakes, Icarus, 228, 247–259.

Morishima, R., S. G. Edgington, L. Spilker, (2012). Regolith grain sizes of Saturn's rings inferred from Cassini-CIRS far-infrared spectra, Icarus, 221, 888–899.

Morishima, R., L. Spilker, K. Ohtsuki, (2011), A multilayer model for thermal infrared emission of Saturns rings III: Thermal inertia inferred from Cassini CIRS, Icarus, 215, 107–127.

Morishima, R., L. Spilker, H. Salo, et al., (2010). A multilayer model for thermal infrared emission of Saturns rings II: Albedo, spins, and vertical mixing of ring particles inferred from Cassini CIRS, Icarus, 210, 330–345.

Morishima, R., H. Salo, K. Ohtsuki, (2009), A multilayer model for thermal infrared emission of Saturns rings: Basic formulation and implications for Earth-based observations, Icarus, 201, 634–654.

Morishima, R. and H. Salo, (2006), Simulations of dense planetary rings: IV. Spinning self-gravitating particles with size distribution, Icarus, 181, 272–291.

Morishima, R. and H. Salo, (2004), Spin rates of small moonlets embedded in planetary rings. I. Three-body calculations, Icarus, 167, 330–346.

Morrison, D. and D. Cruikshank, (1973), Thermal properties of the Galilean satellites, Icarus, 18, 224–236, doi: 10.1016/0019-1035(73)90207-8.

Neish, C. D. and R. D. Lorenz, (2011), Titan's global crater population: A new assessment, Planetary and Space Science, 60, 1, 26–33, doi: 10.1016/j.pss.2011.02.016.

Nicholson, P. D. and M. M. Hedman, (2010). Self-gravity wake parameters in Saturn's A and B rings, Icarus, 206, 410–423.

Nicholson, P. D., M. M. Hedman, R. N. Clark, M. R. Showalter, D. P. Cruikshank, J. N. Cuzzi, G. Filacchione, et al., (2008), A close look at Saturn's rings with Cassini VIMS, Icaurs, 193, 182–212.

Niemann, H. B., S. K. Atreya, J. E. Demick, D. Gautier, J. A. Haberman, D. N. Harpold, W. T. Kasprzak, J. I. Lunine, T. C. Owen, F. Raulin, (2010), Composition of Titan's lower atmosphere and simple surface volatiles as measured by the Cassini-Huygens probe gas chromatograph mass spectrometer experiment, Journal of Geophysical Research: Planets, 115, doi: 10.1029/2010je003659.

Niemann, H. B., S. K. Atreya, S. J. Bauer, G. R. Carignan, J. E. Demick, R. L. Frost, D. Gautier, et al., (2005), The abundances of constituents of Titan's atmosphere from the GCMS instrument on the Huygens probe, Nature, 438, 7069, 779–784, doi: 10.1038/nature04122.

Nixon, C. A., R. D. Lorenz, R. K. Achterberg, A. Buch, P. Coll, R. N. Clark, R. Courtin, et al., (2018), Titan's cold case files-Outstanding questions after Cassini-Huygens, Planetary and Space Science, 155, 50–72, doi: 10.1016/j.pss.2018.02.009.

Nixon, C. A., R. K. Achterberg, M. Adamkovics, B. Bézard, G. L. Bjoraker, T. Cornet, A. G. Hayes, et al., (2016), Titan Science with the James Webb Space Telescope, Publications of the Astronomical Society of the Pacific, 128, 959, doi: 10.1088/1538-3873/128/959/018007.

Nixon, C. A., D. E. Jennings, B. Bézard, S. Vinatier, N. A. Teanby, K. Sung, T. M. Ansty, et al., (2013a), Detection of propene in Titan's stratosphere, Astrophysical Journal Letters, 776, 1, doi: 10.1088/2041-8205/776/1/l14.

Nixon, C. A., N. A. Teanby, P. G. J. Irwin, S. M. Horst, (2013b), Upper limits for PH_3 and H_2S in Titan's atmosphere from Cassini CIRS, Icarus, 224, 1, 253–256, doi: 10.1016/j.icarus.2013.02.024.

Nixon, C. A., B. Temelso, S. Vinatier, N. A. Teanby, B. Bézard, R. K. Achterberg, K. E. Mandt, et al., (2012), Isotopic ratios in Titan's methane: measurements and modeling, The Astrophysical Journal, 749, 2, doi: 10.1088/0004-637X/749/2/159.

Nixon, C. A., R. K. Achterberg, P. N. Romani, M. Allen, X. Zhang, N. A. Teanby, P. G. J. Irwin, F. M. Flasar, (2010a), Abundances of Jupiter's trace hydrocarbons from Voyager and Cassini, Planetary and Space Science, 58, 13, 1667–1680, doi: 10.1016/j.pss.010.05.008.

Nixon, C. A., R. K. Achterberg, N. A. Teanby, P. G. J. Irwin, J.-M. Flaud, I. Kleiner, A. Dehayem-Kamadjeu, et al. (2010b), Upper limits for undetected trace species in the stratosphere of Titan, Faraday Discussions, 147, 65–81, doi: 10.1039/c003771k.

Nixon, C. A., D. E. Jennings, J. M. Flaud, B. Bézard, N. A. Teanby, P. G. J. Irwin, T. M. Ansty, A. Coustenis, S. Vinatier, F. M. Flasar, (2009a), Titan's prolific propane: The Cassini CIRS perspective, Planetary and Space Science, 57, 13, 1573–1585, doi: 10.1016/j.pss.2009.06.021.

Nixon, C. A., N. A. Teanby, S. B. Calcutt, S. Aslam, D. E. Jennings, V. G. Kunde, F. M. Flasar, et al, (2009b), Infrared limb sounding of Titan with the Cassini Composite InfraRed Spectrometer: effects of the mid-IR detector spatial responses, Applied Optics, 48, no. 10, 1912–1925.

Nixon, C. A., et al. (2008a), The 12C/13C isotopic ratio in Titan hydrocarbons from Cassini/CIRS infrared spectra, Icarus, 195, 2, 778–791, doi: 10.1016/j.icarus.2008.01.012.

Nixon, C., D. Jennings, B. Bézard, et al., (2008b), Isotopic ratios in Titan's atmosphere from Cassini CIRS limb sounding: CO2 at low and midlatitudes, The Astrophysical Journal Letters, 681, 2, L101–L103, doi: 10.1086/590553.

Nixon, C. A., R. K. Achterberg, B. J. Conrath, P. G. J. Irwin, N. A. Teanby, T. Fouchet, P. D. Parrish, et al., (2007), Meridional variations of C_2H_2 and C_2H_6 in Jupiter's atmosphere from Cassini CIRS infrared spectra, Icarus, 188, 1, 47–71, doi: 10.1016/j.icarus.2006.11.016.

Ohtsuki, K., (2006a), Rotation rate and velocity dispersion of planetary ring particles with size distribution: I. Formulation and analytic calculation, Icarus, 183, no. 2, 373–383.

Ohtsuki, K., (2006b), Rotation rate and velocity dispersion of planetary ring particles with size distribution II. Numerical simulation for gravitating particles, Icarus, 183, no. 2, 384–395.

Ohtsuki, K. and D. Toyama, (2005), Local N-body simulations for the rotation rates of particles in planetary rings, The Astronomical Journal, 130, no. 3, 1302.

Orton, G. S., L. N. Fletcher, C. M. Lisse, P. W. Chodas, A. Cheng, P. A. Yanamandra-Fisher, K. H. Baines, et al., (2011), The atmospheric influence, size and possible asteroidal nature of the July 2009 Jupiter impactor, Icarus, 211, no. 1, 587–602.

Orton, G. S., P. A. Yanamandra-Fisher, B. M. Fisher, A. J. Friedson, P. D. Parrish, J. F. Nelson, A. S. Bauermeister, et al., (2008), Semi-annual oscillations in Saturn's low-latitude stratospheric temperatures, Nature, 453, 7192, 196–199, doi: 10.1038/nature06897.

Orton, G. S., A. James Friedson, K. H. Baines, T. Z. Martin, R. A. West, J. Caldwell, H. B. Hammel, et al., (1991), Thermal maps of Jupiter: Spatial organization and time dependence of stratospheric temperatures, 1980 to 1990, Science, 252, 5005, 537–542, doi: 10.1126/science.252.5005.537.

Paige, D., J. Bachman, K. Keegan, (1994), Thermal and albedo mapping of the polar regions of Mars using Viking thermal mapper observations: 1. North polar region, Journal of Geophysical Research, vol. 99, Issue E12, pp. 25959–25991, doi: 10.1029/93JE03428.

Paranicas, C., E. Roussos, R. Decker, R. Johnson, A. Hendrix, P. Schenk, T. Cassidy, B. Dalton, C. J. Howett, P. Kollmann, W. Patterson, K. Hand, T. Nordheim, N. Krupp, D. Mitchell, (2014), The lens feature on the inner saturnian satellites, Icarus, 234, 155–161, doi: 10.1016/j.icarus.2014.02.026.

Paranicas, C., E. Roussos, N. Krupp, P. Kollmann, A. R. Hendrix, T. Cassidy, R. E. Johnson, P. Schenk G. Jones, J. Carbary, D. G. Mitchell, K. Dialynas, (2012), Energetic charged particle weathering of Saturn’s inner satellites, Planetary Space Science, 61, 60–65, doi: 10.1016/j.pss.2011.02.012.

Pierel, J. D. R., C. A. Nixon, E. Lellouch, L. N. Fletcher, G. L. Bjoraker, R. K. Achterberg, B. Bézard, B. E. Hesman, P. G. J. Irwin, F. M. Flasar, (2017), D/H Ratios on Saturn and Jupiter from Cassini CIRS, the Astronomical Journal, 154, 5, doi: 10.3847/1538-3881/aa899d.

Pilorz, S., M. Showalter, S. Edgington, (2018a), Occultations of the star Eta Carinae observed with Cassini CIRS, Icarus, in preparation.

Pilorz, S., et al., (2018b). Thermal emissivity, Icarus, in preparation.

Pilorz, S., N. Altobelli, J. Colwell, M. Showalter, (2015), Thermal transport in Saturn’s B-ring inferred from Cassini CIRS, Icarus, 254, 157–177.

Pitman, K. M., B. J. Buratti, J. A. Mosher, (2010), Disk-integrated bolometric Bond albedos and rotational light curves of saturnian satellites from Cassini Visual and Infrared Mapping Spectrometer, Icarus ,206, 537–560, doi: 10.1016/j.icarus.2009.12.001.

Pitman, K. M., B. J. Buratti, J. A. Mosher, J. M. Bauer, T. W. Momary, Robert H. Brown, P. D. Nicholson, M. M. Hedman, (2008), First high solar phase angle observations of Rhea using Cassini VIMS: Upper limits on water vapor and geologic activity, The Astrophysical Journal Letters, 680, no. 1, L65.

Porco, C. C., J. W. Weiss, D. C. Richardson, L. Dones, T. Quinn, H. Throop, (2008), Simulations of the dynamical and light-scattering behavior of Saturn's rings and the derivation of ring particle and disk properties, The Astronomical Journal, 136, no. 5, 2172.

Porco, C. C., P. Helfenstein, P. C. Thomas, A. P. Ingersoll, J. Wisdom, R. West, G. Neukum, et al., (2006), Cassini observes the active south pole of Enceladus, Science, 311, 1393–1401, doi: 10.1126/science.1123013.

Porco, C. C., E. Baker, J. Barbara, K. Beurle, A. Brahic, J. A. Burns, S. Charnoz, et al, (2005), Cassini imaging science: Initial results on Saturn's rings and small satellites, Science, 307, no. 5713, 1226–1236.

Poulet, F., D. P. Cruikshank, J. N. Cuzzi, T. L. Roush, R. G. French, (2003), Compositions of Saturn's rings A, B, and C from high resolution near-infrared spectroscopic observations, Astronomy & Astrophysics, 412, no. 1, 305–316.

Rathbun, J., J. Spencer, L. Tamppari, T. Martin, L. Bernard, L.Travis, (2004), Mapping of Io's thermal radiation by the Galileo Photopolarimeter–Radiometer (PPR) Instrument, Icarus, 169, 127–139, doi: 10.1016/j.icarus.2003.12.021.

Read, P. L., T. E. Dowling, G. Schubert, (2009), Saturn's rotation period from its atmospheric planetary-wave configuration, Nature, 460, 7255, 608–610, doi: 10.1038/nature08194.

Read, P. L., P. J. Gierasch, B. J. Conrath, A. Simon-Miller, T. Fouchet, Y. H. Yamazaki, (2006), Mapping potential-vorticity dynamics on Jupiter. I: Zonal-mean circulation from Cassini and Voyager 1 data, Quarterly Journal of the Royal Meteorological Society, 132, 618, 1577–1603, doi: 10.1256/qj.05.34.

Reffet, E., M. Verdier, C. Ferrari, (2015). Thickness of Saturn's B-ring as derived from seasonal temperature variations measured by Cassini CIRS, Icarus, 254, 276–286.

Ries, P. A. and M. Janssen, (2015), A large-scale anomaly in Enceladus' microwave emission, Icarus, 257, 88–102.

Robbins, S. J., G. R. Stewart, M. C. Lewis, J. E. Colwell, M. Sremčević, (2010), Estimating the masses of Saturn's A and B rings from high-optical depth N-body simulations and stellar occultations, Icarus, 206, no. 2, 431–445.

Rodgers, C. D., (2000), Inverse Methods for Atmospheric Sounding-Theory and Practice, Series on Atmospheric Oceanic and Planetary Physics, World Scientific Publishing Co. Pte. Ltd., Singapore, vol. 2.

- - - - - - - - - - - - - -

Roman, M. T., R. A. West, D. J. Banfield, P. J. Gierasch, R. K. Achterberg, C. A. Nixon, P. C. Thomas (2009), Determining a tilt in Titan's north-south albedo asymmetry from Cassini images, Icarus, 203, 1, 242–249, doi: 10.1016/j.icarus.2009.04.021.

Ross, M. and G. Schubert, (1989), Viscoelastic models of tidal heating in Enceladus, Icarus, 78, 90–101, doi: 10.1016/0019-1035(89)90071-7.

Rothman, L. S. and I. E. Gordon, (2013), The HITRAN molecular database, In Eighth International Conference on Atomic and Molecular Data and Their Applications (ICAMDATA), (eds.) J. D. Gillaspy, W. L. Wiese, Y. A. Podpaly, 30 September–4 October 2012, Gaithersburg, MD, vol. 1545, pp. 223–231, doi: 10.1063/1.4815858.

Rubincam, D. P., (2006), Saturn's rings, the Yarkovsky effects, and the Ring of Fire, Icarus 184, no. 2, 532–542.

Salmon, J., S. Charnoz, A. Crida, A. Brahic, (2010), Long-term and large-scale viscous evolution of dense planetary rings, Icarus, 209, no. 2, 771–785.

Salo, H. and R. G. French, (2010). The opposition and tilt effects of Saturn’s rings from HST observations, Icarus, 210, 785–816.

Salo, H. and R. Karjalainen, (2003), Photometric modeling of Saturn’s rings. I. Monte Carlo method and the effect of nonzero volume filling factor, Icarus, 164, 428–460.

Salo, H., (1995), Simulations of dense planetary rings. III. Self-gravitating identical particles, Icarus, 117, 287–312.

Salo, H., (1987), Numerical simulations of collisions between rotating particles, Icarus, 70, 37–51.

Samuelson, R. E., M. D. Smith, R. K. Achterberg, J. C. Pearl, (2007), Cassini CIRS update on stratospheric ices at Titan's winter pole, Icarus, 18, 1, 63–71, doi: 10.1016/j.icarus.2007.02.005.

Samuelson, R. E., L. A. Mayo, M. A. Knuckles, R. J. Khanna, (1997), C_4N_2 ice in Titan's north polar stratosphere, Planetary and Space Science, 45, 8, 941–948, doi: 10.1016/s0032-0633(97)00088-3.

Samuelson, R. E., (1985), Clouds and aerosols of Titan's atmosphere, In ESA Special Publication, vol. 241.

Samuelson, R. E., R. A. Hanel, V. G. Kunde, W. C. Maguire, (1981), Mean molecular-weight and hydrogen abundance of titans atmosphere, Nature, 292, 5825, 688-693, doi: 10.1038/292688a0.

Sánchez-Lavega, A., G. Fischer, L. N. Fletcher, E. García-Melendo, B. Hesman, S. Pérez-Hoyos, K. M. Sayanagi, L. A. Sromovsky, (2016), The great Saturn storm of 2010–2011, Chapter 13, In Saturn in the 21st Century, (eds.) K. H. Baines, F. M. Flasar, N. Krupp, T. Stallard, Cambridge University Press, pp. 377–416, doi: 10.1017/9781316227220.013.

Sayanagi, K. M., K. H. Baines, U. A. Dyudina, L. N. Fletcher, A. Sánchez-Lavega, R. A. West, (2018), Saturn’s Polar Atmosphere, Chapter 12, In Saturn in the 21st Century, (eds.)

K. H. Baines, F. M. Flasar, N. Krupp, T. Stallard, Cambridge University Press, pp. 337–376, doi: 10.1017/9781316227220.013.

Sayanagi, K. M., U. A. Dyudina, S. P. Ewald, G. Fischer, A. P. Ingersoll, W. S. Kurth, G. D. Muro, C. C. Porco, R. A. West, (2013), Dynamics of Saturn's great storm of 2010–2011 from Cassini ISS and RPWS, Icarus 223, no. 1, 460–478.

Schenk, P., D. P. Hamilton, R. E. Johnson, W. B. McKinnon, C. Paranicas, J. Schmidt, M. R. Showalter, (2011), Plasma, plumes and rings: Saturn system dynamics as recorded in global color patters on its midsize icy satellites, Icarus, 211, 740–757, doi: 10.1016/j.icarus.2010.08.016.

Schinder, P. J., F. M. Flasar, E. A. Marouf, R. G. French, C. A. McGhee, A. J. Kliore, N. J. Rappaport, E. Barbinis, D. Fleischman, A. Anabtawi, (2012), The structure of Titan's atmosphere from Cassini radio occultations: Occultations from the Prime and Equinox missions, Icarus, 221, 2, 1020–1031, doi: 10.1016/j.icarus.2012.10.021.

Schinder, P. J., F. M. Flasar, E. A. Marouf, R. G. French, C. A. McGhee, A. J. Kliore, N. J. Rappaport, E. Barbinis, D. Fleischman, A. Anabtawi (2011a), Saturn's equatorial oscillation: Evidence of descending thermal structure from Cassini radio occultations, Geophysical Research Letters, 38, doi: 10.1029/2011GL047191.

Schinder, P. J., F. M. Flasar, E. A. Marouf, R. G. French, C. A. McGhee, A. J. Kliore, N. J. Rappaport, E. Barbinis, D. Fleischman, A. Anabtawi, (2011b), The structure of Titan's atmosphere from Cassini radio occultations, Icarus, 215, 2, 460–474, doi: 10.1016/j.icarus.2011.07.030.

Schubert, G., J. D. Anderson, B. J. Travis, J. Palguta, (2007), Enceladus: Present internal structure and differentiation by early and long-term radiogenic heating, Icarus, 188, no. 2, 345–355.

Simon-Miller, A. A., B. J. Conrath, P. J. Gierasch, G. S. Orton, R. K. Achterberg, F. M. Flasar, B. M. Fisher (2006), Jupiter's atmospheric temperatures: from Voyager IRIS to Cassini CIRS, Icarus, 180, 1, 98–112, doi: 10.1016/j.icarus.2005.07.019.

Simon-Miller, A. A., P. J. Gierasch, R. F. Beebe, B. Conrath, F. M. Flasar, R. K. Achterberg, Cassini CIRS Team, (2002), New observational results concerning Jupiter's Great Red Spot, Icarus, 158, 1, 249–266, doi: 10.1006/icar.2002.6867.

Sinclair, J. A., G. S. Orton, T. K. Greathouse, L. N. Fletcher, J. I. Moses, V. Hue, P. G. J. Irwin, (2017), Jupiter's auroral-related stratospheric heating and chemistry I: Analysis of Voyager-IRIS and Cassini-CIRS spectra, Icarus, 292, 182–207, doi: 10.1016/j.icarus.2016.12.033.

Sinclair, J. A., P. G. J. Irwin, L. N. Fletcher, T. Greathouse, S. Guerlet, J. Hurley, C. Merlet, (2014), From Voyager-IRIS to Cassini-CIRS: Interannual variability in Saturn's stratosphere?, Icarus, 233, 281–292, doi: 10.1016/j.icarus.2014.02.009.

Sinclair, J. A., P. G. J. Irwin, L. N. Fletcher, J. I. Moses, T. K. Greathouse, A. J. Friedson, B. Hesman, J. Hurley, C. Merlet, (2013), Seasonal variations of temperature, acetylene and

- - - - - - - - - - - - - -

ethane in Saturn's atmosphere from 2005 to 2010, as observed by Cassini-CIRS, Icarus, 225, 1, 257–271, doi: 10.1016/j.icarus.2013.03.011.

Smith, P. H., M. T. Lemmon, R. D. Lorenz, L. A. Sromovsky, J. J. Caldwell, M. D. Allison, (1996), Titan's surface, revealed by HST imaging, Icarus, 119, 2, 336–349, doi: 10.1006/icar.1996.0023.

Spencer, J. R., F. Nimmo, Andrew P. Ingersoll, T. A. Hurford, E. S. Kite, A. R. Rhoden, J. Schmidt, C. J. A. Howett, (2018), Plume origins and plumbing: from ocean to surface, Enceladus and the Icy Moons of Saturn, 163.

Spencer, J. and F. Nimmo, (2013), Enceladus: An active ice world in the Saturn system, Annual Review Earth Planetary Science, 41, 693–717, doi: 10.1146/annurev-earth-050212-124025.

Spencer, J. R., J. C. Pearl, M. Segura, F. M. Flasar, A. Mamoutkine, P. Romani, B. Buratti, A. Hendrix, L. J. Spilker, R. M. C. Lopes, (2006), Cassini encounters Enceladus: Background and the discovery of a south polar hot spot, Science, 311, 1401–1405, doi: 10.1126/science.1121661.

Spencer, J., L. Tamppari, T. Martin, L. Travis, (1999), Temperatures on Europa from Galileo PPR: Nighttime thermal anomalies, Science, 284, 1514–1516.

Spencer, J. R., L. A. Lebofsky, M. V. Sykes, (1989), Systematic biases in radiometric diameter determinations, Icarus, 78, 337–354, doi: 10.1016/0019-1035(89)90182-6.

Spencer, J., (1987), The surfaces of Europa, Ganymede, and Callisto: An investigation using Voyager IRIS thermal infrared spectra, PhD thesis, University of Arizona.

Spilker, L. J., C. Ferrari, A. Altobelli, S. Pilorz, R. Morishima, (2018), Thermal properties of rings and ring particles, Chapter 15, In Planetary Ring Systems. Properties, Structure, and Evolution, (eds.) M. Tiscareno, A. Murray, University of Arizona Press, Tucson, AZ, pp. 399–433, doi: 10.1017/9781316286791.015.

Spilker, L. J., C. Ferrari, R. Morishima, (2013), Saturn’s ring temperatures at equinox, Icarus, 226, 316–322.

Spilker, L. J., S. H. Pilorz, B. D. Wallis, J. C. Pearl, J. N. Cuzzi, S. M. Brooks, N. Altobelli, et al., (2006), Cassini thermal observations of Saturn’s main rings: Implications for particle rotation and vertical mixing, Planetary and Space Science, 54, 1167–1176.

Spilker, L. J., S. H. Pilorz, S. G. Edgington, et al., (2005), Cassini CIRS observations of a roll-off in Saturn ring spectra at submillimeter wavelengths, Earth Moon Planets, 96, 149–163.

Spilker, L. J., C. Ferrari, J. N. Cuzzi, et al., (2003a), Saturn’s rings in the thermal infrared, Planetary and Space Science, 51, 929–935.

Spilker, L. J., S. Pilorz, C. Ferrari, J. Pearl, B. Wallis, (2003b), Thermal and energy balance measurements of Saturn’s C-ring, Bulletin of the American Astronomical Society, 35, 929.

Stofan, E., C. Elachi, J. Lunine, et al., (2007), The lakes of Titan, Nature, 445, 61–64, doi: 10.1038/nature05438.

Stooke, P.J., (2002), Tethys and Dione: New geological interpretations, Lunar Planetary Science Conference, vol. 33, 1553, https://www.lpi.usra.edu/meetings/lpsc2002/pdf/1553.pdf.

Stooke, P.J., (1989), Tethys: Volcanic and structural geology, Lunar Planetary Science Conference, March 13–17, Houston, TX, vol. 20, no. 1543.

Strobel, D. F., S. K. Atreya, B. Bézard, F. Ferri, F. M. Flasar, M. Fulchignoni, E. Lellouch, I. Müller-Wodarg (2009), Atmospheric Structure and Composition, Chapter 10, In Titan from Cassini-Huygens, (eds.) R. H. Brown, J.-P. Lebreton, J. H. Waite, Springer Netherlands, pp. 235–257, doi: 10.1007/978-1-4020-9215-2_10.

Strobel, D. F., (2008), Titan's hydrodynamically escaping atmosphere, Icarus, 193, 2, 588–594, doi: 10.1016/j.icarus.2007.08.014.

Sylvestre, M., N. A. Teanby, S. Vinatier, S. Lebonnois, P. G. J. Irwin, (2018), Seasonal evolution of C_2N_2, C_3H_4, and C_4H_2 abundances in Titan's lower stratosphere, Astronomy & Astrophysics, 609, doi: 10.1051/0004-6361/201630255.

Sylvestre, M., S. Guerlet, T. Fouchet, A. Spiga, F. M. Flasar, B. Hesman, G. L. Bjoraker, (2015), Seasonal changes in Saturn's stratosphere inferred from Cassini/CIRS limb observations, Icarus, 258, 224–238, doi: 10.1016/j.icarus.2015.05.025.

Teanby, N. A., B. Bézard, S. Vinatier, M. Sylvestre, C. A. Nixon, P. G. J. Irwin, R. J. de Kok, S. B. Calcutt, F. M. Flasar, (2017), The formation and evolution of Titan's winter polar vortex, Nature Communications, 8, doi: 10.1038/s41467-017-01839-z.

Teanby, N. A., P. G. J. Irwin, C. A. Nixon, R. de Kok, S. Vinatier, A. Coustenis, E. Sefton-Nash, S. B. Calcutt, F. M. Flasar, (2012), Active upper-atmosphere chemistry and dynamics polar circulation reversal on Titan, Nature, 491, 7426, 732–735, doi: 10.1038/nature11611.

Teanby, N. A., P. G. J. Irwin, C. A. Nixon, and R. de Kok, (2012b), Seasonal change at Titan’s poles, 43rd Lunar and Planetary Science Conference, Woodlands, TX, March 19-23, 2012, 1500.pdf

Teanby, N. A., P. G. J. Irwin, R. de Kok, (2010a), Compositional evidence for Titan's stratospheric tilt, Planetary and Space Science, 58, 5, 792–800, doi: 10.1016/j.pss.2009.12.005.

Teanby, N. A., P. G. J. Irwin, R. de Kok, C. A. Nixon, (2010b), Mapping Titan's HCN in the far infra-red: implications for photochemistry, Faraday Discussions, 147, 51–64, doi: 10.1039/c001690j.

Teanby, N. A., P. G. J. Irwin, R. de Kok, C. A. Nixon, (2010c), Seasonal changes in Titan's polar trace gas abundance observed by Cassini, The Astrophysical Journal Letters, 724, 1, L84–L89, doi: 10.1088/2041-8205/724/1/l84.

Teanby, N. A., R. de Kok, P. G. J. Irwin, (2009a), Small-scale composition and haze layering in Titan's polar vortex, Icarus, 204, 2, 645–657, doi: 10.1016/j.icarus.2009.07.027.

Teanby, N. A., P. G. J. Irwin, R. de Kok, A. Jolly, B. Bézard, C. A. Nixon, S. B. Calcutt, (2009b), Titan's stratospheric C_2N_2, C_3H_4, and C_4H_2 abundances Cassini/CIRS far-infrared spectra, Icarus, 202, 2, 620–631, doi: 10.1016/j.icarus.2009.03.022.

Teanby, N., P. Irwin, R. de Kok, et al., (2009c), Dynamical implications of seasonal and spatial variations in Titan's stratospheric composition, Philosophical Transactions of The Royal Society A-Mathematical Physical and Engineering Sciences, 367, 1889, 697–711, doi: 10.1098/rsta.2008.0164.

Teanby, N. A., R. de Kok, P. G. J. Irwin, S. Osprey, S. Vinatier, P. J. Gierasch, P. L. Read, et al., (2008a), Titan's winter polar vortex structure revealed by chemical tracers, Journal of Geophysical Research-Planets, 113, E12, doi: 10.1029/2008je003218.

Teanby, N. A., P. G. J. Irwin, R. De Kok, C. A. Nixon, A. Coustenis, E. Royer, S. B. Calcutt, et al., (2008b), Global and temporal variations in hydrocarbons and nitriles in Titan's stratosphere for northern winter observed by Cassini/CIRS, Icarus, 193, 2, 595–611, doi: 10.1016/j.icarus.2007.08.017.

Teanby, N. A., P. G. J. Irwin, R. De Kok, S. Vinatier, B. Bézard, C. A. Nixon, F. M. Flasar, et al., (2007), Vertical profiles of HCN, HC_3N, and C_2H_2 in Titan's atmosphere derived Cassini/CIRS data, Icarus, 186, 2, 364–384, doi: 10.1016/j.icarus.2006.09.024.

Teanby, N. A., L. N. Fletcher, P. G. J. Irwin, T. Fouchet, G. S. Orton, (2006a), New upper limits for hydrogen halides on Saturn derived Cassini-CIRS data, Icarus, 185, 2, 466–475, doi: 10.1016/j.icarus.2006.07.011.

Teanby, N., P. G. J. Irwin, R. De Kok, C. A. Nixon, A. Coustenis, B. Bézard, S. B. Calcutt, et al., (2006b), Latitudinal variations of HCN, HC3N, and C2N2 in Titan's stratosphere derived Cassini CIRS data, Icarus, 181, 1, 243–255, doi: 10.1016/j.icarus.2005.11.008.

Thomson, F. S., E. A. Marouf, G. L. Tyler, R. G. French, N. J. Rappoport, (2007), Periodic microstructure in Saturn's rings A and B, Geophysical Research Letters, 34, no. 24.

Tiscareno, M. S., J. A. Burns, J. N. Cuzzi, M. M. Hedman, (2010), Cassini imaging search rules out rings around Rhea, Geophysical Research Letters, vol. 37, Issue 14, L14205, doi: 10.1029/2010GL043663.

Tiscareno, M. S., J. A. Burns, P. D. Nicholson, M. M. Hedman, C. C. Porco, (2007), Cassini imaging of Saturn’s rings: II. A wavelet technique for analysis of density waves and other radial structure in the rings, Icarus, 189, 14–34.

Tokano, T., (2005), Meteorological assessment of the surface temperatures on Titan: constraints on the surface type, Icarus, 173, 1, 222–242, doi: 10.1016/j.icarus.2004.08.019.

Tomasko, M. G., B. Archinal, T. Becker, B. Bézard, M. Bushroe, M. Combes, D. Cook, et al., (2005), Rain, winds and haze during the Huygens probe's descent to Titan's surface, Nature, 438, 7069, 765–778, doi: 10.1038/nature04126.

Verbiscer, A., R. French, M. Showalter, P. Helfenstein, (2007), Enceladus: Cosmic graffiti artist caught in the act, Science, 315, 815, doi: 10.1126/ science.1134681.

Verbiscer, A. and J. Veverka, (1989), Albedo dichotomy of Rhea: Hapke analysis of Voyager photometry, Icarus, 82, 336–353, doi: 10.1016/0019-1035(89)90042-0.

Vinatier, S., B. Schmitt, B. Bézard, P. Rannou, C. Dauphin, R. De Kok, D. E. Jennings, F. M. Flasar, (2018), Study of Titan's fall southern stratospheric polar cloud composition with Cassini/CIRS: detection of benzene ice, Icarus, 310, 89–104.

Vinatier, S., B. Bézard, S. Lebonnois, N. A. Teanby, R. K. Achterberg, N. Gorius, A. Mamoutkine, et al., (2015), Seasonal variations in Titan's middle atmosphere during the northern spring derived Cassini/CIRS observations, Icarus, 250, 95–115, doi: 10.1016/j.icarus.2014.11.019.

Vinatier, S., P. Rannou, C. M. Anderson, B. Bézard, R. de Kok, R. E. Samuelson, (2012), Optical constants of Titan's stratospheric aerosols in the 70–1500 cm^{-1} spectral range constrained by Cassini/CIRS observations, Icarus, 21, 1, 5–12, doi: 10.1016/j.icarus.2012.02.009.

Vinatier, S., B. Bézard, R. de Kok, C. M. Anderson, R. E. Samuelson, C. A. Nixon, A. Mamoutkine, et al., (2010a), Analysis of Cassini/CIRS limb spectra of Titan acquired during the nominal mission II: Aerosol extinction profiles in the 600–1420 cm^{-1} spectral range, Icarus, 210, 2, 852–866, doi: 10.1016/j.icarus.2010.06.024.

Vinatier, S., B. Bézard, C. A. Nixon, A. Mamoutkine, R. C. Carlson, D. E. Jennings, E. A. Guandique, et al., (2010b), Analysis of Cassini/CIRS limb spectra of Titan acquired during the nominal mission: I. Hydrocarbons, nitriles and CO_2 vertical mixing ratio profiles, Icarus, 205, 2, 559–570, doi: 10.1016/j.icarus.2009.08.013.

Vinatier, S., B. Bézard, T. Fouchet, N. A. Teanby, R. de Kok, P. G. J. Irwin, B. J. Conrath, et al., (2007a), Vertical abundance profiles of hydrocarbons in Titan's atmosphere at 15° S and 80° N retrieved Cassini/CIRS spectra, Icarus, 188, 1, 120–138, doi: 10.1016/j.icarus.2006.10.031.

Vinatier, S., B. Bézard, C. A. Nixon, (2007b), The Titan $^{14}N/^{15}N$ and $^{12}C/^{13}C$ isotopic ratios in HCN Cassini/CIRS, Icarus, 191, 2, 712–721, doi: 10.1016/j.icarus.2007.06.001.

Vokrouhlický, D., D. Nesvorný, L. Dones, W. F. Bottke, Thermal forces on planetary ring particles: Application to the main system of Saturn, Astronomy & Astrophysics, 471, no. 2, 717–730.

Waite, J. H., H. Niemann, R. V. Yelle, W. T. Kasprzak, T. E. Cravens, J. G. Luhmann, R. L. McNutt, et al., (2005), Ion Neutral Mass Spectrometer results the first flyby of Titan, Science, 308, 5724, 982–986, doi: 10.1126/science.1110652.

Wilson, E. H. and S. K. Atreya, (2009), Titan's carbon budget and the case of the missing ethane, Journal of Physical Chemistry A, 113, 42, 11221–11226, doi: 10.1021/jp905535a.

Wilson, E. H. and S. K. Atreya, (2004), Current state of modeling the photochemistry of Titan's mutually dependent atmosphere and ionosphere, Journal of Geophysical Research: Planets 109, no. E6, doi: 10.1029/2003JE002181.

Wong, M. H., G. L. Bjoraker, M. D. Smith, F. M. Flasar, C. A. Nixon, (2004), Identification of the 10-μm ammonia ice feature on Jupiter, Planetary and Space Science, 52, 5–6, 385–395, doi: 10.1016/j.pss.2003.06.005.

Yelle, R. V., J. Cui, I. C. F. Müller-Wodarg, (2008), Methane escape Titan's atmosphere, Journal of Geophysical Research: Planets, 113, E10, doi: 10.1029/2007je003031.

Yoder, C. F., (1979), How tidal heating in Io drives the Galilean orbital resonance locks, Nature 279, 76.

Zhang, X., C. A. Nixon, R. L. Shia, R. A. West, P. G. J. Irwin, R. V. Yelle, M. A. Allen, Y. L. Yung, (2013), Radiative forcing of the stratosphere of Jupiter, Part I: Atmospheric cooling rates Voyager to Cassini, Planetary and Space Science, 88, 3–25, doi: 10.1016/j.pss.2013.07.005.